FLORIDA STATE UNIVERSITY COLLEGE OF ARTS AND SCIENCES

DOUBLY-STRANGE BARYON SPECTROSCOPY WITH THE GLUEX EXPERIMENT: GROUND STATE $\Xi(1320)$ PHOTOPRODUCTION CROSS SECTION AND PROPERTIES

 ${\rm By}$

JESSE A. HERNÁNDEZ

A Dissertation submitted to the Department of Physics in partial fulfillment of the requirements for the degree of Doctor of Philosophy

2025

Jesse A. Hernández defended this The members of the supervisory co	
	Volker Credé
	Professor Directing Dissertation
	Anke Meyer-Baese
	University Representative
	Sean Dobbs
	Committee Member
	Cincon Constint
	Simon Capstick Committee Member
	Rachel Yohay Committee Member
	Committee Weinber

The Graduate School has verified and approved the above-named committee members, and certifies that the dissertation has been approved in accordance with university requirements.

To my family, your love and encouragement drove me to always strive	e for my dreams.

ACKNOWLEDGMENTS

I would like to express my deepest gratitude to my advisor, Volker Credé, for his support, guidance, and invaluable mentorship throughout the course of my graduate studies. His encouragement and expertise have shaped both my research and my academic growth. In particular, when I transitioned from the Master's to the Ph.D. program, he saw the potential in me and helped give me the confidence to pursue and complete a Ph.D. in physics; I will be forever grateful for that.

I am also sincerely thankful to my many mentors at Florida State University whose teaching and feedback have enriched my understanding of physics and inspired me throughout this journey. In particular, I would like to thank Simon Capstick for recognizing my potential as a young undergraduate looking for direction. Through the bridge program and his continued mentorship, he provided me with the opportunity and support to grow into the researcher I've become. I'm also deeply thankful to Jorge Piekarewicz, who took me on as a bridge student and mentored me through the completion of my Master's in theoretical nuclear physics. Special thanks to Sean Dobbs, who was always ready to lend technical support and who remains an invaluable resource within the GlueX Collaboration—generous with his time, knowledge, and willingness to help others succeed.

I extend my heartfelt thanks to my colleagues, fellow graduate students, and the many friends I've made during this time, who have offered their time, ideas, and camaraderie. Your support has made both the challenges and successes of this journey more meaningful. In particular, I wish to acknowledge my two best friends, Gabriel Linera Rodriguez and Ronald Melendrez. Gabriel has been a constant source of support and friendship from the very beginning, and I truly don't have the words to express how much I appreciate having had him by my side through this entire endeavor. Ron became a close friend during the final years of my dissertation; he helped me through difficult times and always knew how to lift my spirits—whether it was going to the gym or splitting a whole chicken from Publix.

I am deeply grateful to the members of the GlueX Collaboration, whose collective expertise, teamwork, and spirit of discovery have made significant contributions to my research. It has been a privilege to be part of such a dedicated and inspiring scientific community.

Lastly, I thank my family for their endless patience, love, and encouragement. Their belief in me has been the foundation of this journey, and I could not have done it without their unwavering support. It has also been a privilege and a source of inspiration to watch my nephews grow up over the years—reminding me why I chose to keep going. I wanted to show them that with enough hard work, determination, and the support of incredible people, anything is possible.

TABLE OF CONTENTS

Li	st of '	Tables	X
Li	st of I	Figures	xi
Al	ostrac	et	ix
1	Intr	roduction	1
	1.1	Standard Model of Particle Physics	1
		1.1.1 Foundations of QFT	3
		1.1.2 Electroweak Theory	4
		1.1.3 Quantum Chromodynamics	5
	1.2	Hadron Spectroscopy	10
		1.2.1 Baryon Properties	12
	1.3	Strong QCD Models	14
		1.3.1 The Constituent Quark Model	15
		1.3.2 Lattice QCD	18
	1.4	Motivation and Status	20
	1.5	Ξ Physics at GlueX	22
2	Pre	vious Experimental Results	25
	2.1	Kaon Beam Experiments	26
	2.2	Hyperon Beam Experiments	28
	2.3	Collider Experiments	30
	2.4	Photoproduction Experiments	32
3	Glu	eX Experiment at Jefferson Lab	36
	3.1	CEBAF and Beamline	37
		3.1.1 Photon Source	37
		3.1.2 Beamline	37
	3.2	GLUEX Spectrometer	41
		3.2.1 Tracking Detectors	42

		3.2.2	Electromagnetic Calorimeters	43
		3.2.3	Scintillation Detectors	45
	3.3	Data A	Acquisition and Monitoring	47
4	Dat	a Proc	cessing and Event Selection	50
	4.1	GlueX	Z Data Preprocessing	50
		4.1.1	Track Reconstruction	50
		4.1.2	Particle Identification	51
		4.1.3	Kinematic Fitting	51
		4.1.4	Event Reconstruction	53
	4.2	Event	Selection	55
		4.2.1	Track Selection	55
		4.2.2	Event-Based Selection	56
		4.2.3	Accidental Photons	57
		4.2.4	χ^2_{ν} Cut	60
		4.2.5	Missing-Mass-Squared Cut	64
		4.2.6	Kaon Selection	67
		4.2.7	Rapidity Cuts	70
		4.2.8	Vertex Cuts	74
	4.3	Q-fact	tor Background Subtraction	77
		4.3.1	Application	78
5	Sim	ulation	n Procedure	82
	5.1	Physic	cs Generator	84
		5.1.1	t-channel Production	84
		5.1.2	Intermediate Hyperon Decay	86
	5.2	Data (Comparison	90
6	Exp	erime	ntal Methods and Results	92
	6.1	Exper	imental Cross Section Methodology	92
		6.1.1	Yield Extraction	93
	6.2	Produ	action Cross Section Results	102
		6.2.1	Differential Cross Section	102

		6.2.2	Integrated Total Cross Section	15
	6.3	Cascad	le Properties	16
		6.3.1	Cascade Spin Measurement	16
		6.3.2	Mass Measurement	.0
	6.4	Cascad	le Excitations	.2
		6.4.1	Event Selection	.2
		6.4.2	Results	3
7	Syst	tematic	Uncertainties 11	7
	7.1	Barlow	Test	7
		7.1.1	χ^2_{ν} Variations	.9
		7.1.2	Missing Mass Variations	1
		7.1.3	K_{fast}^+ Rapidity Variations	23
		7.1.4	$\sigma_{flight}(\Xi^{-})$ Variations	25
		7.1.5	$\sigma_{flight}(\Lambda)$ Variations	27
	7.2	Interna	al Systematics	29
		7.2.1	Run Period Comparison	29
		7.2.2	Accidental Subtraction Method	5
		7.2.3	Cascade Yield Extraction	7
		7.2.4	RF Beam Bunch Study	-2
		7.2.5	Spring 2017 Rest Version	-6
	7.3	Extern	al Systematics	8
		7.3.1	Luminosity Normalization	8
		7.3.2	Track Efficiencies	8
8	Con	clusion	n 15	1
	8.1	Summa	ary	1
	8.2	Outloo	k	6
		8.2.1	Ξ Polarization Observables	7
		8.2.2	Excitation Spectrum with GLUEX-II	8
		823	Kr Facility at CLUEY	: '

References		 •										 			 		1	62
Biographical Sketch												 			 		1	73

LIST OF TABLES

1.1	A table of the light quark quantum numbers including isospin, I , strangeness, S , and charge, Q	12
1.2	The lightest ground state baryons composed of light quarks and their masses and quantum numbers	14
1.3	This table shows the known Ξ hyperons and their seen decay channels created from the current listing from the PDG [30]	21
4.1	A table of the timing cuts for all the detector systems used in the pre-selection criteria by GlueX	55
4.2	Table of tuned cuts on GlueX and simulated data in this analysis	57
4.3	Parameters of the signal and background probability-density functions and the constraints imposed on them. A Johnson's S_U pdf was used to describe the signal and a first-order Chebychev polynomial was used to describe the background.	80
6.1	The best fit β values extracted under the spin-1/2 hypothesis to the accepted-corrected angular distributions in data	107
6.2	Table of extracted Ξ^- mass values for data and Monte Carlo simulation and the corrected mass	110
6.3	Table of tuned cuts on GlueX and simulated data in this analysis	114
7.1	All of the performed variations on the nominal cuts to calculate the Barlow test.	118
7.2	Calculated systematic uncertainties for the GlueX-I run period comparison 1	130
7.3	Table showing the track efficiencies for the entire GlueX-I data	149
8.1	Table of the point-by-point systematics of the differential cross section for the GlueX-I data	153
8.2	Table of the differential cross section for the GlueX-I data	155

LIST OF FIGURES

1.1	physics	2
1.2	Quark configurations for a meson (left) and baryon (right)	7
1.3	The strong running coupling of QCD, α_S as a function of the energy scale Q depicting the asymptotic freedom of the theory where the coupling becomes weaker at smaller energy scales. Reproduced from [24]	9
1.4	A schematic representation of handedness (left) and chirality for particles (right).	10
1.5	This figure depicts the various baryons that populate the octet and decuplet of the SU(3) symmetry configurations	16
1.6	A schematic of the proposed evolution of the internal structure of the nucleon with increasing energies	18
1.7	The LQCD results of the spectrum of Ξ presented by the HSC, where the pion mass of 391 MeV is shown on the left and the pion mass of 524 MeV is shown on the right	19
1.8	A depiction of the production and decay of the reaction of study where the ground-state Ξ is assumed to be produced through t -channel meson exchange mediated through excited intermediate hyperons Y^*	23
2.1	(Left) Top view of the MPS spectrometer experimental setup with two kaon detectors placed in the forward and backwards direction. (Right) Results of the missing mass experimental technique showing the spectrum of Ξ hyperons that were resolved in the detectors. Reprinted figure with permission from [46] Copyright 1983 American Physical Society	27
2.2	(Left) The schematic view of the CERN SPS spectrometer. (Right) The resulting Ξ excitation spectrum seen in the ΛK decay channel where the $\Xi(1690)$ and $\Xi(1820)$ resonance are seen. Reproduced from [53] with permission from Springer Nature.	29
2.3	(Left) Initial result of the spectrum of excited Ξ hyperon from the Belle Collaboration in the Λ^0 K_S^0 and Σ^+ K^- decay channel from Ξ_c where the $\Xi(1690)$ is seen in both. Reproduced from [62] CC BY 3.0 (Right) The more recent results from the Belle Collaboration from Ξ_c decay of excited excited Ξ resonances in the $\Xi^ \pi^+$ decay channel where the $\Xi(1530)$, $\Xi(1620)$ and $\Xi(1960)$ are seen. Reproduced from [63] CC BY 4.0	31

2.4	The results of the LHCb Collaboartion's PWA analysis of the Ξ_b decays to excited Ξ hyperons in the ΛK decay channel. Reproduced from [69] CC BY 4.0	33
2.5	Schematic cross sectional view of the CLAS spectrometer. Reprinted from [70] Copyright 2003 with permission from Elsevier	34
2.6	(Left) The missing mass of the two kaons in the reaction $\gamma p \to K^+ K^+ X$ using CLAS g12 data where the ground state octet and decuplet Ξ resonances appear. (Right) The resulting total cross section measured by CLAS for the ground state octet (blue/green) and decuplet (red) Ξ as a function of center-of-mass energy \sqrt{s} . Reprinted figure with permission from [73] Copyright 2018 American Physical Society	35
3.1	(Left) Aerial view of the CEBAF and four experimental halls at Jefferson Lab in Newport News, Virginia. (Right) Schematic view of the CEBAF showing the linear accelerators and recirculating arcs. Reprinted from [75] Copyright 2020 with permission from Elsevier	38
3.2	An annotated schematic of the photon beamline at Gluex. Reprinted from [75] Copyright 2020 with permission from Elsevier	39
3.3	A schematic of the tagger hall for the GLUEX experiment. The dashed red lines represent the curvature of the electrons through the dipole magnet, the blue densely shaded region is the TAGM, and the sparsely populated blue dots over the remainder of the coverage is the TAGH. Reprinted from [75] Copyright 2020 with permission from Elsevier	40
3.4	The left distribution shows the photon flux and polarization as a function of the incoming beam energy measured by the TPOL and PS. The right image is the annotated schematic of the PS. Reprinted from [75] Copyright 2020 Published with permission from Elsevier	41
3.5	This figure shows the schematic of the GlueX Detector, a fully hermetic detector capable of identifying all the final state particles in the analysis channel. Reprinted from [75] Copyright 2020 Published with permission from Elsevier.	42
3.6	The left image shows a pictures of one of the modules of the straw-tube array of the CDC before installation. The right image is a schematic representation of the FDC. Rprinted from [75] Copyright 2020 Published with permission from Elsevier	44
3.7	On the left their is a schematic view of BCAL with the angular coverage. On the right an annotated schematic of the FCAL is shown. Reprinted from [75] Copyright 2020 with permission from Elsevier	45

3.8	On the left an annotated schematic of the SC is shown. On the right an image of the TOF wall is shown before installation. Reprinted from [75] Copyright 2020 with permission from Elsevier	46
3.9	The flow chart represents the data acquisition process and hardware components and capabilities at Gluex. Reprinted from [75] Copyright 2020 with permission from Elsevier.	48
3.10	A schematic representation of the computational processes used for the data monitoring at Gluex. Reprinted from [75] Copyright 2020 with permission from Elsevier.	49
4.1	The left distribution shows the energy loss in the SC as a function of the momentum of the reconstructed track used for PID. The right distribution shows the particle velocity, β as function of the particle track momentum in the TOF detector used for PID. Reprinted from [75] Copyright 2020 with permission from Elsevier	52
4.2	A flow chart of the data processing that occurs at GLUEX from data acquisition and monitoring to analysis ready ROOT trees. Reproduced from [75] Copyright 2020 Published by Elsevier B.V. All rights reserved. Reprinted from [75] Copyright 2020 with permission from Elsevier	54
4.3	Invariant $\Lambda \pi^-$ mass distribution and fit with a Johnson function Eq. (4.18) for the $\Xi(1320)^-$ signal region with all cuts from Table 4.2 applied in the data selection	58
4.4	The RF beam bunch timing for the three GlueX-I run periods	60
4.5	Figure-of-merit study and χ^2_{ν} distributions for GLUEX-I data periods	62
4.6	Fall 2018 mass distributions and fits for $\chi^2_{\nu} \in [2, 12]$	63
4.7	(Top) The FOM (black), $\frac{N_S}{\sqrt{N_S+N_B}}$, and signal-to-background ratio (red), $\frac{N_S}{N_B}$. (Bottom) The missing-mass-squared distributions of data and reconstructed Monte Carlo events for the GLUEX-I run periods	65
4.8	Fall 2018 mass distributions and fits for various missing-mass squared cuts \in [2, 48] (MeV ²)	66
4.9	(<i>Left</i>) Data, (<i>Right</i>) Simulation. 2D distributions of K_1 vs K_2 momentum for the mixed kaons before being ordered by their momentum where the bottom distribution have required to the rapidity cut discussed Section 4.2.7	68
4.10	Rows: (<i>Top</i>) Fast kaon, (<i>Bottom</i>) Slow kaon. Columns: (<i>Left</i>) 2D Momentum vs Polar Angle distributions of GlueX-I	

	data (<i>Middle</i>) 2D Momentum vs Polar Angle distributions of reconstructed MC	69
4.11	Rapidity distribution of the fast kaon ($\textbf{\textit{Left}}$) and slow kaon ($\textbf{\textit{Right}}$) for the GLUEX-I data and simulated data comparison	71
4.12	Momentum distribution of the fast kaon (Left) and slow kaon (Right) for the GlueX-I data with (<i>red points</i>) and without (<i>black points</i>) the fast kaon rapidity cut, and simulated data comparison (<i>blue area</i>)	72
4.13	(\boldsymbol{Left}) fast kaon and (\boldsymbol{Right}) slow kaon 2D Reconstructed vs Generated (Truth) Momentum distributions for kaon momentum	72
4.14	Mandelstam-t distribution for the GlueX-I data with (red points) and without (black points) the fast kaon rapidity cut, and simulated data comparison (blue area)	73
4.15	From left to right: The Z-vertex positions along the beam direction (z-direction), namely, the production vertex, $\Xi(1320)^-$ detached vertex and Λ detached vertex.	74
4.16	Ξ (signed) Z-length, $Z_{\Xi} - Z_{\gamma}$, for data and simulation with no vertex cuts applied for all GlueX-I run periods	75
4.17	Lambda (signed) Z-length, $Z_{\Lambda} - Z_{\Xi}$, for data and simulation with no vertex cuts applied for all GlueX-I run periods	75
4.18	Ξ path length significance for data and simulation with cut value shown for GLUEX-I run periods	77
4.19	Λ path length significance for data and simulation for GLUEX-I run periods. A cut value of $FS_{\Lambda}>0$ is chosen and therefore, the cut line is not visible in these distributions	77
4.20	An example of the fit procedure to one event and its nearest neighbors to extract the Q -factor for the GLUEX-I Spring 2018 run period. The solid blue and pink lines represent the fit function and signal function respectively. The dashed blue and pink line represent the function value at the mass of the event for the fit and signal used to extract the Q -factor	81
4.21	The Ξ invariant mass distributions with the signal and background determined by the Q-Factors and the extracted χ^2_{ν} for all events for all GLUEX-I run periods.	81
5.1	Flow chart of steps to generate simulations at GLUEX. Reprinted from [75] Copyright 2020 with permission from Elsevier	83
5.2	The final product of the combined GlueX-I acceptance-corrected t-distribution fit with an exponential function to extract the t-slope parameter and the generated t-distribution for comparison.	85

5.3	The rapidity for the slow kaon when the simulation is performed in the helicity frame (left) and pseudo-helicity frame (right)	87
5.4	Comparison of real data and Monte Carlo simulations for the Ξ^-, K_{fast}^+ invariant mass and intensity angular distribution of Eq. (5.5)	89
5.5	The momentum distribution for all final state particles for the Fall 2018 run period for data and reconstructed simulation	90
5.6	The momentum distribution for all final state particles for the Fall 2018 run period for reconstructed and generated simulation	91
6.1	(Left) Shows the Johnson S_U fit to reconstructed MC used to obtain the resolution parameters. (Right) The fit to data using the γ , δ obtained from the MC fit on the left	95
6.2	The fits to the $\Xi(1320)$ peak in the $\Lambda\pi^-$ invariant mass spectrum for all energy bins used in measuring the cross section for the GLUEX Fall 2018 run period.	96
6.3	The unbinned maximum likelihood fits to the $\Xi(1320)$ peak in the $\Lambda\pi^-$ invariant mass spectrum for all $-t$ -bins used in the energy bin $8.45 < E_{\gamma} < 8.68$ GeV for the GlueX Fall 2018 run period	97
6.4	Number of $\Xi(1320)$ events found the $\Lambda\pi^-$ invariant mass spectrum extracted from data for all three GlueX-I run periods	98
6.5	Number of $\Xi(1320)$ events found in the $\Lambda\pi^-$ invariant mass spectrum for reconstructed MC for all three GlueX-I run periods	99
6.6	Number of $\Xi(1320)$ events generated from the Monte Carlo simulation for all three GlueX-I run periods	100
6.7	The efficiency for all three GlueX-I run periods from Eq. (6.2)	101
6.8	Differential cross section extracted for the eight E_{γ} bins and eight $-t$ bins for all GlueX-I run periods	103
6.9	Differential cross sections extracted for the eight E_{γ} bins and seven $-t$ bins for all GlueX-I run periods combined through a statistical weighting with systematic uncertainties (blue rectangles)	104
6.10	$\gamma p \to K^+ K^+ \Xi (1320)^-$ total cross section, for all three GLUEX-I run periods compared to the CLAS Collaboration cross section data at lower beam energies [73]	105
6.11	The acceptance-corrected helicity-angular distributions, indicating $J=1/2$ quantum number, for the three Gluex-I run periods, where the black points	

	represent the data, the blue and magenta lines represent the fits and the detector efficiency is in red	108
6.12	The acceptance-corrected helicity-angular distributions, indicating $J=1/2$ quantum number, for the three GLUEX-I data, the black points represent the data, the blue line represents the fit with the fit results in the legend, and the detector efficiency in red	109
6.13	Fits done to the simulated data (Top) and data (Bottom) to extract the Ξ^- mass for the three GlueX-I run periods	111
6.14	A depiction of the production and decay of excited Cascades in the decay $\Xi^{**} \to K^- \Lambda$ as assumed to be produced through t -channel meson exchange mediated through excited intermediate hyperons Y^*	113
6.15	The invariant mass of the excited spectrum in the decay of $\Xi^{-*} \to \Lambda K^-$ from photoproduction of K^+Y^* fit with two Breit-Wigner line-shapes corresponding to the $\Xi(1690)^-$ and $\Xi(1820)^-$	115
6.16	The invariant mass of the excited spectrum in the decay of $\Xi^{-*} \to \Lambda K^-$ from photoproduction of K^+Y^* fit with two Breit-Wigner line-shapes corresponding to the $\Xi(1690)^-$ and $\Xi(1820)^-$ for bins in Mandelstam t labeled in red at the top-left of each distribution	116
7.1	The total cross section and Barlow test significance for all χ^2_{ν} variations used in this study compared to the nominal data analysis	119
7.2	The differential cross section and Barlow test significance for all χ^2_{ν} variations in all energy bins used in this study compared to the nominal data analysis	120
7.3	The total cross section and Barlow test significance for all missing-mass-squared variations used in this study compared to the nominal data analysis	121
7.4	The differential cross section and Barlow test significance for all missing-mass-squared variations in all energy bins used in this study compared to the nominal data analysis	122
7.5	The total cross section and Barlow test significance for all K_F^+ pseudo-rapidity variations used in this study compared to the nominal data analysis	123
7.6	The differential cross section and Barlow test significance for all K_F^+ pseudorapidity variations in all energy bins used in this study compared to the nominal data analysis	124
7.7	The total cross section and Barlow test significance for all Ξ flight significance variations used in this study compared to the nominal data analysis	125

7.8	The differential cross section and Barlow test significance for all Ξ flight significance variations in all energy bins used in this study compared to the nominal data analysis	126
7.9	The total cross section and Barlow test significance for all Λ flight significance variations used in this study compared to the nominal data analysis	127
7.10	The differential cross section and Barlow test significance for all Λ flight significance variations in all energy bins used in this study compared to the nominal data analysis	128
7.11	The ratio of the comparison of all three GlueX-I run periods fit with a Gaussian function with χ^2_{ν} value shown in top right	130
7.12	The significance (Eq. (7.1)) of the comparison of all three GLUEX-I run periods fit with a Gaussian function with χ^2_{ν} value shown in top right	131
7.13	Differential Cross Section comparison between GLUEX Spring 2017 and Spring 2018 data sets	132
7.14	Differential Cross Section comparison between GlueX Spring 2017 and Fall 2018 data sets	133
7.15	Differential Cross Section comparison between GlueX Spring 2018 and Fall 2018 data sets	134
7.16	The differential cross section comparison of the three accidental subtraction methods for the RF method (black), the best χ^2_{ν} method (blue) and the hybrid χ^2_{ν} method (red)	135
7.17	The differential cross section comparison of the RF method (<i>black points</i>), the hybrid χ^2_{ν} method (<i>red</i>), and the standard deviation of the methods (<i>gray band</i>).	136
7.18	An example of the unbinned likelihood fits to data for one energy bin for all six parametrization where the signal function is the same and labeled for each column and the background function for the $(top\ row)$ is a second-order Chebychev polynomial and for the $(bottom\ row)$ is a first-order Chebychev polynomial	137
7.19	The differential cross section comparison of all combinations of signal and background fit variations to the data (<i>blue points</i>) and the standard deviation (<i>gray band</i>) to be used as a point-by-point systematic uncertainty	138
7.20	The differential cross section comparison of the nominal data fit with the signal being a Johnson pdf and second-order Chebychev pdf, Eq. (4.18)), (black points), the background variation being the first-order Chebychev (blue points) and using the extracted yields from the Q-Factor method (red points)	139

7.21	The differential cross section comparison of the nominal data fit with the signal being a Voigtian pdf (black points), and the background variations being the second-order Chenychev (blue points) and the first-order Chebychev (red points)	140
7.22	The differential cross section comparison of the nominal data fit with the signal being a Monte Carlo pdf (black points), and the background variations being the second-order Chenychev (blue points) and the first-order Chebychev (red points)	141
7.23	The differential cross section comparison of the nominal data (black) and the modified data (red) where, the RF-Bunch pattern of the 2018 data sets (8 bunches) were modified to match the 2017 data set (2 bunches)	143
7.24	The differential cross section comparison of the Spring 2018 (red points) and nominal data (black points), where the RF-Bunch pattern of the 2018 data sets (8 bunches) was modified to match the 2017 data sets (2 bunches)	144
7.25	The differential cross section comparison of the Fall 2018 (red points) and nominal data (black points), where the RF-Bunch pattern of the 2018 data sets (8 bunches) was modified to match the 2017 data sets (2 bunches)	145
7.26	The differential cross section comparison of the nominal data (black) and the modified data (red) where, the REST version 3 was used for the Spring 2017 data set	146
7.27	The differential cross section comparison of the Spring 2017 REST version 4 data (black) and the modified data (red) where, the REST version 3 was used for the Spring 2017 data set	147
7.28	The angular distributions for all final state particles for the GLUEX-I data and reconstructed simulation. The dashed blue line indicated the cut off for measuring the track systematic uncertainties (shown in red)	150
8.1	This figure is showing the axis orientation needed in order to calculate the polarization observables, where we are in the center of mass of the beam and target forming the production plane [74]	158
8.2	GLUEX-II spectrometer with added DIRC detector showcasing four long horizontal bar boxes (cherekov radiators) and two photon cameras	159
8.3	The annotated proposed beamline for the K_L facility of the GLUEX experiment	.161
8.4	(Left) The schematic of the CPS detector and (Right) the schematic of the KPT used in the production of the photon and secondary kaon beam for the K_L experiment	161

ABSTRACT

In the light-quark sector, traditional quark models and, more recently, lattice QCD calculations have predicted many more baryon states than have been experimentally observed. The hyperons, baryons with strange-quark content, in particular abundantly lack these observed states, and past observations are statistically limited. For multi-strange hyperons the matter is much worse and the production mechanisms of these states in photoproduction are very poorly understood. By capitalizing on the narrow peaks, as compared to the broad and overlapping N^* and Δ^* states, characteristic of the lowest lying Ξ resonances, the systematic aspects of the spectrum can be analyzed. In addition, we can measure experimental observables such as the production cross section to study the production mechanisms of the Ξ resonances. By accumulating various experimental observables, this goal could be accomplished through Partial Wave Analysis (PWA).

The main body of work presented in this dissertation is the physics analysis and systematic study of the production cross section for the doubly strange octet ground state baryon ($\Xi(1320)$) in the exclusive t-channel photoproduction reaction $\gamma p \to K^+ Y^* \to K^+ (K^+ \Xi^-)_{Y^*}$ where $\Xi^- \to \Lambda \pi^-$ and $\Lambda \to p \pi^-$. The spin quantum number of $\Xi(1320)$ is also extracted and discussed. A preliminary result to extract the mass of $\Xi(1320)$ is also explored as a result of the statistical limitations of current measurements. Furthermore, the spectrum of the excited Ξ^* baryons are explored and discussed in the $\Xi^{*-} \to K^- \Lambda$ decay channel. The studies on the ground state and excited Ξ baryon are performed using the GLUEX Phase-I (GLUEX-I) data set. We have extracted differential cross sections from seven beam photon energy bins for $E_{\gamma} \in [6.4, 11.4]$ GeV¹ and for -t < 2.4 GeV² in the production of $K^+ Y^*$.

¹Natural units (c=1) are used for the entire body of work.

CHAPTER 1

INTRODUCTION

1.1 Standard Model of Particle Physics

The Standard Model of Particle Physics (SM), formulated in the late twentieth century, is the culmination of experimental and theoretical developments and understanding of the fundamental particles and forces that govern the universe. Underpinning the SM are the renormalizable Quantum Field Theories (QFT) that describe the interactions of nature, i.e., the electromagnetic, weak, and strong nuclear interactions, governed by Electroweak Theory (EWT), the unified theory of electromagnetism and weak interaction, and Quantum Chromodynamics (QCD), respectively. The QFTs that encode the physical properties of elementary particles and fields are built on the principle of symmetries based on gauge theory, where specific local and global symmetry groups are responsible for the properties and emergence of gauge bosons that mediate the fundamental forces.

The fundamental particles that make up the SM are depicted in Fig. 1.1 where it is divided into two categories: the three generations of fundamental fermions defined by their half-integer spin, comprising of quarks and leptons and the force carriers defined by their integer spin comprising of four vector bosons and the single scalar Higgs boson. The elementary fermionic matter in the SM consists of six quark flavors (up, down, charm, strange, top, bottom) by generation $\{(u,d), (c,s), (t,b)\}$ and similarly three pairs of leptons (electron, muon, tau) and neutrino partners $\{(e,\nu_e), (\mu,\nu_\mu), (\tau,\nu_\tau)\}$. The force carriers of the theory, the photon, gluon, W and Z bosons, are responsible for mediating the electromagnetic, strong, and weak interactions, respectively. Finally, the Higgs scalar boson ties the theory together and is responsible for the renormalizability of the theory through spontaneous symmetry breaking wherein the fundamental particles by interacting with the Higgs field obtain their mass.

Standard Model of Elementary Particles

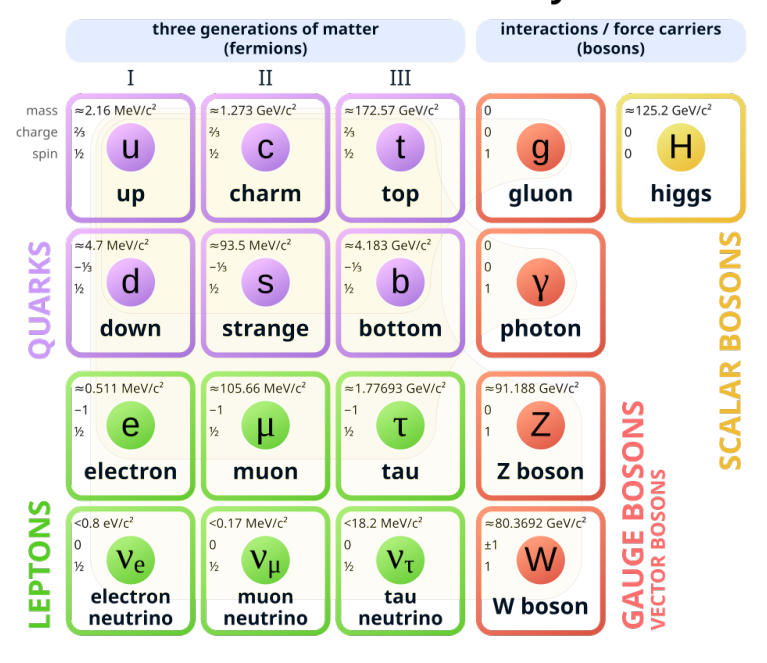


Figure 1.1: The elementary particles and force carriers in the Standard Model of particle physics.

Although the SM can be considered one of the most rigorously tested and accurate theories that describe nature, it is not complete. The theory is not compatible with the gravitational theory of general relativity; it breaks down for regimes where the graviton, the proposed particle mediator of gravitation, is to emerge. The SM only accounts for $\sim 5\%$ of all visible matter in the universe. Furthermore, only $\sim 1\%$ of the mass is generated by the Higgs mechanism with the remaining mass generated by the dynamics of the quarks and gluons in hadrons. The SM does not contain any good fundamental dark matter candidates and fails to describe dark energy. The SM also fails to describe neutrino oscillations because they are massless in the theory, and methods to include massive neutrinos pose theoretical challenges and complications. The SM does not account for the matter-antimatter asymmetry we see in nature today. Among these major open questions in physics, there are many subtle theoretical and experimental results that definitively question the completeness of the SM and Physics Beyond the Standard Model (BSM) is required.

1.1.1 Foundations of QFT

Electromagnetism as a classical field theory was formulated in the mid-20th century by James Clerk Maxwell, concisely summarized by Maxwell's equations of electrodynamics [1]. During this time, the ideas of classical Newtonian mechanics based on Galilean transformations, where space and time are absolute and velocities in inertial frames are added linearly, were incompatible with Maxwell's equations. Instead, Maxwell's equations obey Lorentz transformations, where space and time are intertwined and are no longer absolute quantities, resulting in the constant speed of light. Albert Einstein famously used this inspiration to be utifully formulate the special theory of relativity [2] and reshaped our understanding of classical mechanics. Many unresolved phenomena remained that the classical theory of electromagnetism could not reconcile until the development of quantum mechanics. Max Planck began the quantum revolution through his resolution of the black-body radiation problem in 1900 by showing how to quantize the energy of atoms as an ensemble of harmonic oscillators [3]. On this foundational principle of quantization, the rapid development and mathematical formulation of quantum mechanics emerged by the mid 1920s. The brilliance of combing quantum mechanics and special relativity into one compatible formalism led to the development of QFT; see [4] for a complete historical development.

In 1927 Paul Dirac formulated Quantum Electrodynamics (QED), a relativistic quantum abelian field theory, that was successful in explaining the spontaneous emission of light in atoms [5] and other physical phenomena. It was quickly realized that the theory could explain light-matter interactions only to the first order in perturbation theory. As a consequence, infinite solutions emerged at higher orders and made theoretical results unreliable [6]. Perturbation theory is the mathematically rigorous technique used in quantum mechanics to find approximate solutions to problems that cannot be solved exactly by adding small corrections (perturbation) to a simpler, solvable problem. In the 1940s, advances in experimental precision and capabilities widened the tension between experimental results and current theoretical calculations. In 1947 Hans Bethe published the first reliable calculation in higher orders of perturbation theory with the procedure called renormalization [7] that resolved the problem of infinities in the calculation. Renormalization is a phenomenological approach in

which the bare parameters of the QFT Lagrangian are replaced by their physically measured values. This breakthrough, extended and formalized through the 1950s, allowed calculations to be done at all orders in perturbation theory to calculate experimental results with extraordinary accuracy and success. Furthermore, it propelled QFTs into a category of their own as a complete theory that could potentially be used to describe all microscopic behavior.

As a consequence of the success of QED as a QFT with U(1) gauge symmetry associated with global charge conservation, extensions to non-abelian groups were proposed by Yang and Mills, called Yang-Mills theories with SU(N) gauge group [8], in an effort to describe the other fundamental forces through symmetry. The Yang-Mills theory would prove to be pivotal to the SM but was not taken seriously because it contained spin-1 massless bosons that were known not to exist at the time. Further developments asserting that Yang-Mills symmetries could be spontaneously broken [9] gave a clear path to massive spin-1 bosons. By 1972 the importance and acceptance of Yang-Mills theories in the context of the formulation of the SM was solidified when the theory was proven to be renormalizable [10]. A complete description of the above account is discussed in [11].

1.1.2 Electroweak Theory

EWT as mentioned previously is the unification of QED and the weak interaction under the theoretical developments discussed in Section 1.1.1 and experimental discoveries. One of the driving forces to unify the two fundamental forces began with the discovery of parity-violation in 1956 through the Wu experiment [12]. This experiment, aiming to measure whether the weak interaction violated parity, was motivated by the $\tau - \theta$ puzzle and an extensive review that showed that there was no evidence of parity conservation in the weak interactions at the time [13]. The $\tau - \theta$ puzzle is described by the discovery of two particles that had the same mass and lifetime but in two decay modes that had opposite parity $\tau^+ \to \pi^+ \pi^0$ and $\Theta^+ \to \pi^+ \pi^+ \pi^-$. The solution as a result of the Wu experiment was that these were the same particle with two different decay modes where parity was not conserved.

The formalism of EWT and the unification of electromagnetism and the weak interaction marked one of the great triumphs of the SM. By the 1950s, Quantum Electrodynamics (QED) as an abelian gauge theory of U(1) was well established and used as the theoret-

ical architecture to unify the weak interaction by extending QED as a Yang-Mills theory. Yang-Mills theories impose more stringent local symmetry requirements defined by the non-abelian SU(N) gauge group to the QFT, as opposed to QED that relied on global symmetry requirements.

By imposing local symmetry requirements, technically written as $SU(2) \times U(1)$ gauge symmetry, meant their would emerge more fundamental force carriers that were responsible for these new symmetries. Therefore, the generators of EWT are the weak isospin I, and the weak hypercharge Y, which give rise to four nonphysical gauge bosons: three W bosons of weak isospin and one B boson of hypercharge. These are analogous to the photon in QED that couples to the electric charge arising from the $U_{em}(1)$ symmetry group. After spontaneous symmetry breaking by the Higgs mechanism, the physical particles of the SM emerge as the W^{\pm} , Z, and the massless photon [14, 15]. The electric charge then arises as a linear combination of the weak isospin and the third component of weak hypercharge as

$$Q = I_3 + \frac{1}{2}Y. (1.1)$$

The Higgs boson does not interact with the electric charge directly, and therefore the photon is massless. The Higgs boson interacts with the weak isospin and weak hypercharge, and therefore the physical W and Z bosons are massive. Furthermore, because of their mixing through spontaneous symmetry breaking, the mass difference of the W and Z bosons is determined by

$$m_Z = \frac{m_W}{\cos \theta_W},\tag{1.2}$$

where $\cos \theta_W$ is the famous Weinberg or weak mixing angle, which describes the rotation of the original W and B bosons that spontaneously produce the physical photon and Z boson.

1.1.3 Quantum Chromodynamics

In parallel with the development of EWT the fundamental work of transcribing QED into a Yang-Mills theory also led to the formulation of QCD in its modern form. With the development of advanced particle experiments and technologies such as the bubble chamber in 1950 came a deluge of discoveries of hadrons, composite subatomic particles held together by the strong force, that could not be theoretically explained at the time. The hadrons

are now understood to be made up of quarks and come in two types, namely baryons and mesons. During the 1950s and early 1960s, a time aptly coined the "particle zoo", there were many attempts to categorize or group the hadrons with their charge and isospin and later the concept of *strangeness*. Strangeness was first introduced to explain the long lifetime of some of the newly discovered "strange" particles, where long-lived particles are produced with strangeness conserved but their subsequent weak decays are not; see [16] and references therein.

Historically, the introduction of SU(3) flavor symmetry gave rise to a quantitative explanation and categorization framework for the emergence of dozens of hadrons during this time. The framework coined the "Eightfold Way" by Gell-Mann [17] gave rise to the first description of the multiplet structure of baryons and mesons. By categorizing the hadrons by their strangeness and charge, it was clear that the SU(3) flavor symmetry group was a good approximation for describing the hadrons. Furthermore, this pioneering work by Gell-Mann and collaborators led them to postulate the fundamental degrees of freedom of hadrons, namely quarks [18], and was the foundation for the early quark model, a classification for hadrons in terms of their associated valence quarks. As a consequence of this framework, it was predicted that a new particle made of three strange quarks should exist. The Ω^- baryon was discovered shortly after this prediction and further verified the validity of the model. With the discovery of the Ω^- baryon it became apparent that the quarks should carry another quantum number yet to be introduced. This was also evidenced by the Pauli exclusion principle, which tells us fermions cannot occupy the same quantum state and forbids three similar quarks occupying the same quantum spin state unless there is another quantum number to break the degeneracy. These insights into the properties of quarks led to the addition of another SU(3) gauge degree of freedom, later coined color charge, which might interact via an octet of vector gauge bosons that we now know as gluons [19].

After the developments in QFT discussed in Section 1.1.1, QCD was formally developed in 1973 by Fritzsch, Gell-Mann, and Leutwyler using the concept of color charge as the source of the strong field and is now the theory that describes the strong interaction that binds quarks via gluons to form hadrons [20]. The quarks come in six types, that is, up, down, strange, charm, bottom, and top (u, d, s, c, b, t), and each carry color charge, analogous to

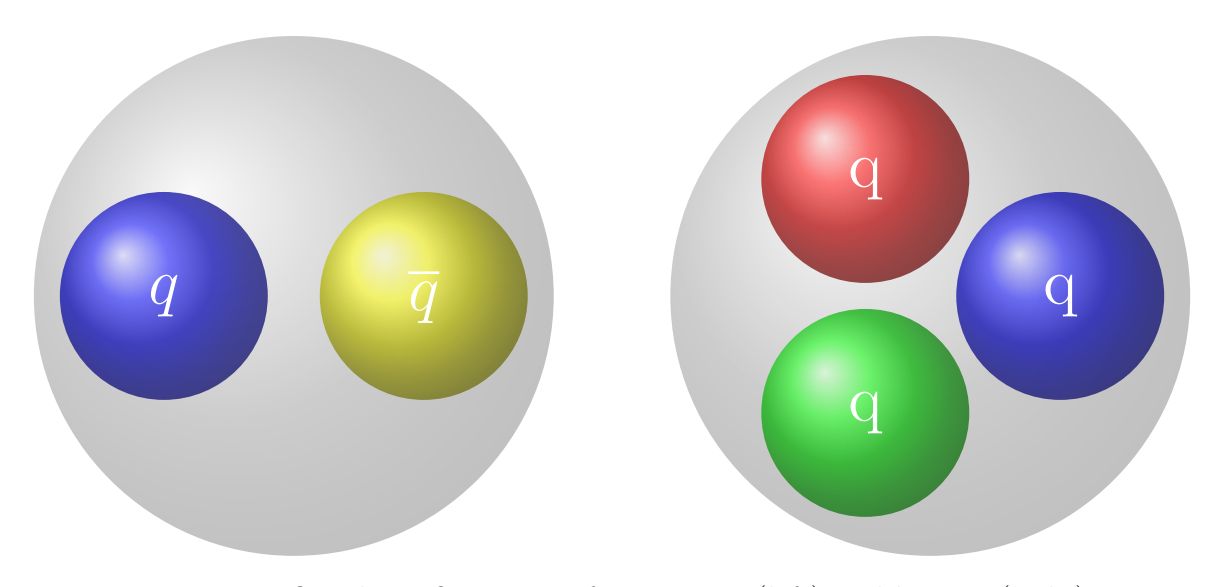


Figure 1.2: Quark configurations for a meson (left) and baryon (right).

the electric charge, which comes in three flavors: red, green, and blue (r,g,b). Hadrons are categorized into two species that form color singlets (colorless) in nature, namely mesons, made up of quark-antiquark pairs $(q\bar{q}...)$ and baryons made up of three quarks (qqq...) and generally they can have additional $q\bar{q}$ pairs that can emerge from the vacuum. The simplified picture of the quark composition of mesons and baryons is shown in Fig. 1.2. QCD has some significant features that make it a robust and challenging field of study, namely, asymptotic freedom, chiral symmetry breaking, and the experimental observation of color confinement.

Color confinement is the phenomenon in which color objects, i.e., quarks and gluons, are confined in hadrons and thus cannot be experimentally observed in nature. This is due to the fact that the force between color objects remains constant as they are pulled apart, and thus the energy density grows to the point where it is more energetically favorable to produce $q\bar{q}$ pairs from the vacuum. Put simply, trying to pull apart two color objects creates more hadrons. This idea can be understood by comparing it to the behavior of photons in QED where the electric field decreases as charged particles are pulled apart. Instead, because of the color charge of gluons and, as a consequence, gluon self-interaction, as quarks are pulled apart the force remains constant and a gluon flux tube or string is formed. The concept of color confinement is not directly produced by QCD and is yet to be analytically proven but is validated through decades of experiments and lattice QCD calculations.

Asymptotic freedom is the phenomenon for which the coupling between two quarks becomes asymptotically weaker as the energy scale increases or the length scale decreases [21, 22. This has significant consequences in high-energy physics, where in the asymptotic limit, the theory becomes perturbative, and therefore QCD can be used with perturbation theory to make theoretical calculations and predictions. As a consequence for high-energy facilities such as the Large Hadron Collider (LHC) at CERN, asymptotically free quarks rapidly convert to a shower of hadrons called jets; this phenomenon is called hadronization. Richard Feynman predicted these quarks as partons [23] from these observations, where you can infer some properties of the quarks from the resulting jets. In contrast, for the energy scales where the formation of hadrons takes place, the theory is no longer perturbative, and conventional theoretical approaches become impossible. In the non-perterbative regime of QCD, also called strong QCD, the hadrons are bound by the effect of the gluon field, potentially leading to confinement, and as a consequence of the short-range behavior of QCD the dynamics inside hadrons is robust and complex. Asymptotic freedom can be shown through calculations and measurements of the strong coupling constant in QCD depicted in Fig. 1.3, where as a function of decreasing distance it increases rapidly leading to the distance scales where the theory transitions from perterbative to strongly interacting.

Chirality is an abstract phenomenon that geometrically represents a mirror image visualized by the left picture of Fig. 1.4 where, classically by inverting all the spatial coordinates of an object (parity transformation) one can specify a chiral object. Therefore, in order to have chiral symmetry, the object must remain the same under this parity transformation. As previously discussed, the weak interaction is a chiral theory because it maximally violates parity symmetry for weak decays leading to beta decay and non-conservation of strangeness. The chirality of a particle can be related to its helicity or handedness, as depicted on the right picture of Fig. 1.4 where we define right-handed particles when the spin and momentum are aligned and left-handed particles when they are anti-aligned. For weak decays it has been shown that only left-handed particles interact and decay and therefore there is a preference in nature that breaks this symmetry. In contrast, the chiral symmetry is broken spontaneously by the Higgs mechanism, where the light masses of the quarks break the chiral symmetry explicitly. Fundamentally, this is due to the formation of a quark

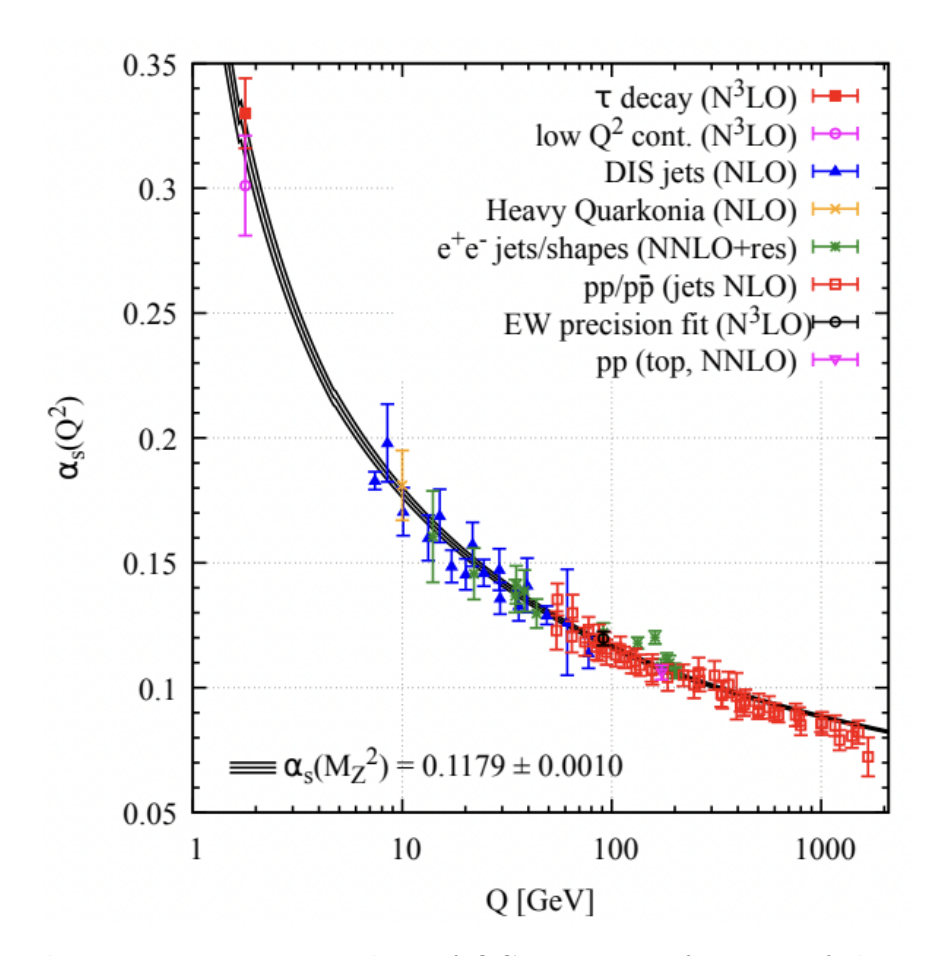


Figure 1.3: The strong running coupling of QCD, α_S as a function of the energy scale Q depicting the asymptotic freedom of the theory where the coupling becomes weaker at smaller energy scales. Reproduced from [24].

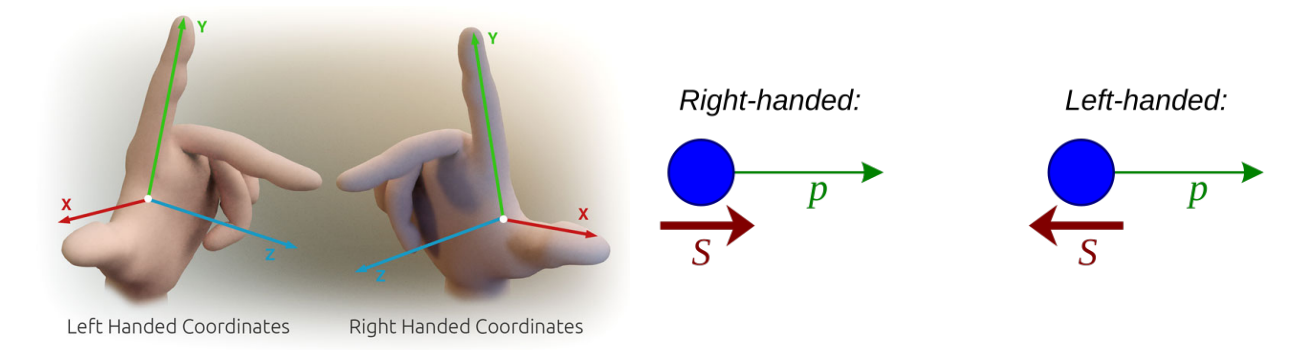


Figure 1.4: A schematic representation of handedness (left) and chirality for particles (right).

condensate that is induced by non-perturbative strong interactions with the QCD vacuum and quantum effects that are not symmetric under the flavor left and right symmetry group, $SU(3)_L \times SU(3)_R$ [25]. This signature of chiral symmetry breaking is seen in nature as the mass differences of the light flavor quarks that generate the masses of nucleons with dynamics of the gluon and quarks. The effect of spontaneous symmetry breaking also leads to the formation of Nambu-Goldstone bosons, nearly massless bosons that correspond in QCD to the eight broken generators of the $SU(3)_L \times SU(3)_R$ symmetry group [19]. These eight light particles are a consequence of the breaking of the chiral symmetry and are a residue of the strong interaction in the non-perturbative limit that form the eight mesons that mediate the hadronic decays through the exchange of pions, kaons, and etas.

1.2 Hadron Spectroscopy

Spectroscopy in its original scope was the discovery that light itself could be split into a spectrum, e.g., taking white light and splitting it into its individual parts through a prism. It was discovered that atoms of different elements could emit and absorb light at specific frequencies and thus form a spectrum of emission and absorption lines with clear unique patterns. This is known as atomic spectroscopy and with this technique came the discovery of several new elements, the study of the composition of celestial bodies and materials, and later the description of the spectrum of the hydrogen atom. Nuclear spectroscopy then made it possible to study the structure and properties of nuclei and their energy levels by

measuring the radiative decays by deflecting charged particles with magnetic fields or by measuring the energy release of nuclei through the absorption of radiation in scintillators.

In order to go deeper into the fundamental constituents of nuclear matter and study the strong force, hadron spectroscopy is needed. Hadron spectroscopy is the experimental exploration of hadrons and their properties through the analysis of hadron production or through hadronic decay processes, analogous to atomic and nuclear spectroscopy, with the goal of studying the spectrum and properties of strongly interacting matter. Hadron spectroscopy is performed in scattering experiments, where typically an incoming beam of particles interacts with nucleons in a fixed target, and the scattering products are analyzed. In fixed target experiments, the interaction of the beam and target results in the scattering of the nucleons in the production of mesons or the excitation of the nucleons in baryon production. The signature of the resonances can be studied in the invariant mass distributions of the reconstructed decay particles and show up as peaks for isolates states. In some cases unraveling the resonances populated in the excitation spectrum from the data, which, unlike the clear spectral lines that are extracted from atomic spectroscopy, can be overlapping and difficult to disentangle. For example, the resonances in the spectrum of the nucleon excitations are typically not isolated and may be composites of many overlapping states requiring sophisticated tools to extract. For resonances that are not isolated, partial wave analyses (PWA) are needed, where complex amplitudes can be extracted from data sets and the resonant states are observed as poles in the complex plane. The need for complex tools is not always warranted when the states are populated as isolated peaks. This seems to be the case for the analysis of the lowest-lying Ξ resonances and in heavy-quark hadrons. The masses of particles are extracted from the invariant mass distributions of their decay products by measuring the outgoing particle momentum and energies at experiments. For the isolated states, the mass and widths can be extracted by fitting the invariant mass distributions directly. Furthermore, by precisely measuring the masses of resonance of the same type but different charges (isospin partners) we can approximate the differences in the quark masses (mass splitting) used to constrain dynamics in quark models.

For the remainder of this work the light baryon sector, baryons made of the three lightest quarks (u, d, s), and in particular the strange baryons, also called hyperons, will be primarily

discussed. With hadron spectroscopy, researchers hope to answer the questions of which hadrons exist, what their properties are, and how are they allowed to evolve or decay? These open questions in the field need to be answered and experimentally verified to gain a full understanding of QCD, where in the strong regime there remain many unanswered questions that could completely reshape our understanding of the theory.

1.2.1 Baryon Properties

In this subsection, the relevant quantum numbers and properties of the light baryons are briefly introduced and later used to form our understanding of the spectrum of light baryons within the quark model in Section 1.3.1. In order to construct the quantum numbers relevant to the baryons the properties of the quarks are identified in Table 1.1 where the isospin, I, strangeness, S, and charge, Q, quantum numbers are shown for the light quarks.

Table 1.1: A table of the light quark quantum numbers including isospin, I, strangeness, S, and charge, Q.

Quark	$ I, I_z>$	S	Q
down	1/2, -1/2 >	0	-1/3
up	1/2, 1/2>	0	2/3
strange	0, 0>	-1	-1/3

As discussed briefly in Section 1.1.3, the baryons are fermions that are composed of three valence quarks. As fermions, baryons follow Fermi-Dirac statistics and obey the Pauli exclusion principle, therefore, their total wavefunction

$$\Psi(total) = \Psi(space)\Psi(spin)\Psi(flavor)\Psi(color)$$
(1.3)

must be antisymmetric under quark exchange. For the ground state, the spatial part of the wavefunction, $\Psi(space)$, represented by the orbital angular momentum quantum number, l, must always be symmetric (l=0) due to spherical symmetry. Conversely, the color wavefunction can only be antisymmetric for all cases under quark exchange because in nature only color singlets are observed. Therefore, for the ground state the $\Psi(spin) \cdot \Psi(flavor)$ part of the total wavefunction must be symmetric. The quark being intrinsic spin-1/2 particles

leads to the construction of $2^3=8$ quark spin states. Combining the three valence quark spins

$$\frac{1}{2} \otimes \frac{1}{2} \otimes \frac{1}{2} = \frac{3}{2}, \ \frac{1}{2}$$
 (1.4)

leads to a degenerate set of ground-state baryons with intrinsic spin-1/2 and spin-3/2 associated with four symmetric and mixed symmetry states. The flavor combinations with the light flavor (u,d,s) quarks have $3^3=27$ possible configurations of ten symmetric, 16 mixed symmetry, and a single antisymmetric wavefunction. From our fundamental understanding of the wavefunctions for each part of the total configuration state, the space of combinations to form the baryons is reduced. Furthermore, the quantum numbers associated with the fundamental symmetries further reduce the possible allowed states. The formalism of these states for the categorization of baryons will be discussed in Section 1.3.1.

Typical categorizations of hadrons are in terms of a few quantum numbers, namely spin, S, orbital angular momentum, L, total angular momentum, J, and parity, P. The total angular momentum

$$\mathcal{J} = \mathcal{L} + \mathcal{S} \tag{1.5}$$

is the addition of a baryon intrinsic spin angular momentum (Eq. (1.4)), and orbital angular momentum of quarks orbiting each other. Parity is the symmetry under an inversion of all spatial coordinates and is briefly discussed in Section 1.1.3 in the context of chirality. It was thought for a very long time that parity was a universally conserved quantity in physics until it was discovered to be broken in weak interactions where the "left" and "right" handed particles violate \mathcal{P} -symmetry. For gravitational, strong, and electromagnetic interactions \mathcal{P} -symmetry is conserved. Although in the context of the total wavefunction of certain particles the parity operation may change sign such that

$$\mathcal{P}\Psi(\vec{r}) = \pm \Psi(\vec{r}),\tag{1.6}$$

where the \pm transformations are labeled even and odd. For baryons, the transformation is related to the orbital angular momentum $(-1)^{\mathcal{L}}$ and defined as positive for the lowest state $(\mathcal{L}=0)$ by convention.

The quantum numbers of the quarks in Table 1.1 can also be used to construct the properties of the hadrons. The charge of the baryon is the combined charge of the underlying

fractional quarks and is always conserved. The isospin, modeled after spin, is a representation of the number of charged states of the baryon by the exchange of up and down quarks. Like spin, the projections of isospin give the number of states by 2I+1 and for example, the Δ baryon with four charged states would have I=3/2. Isospin is an approximate symmetry of QCD and is broken by the small mass difference of the up and down quark. Baryon number, B, is assigned to each quark (B=1/3) and antiquark (B=-1/3), and gives conventional three-quark baryons B=1. The baryon number in any hadronic reaction must be conserved because the proton remains stable and is never experimentally seen to decay. Although conventional baryons are considered three quark states, exotic baryons that maintain B=1 such as pentaquarks, four quarks (B=4/3) and an antiquark (B=-1/3), and other configurations are theoretically allowed in QCD. Interestingly, the matter-antimatter asymmetry seen today would suggest that baryon number is not conserved and remains an open question. Table 1.2 below shows all the ground state baryons ($\mathcal{J}=(1/2,\ 3/2)$) their relevant quantum numbers and mass.

Table 1.2: The lightest ground state baryons composed of light quarks and their masses and quantum numbers.

Baryon	Mass	$\mathcal{J}^{\mathcal{P}}$	I	S
\overline{N}	939	$1/2^{+}$	1/2	0
Λ	1116	$1/2^{+}$	0	-1
\sum	1193	$1/2^{+}$	1	-1
Δ	1232	$3/2^{+}$	3/2	-1
Ξ	1320	$1/2^{+}$	1/2	-2
\sum^*	1385	$3/2^{+}$	1	-1
Ξ^*	1530	$3/2^{+}$	1/2	-2
Ω	1672	$3/2^{+}$	0	-3

1.3 Strong QCD Models

As discussed in Section 1.1.3, as a consequence of asymptotic freedom and quark confinement, the theory of QCD becomes non-perturbative at the energies where hadrons are formed. This leads to the consequence that providing a complete theoretical framework and

description of strongly interacting matter in the strong QCD regime is nearly impossible. Furthermore, there is no clear path to go from the full theory of QCD, the QCD Lagrangian in the SM, to a complete description of the spectrum of hadrons and their properties. In the subsections that follow, some of the models that have driven our understanding of the spectrum of hadrons and the open questions that these imply for experimental searches will be discussed. In particular, quark models and lattice QCD (LQCD) have given insights into the systematics of the spectrum of hadrons and their properties to guide our experimental searches and further our understanding of strong QCD.

1.3.1 The Constituent Quark Model

The traditional quark model, predated by QCD, initially emerged from a classification scheme named "The Eightfold Way" to account for the influx of experimentally observed particles seen in the mid-20th century as discussed in Section 1.1.3. At the time of Gell-Mann's paper in 1961, the schematic representation of all hadrons was characterized by the particle type, i.e., mesons and baryons, and was further divided by their total spin angular momentum quantum number \mathcal{J} . The mesons form groups of octets and singlets and the baryons form groups of octets and decuplets, where by further dividing the groups into the third component of isospin I_3 , and hypercharge Y, or charge Q, and strangeness S, quantum numbers, these patterns emerged. In Fig. 1.5, an example of the baryon octet and decuplet structures formed in this representation can be seen where the axis depicts the quantum numbers in the modern representation using charge (diagonal axis) and strangeness (vertical axis). The ground state octet, $\mathcal{J}=1/2$, is composed from top to bottom of the proton and neutron (S=0), the Σ and Λ hyperons (S=-1) and the Ξ hyperon (S=-2). The "ground state" decuplet, J = 3/2, is composed from top to bottom of the Δ baryons, and again the excited Σ^* , Ξ^* , and Ω hyperons with S=0,-1,-2,-3 respectively. The underlying structure or symmetry that is encoded in this representation, namely SU(3)flavor symmetry, gave rise to the idea of quarks as the constituents of the hadrons.

The multiplet structure can be described by the approximate groups of SU(3) flavor and SU(6) spin-flavor symmetry in the isospin symmetric limit where the masses of the lightest quarks are approximately equal. In the 8-dimensional vector space of SU(3)_f, we

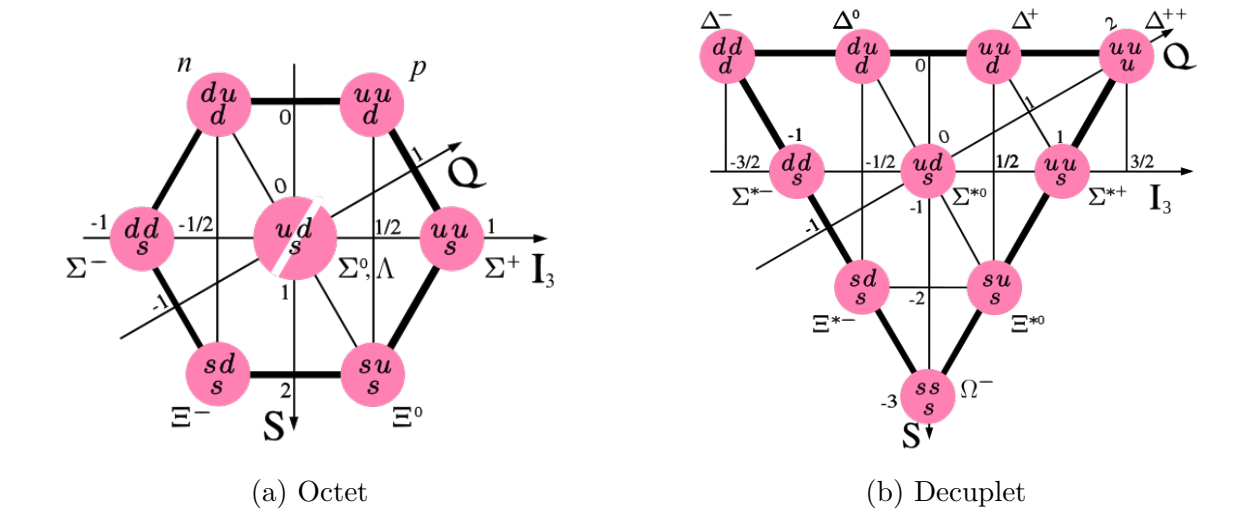


Figure 1.5: This figure depicts the various baryons that populate the octet and decuplet of the SU(3) symmetry configurations. The multiplet structures are categorized by their quantum numbers, i.e., isospin projection, I_3 , charge, Q, and strangeness, S.

can construct our light quark degrees of freedom in the fundamental representation, that is, triplet state,

$$|u\rangle = \begin{pmatrix} 1\\0\\0 \end{pmatrix}, \quad |d\rangle = \begin{pmatrix} 0\\1\\0 \end{pmatrix}, \quad |s\rangle = \begin{pmatrix} 0\\0\\1 \end{pmatrix}.$$
 (1.7)

In this basis there exists some unitary transformation, i.e., flavor rotation, that interchanges any two quark flavors. In the presence of only the strong force, this is an exact symmetry to first order. In general, the emergence of the structure of the baryons is then seen through the combination of three light quarks:

$$\mathbf{3} \otimes \mathbf{3} \otimes \mathbf{3} = \mathbf{10}_S \oplus \mathbf{8}_M \oplus \mathbf{8}_M \oplus \mathbf{8}_A, \tag{1.8}$$

where the subscripts stand for symmetric, mixed symmetric, and antisymmetric under the interchange of quark flavors. The combination of the light quarks forms the multiplet structure, that is, the singlet, decuplet, and octet structures depicted in Fig. 1.5. Due to Fermi statistics, the singlet is not observed in nature for the ground state multiplet [24].

Furthermore, this formalism can be extended to add the spin states of the spin-1/2 quarks, where now we can have spin-up or spin-down quarks that form the baryons. When

combining the three light quarks in SU(6) flavor-spin the multiplet structure is described by

$$\mathbf{6} \otimes \mathbf{6} \otimes \mathbf{6} = \mathbf{56}_S \oplus \mathbf{70}_M \oplus \mathbf{70}_M \oplus \mathbf{20}_A. \tag{1.9}$$

The SU(6) super-multiplets on the right side of Eq. 1.9 further reduce to the SU(3) multiplets with the superscripts denoting the spin degeneracy 2S + 1 in terms of the total spins of the quark system,

$$\mathbf{56} = {}^{4}\mathbf{10} \oplus {}^{2}\mathbf{8},\tag{1.10}$$

$$70 = {}^{2}10 \oplus {}^{4}8 \oplus {}^{2}8 \oplus {}^{2}1, \tag{1.11}$$

$$20 = {}^{2}8 \oplus {}^{4}1. \tag{1.12}$$

Note that the 56-plet of Eq. 1.10 contains the ground state octet with $J^P = \frac{1}{2}^+$ and decuplet with $J^P = \frac{3}{2}^+$. The 70-plet of Eq. 1.11 contains the first excitation with L = 1 that decomposes to decuplet states with $J^P = \frac{3}{2}^-, \frac{1}{2}^-$, and octet states with $J^P = \frac{5}{2}^-, \frac{3}{2}^-, \frac{1}{2}^-$.

The dynamics and structure inside of hadrons determined by QCD is quite robust and not entirely understood but can be described as a literal sea of gluons, valence quarks and virtual gluons and quarks. The dynamics driven by chiral symmetry breaking and quantum effects can be considerably simplified at the low-energy or strong regime by introducing *constituent quarks*. Therefore, the heavier constituent quarks encode explicitly the underlying dynamics and binding energy of the hadron that gives it its mass. Figure 1.6 shows a schematic representation of how the internal dynamics of the hadron may change with energy, where at the lowest energy limit the internal structure is depicted by the heavy constituent quark masses and at the opposite end the complex sea of real and virtual quarks and gluons dominate. The quark model then assumes the constituent quarks as static and the combined heavy effective masses of these quarks make up the total mass of the hadrons.

Quark potential models were then developed extending the symmetry arguments of the early quark model that include quark dynamics in order to reproduce the hadron spectrum and properties, e.g., magnetic moments, etc. Following the symmetry formalism, the conventional quark model is extended by adding by hand a confining interaction, spin-dependent interactions of various forms with their subsequent requirements, and requiring the strange

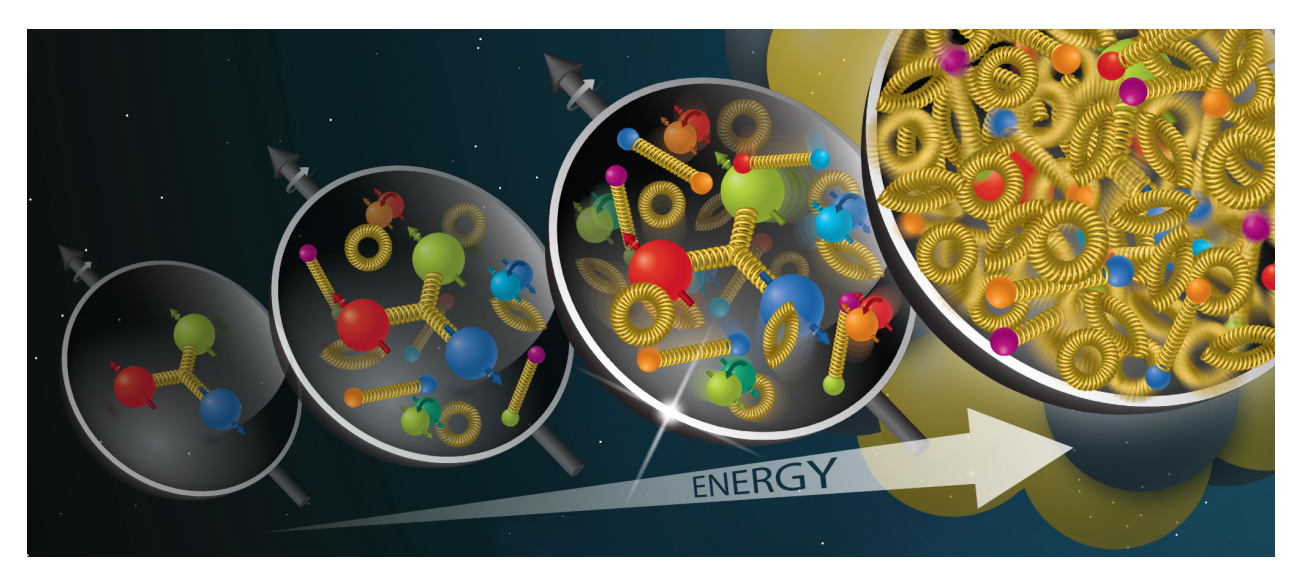


Figure 1.6: A schematic of the proposed evolution of the internal structure of the nucleon with increasing energies.

quark mass be slightly heavier than the (u, d) quarks to split the SU(3) flavor multiplet. For a detailed review of the various potential quarks models and interactions used to predict the hadron spectrum and some of their properties, see [26] and references therein. The quark models continue to serve as a guidance into some of the systematics of the spectrum of hadrons and unknowingly agree quite well with nature. Although quark models continue to be good tools for studying strong QCD, it is not entirely clear what the direct connection is to the full theory of QCD.

1.3.2 Lattice QCD

Lattice gauge theory, formulated by Kenneth Wilson in 1974 shortly after QCD was discovered [27], is a non-perturbative numerical approach to solving the full QCD theory to first principles formulated in a discrete spacetime lattice. The implementation of LQCD follows a few steps: the discretizations of spacetime into four-dimensional Euclidean space such as a hypercubic grid, putting in the gauge and fermion fields onto the lattice, construction of the action of the system or mathematical evolution of the system, definition of the integration over the path integrals defined, and finally the construction of the operators to derive the physics. A complete guide of the mathematical construction and formalism of LQCD can

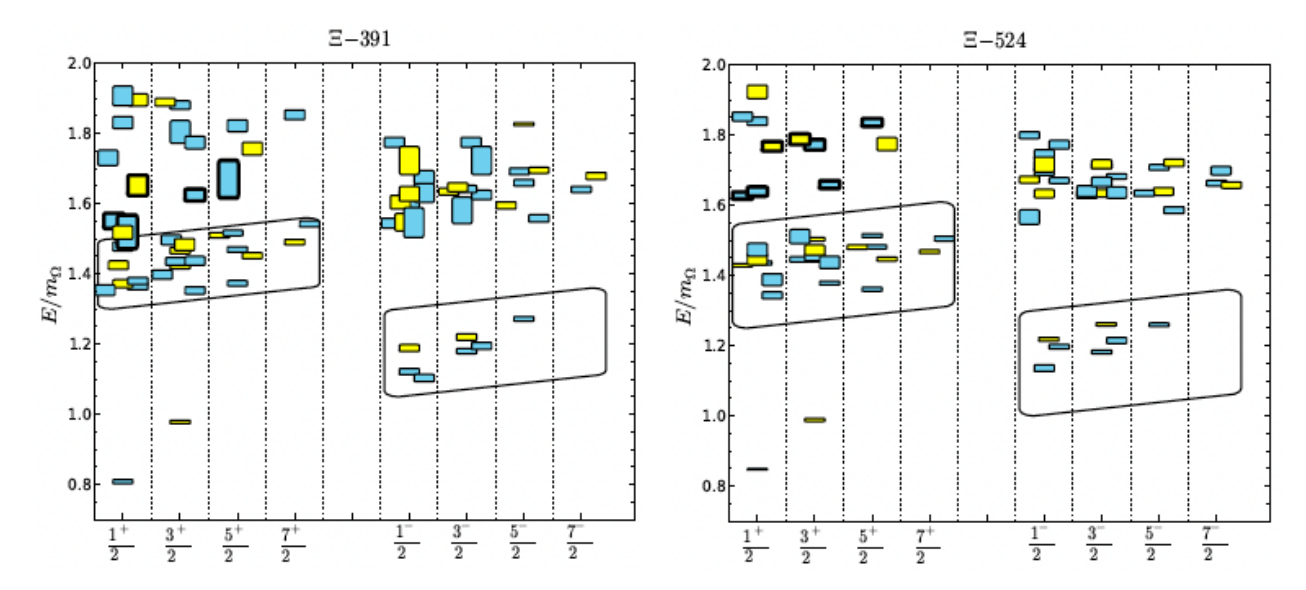


Figure 1.7: The LQCD results of the spectrum of Ξ presented by the HSC, where the pion mass of 391 MeV is shown on the left and the pion mass of 524 MeV is shown on the right. The blue shaded regions are the decuplet flavor states and the yellow shaded regions are the octet flavor states. Furthermore, the boxed regions are emphasizing the states associates with the first parity \pm excited states. Reprinted figure with permission from [29] Copyright 2013 American Physical Society.

be found in [28]. The lattice gauge theory is discretized by the lattice spacing, a. The inverse 1/a is used as a regulator, that is, the parameter used to make the calculations finite and, therefore, mathematically well defined. On the lattice the quark fields are defined at the lattice sites, and the gluon fields are defined on the links connecting the neighboring sites. Once the action of the fields, path integral formulation and operators are defined, computationally intensive Monte Carlo methods are used to solve the integrals dynamically. The lattice spacings for interpretable physical parameters must be extrapolated to $a \to 0$ to the continuum limit where QCD lives. The simulations on the lattice must be done on super-computing facilities and allow for the extraction of non-perturbative phenomena such as confinement and relevant physical observables that can be measured in the lab.

The limitations of these calculations arise from computational scaling of the numerical methods with decreasing quark masses. The calculations are then typically performed at heavy quark masses and extrapolated to the real values using chiral perturbation theory [28]. State-of-the-art facilities and numerical algorithms are now capable of reaching very close

to the physical masses of the light quarks. Although the excitations of the spectrum remain computationally limited at the physical masses, much progress is being made. The Hadron Spectrum Collaboration (HSC) has performed the LQCD calculation to extract the baryon spectrum for the light quark flavor (u, d, s) at pions masses of $m_{\pi} = 391, 524$ [29]. Figure 1.7 shows the results of the calculation for the Ξ baryon at the two pion masses and shows good agreement with the level scheme of the quark models discussed in Section 1.3.1. This figure shows the ground state and excitation spectrum of the octet (blue) and decuplet (yellow) states with $\mathcal{J}^{\mathcal{P}} \leq \frac{7}{2}^{\pm}$.

1.4 Motivation and Status

Detailed experimental information on the spectrum, structure, and decays of strangeness S=-2 Ξ (Ξ) baryons is very limited compared to non-strange and strangeness S=-1baryons. In recent years baryon spectroscopy has been mostly studied in photoproduction through nucleon excitations, N- and Δ - resonances, at Jefferson Lab with great success. In contrast to well studied nucleon excitations, the resonances with strange content remain poorly understood. In particular, the Ξ baryon composed of two strange quarks and either an up- or down-quark is one of the least known about baryon resonances in the hierarchy of light-flavor baryons. Among the known doubly strange states, the two ground state Ξ hyperons, the octet member $\Xi(1320)$ and the decuplet member $\Xi(1530)$, have a four-star status in the Particle Data Group (PDG) [30], with only four other three-star¹ candidates. On the other hand, more than 20 N^* and Δ^* resonances are rated with at least three stars by the PDG. And of the six Ξ states that have at least three-star ratings, only two are listed with weak experimental evidence for their spin-parity $(\mathcal{J}^{\mathcal{P}})$ quantum numbers: $\Xi(1530)\frac{3}{2}^+$ [31], $\Xi(1820)\frac{3}{2}^{-}$ [32]. The status of the known Ξ states and likelihood of their existence from experimental evidence is shown in Table 1.3 and has not changed much since 1988 [24]. Only recently, the status of the $\Xi(1620)$ rating has been improved to a two-star rating [30]. All other $\mathcal{J}^{\mathcal{P}}$ assignments are merely based on quark model predictions. GlueX has already

¹See Table 1.3 for meaning of the star system used by the PDG.

Table 1.3: This table shows the known Ξ hyperons and their seen decay channels created from the current listing from the PDG [30]. The star rating system ranging from 4 stars to 1 star meaning its existence is certain to evidence of existence is poor, respectively.

Particle	Status	J^P	Seen Channels
$\Xi(1320)$	****	$\frac{1}{2}^{+}$	$\Rightarrow \Lambda \pi$ (weak decay)
$\Xi(1530)$	****	$\frac{\frac{1}{2}}{\frac{3}{2}}$ +	$\Rightarrow \Xi \pi$
$\Xi(1620)$	**		$\Rightarrow \Xi \pi$
$\Xi(1690)$	***	$\frac{1}{2}^{-}$?	$\Rightarrow \Xi \pi, YK$
$\Xi(1820)$	***	$\frac{1}{2}^{-}$?	$\Rightarrow \Xi \pi, YK, \Xi(1530)\pi$
$\Xi(1950)$	***		$\Rightarrow \Xi \pi, \ \Lambda K, \ \Xi(1530)\pi$
$\Xi(2030)$	***	$\frac{5}{2}$?	$\Rightarrow Y K$
$\Xi(2120)$	*		$\Rightarrow \Lambda K$
$\Xi(2250)$	**		3-body decays
$\Xi(2370)$	**		3-body decays
$\Xi(2500)$	*		$\Rightarrow YK$, 3-body decays

observed many hints for doubly strange Ξ excited states, some of which will be discussed in the analysis of $\Xi^{*-} \to K^-\Lambda$.

SU(3) flavor symmetry predicts as many Ξ resonances as N^* and Δ^* states combined, suggesting that many more Ξ resonances remain undiscovered. For every N^* state, there should be a corresponding octet Ξ^* state with similar properties. Furthermore, since the decuplet consists of Δ^* , Σ^* , Ξ^* , and Ω^* states, for every Δ^* state a decuplet Ξ^* with similar properties can be expected. In a simple quark model picture, Section 1.3.1, the strange states will fit into multiplets that correspond to those of the u, d sector. However, it could be that the dynamics of the excited baryons differs from those of the lowest-lying states; for example, the pattern of their decays may be systematically different. Are there doubly strange baryons with properties similar to those of the $\Lambda(1405)$ with $J^P = 1/2^-$ and the Roper N^* with $J^P = 1/2^+$, which do not easily fit the conventional picture of traditional quark models where the double-pole structure of the $\Lambda(1405)$ cannot be explained and the masses of the first radial excitations are typically underestimated [33]? The dependence of the physics of these unusual states on the number of strange quarks is of crucial importance to the understanding of them, which motivates the collection of a significant database on

multi-strange baryons.

In addition, the mechanism of producing doubly strange baryons is not well understood. In order to understand what produces the \(\mathbb{\Xi}\) hyperon, many accessible observables need to be experimentally extracted and a PWA conducted, which is theoretically challenging. The observables that can be extracted from the GlueX data are the differential cross section (current work) and polarization observables. Although the production cross sections for Ξ hyperons are low in photoproduction, the high-intensity photon beam available to the experiment makes these measurements possible. Understanding the underlying mechanism of production of the \(\pi\) states has been attempted theoretically in a relativistic meson-exchange model of hadron interactions [34]. This model was used to try to understand the photoproduction of the ground state Ξ resonances seen by the CLAS experiment, to be discussed in Section 2.4. The model developed by Nakayama and collaborators was later extended by including hyperons of higher mass and spin as part of the production mechanism and matched the data much better [35]. For GlueX energies the high mass and spin hyperons are easier to populate and produce the Ξ resonances. Therefore, acquiring more data at higher energies could help refine the models for the production of the Ξ resonance to interpret experimental results. The mass splitting of the isospin partners of the ground state SU(3) multiplet is also accessible using the data at GlueX and would give us a better understanding of the flavor symmetry breaking mentioned in Section 1.1.3 that is related to the difference in the quark masses.

1.5 Ξ Physics at GlueX

The Ξ octet ground states $(\Xi^0, \underline{\Xi^-})$ are studied in the GlueX experiment *via* exclusive t channel (meson exchange) processes in the reactions:

$$\gamma p \to K Y^* \to K^+ (\Xi^- K^+), K^+ (\Xi^0 K^0), K^0 (\Xi^0 K^+).$$
 (1.13)

In this first GlueX Ξ analysis, we have focused on the negatively charged ground state $\Xi(1320)^-$ to avoid a mixed final state of tracks and photons (underlined final state). Figure 1.8 shows the assumed production process [34] where both the red-highlighted t channel

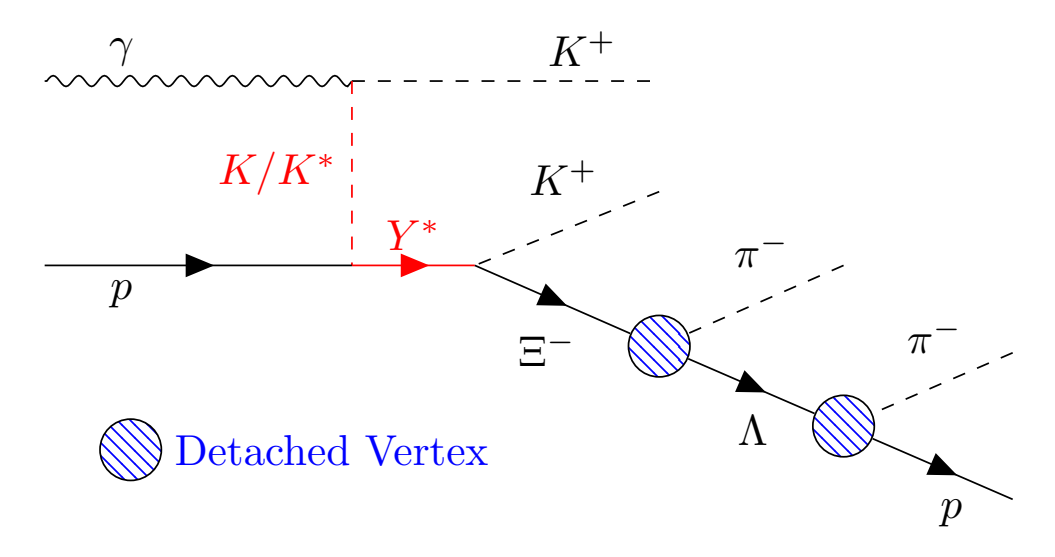


Figure 1.8: A depiction of the production and decay of the reaction of study where the ground-state Ξ is assumed to be produced through t-channel meson exchange mediated through excited intermediate hyperons Y^* .

exchanges and the Y^* hyperon resonances are unknown and the blue blobs indicate the detached vertices associated with the long-lived particle decays of the $\Xi(1320)$ and Λ . Because we know very little about the production, we have extracted the differential cross sections for the reaction $\gamma p \to K^+ K^+ \pi^- \pi^- p'$ under the assumption that the $(\pi^- \pi^- p')$ system originates from $\Xi^- \to \Lambda \pi^- \to (p'\pi^-)\pi^-$. In this analysis, the focus is less on the search for Ξ excited states and more on how doubly strange baryons are produced in photoproduction off the proton as discussed in Section 1.4. This reaction is quite robust and complex with a charged five-particle track final state mediated through electromagnetic production, the strong decay of the intermediate hyperon, and the weak decays of the Ξ and Λ hyperons.

Moreover, the Ξ excitation spectrum has also been studied in the GLUEX experiment in multiple final particle states with exclusive t channel production with final states:

$$\gamma p \to K Y^* \to K^+ (K^+ \Xi^{-*}) \to K^+ (K^+ [\Xi^- \pi^0]), K^+ (K^+ [K^- \Lambda]).$$
 (1.14)

The final state of $K^+(K^+\Xi^-\pi^0)$ is analyzed by collaborators of GLUEX and shows strong evidence for the ground state decuplet $\Xi(1530)^-$ and some weaker evidence for the excited states $\Xi(1620)^-$ and $\Xi(1690)^-$. The final state $K^+(K^+K^-\Lambda)$ (underlined) is analyzed and

discussed in this dissertation with evidence of the excited states $\Xi(1690)^-$ and $\Xi(1820)^-$ using all of the GLUEX-I data.

As an added experimental bonus, studying the Ξ hyperons gives us a clear avenue to better understand the systematics of the GLUEX experiment because it is currently used as a reference channel to improve the tracking algorithm, detector calibration, and the application of secondary vertex constraints in kinematic fitting. Kinematic fitting has proven to be a challenge for complex channels but vital for the reconstruction of the decay chain of complex reactions and the search for exotic mesons. The studies and analysis techniques that we have developed and implemented will be needed in the future for the analysis of hybrid mesons with more complicated final states. The program for studying Ξ hyperons at GlueX is extremely promising and has wide-spread implications in understanding the light-flavor sector of strong QCD and proves to be a robust avenue to understand many open questions in hadron physics.

CHAPTER 2

PREVIOUS EXPERIMENTAL RESULTS

Most of the data available on the Ξ hyperons were taken using bubble chamber and fixed target experiments from the 1960s-80s using kaon beams with fairly low statistics. The first electronic experiments to make significant contributions began in the 1980s using kaon beams and short-lived hyperon beams with very high statistics able to precisely measure the hyperon properties. In the last couple of decades, contributions to the Ξ data have come primarily from collider experiments and complementary photoproduction experiments. A recent review of the experimental results of the last 70 years of baryon spectroscopy with strangeness, as well as the status of all observed Ξ resonances, can be found in [33] and references therein.

Historically, the first discovery of hadrons with strange content was in cosmic ray experiments in the 1940s, where the K^+ meson and the Λ^0 baryon were identified. As discussed previously, with advancements in detector facilities, their was an explosion of particle discoveries from the 1950s-60s. During this time, all of the ground-state hyperons had been discovered with the final observation of Ω^- in 1964, which was famously predicted by the quark model. For experiments to study hyperons, it is ideal that the beam used contains some unit of strangeness because of flavor conservation; up until the 1990s this requirement was met. In the last 20 years, the collider experiments using non-strange probes or photoproduction have made it so that the study of hyperons can only take place as part of a final state in associated strangeness production. As a consequence, the study of doubly strange baryons is difficult due to the complex nature of the topology of their decay chains, in part due to the suppression of the direct production of doubly strange baryons in weak decays due to the GIM mechanism [36].

2.1 Kaon Beam Experiments

Up to the mid-1980s, kaon beams incident on nucleon targets, primarily on protons in the reaction K^-p , contributed most of our knowledge of the known spectrum of doubly strange hyperons. These experiments were primarily performed with a kaon beam incident on hydrogen in a bubble chamber up until the late-1970s to the first electronic experiments in the 1980s. The bubble chamber was proposed in 1952 where the properties of a superheated liquid and its relation to bubble formation were leveraged to identify particles [37]. Furthermore, by surrounding the chamber with a magnetic field, the paths of the particles are bent proportional to their mass-to-charge ratio to be identified. The ionized tracks could then be recorded with several mounted cameras. These experiments had extremely good analyzing power, but were very limited in statistics until electronic experiments were developed later on. In this section, the global spectroscopy program and contributions to the spectrum of doubly strange hyperons are discussed with kaon beams.

Lawrence Radiation Laboratory at the University of California Berkeley performed studies of Ξ hyperons for energies from threshold at 1.05 to 1.7 GeV [38] and 2.45 to 2.7 GeV [39, 40] using a K^- beam with a 72-in hydrogen bubble chamber. The latter publication identified the first observation of the $\Xi(1820)$ hyperon in decays to $\Xi\pi$, $\Xi(1530)\pi$, and $\Lambda \overline{K}$. The $\Xi(1820)$ was shortly afterwards confirmed using the Saclay 80 cm bubble chamber with a 3 GeV K^- beam in the decay $\Lambda \overline{K}$ and showed weaker evidence of the $\Xi(1950)$ resonance using the CERN Proton Synchrotron (PS) [41].

Brookhaven National Laboratory (BNL) studied Ξ hyperons with K^-p interactions at 3.9, 4.6, and 5.0 GeV with an 80-in hydrogen bubble chamber at the Alternating Gradient Synchrotron (AGS). They report concrete evidence for the suggested $\Xi(1950)$ hyperon and propose it could be a candidate for the excited octet using the Gell-Mann-Okubo mass relation [42]. Furthermore, BNL published results giving stronger evidence for the existence of the $\Xi(1820)$ hyperon and provided new evidence for the existence of $\Xi(2030)$ and $\Xi(2500)$ hyperons [43]. BNL also published results from data using the 31-in bubble chamber showing the existence of $\Xi(1620)$ hyperon resonance [44]. A nice review of the findings of these data, taken over two running periods, using the BNL 31-in bubble chamber is given in [45]. In the

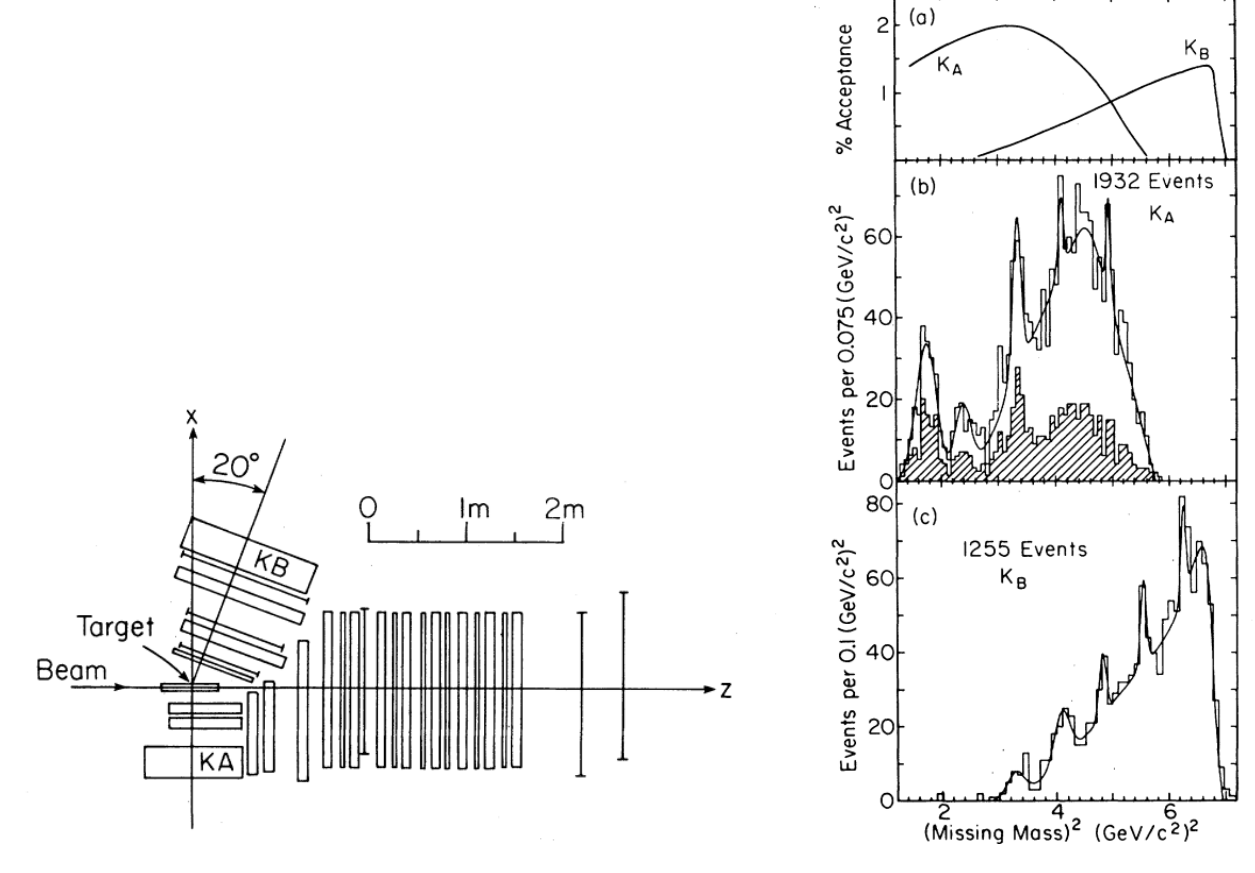


Figure 2.1: (Left) Top view of the MPS spectrometer experimental setup with two kaon detectors placed in the forward and backwards direction. (Right) Results of the missing mass experimental technique showing the spectrum of Ξ hyperons that were resolved in the detectors. Reprinted figure with permission from [46] Copyright 1983 American Physical Society.

early 1980s, BNL employed electronic methods of detection using a 5 GeV K^- beam and the Multiparticle Spectrometer (MPS) shown in Fig. 2.1 (left) where the two kaon detectors (K_A, K_B) made of layers of brass plates and scintillating material were implemented. Data taken with the MPS in the inclusive reaction $K^- p \to K_{slow}^+ X^-$ with a missing mass technique were published where they observed the $\Xi(1320), \Xi(1530), \Xi(1820), \Xi(2030), \Xi(2250), \Xi(2370)$ and $\Xi(2500)$ shown in Fig. 2.1 (right) [46]. These results confirmed and established the existence of $\Xi(2250)$ at the time.

Argonne National Laboratory (ANL) performed studies on Ξ hyperons with 5.5 GeV K^-p interactions with the MURA 30-in bubble chamber at the Argon Zero Gradient Syn-

chrotron (ZGS). ANL published their results on the Ξ hyperons where they report properties of the ground state octet and decuplet Ξ hyperon and their findings on the $\Xi(1930)$ and $\Xi(2250)$ [47].

The European Organization for Nuclear Research (CERN) studied Ξ hyperons with K^-p interactions using various experimental equipment. Further evidence of $\Xi(2030)$ was published shortly after in combination with evidence of $\Xi(2250)$ and $\Xi(2500)$ resonances using a 10 GeV K^- beam at CERN PS on the 150 cm British and 200 cm CERN bubble chambers [48]. Several years later results using the CERN 2 m hydrogen bubble chamber (HBC) were published for K^- beams of 3.13, 3.30, and 3.58 GeV showing further evidence for the $\Xi(1620)$ hyperon resonance in various reactions of $\Xi\pi$ [49]. The results using the 2m CERN HBC were also published for the first evidence of $\Xi(1690)$ with an enhancement in both neutral and negative charge channels using a coupled channel analysis in $\Lambda \overline{K}$ and $\Sigma \overline{K}$ [50].

Stanford Linear Accelerator Center (SLAC) using the large-aperture superconducting-solenoid (LASS) spectrometer with an 11 GeV rf-separated K^- beam was the last of the kaon beam facilities [51]. They accumulated a large sample of inclusively produced $\Xi(1320)$ and $\Xi(1530)$ hyperons. Using these large samples of data, they report on the production characteristics of the decays, polarization, and decay parameters of the ground states, and on their search for higher mass hyperon resonances [52]. For the higher-mass hyperons they report no resonance in the $\Xi^-\pi^+$ invariant mass and confirm the $\Xi(1820) \to \Xi(1530)\pi^-$ decay channel. The observations from this work show that the hyperons are predominantly produced in the forward direction, evident of hyperon-exchange as the production mechanism, or daughters of baryon states that were produced in hyperon-exchange.

2.2 Hyperon Beam Experiments

Following the global spectroscopy program using kaon beams discussed above and in order to obtain higher statistics to measure precise interaction and decay properties of the hyperons, hyperon beam facilities at high energies were constructed. These experiments functioned by producing high-energy hyperons with higher-energy protons on a production

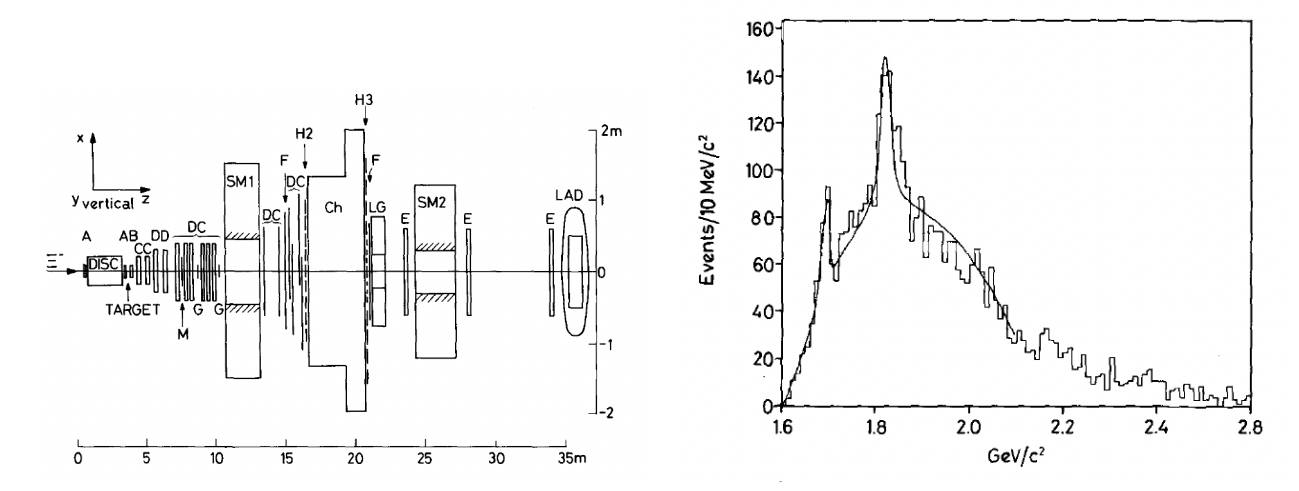


Figure 2.2: (Left) The schematic view of the CERN SPS spectrometer. (Right) The resulting Ξ excitation spectrum seen in the ΛK decay channel where the $\Xi(1690)$ and $\Xi(1820)$ resonance are seen. Reproduced from [53] with permission from Springer Nature.

target, e.g., beryllium. The hyperon beams were limited by their short decay lengths, and thus limited fluxes for experiments. The decay lengths could be extended with ever higher hyperon beam energies, providing longer decay lengths and the ability to study even the Ω hyperon.

Pioneering experimental efforts to construct hyperon beams were first implemented at the CERN PS and BNL AGS facilities at lower hyperon energies up to ~ 20 GeV. Following the experience gained from these previous experiments in the construction of hyperon beams, the CERN Super Proton Synchrotron (SPS) provided hyperon beam energies between 70 and 135 GeV [54] and was later upgraded to operate with hyperon energies between 330 to 345 GeV [55]. The above references and references therein give a review of the experimental setup and results of the CERN experiments. In addition to the production and decay properties, these experiments contributed to the existing spectrum of Ξ hyperons in various new decay channels through diffractive studies using $\Xi^- N$ [56], $\Xi^- Be$ [53, 57], Σ^- on copper and carbon targets [58]. The experimental apparatus with the beryllium target in the interaction K^- , Be and the resulting ΛK invariant mass is shown in Fig. 2.2. The final facility to use hyperon beams was the Fermi National Accelerator Facility (FNAL or Fermilab) where the highest hyperon momentum of 600 GeV Σ^- baryon delivered to the

SELEX experiment [59] was used. The Fermilab experimental groups contributed primarily to precision measurements of the properties of the ground-state hyperons and rare decays.

2.3 Collider Experiments

Very recently collider experiments, primarily interested in the heavy-quark sector (production of heavy hadrons with charm or bottom-quark content), have also been able to make contributions to the light doubly strange hyperon sector. These facilities produce copious amounts of heavy baryons or charmed mesons with large statistical samples. The light, doubly strange hyperons can then be studied in their subsequent decay reactions. In this section, the Ξ hyperon results from e^+e^- collider experiments and the proton-proton (pp) collider at LHCb will be reviewed.

The **Belle Collaboration** uses the KEKB accelerator, a two-ring asymmetric energy electron–positron collider [60], with the Belle detector [61] in Japan to study rare B-meson decays. They first published results for the existence of $\Xi(1690)$ in the Λ_c^+ decay processes [62]

$$\Lambda_c^+ \to \Xi (1690)^0 K^+ \to (\Sigma^+ K^-) K^+, (\Lambda^0 K_S^0) K^+.$$
 (2.1)

Figure Fig. 2.3 (left) shows the results of the $\Xi(1690)$ resonance in both decay channels. They later published results of the excited Ξ spectrum that is seen in the decay of $\Xi_c^+ \to \Xi^- \pi^+ \pi^+$. They report the observation of $\Xi(1620)$ with mass and width measurement and the existence of $\Xi(1690)$ with 4σ likelihood in the same data [63]. Figure 2.3 shows the results of the analysis where the right distribution (signal region) clearly shows the resonances discussed in the $\Xi^-\pi^+$ invariant mass.

Using the **BABAR** detector at the SLAC PEP-II asymmetric energy e^+e^- collider, results for the spectrum and spin properties of Ξ hyperons are presented. The $\Xi(1690)$ was observed in the $\Lambda \overline{K}$ channel for the reaction $\Lambda_c \to \Lambda \overline{K}^0 K^+$. The subsequent mass and width were then extracted and the spin was found to be consistent with spin-1/2 by studying the angular distribution [64]. These results were released in 2006 for peer-review but never published. Published results on the spin of the ground state decuplet Ξ in the decay process $\Lambda_c \to \Xi^- \pi^+ K^+$ showed that the $\Xi(1530)$ hyperon has spin and parity $3/2^+$. The analysis

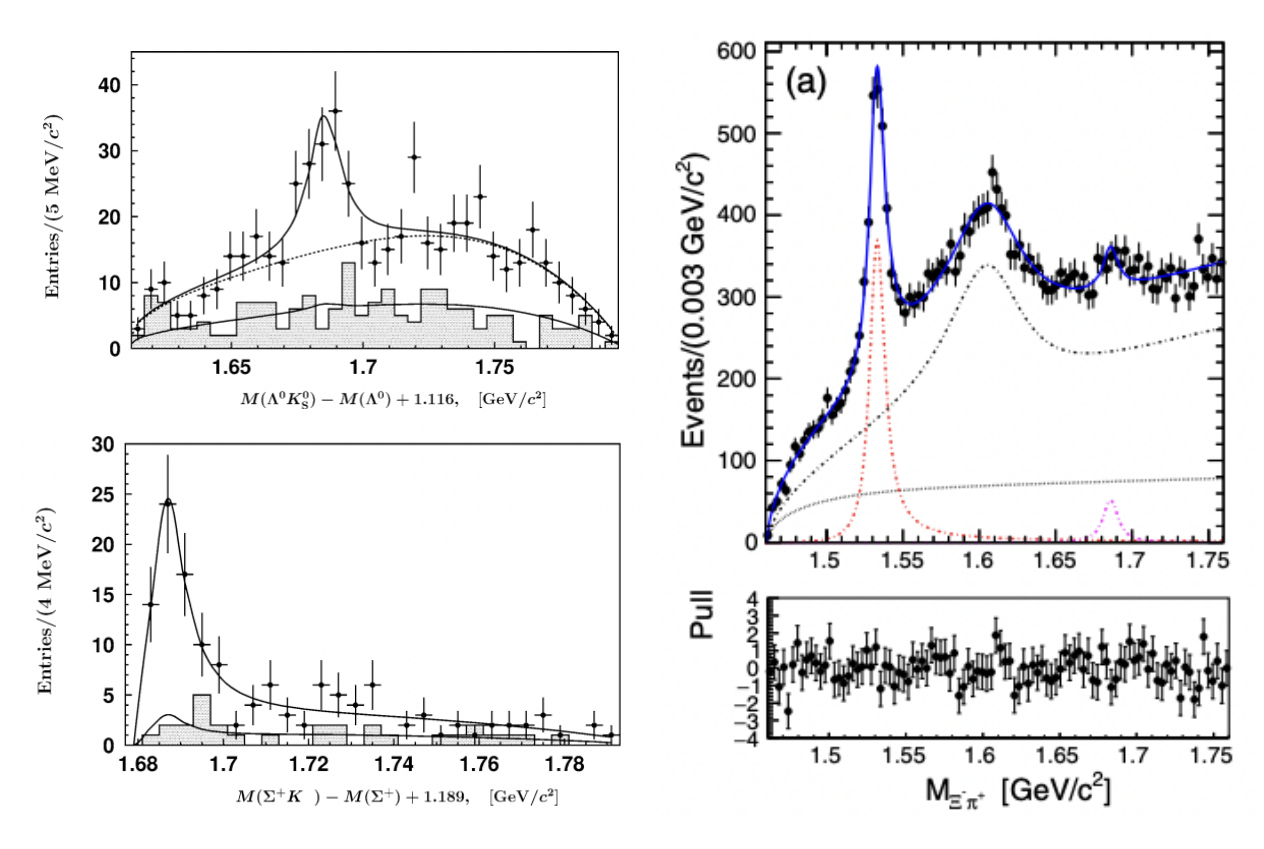


Figure 2.3: (Left) Initial result of the spectrum of excited Ξ hyperon from the Belle Collaboration in the Λ^0 K_S^0 and Σ^+ K^- decay channel from Ξ_c where the $\Xi(1690)$ is seen in both. Reproduced from [62] CC BY 3.0 (Right) The more recent results from the Belle Collaboration from Ξ_c decay of excited excited Ξ resonances in the $\Xi^ \pi^+$ decay channel where the $\Xi(1530)$, $\Xi(1620)$ and $\Xi(1960)$ are seen. Reproduced from [63] CC BY 4.0

also indicates that the $\Xi(1690)$ is consistent with spin and parity $1/2^-$ suggested by an $S^{1/2}$ amplitude at high mass and potential interference behavior at ~ 1.7 GeV [65].

The **BESIII Collaboration** has very recently published results on Ξ hyperons using the BESIII detector at the upgraded Beijing Electron-Positron Collider (BEPCII) [66] through decays of highly excited charmonium states. They first showed a significant $\Xi(1820)$ peak in the reaction $e^+e^- \to \Xi^- \overline{\Xi}^+$ and extracted its mass and width in the energy range 4.009 to 4.6 GeV [67]. They also report on the PWA analysis of the Ξ excitations seen in the charmonium decay $\psi(3686) \to K^- \Lambda \overline{\Xi}^+ + c.c.$ in the $K^- \Lambda$ system. In this analysis, the $\Xi(1690)$ and $\Xi(1820)$ resonances are observed with high significance, and then a PWA analysis is performed to extract the spin-parity, masses, widths, and branching fractions [68]. The spin and parity of $\Xi(1690)$ and $\Xi(1820)$ are determined to be $1/2^-$ and $3/2^-$. The masses are consistent with other measurements, but the widths of the PWA extraction are much broader and in tension with other direct measurements.

The **LHCb Collaboration** has also very recently published results on the Ξ hyperon spectrum using the LHCb detector using pp collision data in an amplitude analysis of $\Xi_b \to J/\psi \Lambda K^-$. They report the first observation of $\Xi(1690)$ and $\Xi(1820)$ in the decay of Ξ_b and determine their mass and width in the framework of the full amplitude analysis [69]. The results of the full amplitude analysis are shown in Fig. 2.4 where the partial waves of the four three-star Ξ resonances reported by the PDG are used, see Table 1.3.

2.4 Photoproduction Experiments

The modern landscape of experiments, alongside collider facilities, consists of spectroscopy programs in nuclear physics using electromagnetically induced reactions. For electromagnetically induced reactions the production of doubly strange hyperons is challenging due to small cross sections. Facilities that use photon beams overcome this difficulty by having very high luminosities and sophisticated detector and read-out systems. The nuclear physics programs at Jefferson Lab using electron and photon beams at the moment are the only photoproduction experiments that study doubly strange hyperons.

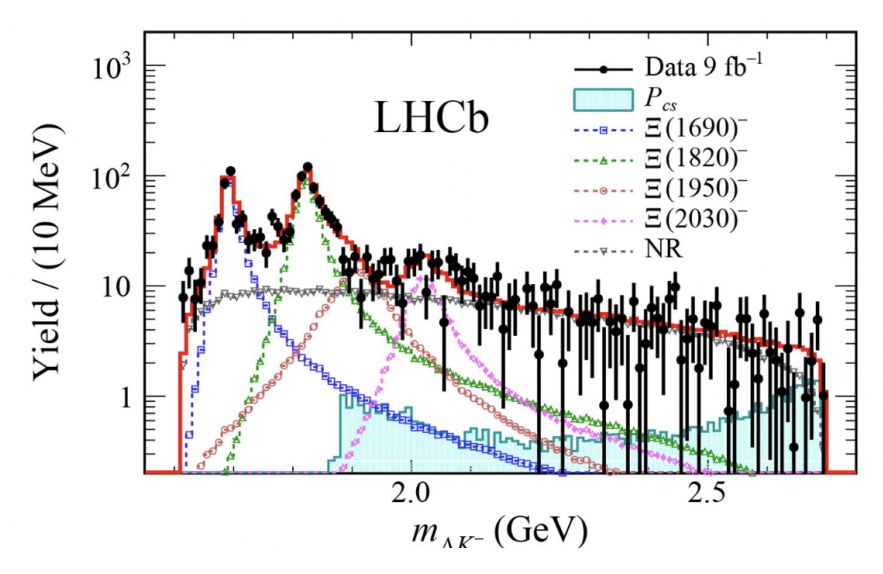


Figure 2.4: The results of the LHCb Collaboartion's PWA analysis of the Ξ_b decays to excited Ξ hyperons in the ΛK decay channel. Reproduced from [69] CC BY 4.0

The CLAS Collaboration, using the **CEBAF Large Acceptance Spectrometer** (CLAS) housed in Hall B at Jefferson Lab, has published Ξ hyperon results using data from three experimental runs denoted: g6, g11, and g12. The CLAS spectrometer is shown in Fig. 2.5. It is designed with a toroidal magnetic field to deflect particles away from the target, drift chambers for charged particle identification, Cherenkov detectors for electron identification, scintillating detectors for TOF information, and electromagnetic calorimeters for neutral shower identification. The detector is segmented into six virtually independent spectrometers allowing full reconstruction of charged particle tracks with very good momentum ($\sim 1\%$) and polar angular resolution. In contrast, the limited polar angle coverage of the electromagnetic calorimeters made exclusive final-state particle detection impossible [70].

The CLAS collaboration has been able to produce some results in photoproduction for the measurement of observables of the ground state octet and decuplet Ξ at low energy (< 5 GeV). They first published the feasibility of producing the Ξ resonances using the g6a and g6b experiments in the photon energy range 3.2 to 3.9 GeV. The results were clear peaks of $\Xi(1320)$ in the g6a data and $\Xi(1530)$ in the g6a and g6b data samples using a missing mass analysis [71]. This was followed by the first measurement of the differential (total) cross section up to an energy of 3.85 (4.75) GeV using g11 data [72] and the mass splitting of the

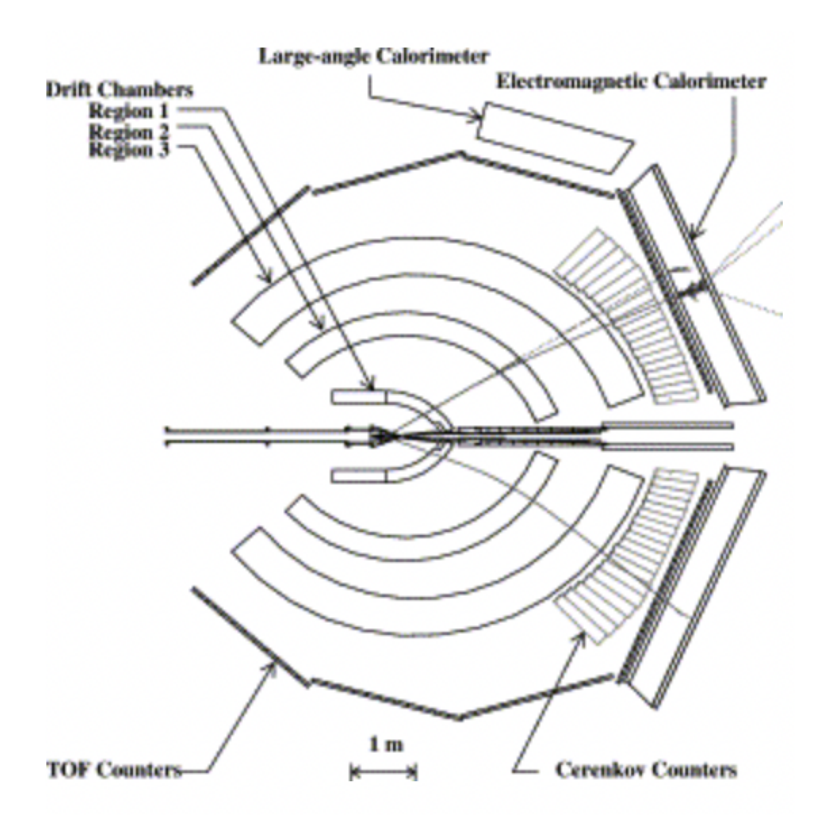


Figure 2.5: Schematic cross sectional view of the CLAS spectrometer. Reprinted from [70] Copyright 2003 with permission from Elsevier.

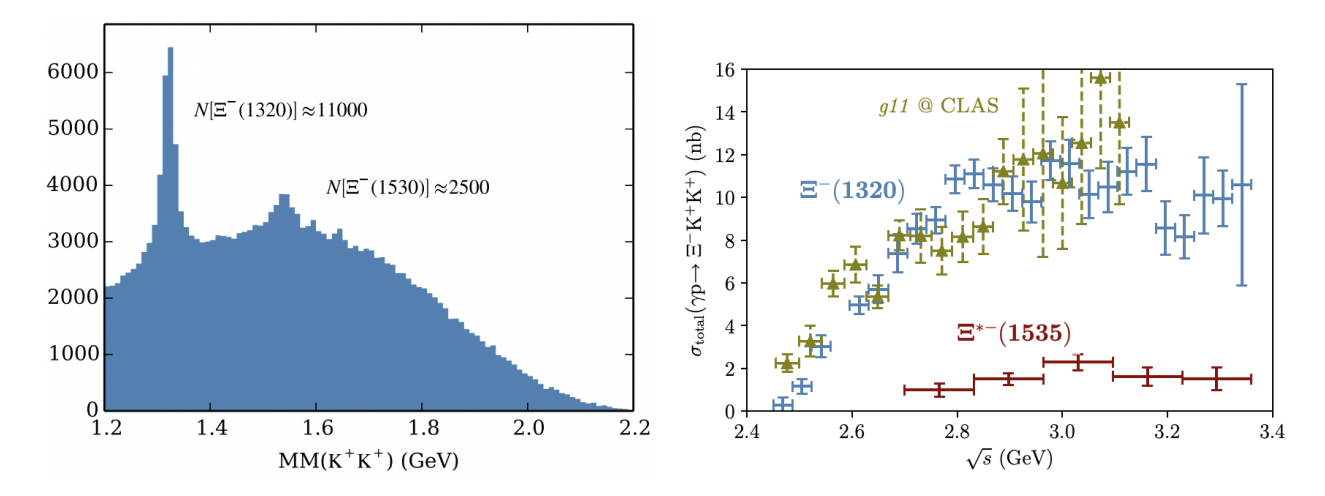


Figure 2.6: (Left) The missing mass of the two kaons in the reaction $\gamma p \to K^+ K^+ X$ using CLAS g12 data where the ground state octet and decuplet Ξ resonances appear. (Right) The resulting total cross section measured by CLAS for the ground state octet (blue/green) and decuplet (red) Ξ as a function of center-of-mass energy \sqrt{s} . Reprinted figure with permission from [73] Copyright 2018 American Physical Society.

ground state doublet (Ξ^-, Ξ^0) . More recently, in 2018, the CLAS collaboration published results on the photoproduction of Ξ hyperons that extend the center-of-mass energy and statistics from previous results with the g12 experiment [73]. They report on the total cross section for both the ground state octet and decuplet Ξ and do not find any other excitations. Furthermore, they report some upper limits for the cross sections of the missing Ξ resonances at 1690, 1820 and 1950 MeV². The results of the analysis show the spectrum from the missing mass of the kaons $M(K^+K^+)$ (left) and the total cross section (right) in Fig. 2.6.

In an effort to shed light on the production mechanism of the Ξ hyperons, CLAS also measured the induced polarization, \mathbf{P} , and the transferred polarization from circularly polarized real photons [74]. The results were compared to a relativistic meson-exchange model [34] showing good agreement with the data. The model used reinforced that Ξ hyperons are predominantly produced from high-mass, high-spin hyperons generated in t channel K/K^* exchange. The procedure for obtaining the polarization observables will be discussed in Section 8.2.1.

CHAPTER 3

GLUEX EXPERIMENT AT JEFFERSON LAB

The Gluonic Excitation (GLUEX) experiment resides in Hall D at the Thomas Jefferson National Accelerator Facility (Jefferson Lab) in Newport News, Virginia. A high-intensity linearly polarized photon beam is produced by a 12 GeV electron beam on a diamond radiator through bremsstrahlung radiation, also called breaking radiation. Downstream, the photon beam is incident on a hydrogen target where the almost hermetic GLUEX spectrometer, housing advanced particle identification systems, detects all charged tracks and neutral showers exclusively. With completion of the GLUEX-I data collection, there are 125 pb⁻¹ of data in the range of the coherent peak, $8.2 < E_{\gamma} < 9$ GeV, where the beam intensity and polarization are at its maximum. Furthermore, for calculations of cross sections in a wider range, $E_{\gamma} > 6$ GeV there is 439.6 pb⁻¹ of data available. Furthermore, with the completion of the GLUEX-II data taking with higher beam intensities, this will be the largest set of data for photoproduction.

The Gluex experiment was commissioned to map the spectrum of mesons and search for exotic hybrid states, states outside of simple quark-antiquark interactions such as gluonic excitations allowed by QCD. Furthermore, as a consequence of the high-intensity photon beam, a robust baryon spectroscopy program has been developed and could be essential to disentangle baryon signals in the search for exotic mesons. For example, baryon spectroscopy with strangeness gives us an avenue to further study the kaon systematics of the experiment. The Gluex experiment facilitates a robust photoproduction program with many physics outcomes and goals to further our understanding of strong QCD with contributions from over thirty partner institutions and over one hundred users. For a complete discussion of the detector systems in the following sections, please refer to [75] and the references therein.

3.1 CEBAF and Beamline

3.1.1 Photon Source

The Continuous Electron Beam Accelerator Facility (CEBAF) is a recirculating superconducting radio-frequency (RF) linear accelerator that provides continuous wave electron
beams to multiple experimental halls. It has a racetrack design with two parallel linacs connected by multiple recirculation arcs capable of reaching energies of up to 12 GeV with multiple passes into Hall D. The experimental facilities at Jefferson Lab are pictured in Fig. 3.1
The electron beam is produced through the photoelectric effect with multiple lasers on a photocathode, each tuned for various experiments. The electron beam bunches are produced in
4 nanosecond (ns) intervals with very precise timing information. Each RF linear accelerator
contains 25 cryomodules housing niobium accelerating cavities. With this accelerator technology, precise timing information is available to the experiment to determine the timing of
individual beam bunches passing through the target. The electron beam bunches directed
to Hall D are incident on a diamond radiator to produce a linearly polarized photon beam
through bremsstrahlung radiation, the process by which slowing charged particles produce
photons as energy loss.

3.1.2 Beamline

The photon beam in the coherent peak (8.4-9.0 GeV) is $\sim 40\%$ linearly polarized. The photon beam then goes through the tagger facility, where individual photons are tagged by diverting the corresponding electrons in a magnetic field and measuring their deposited energy, momentum, and timing information. Downstream of the tagger hall, a few systems are used to clean up and tune the beam. A tungsten keV filter is used to limit very low energy photons (10-100 keV) that were seen to cause random hits in the central drift chambers. The beam profiler, used during beam setup, consists of two planes of scintillating fibers in the x- and y-directions and is used to monitor the beam intensity in the x-y plane to ensure the beam is centered. An active collimator is then used to monitor the beam position and provide a slow feedback loop to lock the photon beam and provide micro-adjustments of the electron beam to prevent photon beam drift. The beam is then passed through a system of

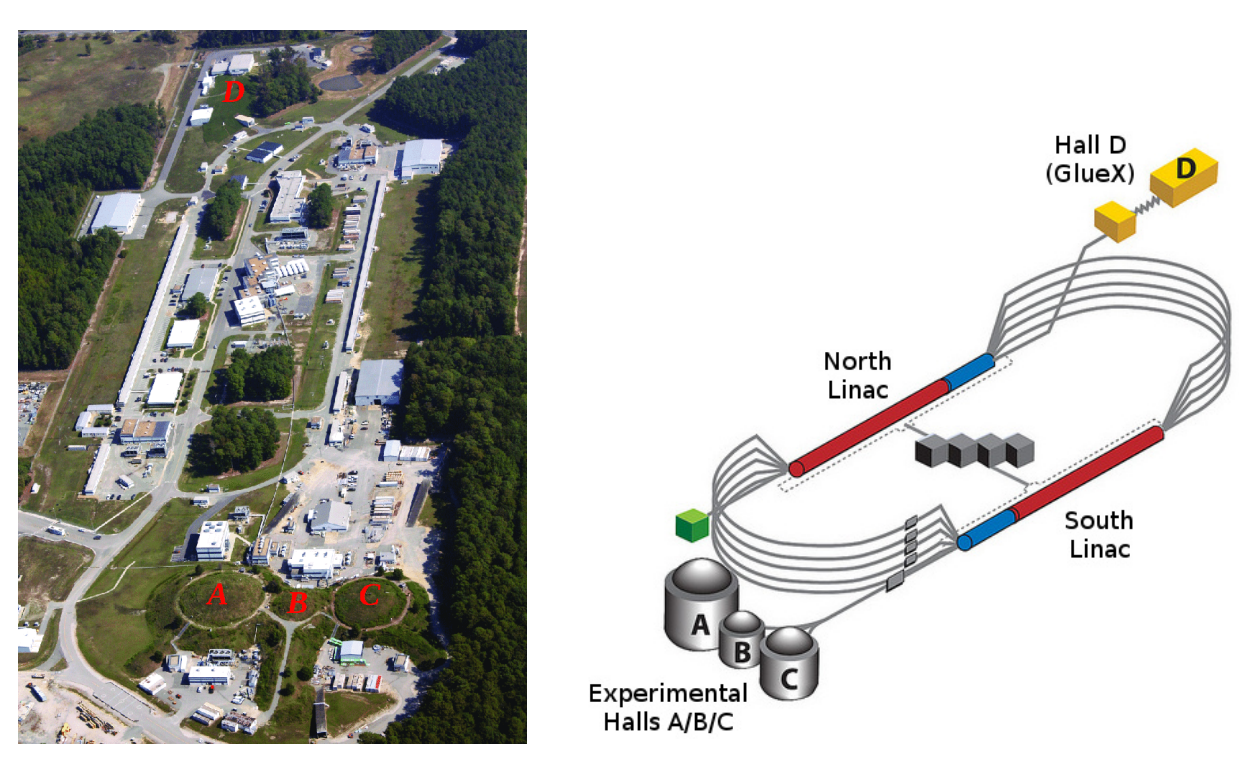


Figure 3.1: (Left) Aerial view of the CEBAF and four experimental halls at Jefferson Lab in Newport News, Virginia. (Right) Schematic view of the CEBAF showing the linear accelerators and recirculating arcs. Reprinted from [75] Copyright 2020 with permission from Elsevier.

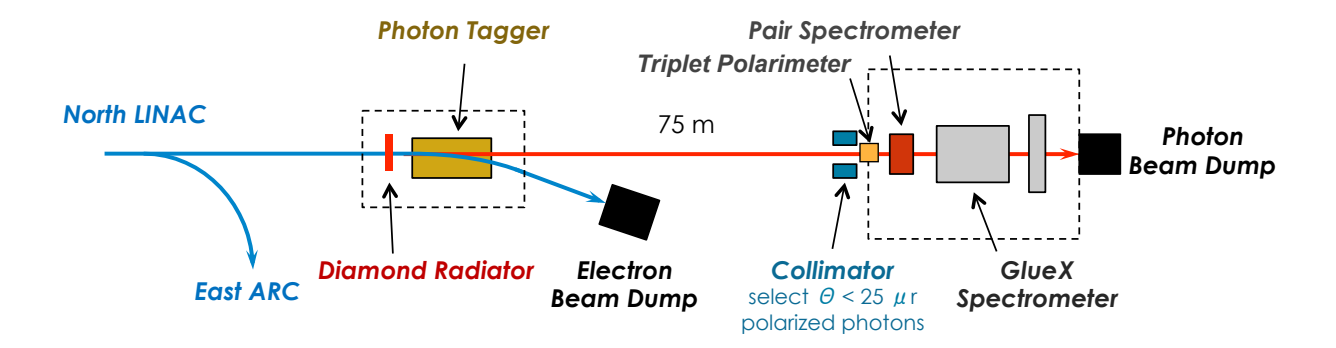


Figure 3.2: An annotated schematic of the photon beamline at GlueX. Reprinted from [75] Copyright 2020 with permission from Elsevier.

collimators to suppress the incoherent part of the beam and increase the polarization of the beam. After leaving the collimator cave, the triplet polarimeter (TPOL) is used to measure the polarization of the beam through triplet photoproduction [75], the process by which the polarized beam by interacting with an atomic electron produces a highly energetic electron pair e^+e^- . A beryllium converter is used for this process, where the recoiling atomic electron is then analyzed to obtain the beam polarization. The subsequent forward-going electron pair is measured by the pair spectrometer (PS) and used to obtain the photon flux. The schematic of the entire beamline is shown in Fig. 3.2.

Photon Tagger Hall. After passing through the diamond radiator, the remaining electrons and photons are focused to the tagger magnet through a quadrupole magnet. The electron trajectory is then curved in the horizontal plane by the tagger dipole magnet into an array of scintillating detectors to readout the post-bremsstrahlung electron energy, E_e . The incident electron energy, E_0 , is precisely known and the outgoing electron energy is measured. Therefore, the photon energy can be determined using $E_{\gamma} = E_0 - E_e$, and the photon is "tagged" or identified. The electrons that do not radiate most of their energy are curved into an electron beam dump. The scintillating region where the post-bremsstrahlung electrons are curved covers 25 - 97% of the full electron beam energy and is divided into two subregions. The Tagger Microscope (TAGM) is a high-resolution hodoscope that counts post-bremsstrahlung electrons corresponding to the primary coherent peak (8.2 – 9.2 GeV). The Tagger Hodoscope (TAGH) is designed to tag electrons in a larger range of energies and

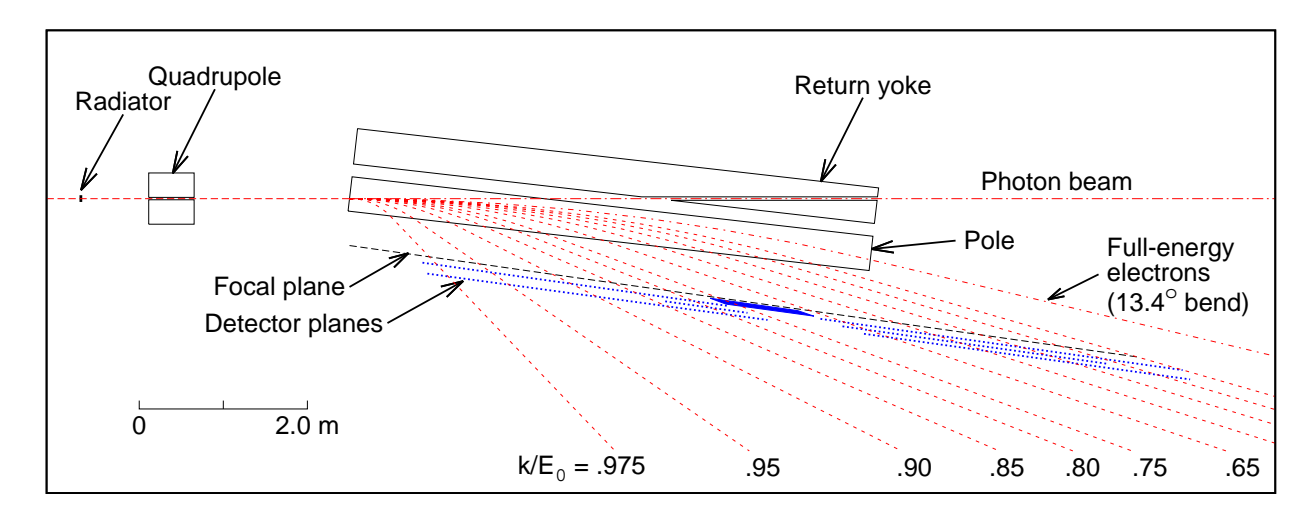


Figure 3.3: A schematic of the tagger hall for the GLUEX experiment. The dashed red lines represent the curvature of the electrons through the dipole magnet, the blue densely shaded region is the TAGM, and the sparsely populated blue dots over the remainder of the coverage is the TAGH. Reprinted from [75] Copyright 2020 with permission from Elsevier.

is much less granular than the TAGM. Figure Fig. 3.3 shows the schematic of the tagger magnet hall. The tagger dipole magnet curves electrons ($dotted\ red\ curves$) represented as the amount of energy radiated as photons, k. The coverage of the TAGM and TAGH focal plane detector array is shown by the blue compact area and the small blue dots, respectively. Once the photon bunches are tagged, it is focused and monitored through the beamline.

Pair Spectrometer. The PS serves many purposes, including measuring the spectrum of the collimated photon beam, determining the fraction of linear polarization in the coherent peak, providing coincidence of pairs of electrons with the TPOL recoil detector, monitoring of the photon flux, and calibrations of the TAGM and TAGH detectors. The PS is used to detect the e^+e^- pairs produced by the converter, material that converts photons to e^+e^- pairs, in order to reconstruct the beam photons. The electron-positron pair are split by a dipole magnet and detected in two sets of scintillator detectors: a high granularity hodoscope for precise momentum measurements and a set of coarse counters used as a PS trigger for electron-positron coincidence; see Fig. 3.4 for the PS schematic (right).

Of particular interest is the photon flux determination incident on the GLUEX target for the extraction of cross sections; see the measured flux in Fig. 3.4 (left). The photon flux

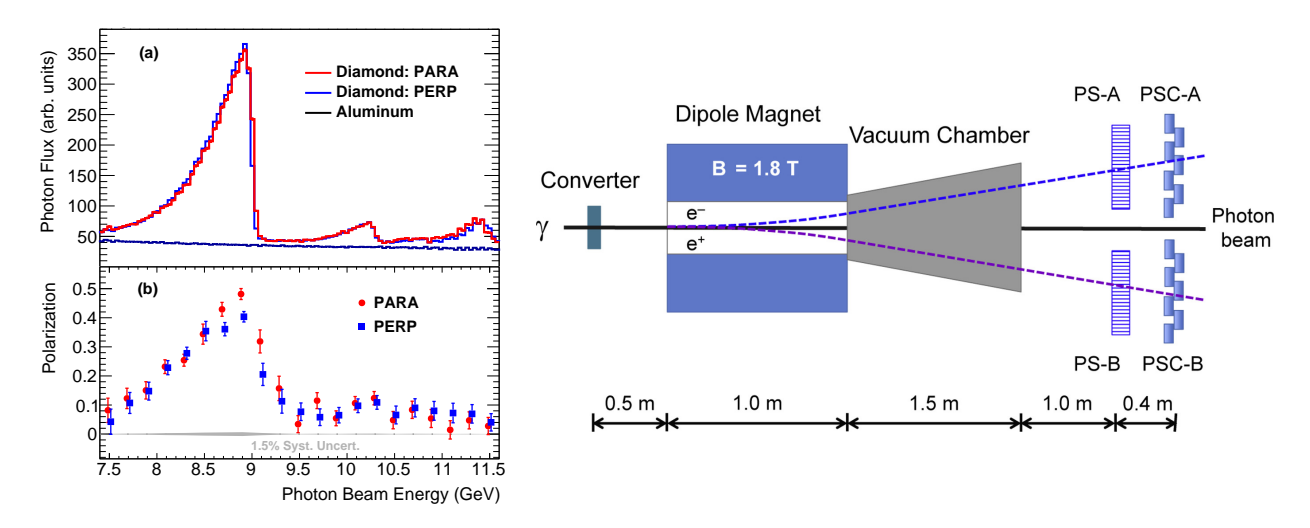


Figure 3.4: The left distribution shows the photon flux and polarization as a function of the incoming beam energy measured by the TPOL and PS. The right image is the annotated schematic of the PS. Reprinted from [75] Copyright 2020 Published with permission from Elsevier.

is determined by converting a known fraction of beam photons to e^+e^- pairs and counting them in the PS as a function of energy. The number of beam photons is obtained for all run periods for each tagger counter. In order to determine the detection efficiency of the PS, a high-efficiency calorimeter called the Total Absorption Counter (TAC) is used at low beam currents. The TAC is used to count all photons that pass through the GLUEX detector. The absolute flux calibration is determined by measuring the number of e^+e^- pairs for a given number of photons of the same energy measured by the TAC. An overall normalization to the flux must also be considered because not all of the tagged photons will reach the detector. This normalization is obtained by taking the ratio of tagged TAC events, coincident in the tagger and TAC, to the tagged pairs detected in the PS, coincident in the tagger and PS. This ratio is then used to convert the tagged rate in the PS during normal operations into a total photon count used for measurements.

3.2 GlueX Spectrometer

Once the beam is tuned and calibrated for the experiment, it is incident on a liquid hydrogen cryotarget. The spectrometer houses the Central Drift Chamber (CDC), Forward

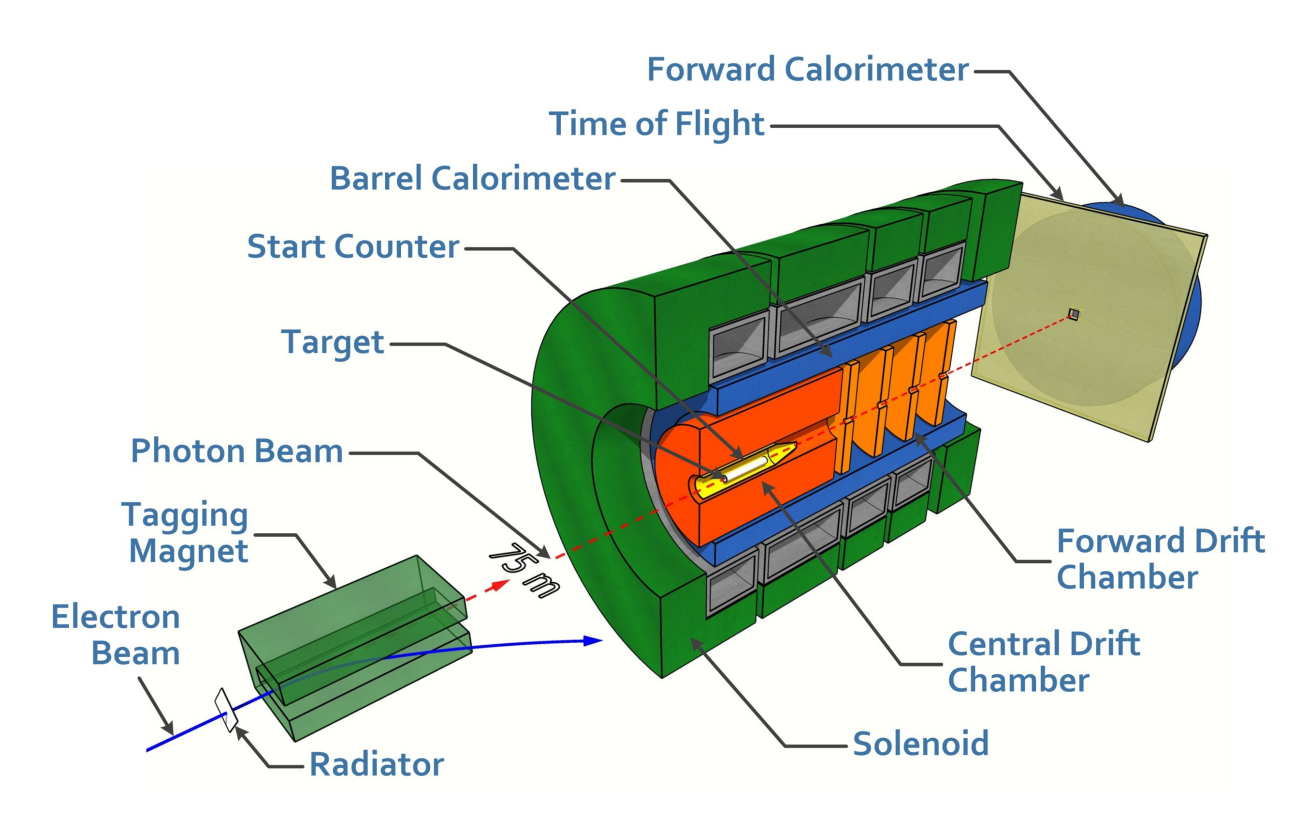


Figure 3.5: This figure shows the schematic of the GlueX Detector, a fully hermetic detector capable of identifying all the final state particles in the analysis channel. Reprinted from [75] Copyright 2020 Published with permission from Elsevier.

Drift Chamber (FDC), Start Counter (SC), and Barrel Calorimeter (BCAL) surrounded by a 2T superconducting solenoid magnet. Further downstream, the Time-of-Flight (TOF) detector and Forward Calorimeter (FCAL) are positioned for identification of forward-going particles. The signals from all detectors are read out using flash Analog-to-Digital Converters (ADC) and/or pipeline Time-to-Digital Converters (TDC). A complete schematic of the beamline with the GLUEX spectrometer and all the annotated detector systems is shown in Fig. 3.5.

3.2.1 Tracking Detectors

The tracking detectors are used to track charged particles by providing position, timing, and energy loss measurements for charged track event reconstruction. As charged particles pass through the active volume of the drift chamber, the enclosed gas is ionized; free electrons and atomic ions are formed from the neutral gas. The ionized electrons drift towards the

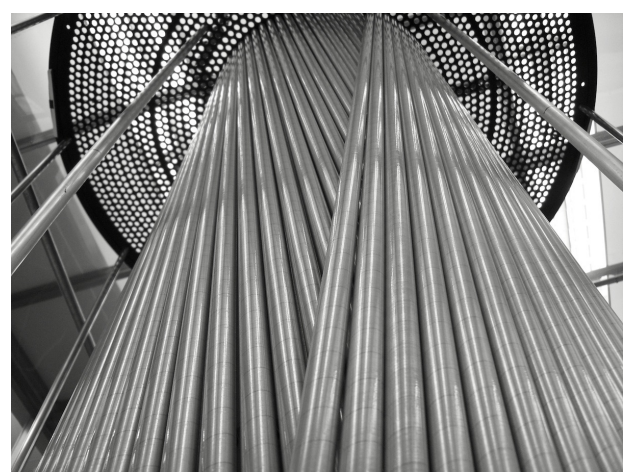
wire in the presence of an electric field, based on the electric potential between the anode and cathode, and produce a measurable current at the wire. Understanding the drift velocity and the time it takes for the ionized electron to travel from the moment of ionization to when the electrons reach the wire allows for a precise measurement of the position of the particle. Using the information from many chambers together, the trajectory of the particle can be reconstructed by finding the best fit for all hits in the chambers. Furthermore, by applying a magnetic field, the curvature of the trajectory of the reconstructed track can be used to obtain momentum and energy loss along its trajectory for particle identification.

The CDC is made up of 3522 straw tubes, each containing a gold-plated tungsten anode wire and an inner layer of aluminum on the walls to form the cathode. The active volume of the CDC surrounds the target and SC in a cylinder that covers the polar angles between $6^{\circ} - 168^{\circ}$ and is optimized for the polar angles between $29^{\circ} - 132^{\circ}$ of the particle trajectory. The active volume is filled with a gas mixture of 50% argon and 50% carbon dioxide to provide good position resolution. The cross-sectional schematic of the CDC is shown in Fig. 3.6 (left).

The FDC is composed of 24 1 meter diameter disc-shaped planar drift chambers made with two cathode planes and the wire plane in between, see Fig. 3.6 (right). The two cathode design is optimized for good multi-track separation due to the high particle density in the forward polar angles with coverage from $1^{\circ} - 10^{\circ}$ and partial coverage up to 20° . The wire plane uses a combination of sense wires used to detect the ionization and field wires used to shape the electric field. The drift chambers are filled with a "slow" gas mixture of 40% argon and 60% carbon dioxide to reduce the magnetic field affect.

3.2.2 Electromagnetic Calorimeters

Electromagnetic calorimeters are designed to measure the deposited energy of neutral showers from photons and charged particles that interact electromagnetically with the detector material. High-momentum photons primarily interact with the calorimeter material via pair production, where the photon converts to a e^+e^- pair via interactions with an atomic nuclei or electron. The subsequent pairs of high-energy electrons and positrons then emit photons via bremsstrahlung radiation. The combination of pair production followed by bremsstrahlung radiation causes a cascade of particles of decreasing energy within the



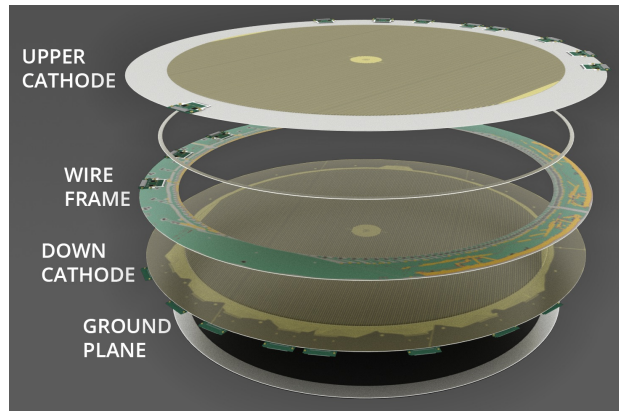


Figure 3.6: The left image shows a pictures of one of the modules of the straw-tube array of the CDC before installation. The right image is a schematic representation of the FDC. Rprinted from [75] Copyright 2020 Published with permission from Elsevier.

calorimeter, and the light generated is collected via light guides. The generated light is transported to photomultiplier tubes that amplify the light collected by the photoelectric effect and secondary emission and convert it to a measurable electronic signal to be characterized and reconstruct the shower.

The BCAL is housed between the magnet and the drift chambers and is a sampling calorimeter, as opposed to a homogeneous calorimeter, composed of layers of lead and scintillating material. The light collected in the BCAL is transported to silicon photomultiplier tubes (PMT) because of their insensitivity to magnetic fields. Photon showers of energies of 0.05 GeV and up to several GeV are detected within the polar angles of $11^{\circ} - 126^{\circ}$ and full 2π azimuthal angle coverage, see Fig. 3.7 (left). The BCAL array consists of 48 modules each with a trapezoidal cross section spanning 390 centimeters along the beam axis.

The FCAL is placed in the forward direction, 5.6 meters downstream of the target center and is made of 2800 lead glass blocks, each with its own PMT in a circular array, shown in Fig. 3.7 (right). Photon showers of energies of 0.1 GeV and up to several GeV are detected within polar angles of $1^{\circ} - 11^{\circ}$.

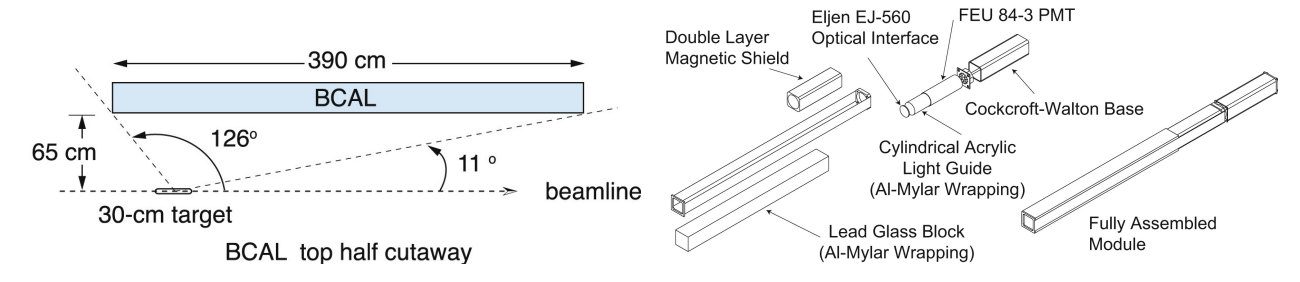


Figure 3.7: On the left their is a schematic view of BCAL with the angular coverage. On the right an annotated schematic of the FCAL is shown. Reprinted from [75] Copyright 2020 with permission from Elsevier.

3.2.3 Scintillation Detectors

The scintillation detectors that are part of the spectrometer, namely the SC and TOF, are used primarily for timing information and help facilitate particle identification.

The SC is a barrel-shaped detector immediately surrounding the target cell (see Fig. 3.8) that covers 90% of the solid angle for particle trajectories relative to the target center. It consists of 30 scintillating paddles following the pencil-shaped design of the detector; the geometric shape provides increased solid angle coverage and acceptance. The light from the scintillator paddles is read out by silicon PMTs. The primary purpose of the SC is to identify the beam photon bunch from which an event originated through precise timing resolution. The energy loss dE/dx is also used in coincidence with the TOF for charged particle identification. Furthermore, particle identification (PID) capabilities allow for the identification of low-momentum protons that do not pass through the CDC and pion-proton separation up to 0.9 GeV.

The TOF detector is a two-plane hodoscope detector system made up of a wall of vertical and horizontal scintillators 5.5 meters downstream of the target center. The TOF provides fast timing information for all charged particles through the detector with polar angle coverage from $0.6^{\circ} - 13^{\circ}$. This allows for the total particle flight time to be obtained together with the initial interaction time at the target determined by the SC leading to particle identification.

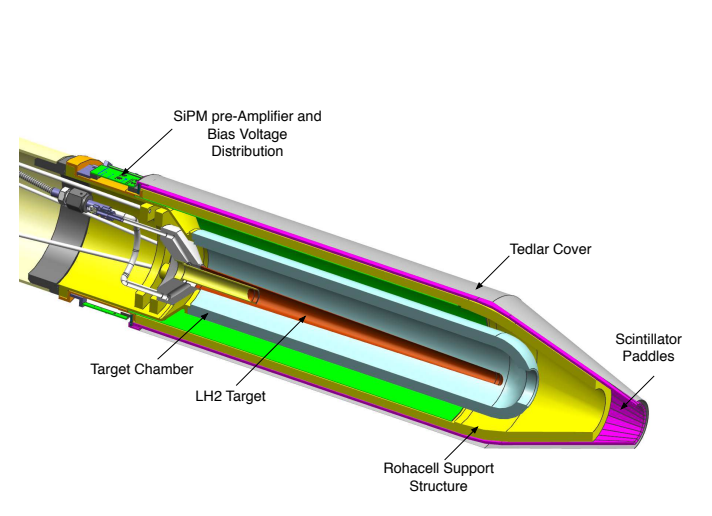




Figure 3.8: On the left an annotated schematic of the SC is shown. On the right an image of the TOF wall is shown before installation. Reprinted from [75] Copyright 2020 with permission from Elsevier..

3.3 Data Acquisition and Monitoring

When the GLUEX detector systems and beamline are in operation a trigger system is implemented to assure that the experiment is recording the highest quality hadronic interactions while reducing background rates. The experiment uses two types of triggers to assure the quality of events being recorded: the PS trigger, the coincidence of electrons in the PS detector arms as discussed in Section 3.1.2, and physics triggers based on the energy deposition in the BCAL and FCAL. The physics triggers are accepted when the following energy conditions are met in the BCAL and FCAL:

- 1. $2 \times E_{FCAL} + E_{BCAL} > 1 \text{ GeV} \wedge E_{FCAL} > 0 \text{ GeV}$,
- 2. $E_{BCAL} > 1.2 \text{ GeV}.$

The main physics trigger condition (1.) is based on the fact that most of the high-energy hadronic interactions produce forward-going energy. The second trigger condition is used to accept events that release large transverse energy in the BCAL, for example, the J/ψ meson reaction.

The trigger conditions described also need to meet the data storage and transfer capabilities of the Data Acquisition (DAQ) system. When a trigger is satisfied, the data from the electronic modules are read by a crate Readout Controller (ROC) at about 20 – 70 Mb/s. The data is then transferred via 1 Gb ethernet links to the Data Concentrators (DC) that build partial events from various crates from buffers of event fragments from 40 triggers at a time. The partially built events are then transferred at a rate of 200 – 700 Mb/s to the Event Builder (EB). The EB uses all of the data from the DC programs to build the complete events and then the Event Recorder (RC) writes the data to local storage on the RAID system storage disk arrays. The ROC, DC and EB/ER all run on dedicated computer nodes that are connected to a 40 Gb Ethernet switch and 56 Gb Infiniband switch (low speed/low latency). The Fig. 3.9 shows a flow chart depicting the DAQ configuration for GLUEX. The Ethernet system is only used for the DAQ system nodes, and the Infiniband system is used to transfer events for data monitoring purposes. The livetime of the DAQ is typically in the 92% – 100% range where the deadtime arises from the readout electronics.

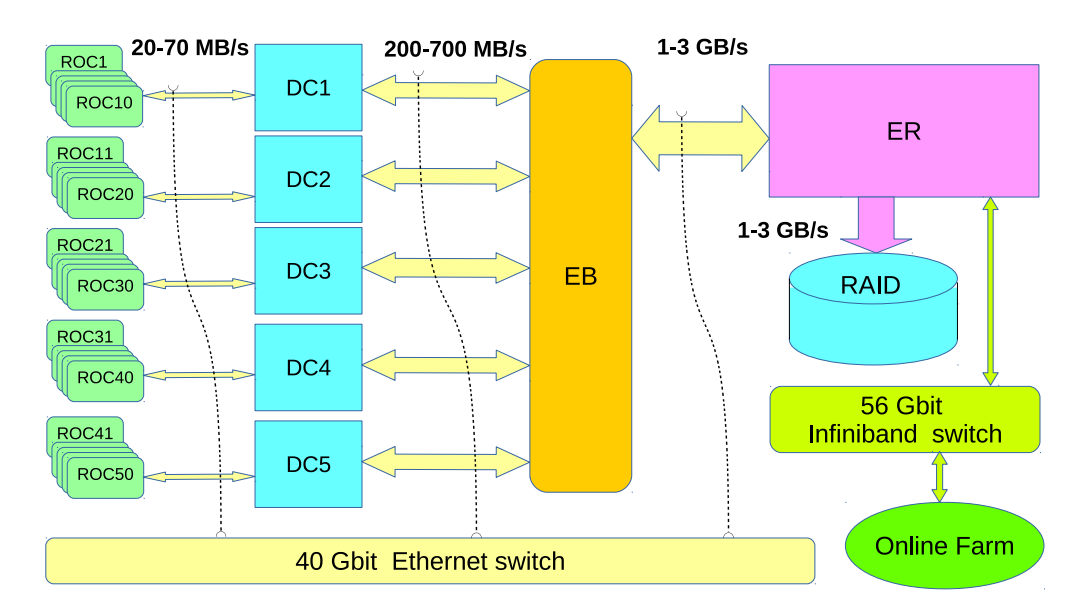


Figure 3.9: The flow chart represents the data acquisition process and hardware components and capabilities at GlueX. Reprinted from [75] Copyright 2020 with permission from Elsevier.

During machine operation, the Online Monitoring system allows live and near-term monitoring of the data using the *RootSpy* system written for GLUEX. The integration of the monitoring system and the DAQ is represented in Fig. 3.10 showing the flow chart of the online monitoring at GLUEX. Once the EB has built the event as part of the DAQ system, the Event Transfer (ET) process takes a subset of the data stream for monitoring on a dedicated monitoring computing farm. About 10% of the data stream is processed for low-level monitoring and 2% fully reconstructed for higher-level analysis. Each farm node generates histograms that are combined by RootSpy and displayed for monitoring to shift workers. The RootSpy output can also be processed through various client programs to verify uniformity and data quality.

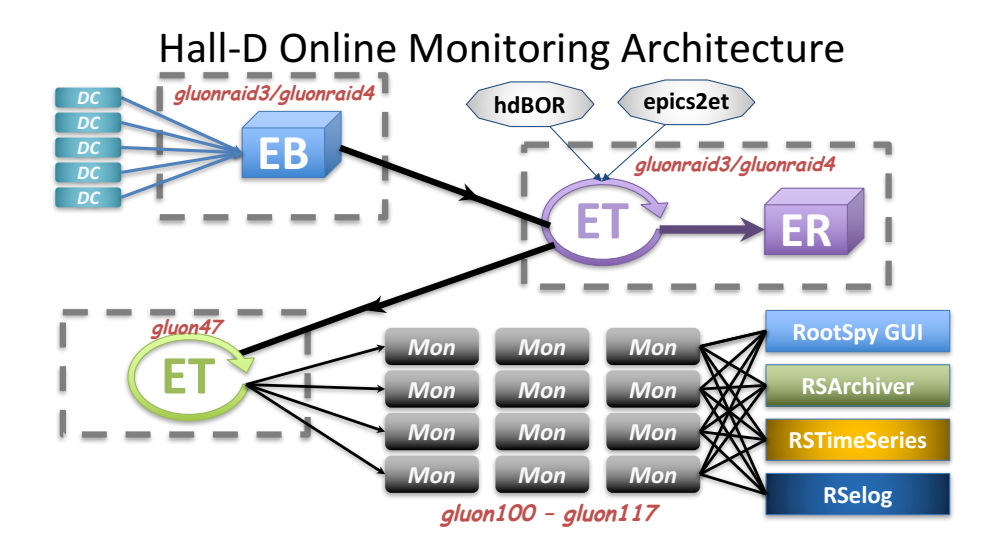


Figure 3.10: A schematic representation of the computational processes used for the data monitoring at GlueX. Reprinted from [75] Copyright 2020 with permission from Elsevier.

CHAPTER 4

DATA PROCESSING AND EVENT SELECTION

4.1 GlueX Data Preprocessing

For this research, all GLUEX-I data were used and the focus will be on this generation of data. GLUEX-I data were taken in three main run periods from 2017 to 2018 and acquired 125 pb^{-1} of production data in the coherent peak and 439.6 pb^{-1} for photon energies $E_{\gamma} > 6.0 \text{ GeV}$.

4.1.1 Track Reconstruction

For charged particles, the track reconstruction algorithm at GLUEX is performed in three parts. The first part is to look for hits in the FDC and CDC and is categorized by pattern recognition. The hits in adjacent layers of the FDC packages are formed into track segments and linked together to form FDC track candidates using a helical model. A similar procedure is performed for the CDC, where the hits in the CDC segments are linked, and a fitting procedure is used to find the parameters of the track candidates. Candidates that pass through both the FDC and the CDC in the polar angle range of $5^{\circ} - 20^{\circ}$ are further linked together.

The second stage of the track reconstruction involves using a Kalman filter to find the track parameters at the position of closest approach of the track to the beamline. The Kalman filter is a statistical and recursive procedure that takes all the measurements in multiple time steps to estimate the track parameters. It is done in steps using the measured values starting from the hits farthest from the beam line. The estimated parameters from the first step are used as the prior in the Kalman filter. All effects from energy loss and multiple scattering are taken into account from the magnetic information of the solenoid

magnet at each step. The filter first assumes that all tracks are pions except for tracks with a momentum p < 0.8 GeV; the lower momentum tracks are fitted as a proton hypothesis.

The final step for the track reconstruction is to match the fitted tracks from the Kalman filter to either of the scintillating detectors (SC/TOF) or the electromagnetic calorimeters (BCAL/FCAL) to obtain the start time of the track. With an initial reference time, the drift time to each wire in the drift chambers for a given track can be used in the fit. Finally, each track is refitted with the drift information and the mass of all charged particles in the set $\{e^{\pm}, \pi^{\pm}, K^{\pm}, p^{\pm}\}$ individually.

4.1.2 Particle Identification

In addition to the algorithmic approach to reconstructing tracks, the SC and TOF detectors are used for PID as briefly mentioned in Section 3.2.3. By measuring the change in energy along the scintillating material in the SC, dE/dx, the pions and protons can be distinguished from each other up to p < 0.9 GeV. The energy loss is plotted against momentum in Fig. 4.1 (left) where the curved band represents protons and the horizontal bands are electrons, pions, and kaons. Furthermore, the TOF detector is also used for PID because using the timing information from the SC we can determine the velocity of the particle along its trajectory. By plotting the relativistic particle velocity, β^1 , against its momentum for events with three fully reconstructed positively-charged tracks one can see clear particle separation in Fig. 4.1 (right). From top to bottom, the bands represent e^+ , π^+ , K^+ , p. The TOF detector provides 4σ separation between the combined pion/positron and kaon bands at p = 2 GeV, 4σ separation between the combined pion/positron/kaon and proton bands at p = 4 GeV.

4.1.3 Kinematic Fitting

Kinematic fitting is a powerful analysis tool implemented at GLUEX to improve the resolution of the measured data and identify different reactions. The measured values can be used to construct four-vectors of particles. When experiments are performed, the measured values have specific uncertainties that are identified from many factors, such as detector

¹In natural units $\beta = v$, where v is the particle velocity.

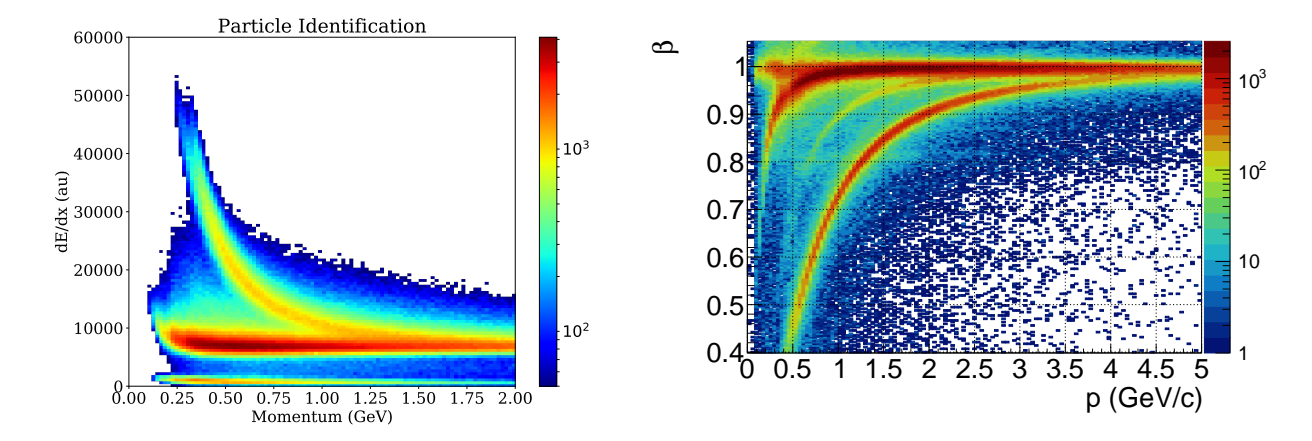


Figure 4.1: The left distribution shows the energy loss in the SC as a function of the momentum of the reconstructed track used for PID. The right distribution shows the particle velocity, β as function of the particle track momentum in the TOF detector used for PID. Reprinted from [75] Copyright 2020 with permission from Elsevier.

limitations. Kinematic fitting works by taking the measured four-vectors of a reconstructed event and applying physical constraints to better estimate the measured four-vectors within their given experimental uncertainty. Physical constraints that are typically used are momentum and energy conservation of initial and final particles, fixing the invariant mass of intermediate particles, and vertex constraints (allowing particles to converge to the same position) or any combination of constraints.

The implementation of kinematic fitting with constraints is done through a least squares procedure and the use of Lagrangian multipliers [76], where the optimal fit function is determined to better estimate the parameters and uncertainties by a χ^2 -minimization. In matrix form, the χ^2 with constraints can be written as:

$$\chi^2 = (\boldsymbol{y} - \boldsymbol{\eta})^T \boldsymbol{V_y}^{-1} (\boldsymbol{y} - \boldsymbol{\eta}) - 2\boldsymbol{\lambda}^T \boldsymbol{f}, \tag{4.1}$$

where η are the estimates of the measured experimental values, y; V is the covariance matrix, λ are the unknown Lagrange multipliers, and f are the constraint equations. The procedure to minimize the χ^2 , where the partial derivatives of all variables are set to zero, results in a set of solvable equations:

$$V_{\boldsymbol{y}}^{-1}(\boldsymbol{y}-\boldsymbol{\eta})\left(\frac{\partial \boldsymbol{f}}{\partial \boldsymbol{\eta}}\right)^{T} \boldsymbol{\lambda} = 0, \quad \boldsymbol{f} = 0, \quad \left(\frac{\partial \boldsymbol{f}}{\partial \boldsymbol{\xi}}\right)^{T} \boldsymbol{\lambda} = 0,$$
 (4.2)

where ξ are the unknown parameters. In most cases, the constraint equations, f, are nonlinear in the variables (η, ξ) and Eq. (4.2) must be solved iteratively about the critical point; the general procedure is given in [76]. For the experiment, this iterative process happens for each step of the particle reconstruction and returns the kinematically fitted four-vectors for each track. Ultimately, this means the constraints act to "pull" the track four-momentum towards their unconstrained values within their uncertainties. The minimized χ^2 values determined from the minimization fit procedure can then be used in the event-based selection to filter out events that are not kinematically fit well. Finally, by using uncertainty propagation, we can obtain the new covariance matrix of the kinematically fitted parameters from all iterations to obtain improved uncertainties and variable correlations.

4.1.4 Event Reconstruction

The full processing of the raw data obtained from the detector systems goes through various production steps before it is ready for physics analysis. A flow chart showing the data processing production stages is shown in Fig. 4.2. The raw data undergo calibration and reconstruction steps before being formatted into reaction-specific analysis ROOT trees for event-based processing. Data acquisition and monitoring practices were discussed in Section 3.3. In practice, a subset of $\sim 10\%$ of the data may go through the same monitoring procedure discussed in Fig. 3.10 many times to study improvements from calibrations and reconstruction software updates; the monitoring histograms are written and stored on the GLUEX webpage.

Once the experts are satisfied with the reconstruction software and calibrations to the subset of monitoring data, a full production pass of the reconstruction software is performed. For Gluex-I the 3 PB of raw data files were processed into 500 TB of Reconstructed Event Storage (REST) physics data files. Full reconstruction launches are performed every few months or as needed depending on software improvements as mentioned above. Running the reconstruction software over the raw data is computationally intensive and is run in multi-threaded mode on the computing farm at JLab. Offsite high-performance computing facilities are also used for production processing, specifically the National Energy Research Supercomputing Center (NERSC) and the Pittsburgh Supercomputing Center (PSC).

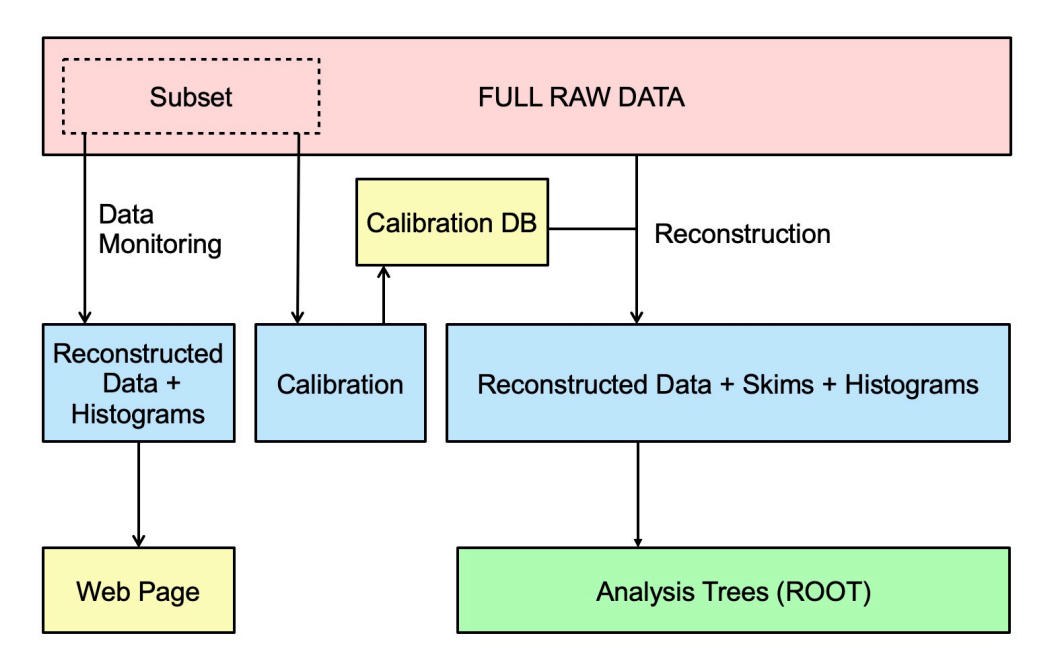


Figure 4.2: A flow chart of the data processing that occurs at GLUEX from data acquisition and monitoring to analysis ready ROOT trees. Reproduced from [75] Copyright 2020 Published by Elsevier B.V. All rights reserved. Reprinted from [75] Copyright 2020 with permission from Elsevier.

The full set of REST data files is still too large for individual analyzers. A system is used to extract reaction-specific files into ROOT trees for more timely and efficient analysis. ROOT is a powerful all-in-one analysis framework built for use with C++ with built-in tools for interactive analysis and handling of large data sets. Users are able to submit individual reaction requests via the webpage and then an analysis launch is performed where up to one hundred reactions can be processed at once. Each submitted reaction is processed with the Gluex analysis library with the Jlab Analysis Framework (Jana) [77]. This creates reaction-specific particle combinations from the reconstructed tracks and showers in the REST files. At this stage in the event production some common selection criteria for exclusivity and PID are implemented before performing a kinematic fit. The resulting ROOT files are typically small enough to be transferred to the home institution or personal computers for advanced analysis.

Table 4.1: A table of the timing cuts for all the detector systems used in the pre-selection criteria by GlueX.

Track	$\Delta t_{ m RF} \ (m ns)$				
	BCAL	TOF	FCAL	SC	
π^{\pm}	±1.0	± 0.5	±2.0	±2.5	
K^{\pm}	± 0.75	± 0.3	± 2.5	± 2.5	
p	± 1.0	± 0.6	± 2.0	± 2.5	

4.2 Event Selection

4.2.1 Track Selection

As discussed in Section 4.1.4, during an analysis launch there are some standard cuts and reaction-specific selections for exclusivity and PID applied. The preselection cuts include timing cuts, energy loss cuts, and very loose particle mass cuts, where the former two are good for PID. The RF time information $t_{\rm RF}$ from the accelerator is used to determine when a beam photon bunch enters the target. The flight time of the charged track is measured t_{meas} from the timing information of the reconstructed tracks in the highest resolution detector to the particle production. The difference of the measured time and the RF time after they have been extrapolated to the target center under the assumption of a particle mass is defined as

$$\Delta t_{\rm RF} = t_{meas} - t_{\rm RF}.\tag{4.3}$$

 $\Delta t_{\rm RF}$ can be used to distinguish between the different particle mass hypotheses for similar tracks. The timing cuts for the charged tracks relevant to our analysis (Section 4.2) are listed in Table 4.1. Energy loss cuts in the CDC are also used and are particularly good for reasonable PID of proton and pion tracks at large angles. The CDC are based on energy loss and momentum distributions similar to Fig. 4.1 and take the form

$$dE/dx < \exp(-7.0\,p + 3.0) + 6.2\tag{4.4}$$

for all pion and kaon tracks where dE/dx is the energy loss and p is the momentum of the specific track.

When submitting jobs for an analysis launch, the user specifies the number of tracks required and the kinematic fit constraints of the reaction. For our reaction

$$\gamma p \to K_{fast}^+ K_{slow}^+ \Xi^- \\ \to \pi_{\Xi^-}^- \Lambda \\ \to \pi_{\Lambda}^- p$$
 (4.5)

we impose the requirement that there must be five charged tracks with the final state particles being $K^+K^+\pi^-\pi^-p$ under the assumption that Ξ^- is reconstructed with the invariant mass of the $\pi^+\Lambda$ system and the $\Lambda \to \pi^-p$, see Eq. (4.5). The physical constraints to the kinematic fit are:

- 1. all reconstructed particle masses are constrained to their PDG masses [30] except the $\Xi(1320)$ baryon,
- 2. four-momentum conservation (x,y,z momentum and energy),
- 3. all vertices are constrained, meaning the decaying particles are tracked and compared to the parent particle decay vertex.

This accounts for a total of 10 independent constraint equations (19 constraints and 9 unknowns) in the kinematic fit. In this reaction the $\Xi \to \Lambda \pi^-$ has its mass unconstrained and but the $\Lambda \to \pi p$ has its mass constrained. The three vertex constraints are where $\{K_1^+, K_2^+, \Xi^-\}$ share the production vertex, $\{\pi_1^-, \Lambda\}$ share the same detached Ξ vertex, and $\{\pi_2^-, p\}$ share the same detached Λ vertex. The remainder of the analysis selection is done on the processed reaction-specific ROOT trees.

4.2.2 Event-Based Selection

A summary of the event selection criteria used in the analysis of GLUEX and simulated data for the photoproduction ground state $\Xi(1320)$ baryon reaction can be seen in Table 4.2. In the following sections, each cut and the justification through figure-of-merit (FOM) studies or data/simulation comparisons will be discussed in detail. Several sets of Monte Carlo (MC) simulations were also generated for this analysis. The details of the procedure and results are discussed in detail in Chapter 5. For all distributions that show the generated (thrown) Monte Carlo events they are labeled $Gen\ MC$ and the reconstructed Monte Carlo events as

Table 4.2: Table of tuned cuts on GlueX and simulated data in this analysis.

Event Selection	Selection Criteria	Section
Multiple Combos	Hybrid χ^2_{ν} Combo	4.2.3
$\chi^2_ u$	< 8	4.2.4
$\frac{1}{ \mathrm{MM}_X\left(\gamma p \to X K^+ K^+ \Xi^-\right)) ^2}$	$< 20 \; (MeV)^2$	4.2.5
Kaon Selection	$ \overrightarrow{\boldsymbol{p}}(K_{fast}^+) > \overrightarrow{\boldsymbol{p}}(K_{slow}^+) $	4.2.6
Rapidity, y	$y(K_{fast}^+) > 2$	4.2.7
Target Region, Z_t	$50.4 \text{ cm} < Z_t < 79.1 \text{ cm}$	4.2.8
Ξ^- Flight Significance, $d_{\Xi}^{\pm}/\sigma_{d_{\Xi}}$	> 2	4.2.8
Λ Flight Significance, $d_{\Lambda}^{\pm}/\sigma_{d_{\Lambda}}$	> 0	4.2.8

Recon MC (these are the events that will be compared with real data). For all distributions, we have handled multiple combos per event and accidental beam photons by choosing the final-state combos with the best reduced χ^2 (denoted χ^2) for each unique photon followed by an accidental sideband subtraction. This is known as the hybrid χ^2 method, to be discussed in Section 4.2.3. For comparisons between the data and the simulation, the background has been subtracted in the data using the Q-factor background subtraction method explained in Section 4.3 unless otherwise stated. Figure 4.3 shows the $\Xi(1320)^-$ in the invariant mass of $\Lambda\pi^-$ after all event selection criteria and cuts have been applied to the entire GlueX-I data. Furthermore, the mass distribution is fitted to extract the Ξ total yield with more than 10k events after selection.

4.2.3 Accidental Photons

The handling of accidental beam photons in the GlueX experiment can be done in a number of ways. In this section, the three recommended methods will be explored. In the GlueX experiment, precise beam photon bunch timing information into the target is available because of the radio frequency (RF) timing precision of the accelerator, discussed in Section 4.2.1. The RF beam bunches come in intervals of 4.008 ns or less often, in 2.004 ns. Using this information with the reconstruction of tracks, the best RF beam bunches associated with a given reconstructed event are recorded. In the experiment, there may

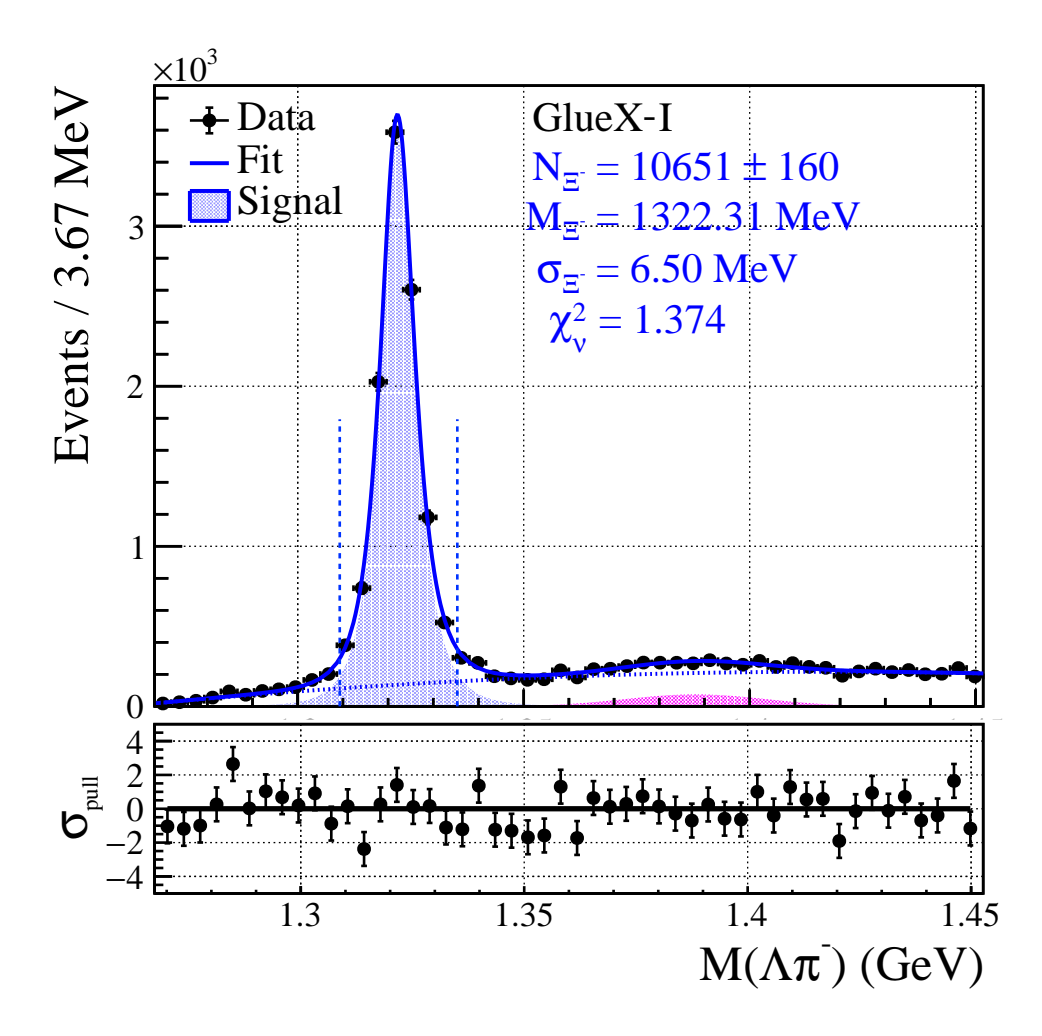


Figure 4.3: Invariant $\Lambda \pi^-$ mass distribution and fit with a Johnson function Eq. (4.18) for the $\Xi(1320)^-$ signal region with all cuts from Table 4.2 applied in the data selection.

be multiple photons in a single beam bunch that are very kinematically similar to each other (accidental photons) and need to be subtracted out. Because of the precise timing information and the pulsed nature of beam we are able to retrieve information from in-time photons (within the 4 ns window) and out-of-time photons with respect to the event. The RF beam bunches for all three GLUEX-I run periods are shown in Fig. 4.4, where you can see the in-time peak shaded green (beam photons associated with our final state) and the out-of-time peaks shaded red. This information is used to perform a sideband subtraction to statistically omit accidental photons that may be within the 4 ns window. The three methods for dealing with accidental beam photons are as follows:

- 1. **RF** subtraction method: Keep both in-time and out-of-time beam photons and using the RF-timing information a statistical side-band subtraction is performed to subtract accidentals that fall into the in-time peak.
- 2. **Best** χ^2_{ν} **method:** Keep only in-time beam photons, and rank all possible combinations (beam photons + final state) per event based on the reduced χ^2 generated by the kinematic fitter. The combination with the smallest χ^2_{ν} value is chosen. This assumes that the best photon has been selected and that no side-band subtraction is applied.
- 3. **Hybrid** χ^2_{ν} **method:** Rank all possible final-state combos only by the reduced χ^2 and keep all photon combinations. Then choose the best final-state combo associated with each unique initial-state photon and finally apply the RF side-band subtraction of method 1.

The downside of Method 1 is that the we are keeping all of the photon combinations associated with the final-state kinematics. It has been studied in the large statistics limit that this method converges to the correct results for measurements such as the cross section. The downside of Method 2 is that no information from the out-of-time region is used, so it is merely assumed that the chosen photon is the correct incident photon. Furthermore, the method for obtaining the flux normalization uses RF subtraction, and there is some systematic difference when measuring the cross section or other observables that use the flux normalization. The final method is considered to be the "most correct" way to do the accidental subtraction due to its comparability to the photon flux determination and removes a certain level of arbitrariness by choosing the combination with the best final-state

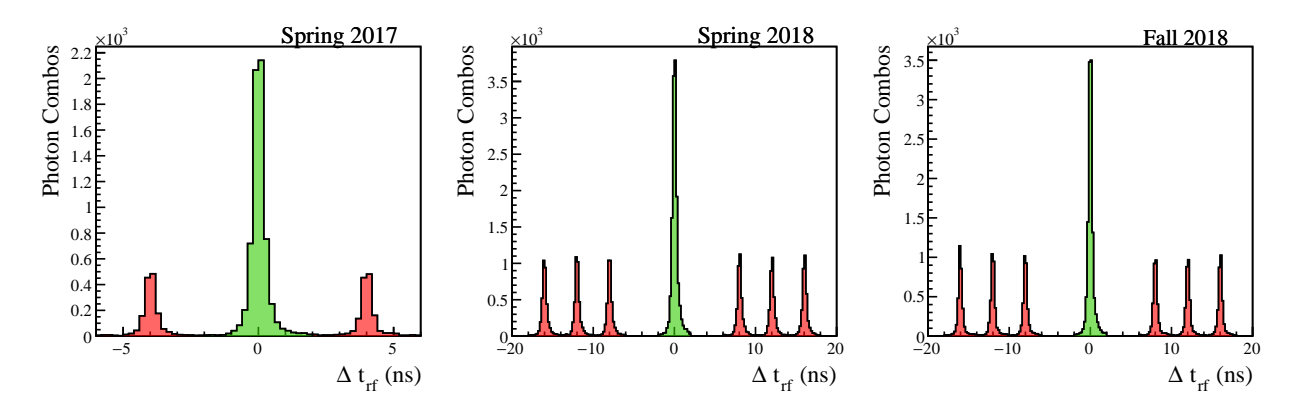


Figure 4.4: The RF beam bunch timing for the three GLUEX-I run periods. For the 2018 run periods, the first RF bunch is cut out to assure no overlap with the in-time RF bunch.

hypotheses. The effect of the different methods for handling the accidental beam photons to obtain a systematic uncertainty is discussed in Section 7.2.2. For the remainder of the analysis, the hybrid method will be applied in order to be consistent with the photon flux for the cross section measurement.

4.2.4 χ^2_{ν} Cut

The reduced χ^2 (or χ^2_{ν}) is defined as χ^2 per degree of freedom based on the results of the kinematic fit to the data. The χ^2_{ν} represents a universal parameter that allows a simultaneous comparison for all physical constraints in a multidimensional phase space. Kinematic fitting is performed using a Constrained Least Squares fitting method and is discussed in Section 4.1.3. Moreover, in this iterative process, the particle four-vectors are modified within their uncertainties to better match the physical constraints. This modification gives better data resolution and allows for a powerful statistical tool in the event selection. We have discussed the physical constraints to the kinematic fit in Section 4.2.1.

The selected cut-off value for χ^2_{ν} is deduced through a figure-of-merit (FOM) study where the FOM is defined as

$$FOM = \frac{N_S}{\sqrt{N_S + N_B}} , \qquad (4.6)$$

and N_S , N_B denote the Ξ signal and background yields. The invariant $\Lambda \pi^-$ mass distribution showing the Ξ was used to extract the signal and background yields in a 2σ window around

the signal. Various values were studied for $\chi^2_{\nu} \in [2,12]$ while the remaining cuts from Table 4.2 remained fixed. The results of this study can be seen in the first row of Fig. 4.5, where each point of the FOM distribution coincides with a fit to the data shown in Fig. 4.6 for the Fall 2018 (GlueX-I) run period. Furthermore, the signal-to-background ratio, N_S/N_B , is plotted in red as a reference to show how the relative background is reduced with a tighter cut. The cut value is defined as the point where the FOM begins to plateau, which means that the significance of the signal with respect to the background is maximized and no longer changes. The second row of Fig. 4.5 shows the χ^2_{ν} of the GlueX-I data compared to the simulated data, where the cuts from Table 4.2 are applied except the χ^2_{ν} cut itself. The good agreement between the data and the simulated data indicates that the kinematic fitter is exhibiting the same behavior for both the data and the simulated data. Furthermore, the peak near a value of $\chi^2_{\nu} = 1$ represents events that have well-constrained kinematics. The slight excess in χ^2_{ν} seen in Fig. 4.5 for the data is most likely due to a small amount of remaining background ($\sim 5\,\%$) present under the Ξ peak.

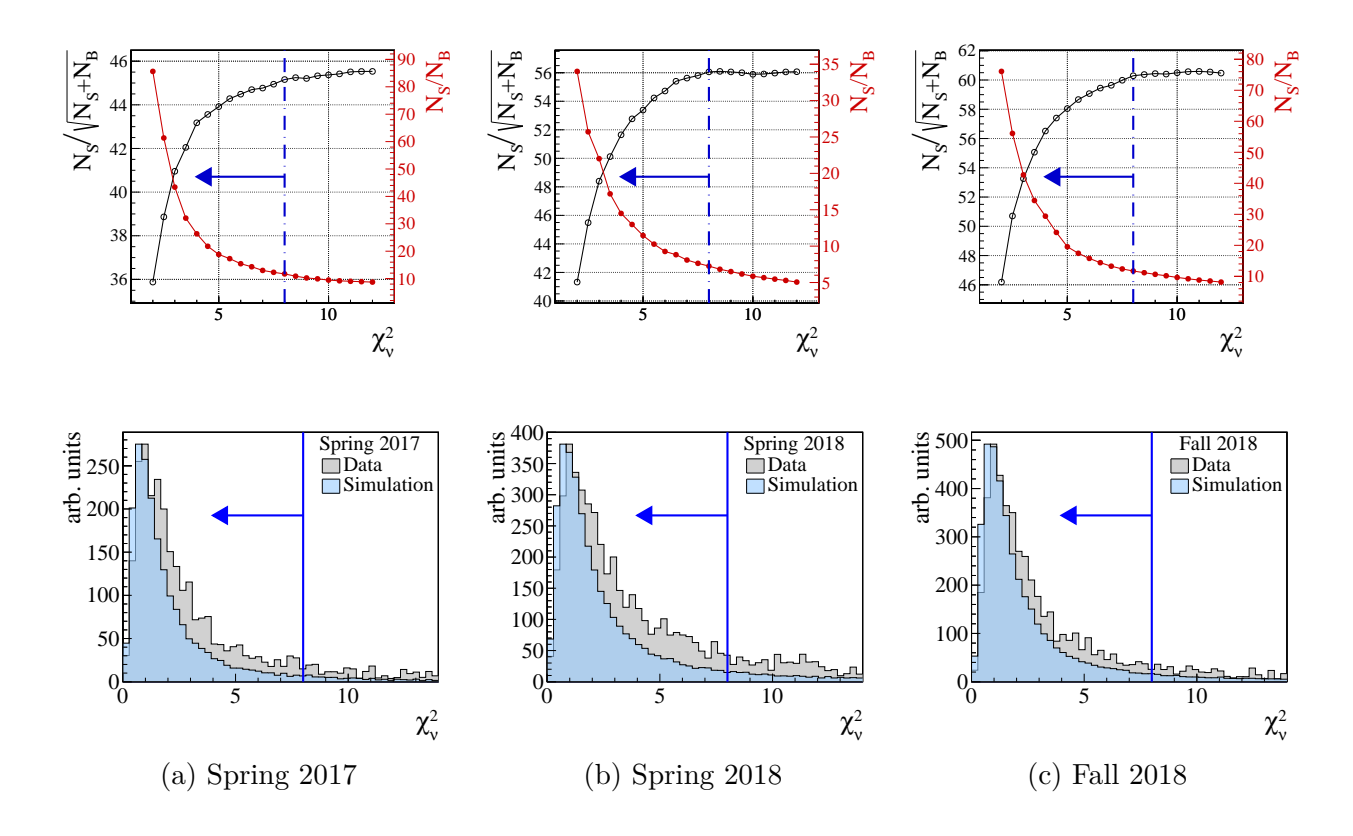


Figure 4.5: **(Top)** The figure of merit (black), $\frac{N_S}{\sqrt{N_S+N_B}}$, and signal-to-background ratio (red), $\frac{N_S}{N_B}$, where N_S , N_B are the signal and background yields from fits to the invariant mass of the Ξ shown in Fig. 4.6 for the Fall 2018 GLUEX-I run period. **(Bottom)** The χ^2_{ν} distributions of GLUEX-I for data and simulated events.

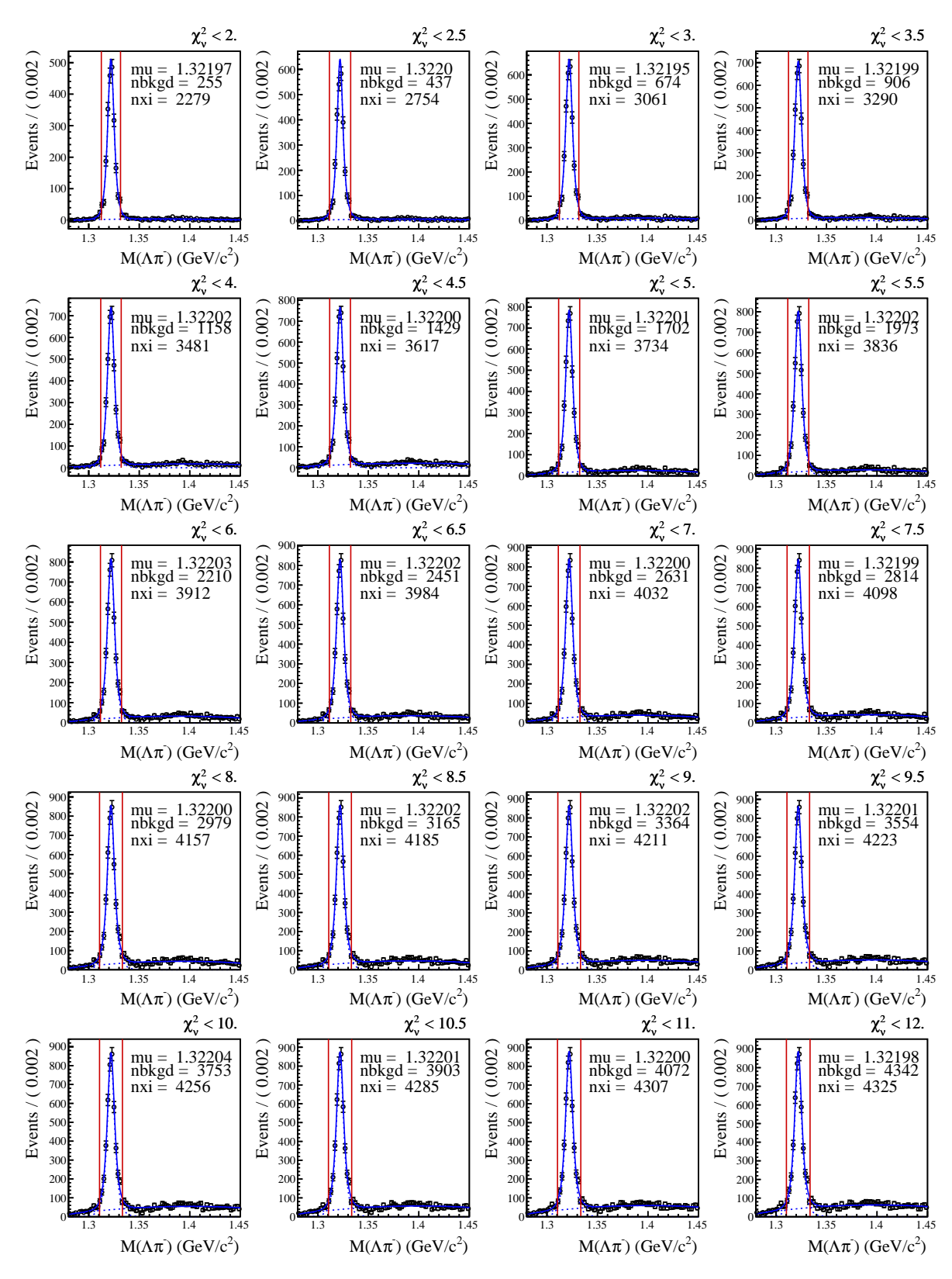


Figure 4.6: Fall 2018 mass distributions and fits for $\chi^2_{\nu} \in [2, 12]$. The legend shows the value of the central position of the peak (mu), and the number of background (nbkgd) and signal (nxi) events.

4.2.5 Missing-Mass-Squared Cut

The missing mass squared is defined as the residual mass of the total reaction. The missing mass four-vector is constructed from all of the observed particle four-vectors in an event,

$$p_{MM}^{\mu} = (p_{\gamma}^{\mu} + p_{target}^{\mu}) - (p_{K_{1}^{+}}^{\mu} + p_{K_{2}^{+}}^{\mu} + p_{\pi_{1}^{-}}^{\mu} + p_{\pi_{2}^{-}}^{\mu} + p_{p}^{\mu}), \tag{4.7}$$

where the squared magnitude of the missing-mass four-vector is given as

$$MM_X (\gamma p \to X K^+ K^+ \pi^- \pi^- p)^2 = |p_{MM_X}^{\mu}|^2.$$
 (4.8)

In principle, the missing mass would be zero because the GLUEX detector is almost completely hermetic and highly efficient at detecting all final-state particles. In practice, we see a distribution around zero due to detector resolution, efficiency, and combinatorial background from accidental beam photons and final-state particles. Due to the physical constraint, a cut around zero is used to reduce background events. The same FOM procedure described in Section 4.2.4 is applied here, albeit one difference being that $\chi^2_{\nu} < 14$ is used to find the optimal cut-off for the MM_X^2 . The results are shown in the top row of Fig. 4.7 where again the FOM is plotted for several values of the missing-mass squared cut and each point is associated with a fit to $\Xi(1320)$ in the invariant mass of $\Lambda \pi^-$. These fits are shown in Fig. 4.8. The second row of Fig. 4.7 shows the comparison of the data and simulation and the cut values determined from the FOM for the three GLUEX-I run periods.

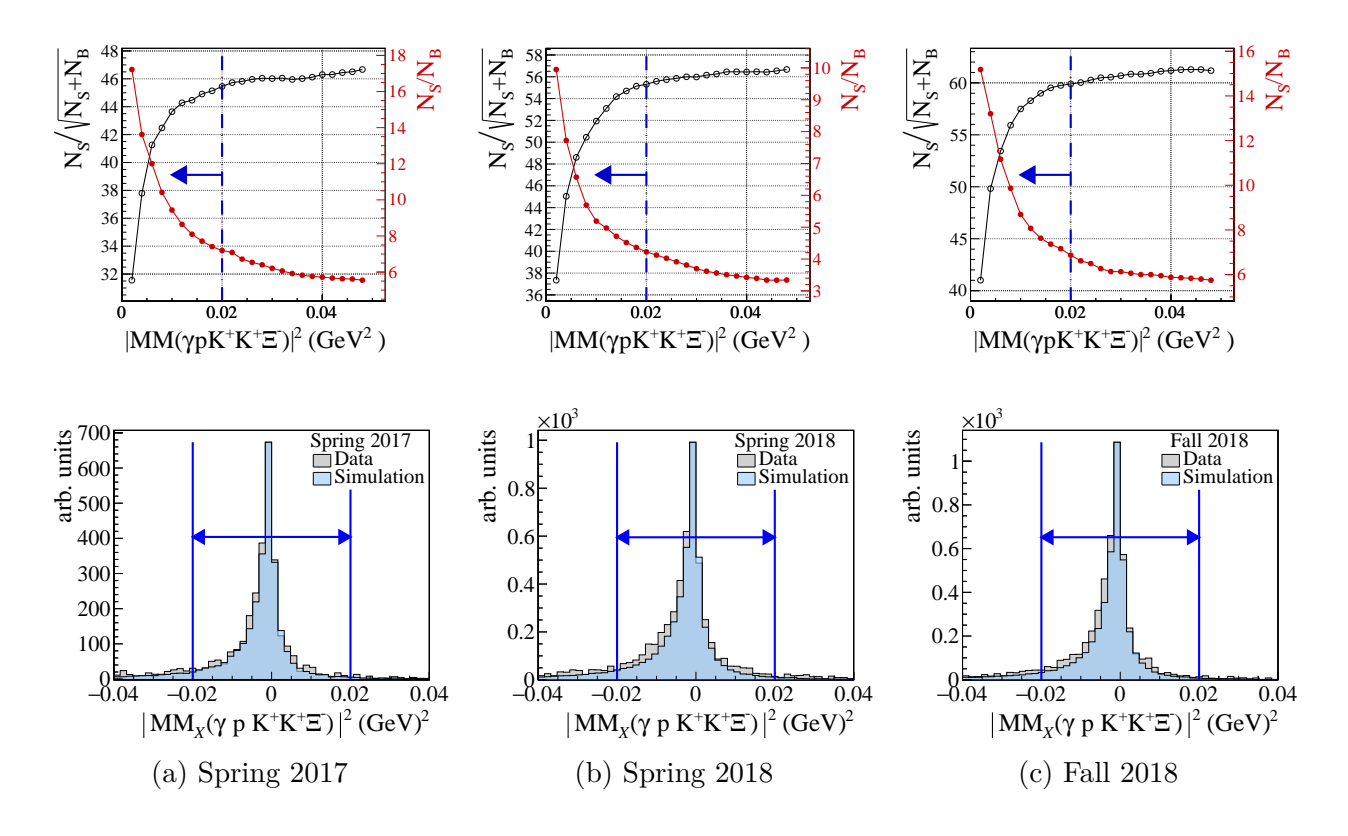


Figure 4.7: **(Top)** The FOM (black), $\frac{N_S}{\sqrt{N_S+N_B}}$, and signal-to-background ratio (red), $\frac{N_S}{N_B}$. **(Bottom)** The missing-mass-squared distributions of data and reconstructed Monte Carlo events for the GLUEX-I run periods.

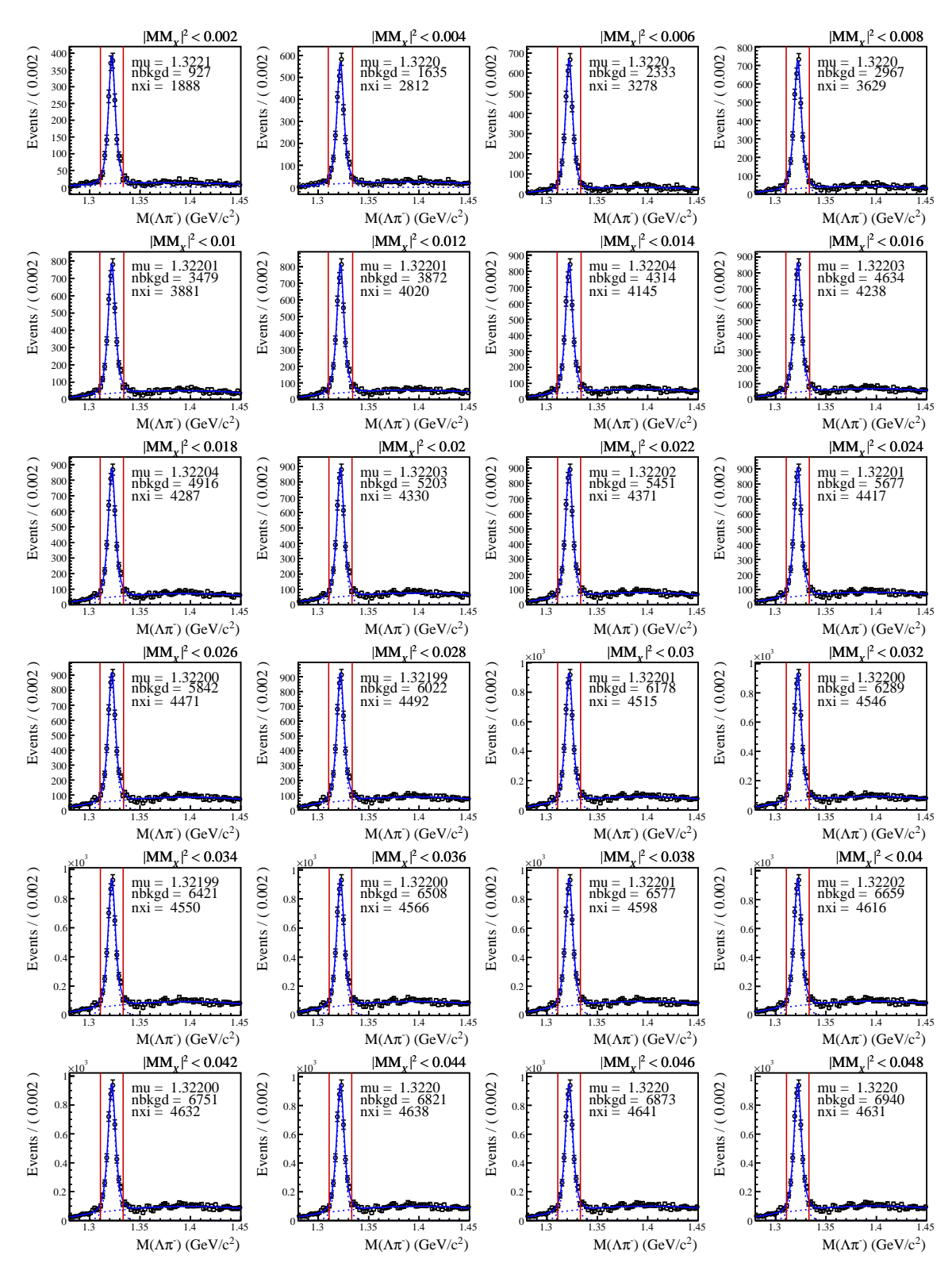


Figure 4.8: Fall 2018 mass distributions and fits for various missing-mass squared cuts $\in [2, 48] \, (\text{MeV}^2)$. A final value of 20 (MeV^2) is chosen. See Fig. 4.6 for details of the legend.

4.2.6 Kaon Selection

In the reaction of study as shown in Fig. 1.8, the kaon tracks coming from the production vertex need to be appropriately selected and identified. The selection of the two kaons is quite important for the measurement of the differential cross section, $d\sigma/dt$, due to the binning in the Mandelstam variable -t, which is dependent on the kinematics of the production kaon. The two kaons in the reaction can be separated based on particle momentum because at the Gluex energies, the initial "fast" kaon is highly boosted through t-channel production and, as a consequence, receives most of the production momentum. The "slow" kaon is then produced in the decay of the intermediate hyperon with the Ξ . We refer to these as K_{fast}^+ and K_{slow}^+ throughout the dissertation. The kaons will be called K_1^+ and K_2^+ when using the particles that are arbitrarily chosen by the reconstruction software in the analysis (for comparison and verification). Understanding this notation we can now introduce the Mandelstam-t variable mentioned above

$$t = \left(p_{\gamma}^{\mu} - p_{K_{fast}^{+}}^{\mu}\right)^{2},\tag{4.9}$$

where p^{μ} are the particle 4-vectors. This is the momentum transfer squared at the t-channel γK_{fast}^+ vertex in the reaction.

In Fig. 4.9, the 2D kaon momentum distributions are shown for the case when the two kaons are not ordered by their momentum as described above. The cuts from Table 4.2 are applied but without any kaon selection criteria (yet) for data (left side) and simulated data (right side) for the GLUEX-I data. Two kinematic regions are clearly separable. The weakly overlapping region for $|\vec{p}| < 2$ GeV may be due to π/K misidentification. The two separable kinematic regions of interest show clearly that there is always a low and high momentum kaon. This is further evident in the simulated data where there is no overlapping region and the kaons can be almost unambiguously separated. Therefore, the kaon with the larger momentum is chosen as the fast kaon produced at the primary production vertex, K_{fast}^+ , and the slow kaon, K_{slow}^+ , should be produced from the decay of the intermediate hyperon.

Due to the importance of the kaon selection, the simulated data were used to verify that the kaons were selected correctly. This is done by accessing the generated (truth) information

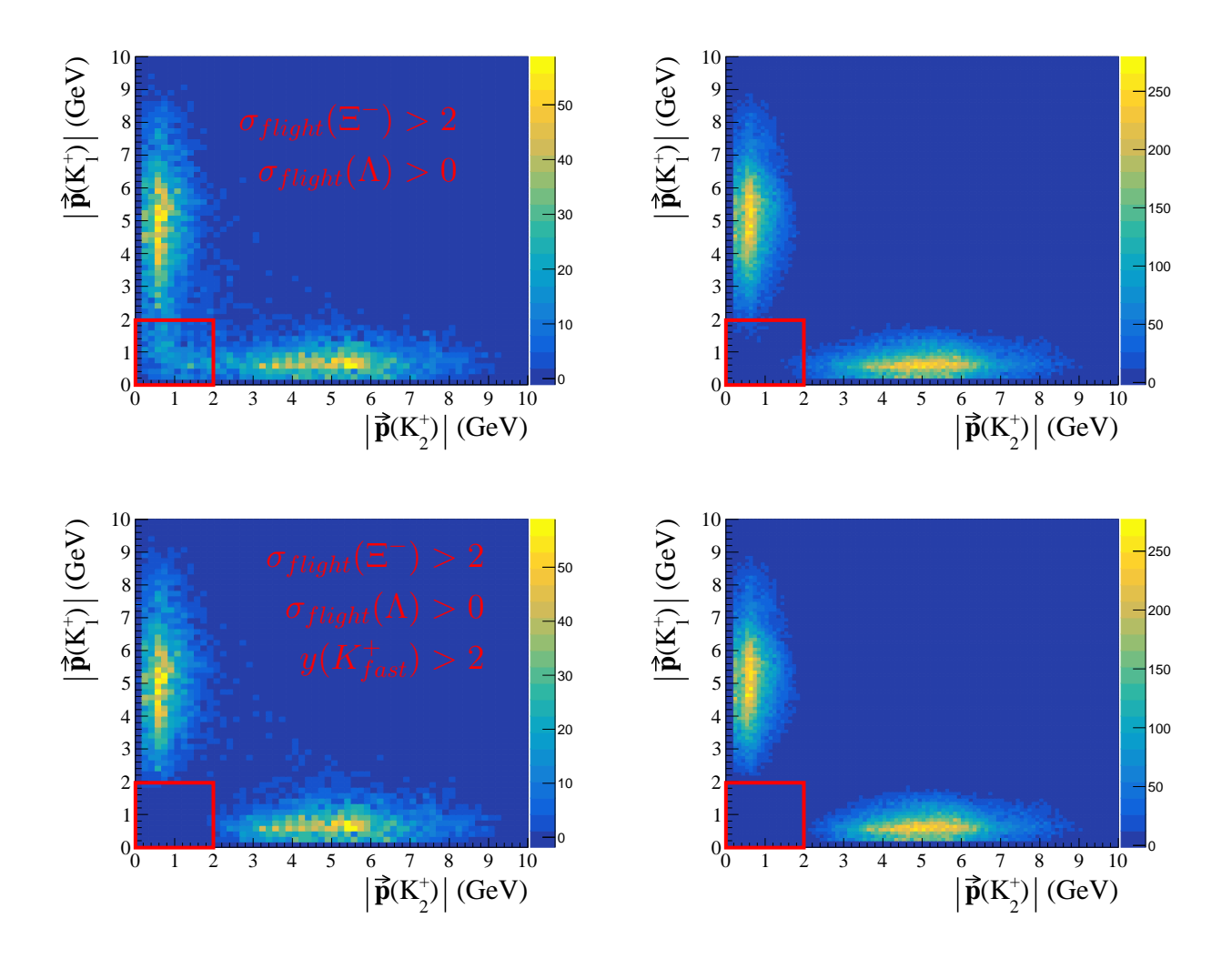


Figure 4.9: (*Left*) Data, (*Right*) Simulation. 2D distributions of K_1 vs K_2 momentum for the mixed kaons before being ordered by their momentum where the bottom distribution have required to the rapidity cut discussed Section 4.2.7.

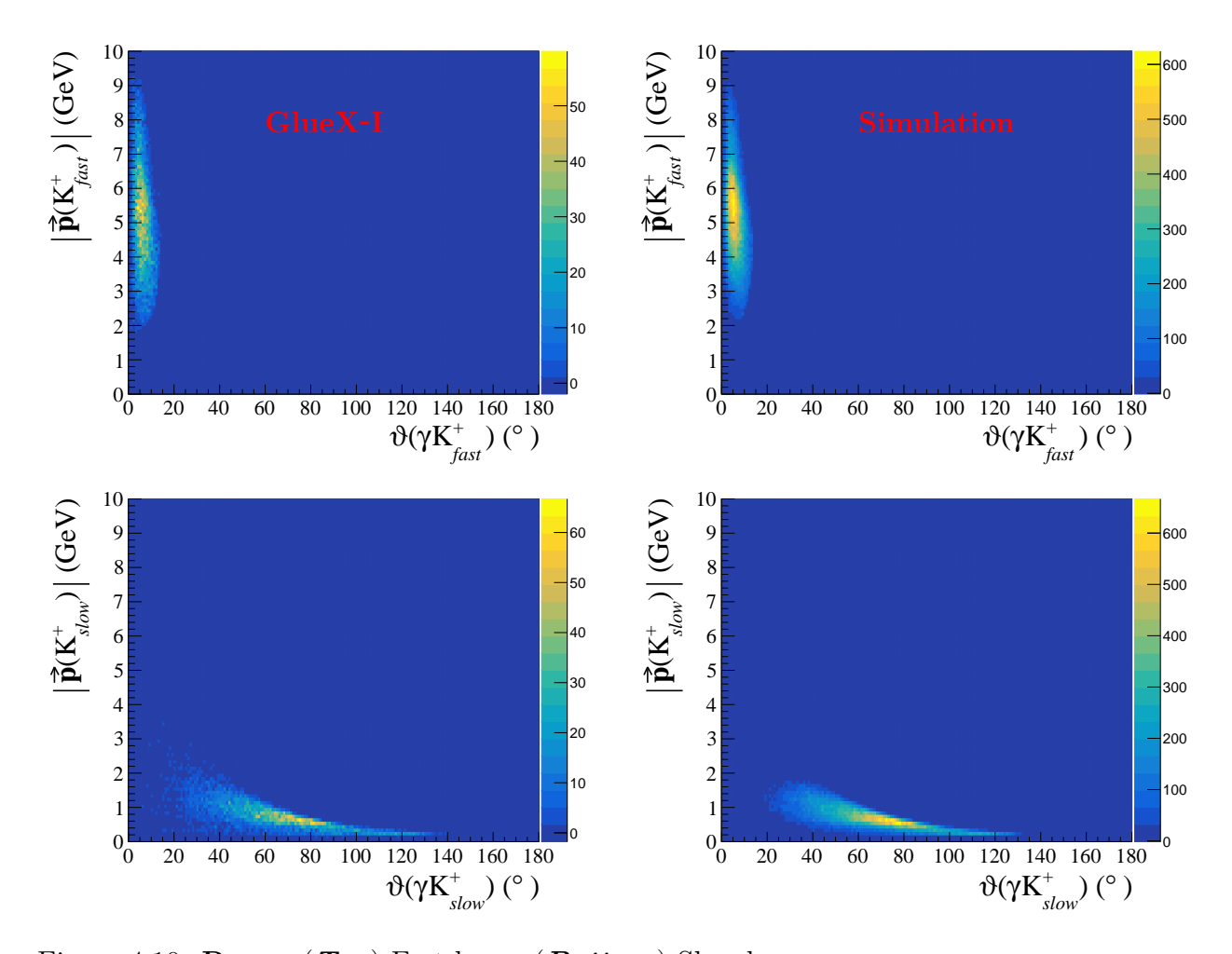


Figure 4.10: **Rows:** (*Top*) Fast kaon, (*Bottom*) Slow kaon. Columns: (*Left*) 2D Momentum vs Polar Angle distributions of GLUEX-I data (*Middle*) 2D Momentum vs Polar Angle distributions of reconstructed MC.

for the kaon that is chosen after the reconstruction of the simulated data. Figure 4.10 shows the reconstructed momentum vs. polar angle distributions (left) for fast (top) and slow (bottom) kaons, and the comparison of the reconstructed and generated momentum (right). Finally, it is seen from the figure that the kaons in the simulations are separated very well after selection and that they agreement well with the data Fig. 4.10.

4.2.7 Rapidity Cuts

In experimental hadron and particle physics, the rapidity is defined as

$$y = \frac{1}{2} \ln \left(\frac{E + p_z}{E - p_z} \right) , \tag{4.10}$$

where E is the energy of the particle and p_z is its momentum along the beam axis. The rapidity is a powerful tool that is invariant under Lorentz transformations and is related to the angle of the particle along the beam direction. This provides a powerful tool in the analysis framework for event selection.

After further investigation, the kaon selection (fast and slow assignments) described in Section 4.2.6 shows a pile-up in the kinematics of the K_{fast}^+ at the low-momentum tail. This is shown in the left distribution of Fig. 4.11, where the GLUEX-I data is compared to the simulated data. Below ~ 3 GeV there is an accumulation of events not seen in the simulation. The possible cause of this pile-up in the low-momentum region of the data could be from possibly mislabeling the kaons in terms of fast and slow, the misidentification of the kaons for pions, or potentially a different topology not modeled in the simulation. By looking at the rapidity distribution in data and simulated data we are able to disentangle the discrepancy that is seen for the reconstructed kaon momentum distributions.

Figure 4.11 shows the rapidity distributions for both the fast and slow assigned kaons where we require the rapidity to be $y(K_{fast}^+) > 2$ (blue line) to match the simulated data. Another powerful feature of the rapidity is that for a given reaction, in theory, it should be symmetric modulo real detector affects. This is because it is describing the boost along the beam that for a single reaction should produce a symmetric cone around its decay. In the data at the low rapidity values, there is a larger deviation from symmetry and disagreement with the simulated data that leads to the cuts shown. The slow kaon rapidity in Fig. 4.11 seems to deviate from the symmetry and this is most likely due to having multiple Y^* contributions that constitute the production of the $\Xi(1320)$.

Kaon Selection Improvement. As discussed in the previous section the rapidity cut allows us to correct the particle kaon momentum distribution. Figure 4.12 shows the affect of the cut $(y(K_{fast}^+) > 2)$ on the momentum distributions of the fast and slow moving kaons

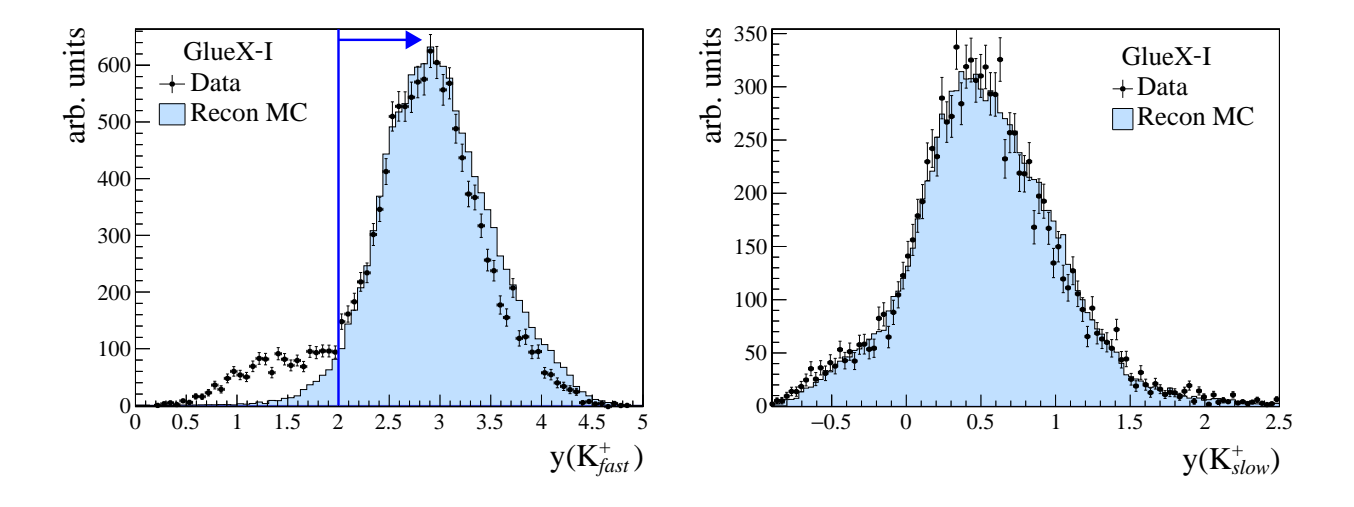


Figure 4.11: Rapidity distribution of the fast kaon ($\textbf{\textit{Left}}$) and slow kaon ($\textbf{\textit{Right}}$) for the GlueX-I data and simulated data comparison.

compared to the simulated data. It is clearly seen that in the momentum range (0, 2.8) GeV (shaded red region) for the fast kaon (black points) the simulation (blue area) does not agree with data. In the same distribution, applying the rapidity cut to the black points results in the correction (red data points). To verify that we are choosing the correct kaon for the fast and slow assignments we can access the generated true results and compare it to our procedure in the reconstructed monte carlo simulation discussed here and in Section 4.2.6 for selecting the kaons. Figure Fig. 4.13 shows the comparison of the generated vs reconstructed kaons as a 2D distribution where we have a one-to-one matching of the true kaons to the reconstructed kaons in the simulation. Due to this study with simulated data we conclude that they are indeed seperable and the tails in data could be from pion misidentification, or the low momentum fast kaons could be from a different topology than what is simulated. This effect is also seen as a deviation of data and simulated data at high Mandelstam-t region where we have small acceptance.

Mandelstam-t Improvement. Recall the Mandelstam t variable in this reaction is defined as Eq. (4.9), where the fast kaon 4-vector is identified and verified through the methods discussed in Section 4.2.6. As an added effect and more evidence to the potential of these events being a background, there is a correction to the t-distribution. Figure 4.14

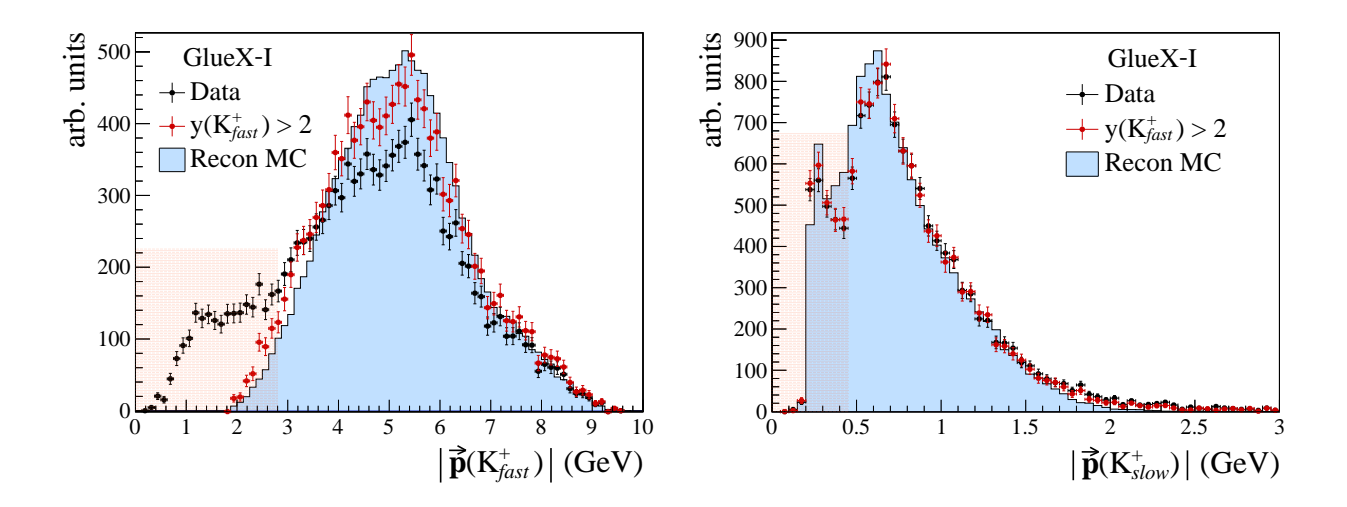


Figure 4.12: Momentum distribution of the fast kaon (**Left**) and slow kaon (**Right**) for the GLUEX-I data with (*red points*) and without (*black points*) the fast kaon rapidity cut, and simulated data comparison (*blue area*).

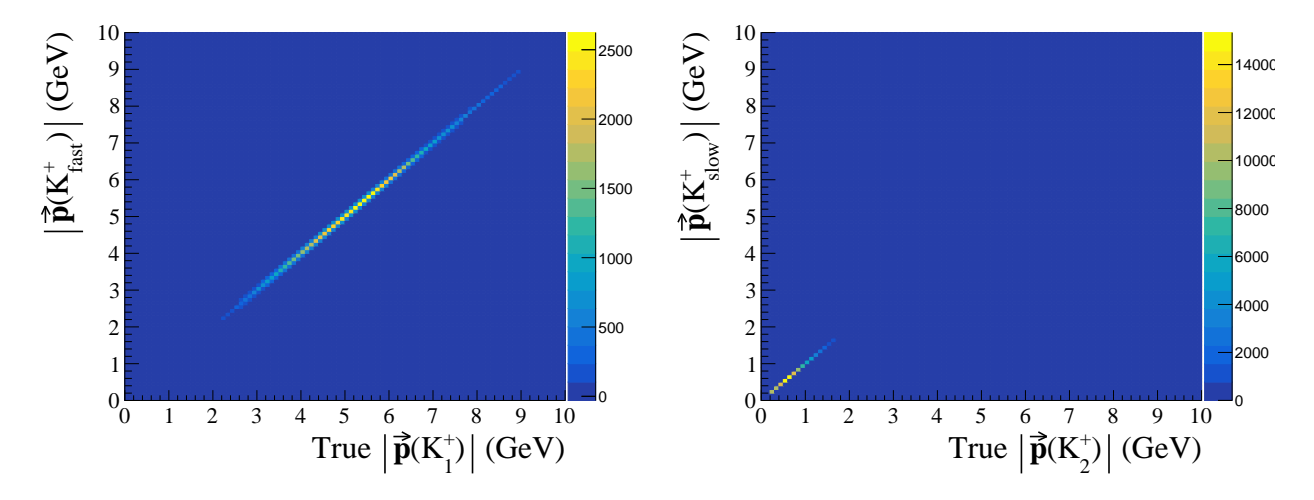


Figure 4.13: (Left) fast kaon and (Right) slow kaon 2D Reconstructed vs Generated (Truth) Momentum distributions for kaon momentum.

shows the effect of the rapidity cut in data as compared to the simulated data. It can be seen that above about 2 GeV^2 the data deviates from the simulated data. The flattening of the -t distribution in data could further indicate a completely different production mechanism in this kinematic region or potential contamination from other topologies.

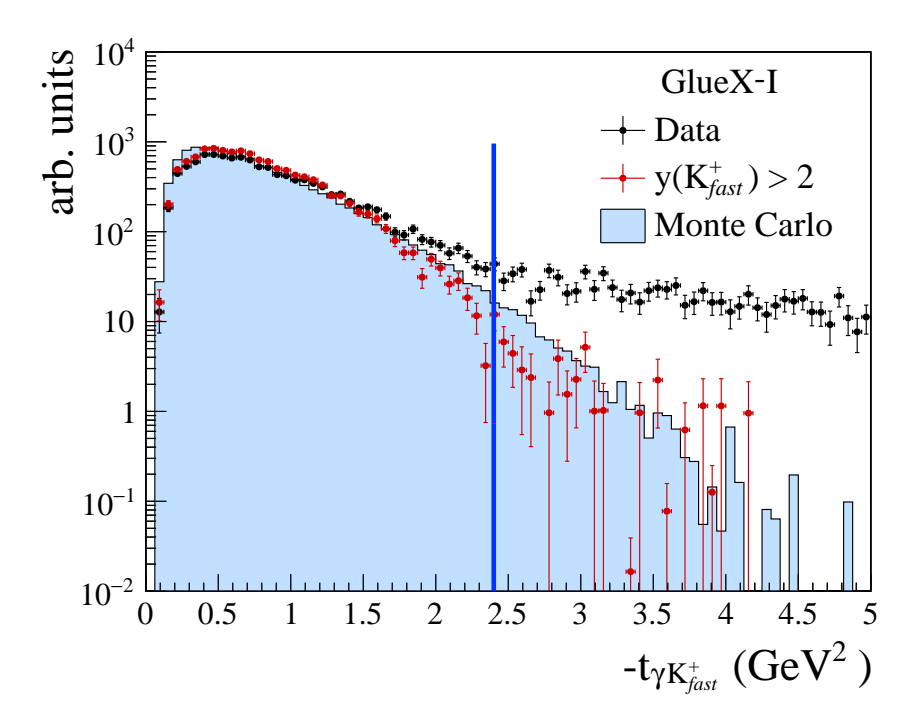


Figure 4.14: Mandelstam-t distribution for the GLUEX-I data with ($red\ points$) and without ($black\ points$) the fast kaon rapidity cut, and simulated data comparison ($blue\ area$).

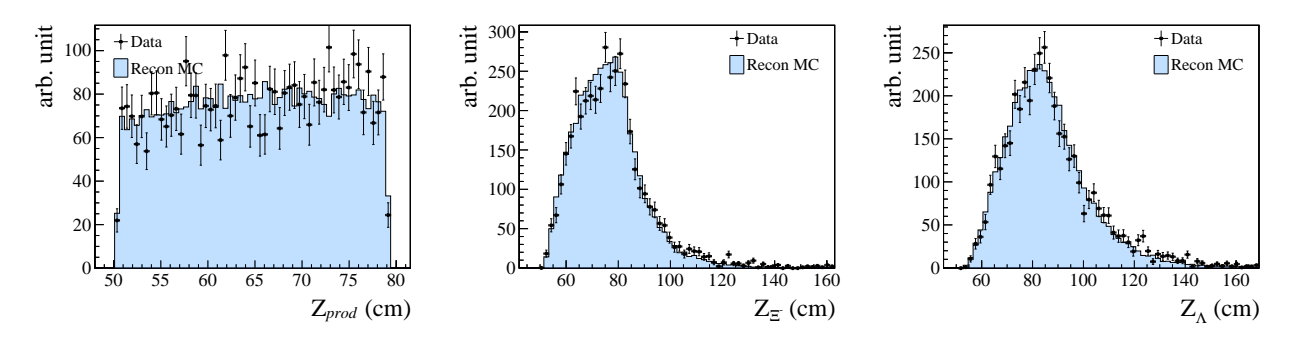


Figure 4.15: From left to right: The Z-vertex positions along the beam direction (z-direction), namely, the production vertex, $\Xi(1320)^-$ detached vertex and Λ detached vertex.

4.2.8 Vertex Cuts

The GLUEX kinematic fitter allows us to reconstruct the vertex positions of the detached vertices of weakly decaying particles. The Ξ and Λ particles decay weekly and thus have a long lifetime and therefore travel a measurable distance in the detector. The primary production, Ξ , and Λ vertex positions along the beam direction, Z, are shown in Fig. 4.15 where a cut on the production vertex of 50.4 cm $< Z_t < 79.1$ cm has been applied. This limits the production vertex to the physical target length.

Because all secondary vertices are boosted in the forward direction in the lab system, it is useful to look at the difference in the vertex positions to verify that the ordering is correct. In Figs. 4.16 and 4.17, the difference of the vertex positions along the z-direction for the (γ, Ξ) and (Ξ, Λ) systems are shown where no vertex cuts are applied. We conclude from these figures that the ordering of the vertices is not correctly reconstructed for all events if the difference is negative. Furthermore, the events with negative values that pass our cuts are determined to be background events. Therefore we do not place any cut directly on the z-vertex position differences. Instead we will use the vertex information that is extracted from the kinematic fit to ensure the proper placement of the vertices and the quality of the vertex reconstruction.

As mentioned above, from the kinematic fit, the vertex positions and their uncertainties can be extracted. Using the information of the vertex positions we can construct the path

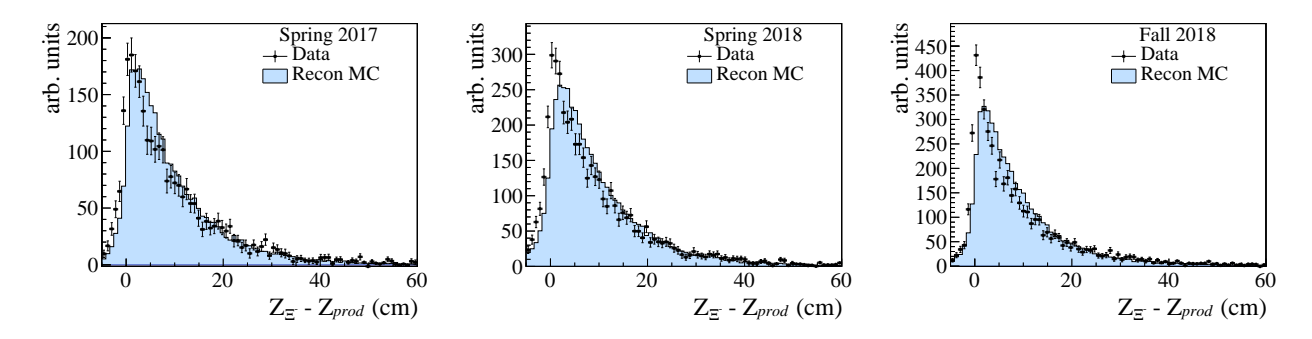


Figure 4.16: Ξ (signed) Z-length, $Z_{\Xi}-Z_{\gamma}$, for data and simulation with no vertex cuts applied for all GLUEX-I run periods.

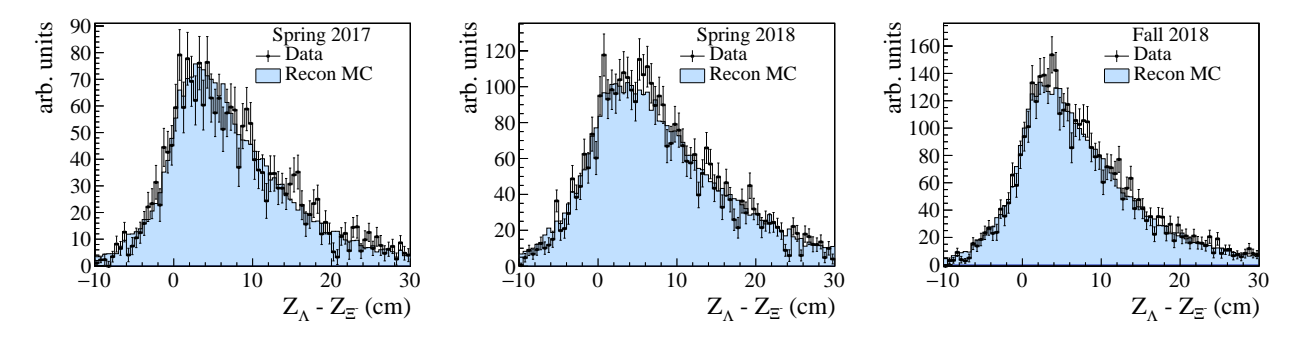


Figure 4.17: Lambda (signed) Z-length, $Z_{\Lambda}-Z_{\Xi}$, for data and simulation with no vertex cuts applied for all GLUEX-I run periods.

length of the long-lived particle:

$$d_{\Xi,\Lambda} = |\vec{x}_{\Xi,\Lambda} - \vec{x}_{\gamma,\Xi}|, \tag{4.11}$$

where Eq. (4.11) is produced from the reconstructed particle position vectors, \vec{x} , and its uncertainty σ_d is determined by the reconstruction of the vertex position from the kinematic fit. In order to distinguish the vertex position, the sign can be extracted by comparing the displacement path vector \vec{d} , and the particle decay momentum vector \vec{p} ; they must be along the same direction. Therefore, we can construct the angular distribution between the displacement path vector and the decay particle momentum vector as

$$\cos \theta = \frac{\vec{d} \cdot \vec{p}}{|\vec{d}||\vec{p}|},\tag{4.12}$$

$$\equiv \begin{cases} +1, & d \uparrow p \\ -1, & d \uparrow p \end{cases} , \tag{4.13}$$

where Eq. (4.12) is equivalent to Eq. (4.13) when constructed using the kinematic fit 4-vectors and is used to assign the correct signed value in Eq. (4.14). The (signed) flight significance is then defined for the Ξ^- and Λ long-lived baryons as

$$\sigma_{flight}(\Xi, \Lambda) = \pm \frac{d_{\Xi, \Lambda}}{\sigma_d} = \pm \frac{|\vec{x}_{\Xi, \Lambda} - \vec{x}_{\gamma, \Xi}|}{\sigma_d}, \tag{4.14}$$

The (signed) flight significance of the particle gives a quantitative parameter of how well the vertex positions are reconstructed and when $\sigma_{flight} > 0$ enforces the physically correct vertex positioning.

 Ξ/Λ Flight Significance. The Ξ baryon in our reaction decays weakly into a $\Lambda\pi$ pair, $\Xi \to \Lambda\pi^-$, with a lifetime of (0.1639 ± 0.0015) ns quoted as the world average by the Particle Data Group (PDG) [30]. In Fig. 4.18, the $\sigma_{flight}(\Xi^-)$ is shown for the three GLUEX-I run periods, where we observe a small discrepancy at low values between the data and simulation. This discrepancy between the data and simulation justifies a cut of $\sigma_{flight}(\Xi^-) > 2$.

Similarly, the Λ baryon in our reaction decays weakly into a (πp) pair, $\Lambda \to p\pi^-$, with a lifetime of (0.2632 ± 0.0020) ns quoted as the world average by the PDG [30]. In Fig. 4.19, the $\sigma_{flight}(\Lambda)$ is shown for the three GLUEX-I run periods, where it is verified that the

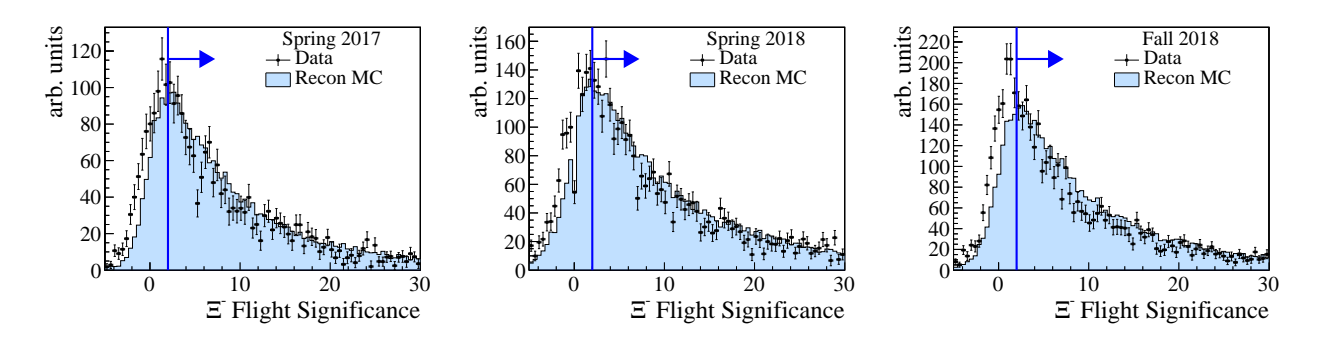


Figure 4.18: Ξ path length significance for data and simulation with cut value shown for GLUEX-I run periods.

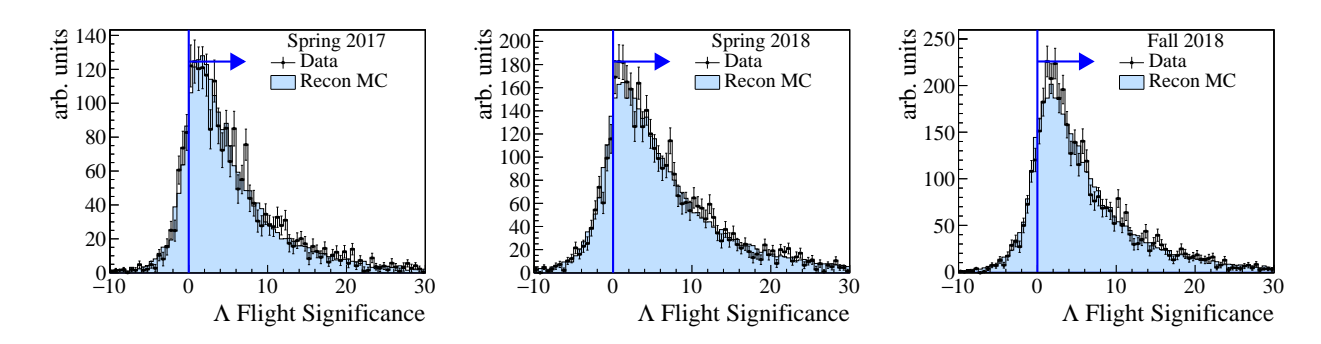


Figure 4.19: Λ path length significance for data and simulation for GLUEX-I run periods. A cut value of FS_{Λ} > 0 is chosen and therefore, the cut line is not visible in these distributions.

data and weighted simulated data are in excellent agreement. Therefore, we only impose a cut to constrain the vertex position to be upstream from the production of the Ξ , i.e., $\sigma_{flight}(\Lambda) > 0$.

4.3 Q-factor Background Subtraction

In this section, we will introduce the Q-factor background subtraction method. Up to this point and for the remainder of the report, all the data distributions are background subtracted using this method unless explicitly mentioned otherwise. For the best comparison between data and Monte Carlo the background in data must be subtracted because the simulated data does not include any background. Furthermore, the procedure was used to construct the 2D distributions used in our Monte Carlo generation technique that is

discussed in Chapter 5. This method will also be used for future measurements that would need an analysis with only signal events such as the spin measurement (see Section 6.3.1) and future polarization measurements. It is important to note that the Q-factors that have been extracted for the GLUEX-I data have not been used for the measurement of the Ξ photoproduction cross section.

In this multivariate sideband subtraction event-based method [78], the set of coordinates that describe the multi-dimensional phase space of the reaction are categorized into two types: reference and non-reference coordinates. The signal and background shapes have to be known a priori in the reference coordinate but this knowledge is not required in the non-reference coordinates. Mass is typically chosen as the reference coordinate. For each event, we then set out to find the N_c nearest neighbors in the phase space of the non-reference coordinates. This was similar to binning the data using a dynamical bin width in the non-reference coordinates and making sure that we had N_c events per fit.

The mass distribution of the N_c events (including the candidate event) in the reference coordinate is then fitted with a total function defined as:

$$f(x) = N \cdot [f_s \cdot S(x) + (1 - f_s) \cdot B(x)], \qquad (4.15)$$

where S(x) denotes the signal and B(x) the background probability density function. N is a normalization constant and f_s is the signal fraction with a value between 0 and 1. The Roofit package of the CERN ROOT software [79] has been used for the fit procedure. Since N_c is usually a small number (of the order of a few hundred events), an unbinned maximum likelihood method has been used for the fitting. The Q-factor itself is then given by:

$$Q = \frac{s(x)}{s(x) + b(x)}, (4.16)$$

where x is the reference coordinate value of the candidate event, $s(x) = f_s \cdot S(x)$ and $b(x) = (1 - f_s) \cdot B(x)$. The Q-factor can then be used as an event weight to determine the signal contribution to any physical distribution.

4.3.1 Application

In our $\Xi(1320)$ reaction, the following seven kinematic variables have been chosen to define the multidimensional kinematic phase space:

- The incoming photon energy, E_{γ} , for the full GLUEX-I energy range (6.4,11.4) GeV,
- The high-momentum kaon, K_F^+ , angular variables $(\cos \vartheta^{K_F^+}, \phi^{K_F^+})$ in the lab frame,
- The low-momentum kaon, K_S^+ , angular variables $(\cos \vartheta_{\mathcal{H}}^{K_S^+}, \phi_{\mathcal{H}}^{K_S^+})$ in the helicity frame of the intermediate hyperon (Y^*) ,
- The Ξ decay (first) pion, π_{Ξ} , angular variables $(\cos \vartheta_{\mathcal{H}}^{\pi_{\Xi}^{+}}, \phi_{\mathcal{H}}^{\pi_{\Xi}^{+}})$ in the helicity frame of the $\Xi(1320)$ and,
- The measured invariant mass of $p\pi_{\Lambda}^-$ system $(M(p\pi_{\Lambda}^-))$.

For each candidate event, the events closest in the kinematic phase space defined by the seven non-reference coordinates are selected to perform event-based unbinned maximum likelihood fits [79] in the reference coordinate. In this analysis, the reference coordinate is the invariant mass of the $\Lambda \pi_{\Xi}^-$ system in the range (1.28, 1.45) GeV².

To locate the nearest-neighbor events, the following equation describing the distance metric between event a and b, D_{ab} , was used:

$$D_{ab}^{2} = \sum_{i=1}^{4} \left(\frac{\Gamma_{i}^{a} - \Gamma_{i}^{b}}{\Delta_{i}} \right)^{2}, \tag{4.17}$$

where Γ_i was the i^{th} non-reference coordinate and Δ_i was the maximum range of the non-reference coordinate Γ_i .

The Q-factor machinery is applied to each GLUEX-I run period separately. We chose 150 nearest neighbors for each candidate event (excluding the candidate itself). The four-parameter Johnson's S_u -distribution function [80] was used for the signal as a probability density function (pdf) defined as:

$$pdf [Johnson S_u] = \frac{\delta}{\lambda \sqrt{2\pi}} \frac{1}{\sqrt{1 + \left(\frac{x-\mu}{\lambda}\right)^2}} \exp\left[-\frac{1}{2} \left(\gamma + \delta \sinh^{-1} \left(\frac{x-\mu}{\lambda}\right)\right)^2\right], \quad (4.18)$$

where this pdf is a result of a transformation of a normal distribution of the form:

$$z = \gamma + \delta \sinh^{-1} \left(\frac{x - \mu}{\lambda} \right). \tag{4.19}$$

The statistical mean $\overline{\mu}$ (not to be confused with the parameter μ) of the Johnson S_u is written as

$$\overline{\mu} = \lambda \exp\left(\frac{\delta^{-2}}{2}\right) \sinh\left(\frac{\gamma}{\delta}\right) \tag{4.20}$$

and the statistical variance is:

$$\sigma^2 = \frac{\lambda}{2} \left(\exp(\delta^{-2}) - 1 \right) \left(\exp(\delta^{-2}) \cosh\left(\frac{2\gamma}{\delta}\right) + 1 \right). \tag{4.21}$$

For the background pdf, we chose a second-order Chebyshev polynomial. The parameters and the constraints imposed on the fit are shown in Table 4.3. The total pdf was constructed from the signal and background pdfs (Equation 4.15) and the Q-factor of the candidate event was determined according to Equation 4.16.

Table 4.3: Parameters of the signal and background probability-density functions and the constraints imposed on them. A Johnson's S_U pdf was used to describe the signal and a first-order Chebychev polynomial was used to describe the background.

	Parameters	Initial Value Constraints
	ξ	$ 1.322 \text{ GeV}^2 \pm 5.5 \text{ MeV}$
Johnson S_u pdf	λ	5.5 MeV (2, 7) MeV
	δ	1.3 (1, 2)
	γ	0 fixed
Chebychev pdf	c_0	0.8 (-1.0, 1.5)

Figure 4.20 shows an example fit to the mass distribution using the unbinned maximum likelihood method, and the fit parameters of the signal and background pdfs were determined. Superimposed are the total fit function (blue solid line), the signal pdf (red solid line) and the background pdf (yellow solid line). The pdfs were normalized to the number of events in the distribution. The dotted blue and pink lines show the extracted singular values for the Q-factor governed by Eq. (4.16).

Figure 4.21 shows the prominent $\Xi(1320)^-$ signal for the three GLUEX-I datasets using the Q-factors extracted from the above procedure (Top Row) and the subsequent constructed χ^2_{ν} for the unbinned maximum likelihood fits performed for each event (Bottom Row).

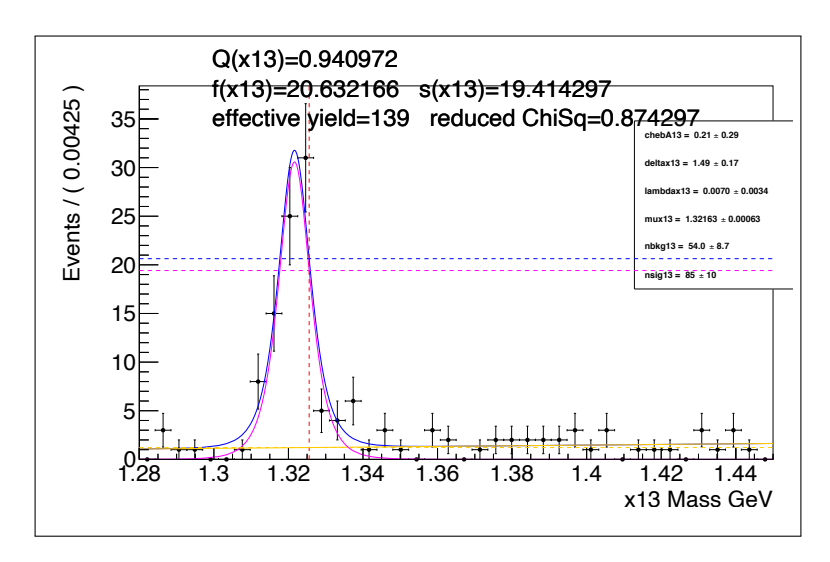


Figure 4.20: An example of the fit procedure to one event and its nearest neighbors to extract the Q-factor for the GLUEX-I Spring 2018 run period. The solid blue and pink lines represent the fit function and signal function respectively. The dashed blue and pink line represent the function value at the mass of the event for the fit and signal used to extract the Q-factor.

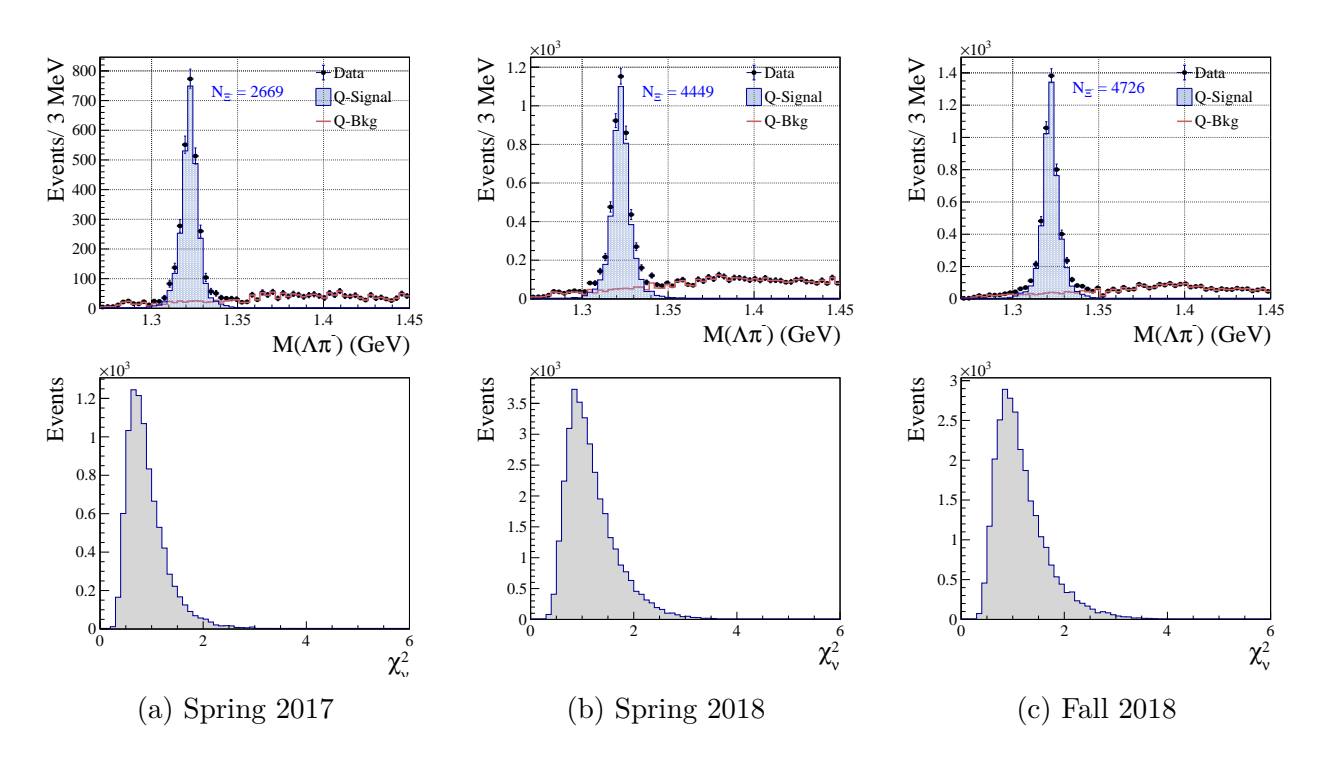


Figure 4.21: The Ξ invariant mass distributions with the signal and background determined by the Q-Factors and the extracted χ^2_{ν} for all events for all GLUEX-I run periods.

CHAPTER 5

SIMULATION PROCEDURE

Monte Carlo (MC) simulation of events is performed on the JLab computing farm with the GEANT4 framework [81]. The detector geometries, materials, and magnetic field maps of the experiment are represented in GEANT4 and used for the reconstruction of the generated MC events. In the simulation framework many event generators can be specified as inputs. The event generator produces the particles at the primary vertex inside the hydrogen target with timing information that matches the RF structure of the beam. The generated events are passed to GEANT4 to be simulated through the detector systems followed by data smearing and reconstruction to REST files. The smearing process gives the generated data resolution to match each run period in data and backgrounds can be added such as random triggers. The reconstruction procedure used is the same for the analysis version that is being simulated to match all calibrations and reconstruction software to the data. A flow chart of the procedure from generation to reconstruction as described above is shown in Fig. 5.1. The products of the final reconstruction are ROOT files that contain the same information as the data ROOT files as well as the truth information that can be retrieved because we know exactly what was generated.

The event generator developed for GLUEX GEN_AMP_V2 [82] has been used for the generation of Monte Carlo events because the (decay) properties of the intermediate hyperon can be modeled directly from the data. Previously, a pure phase-space generator was used called GENR8. Although the parameters used for GENR8 [83] are extracted in such a way to emulate the GLUEX data, it was still just a flat phase-space representation and not good enough to replicate the complicated final-state particle kinematics of this reaction. It was found that the flat angular distributions generated in the rest-frame of the parent particles for the phase-space Monte Carlo cannot describe the decay angular distribution of $Y^* \to K^+_{slow}\Xi^-$ events. Therefore, the current infrastructure was extended to allow for physics input from data to the framework of GEN_AMP_V2.

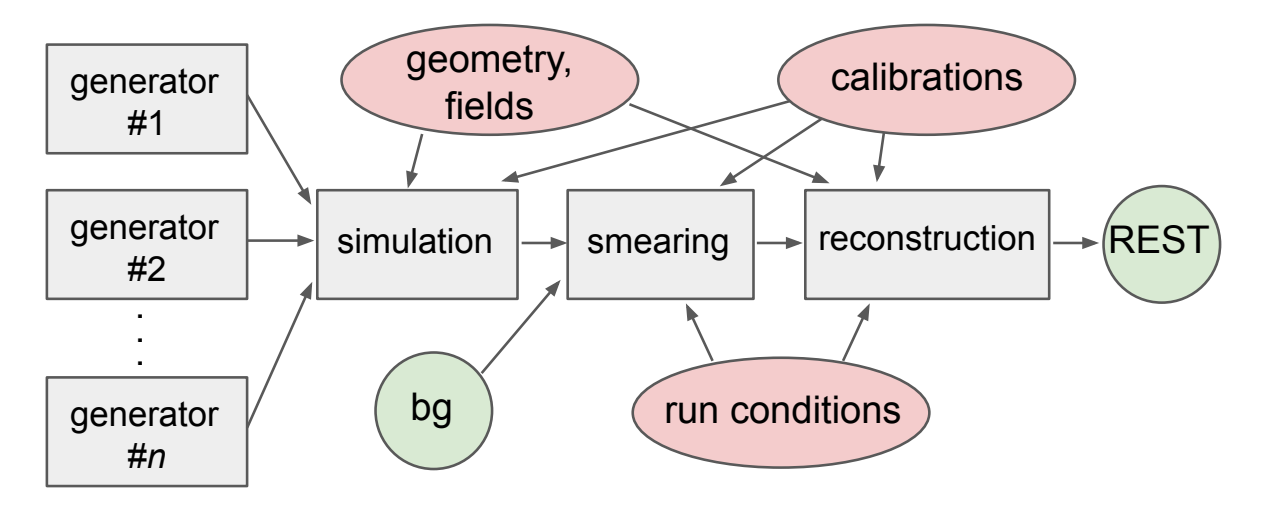


Figure 5.1: Flow chart of steps to generate simulations at GlueX. Reprinted from [75] Copyright 2020 with permission from Elsevier.

To generate Monte Carlo events in the GEN_AMP_V2 framework, the only input parameter is the t slope, b, associated with the primary t channel production. Furthermore, the subsequent decay of the Y^* hyperons are generated from the observed invariant mass and the helicity-angular distribution of the $Xi(1320)^-$ in the rest frame of the intermediate hyperon. Specifically, the final state $K^+K^+\Xi^-$ is generated through t channel production of a K^++Y^* with the subsequent decay of the intermediate hyperon, that is, $Y^* \to K^+\Xi^-$. The t slope is estimated from the background-subtracted and acceptance-corrected t-distribution using the data and a recursive method is applied to finalize the value used in the simulation. Since the intermediate hyperons producing the $\Xi(1320)$ baryon are unknown, the hyperon properties required in the generation are taken from the data. Using the AmpTools framework, the background-subtracted and acceptance-corrected distributions from data that describe the intermediate hyperon decay are used as physics inputs. Following the generation of $K^+K^+\Xi^-$ produced through Y^* decays, the generated events are then given to GEANT4 where the Ξ and Λ baryons are able to decay weakly according to their lifetime and measured properties through the GLUEX detector system in GEANT4. Finally, the simulated detector events are smeared and reconstructed with the same software as the data events.

5.1 Physics Generator

5.1.1 *t*-channel Production

The t-slope input for the simulation provides the important kinematic information for the primary t-channel production, i.e., $\gamma p \to K_{fast}^+ Y^*$. When generating the t-channel reaction using GEN_AMP_V2, the t-distribution is constructed with the original input t-slope acquired from the recursive study as mentioned above. To preserve the line-shape from the original input the initial production is decoupled from the decay of the Y^* . When constructing the t-intensity distribution in the generator the t-slope, b, is the exponential slope constant defined as

$$f(t) = A e^{-bt}, (5.1)$$

where t is the Mandelstam variable defined in Eq. (4.9). The distribution of Fig. 5.2 shows the t-distribution comparison of data (corrected for detector effects) and simulated thrown data (truth) using Eq. (5.1) to determine that it is properly reproduced.

The process of determining the appropriate t-slope for the simulation is an iterative process outlined below:

- 1. The simulation is generated with a starting t-slope value.
- 2. The data is acceptance corrected with the previous simulation and the t-slope is extracted from an exponential fit to Eq. (5.1).
- 3. The value is compared to what was originally input into the simulation and regenerated with the new value.
- 4. The process above is iterated until the input simulation value is in agreement with acceptance corrected data.

In Fig. 5.2, the final step of the iteration process is shown for the GlueX-I data, showing the comparison of the acceptance-corrected t-distribution in data versus the generated (thrown) distribution, which is also fit with an exponential with a t-slope value extracted (b = 1.43). The extracted b is the value used for the generation of the Monte Carlo and in good agreement with the corrected data up to $\sim 2.5 \text{ GeV}^2$.

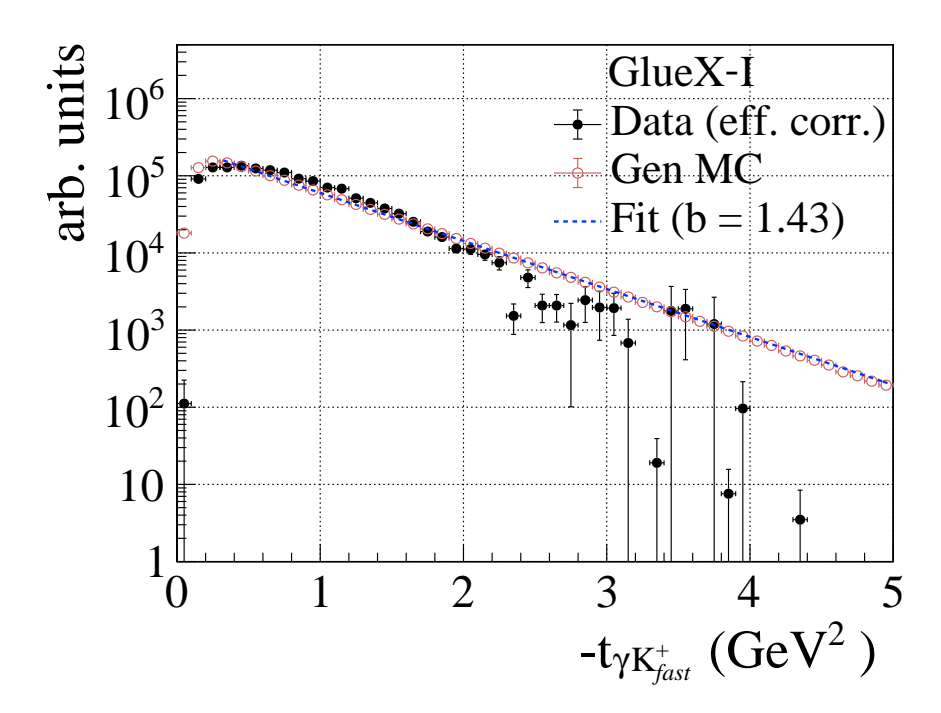


Figure 5.2: The final product of the combined GlueX-I acceptance-corrected t-distribution fit with an exponential function to extract the t-slope parameter and the generated t-distribution for comparison.

5.1.2 Intermediate Hyperon Decay

In the AmpTools framework [84], the generation can be appropriately weighted to the input distributions by introducing the relevant kinematic variables and their observed data distributions. For this approach, the program was modified to take a two-dimensional histogram of the mass of the Y^* in the invariant mass of $K_{fast}^+\Xi^-$ and angular intensity distribution of the Ξ^- in the rest frame of the Y^* from data to be used as a probability distribution to generate events. In short, this is an amplitude that can be used to simulate the properties of the intermediate hyperon in the AmpTools framework. Traditionally, the decay distributions of the parent particles are the invariant mass and the intensity angular distribution in the helicity frame described in Section 5.1.2. For the purposes of generating Monte Carlo that match the kinematic distributions of the data to obtain the detector efficiency, the traditional helicity frame needed to be slightly modified due to the way the generator is producing the four-vectors. To match the procedure in the generator the 2D data distribution was created with the angular intensity in the pseudo-helicity frame that is defined in Section 5.1.2.

Helicity Frame. For the helicity angular distribution, the particle 4-vectors must be boosted into the overall center-of-mass (c.m.) frame followed by a second boost into the rest frame of the Y^* hyperon along the Y^* direction in the c..m frame. In the rest frame of the Y^* hyperon the z-direction is defined along that of the boosted hyperon in the c.m. frame and the y-direction is perpendicular to the production plane of the Y^* ; the helicity frame is explicitly defined to be [85]:

$$\hat{y}_{\mathcal{H}} = \frac{\vec{p}_{c.m.}^{\gamma} \times \vec{p}_{c.m.}^{Y^*}}{|\vec{p}_{c.m.}^{\gamma} \times \vec{p}_{c.m.}^{Y^*}|}, \qquad \hat{z}_{\mathcal{H}} = \frac{p_{z,c.m.}^{Y^*}}{|\vec{p}_{c.m.}^{Y^*}|}, \qquad \hat{x}_{\mathcal{H}} = \hat{y}_{\mathcal{H}} \times \hat{z}_{\mathcal{H}}, \qquad (5.2)$$

where the particle momenta are in the c.m. frame. The helicity angle is then the angle between $\hat{z}_{\mathcal{H}}$ and one of the decay particles, e.g., \vec{p}^{Ξ^-} , in the helicity frame, written as

$$\cos \vartheta_{\mathcal{H}}^{\Xi^{-}} = \frac{p_{z,\mathcal{H}}^{\Xi^{-}}}{|\vec{p}_{\mathcal{H}}^{\Xi^{-}}|}.$$
 (5.3)

Pseudo-Helicity Frame. The 4-vectors within the GEN_AMP_V2 framework are generated directly in the rest frame of the parent particles and then weighted (accept/reject) depending on the given amplitude used. It was found that if we used the helicity angular

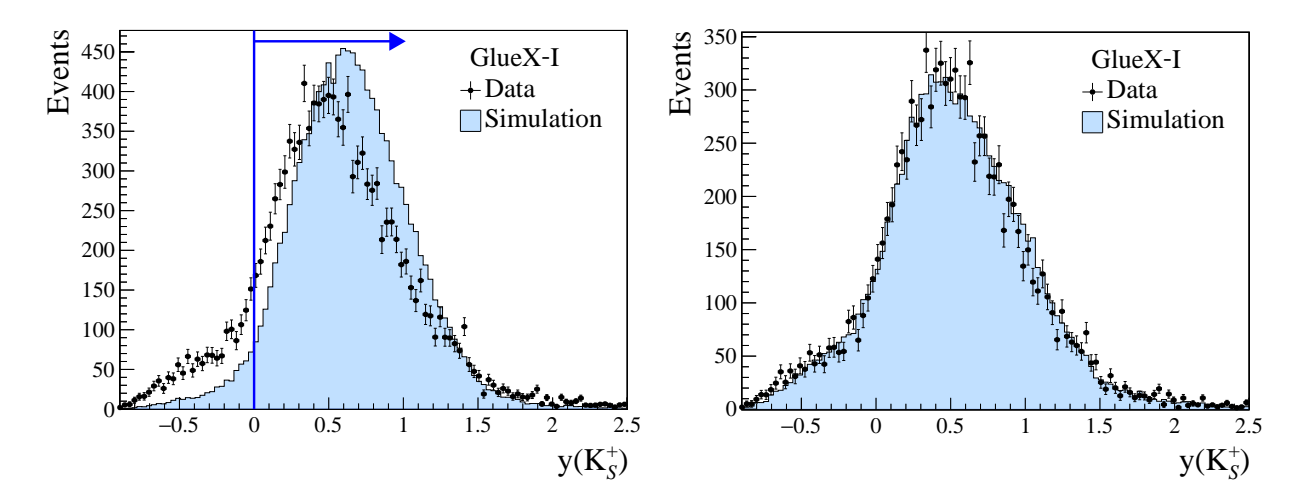


Figure 5.3: (*Left*) Rapidity distribution of the slow kaon. (*Right*) momentum distribution of the slow kaon for the GLUEX-I data and the old simulation using the 4-vectors in the helicity frame as defined in Eqs. (5.2) and (5.3).

distribution for the amplitude as defined above in Eqs. (5.2) and (5.3) when generating the 4-vectors there was a shift in the angular distributions of the Y^* decay particles. This is illustrated in Fig. 5.3 where the left histogram shows the shift in the slow kaon pseudorapidity and the right histogram shows the effect on the slow kaon momentum distribution, where the simulation has a much broader momentum distribution.

The solution for the above issue was to directly boost into the rest frame of the Y^* and define this pseudo-helicity where the unit vectors are constructed using the particle momenta in the lab frame:

$$\hat{y} = \frac{\vec{p}_{lab}^{\gamma} \times \vec{p}_{lab}^{Y^*}}{|\vec{p}_{lab}^{\gamma} \times \vec{p}_{lab}^{Y^*}|}, \qquad \hat{z} = \frac{\vec{p}_{z,lab}^{Y^*}}{|\vec{p}_{lab}^{Y^*}|}, \qquad \hat{x} = \hat{y} \times \hat{z} , \qquad (5.4)$$

where the angular distribution is similarly defined as

$$\cos \theta_{h^*}^{\Xi^-} = \frac{p_{z,h^*}^{\Xi^-}}{|\vec{p}_{h^*}^{\Xi^-}|}.$$
 (5.5)

Therefore, for the generation and reconstruction of the simulated data the distributions of importance are this *pseudo-helicity* angular distribution given by Eq. (5.5) and the invariant mass candidates of the Y^* .

The helicity angle in the rest frame of the Y^* from Eq. (5.5) is used to generate the final particles before given to GEANT4 to properly simulate subsequent weak decays through the detector. The left distributions of Fig. 5.4 compare the invariant mass $K_{fast}^+\Xi^-$ from real data to the simulated data. The right distributions compares the helicity angle for real data and simulated data.

Figure 5.4 shows good agreement of the data and simulation (right distributions). Because the acceptance-corrected 2D distribution of hyperon mass vs. pseudo-helicity angle are used for the generation of the events, this process may need to be iterated in a similar way to the t-distribution.

2D MC Generation Results. The procedure for generating events and reconstructing the $\Xi(1320)^-$ are as follows:

- 1. Build the background subtracted 2D data distribution that contains the Ξ helicity-angle in the rest-frame of the Y^* and the invariant mass of the Y^* from data.
- 2. Generate the MC in the GEN_AMP_V2 framework as described above with the data that has not been acceptance corrected as a starting point.
- 3. Repeat step 1 but now acceptance correct the 2D distribution using the newly generated MC sample.
- 4. Generate the next iteration of MC and repeat if needed.

The results of the final iteration of the procedure listed above is shown in Fig. 5.4, where the left distributions are the invariant mass candidates and the right distributions are the helicity-angle of the Y^* hyperon for the acceptance-corrected data (top) and the reconstructed data (left) vs the equivalent simulated data. From the figure below, the mass and helicity-angle distributions agree very well. This is a great improvement due to the pseudo-helicity definition and consistency with the generator. We feel that this is still a valid parameter to use because it is coming from the data and reproduces the final-state particles very well to simulate the detector efficiency.

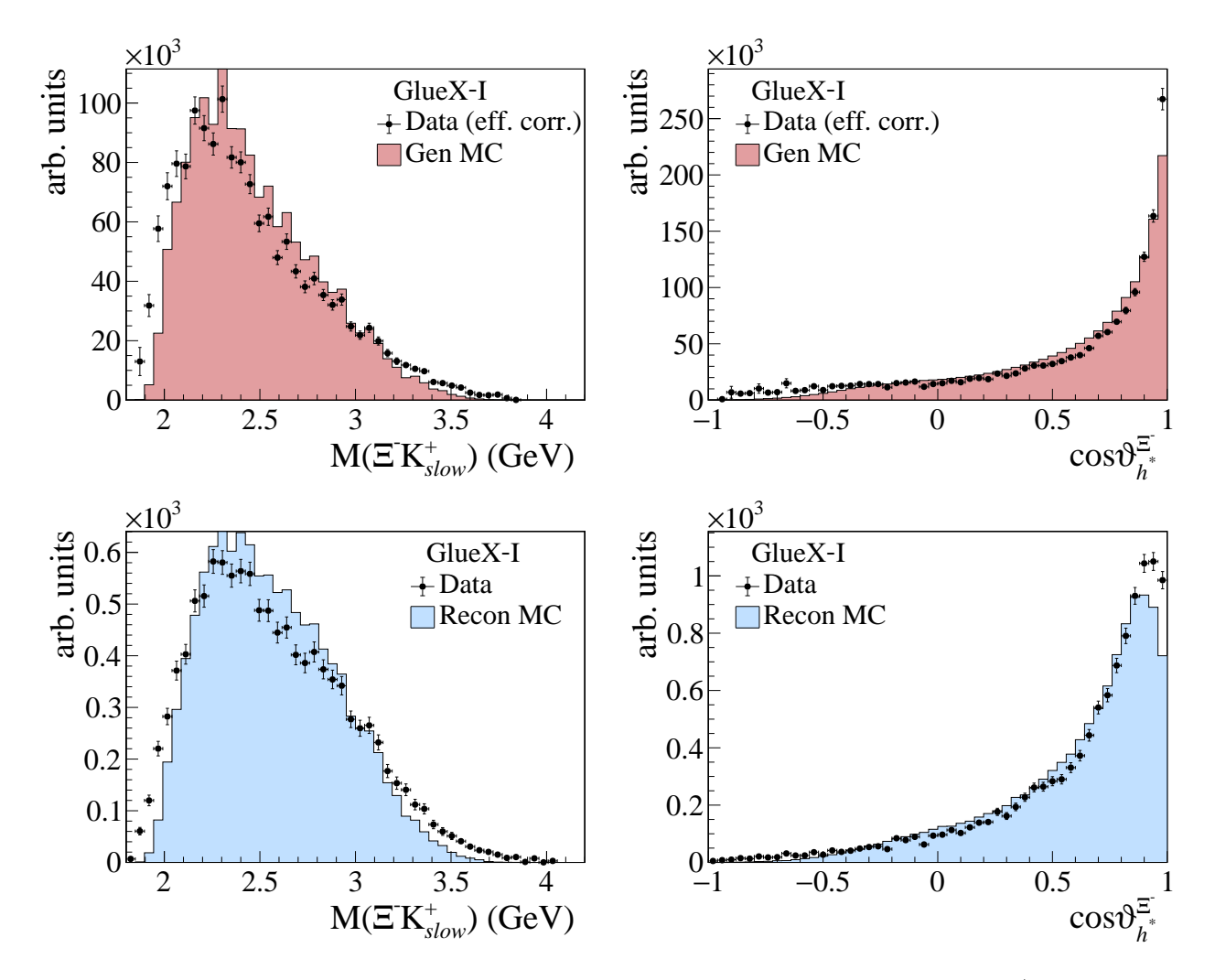


Figure 5.4: Comparison of real data and Monte Carlo simulations for the $\Xi^-,^+_{fast}$ invariant mass and intensity angular distribution of Eq. (5.5). The top row shows efficiency-corrected data (black points) versus generated Monte Carlo (red histogram), while the bottom row compares reconstructed real data (black points) to reconstructed Monte Carlo simulations (blue histogram). The left column presents the invariant mass distributions of the intermediate hyperon Y^* candidates, and the right column displays the angular distribution of the Ξ baryon in the rest frame of the Y^* hyperon defined by Eq. (5.5).

5.2 Data Comparison

In the following, Fig. 5.5 shows the comparison of data and simulated data for the GLUEX-I run periods; the data and simulation agree well. As mentioned in Section 4.3 the data are background subtracted using the Q-Factors for all comparisons between the data and the reconstructed MC. Furthermore, the reconstructed MC are normalized to the integral of the data distribution for data/MC comparison because there are far more generated events. The proton momentum distribution is now in excellent agreement. Previously, they were typically shifted to the right in the simulation. With the new simulations discussed in Section 5.1.2 there is now perfect agreement with the slow kaon kinematics, which has not been possible until now.

Figure 5.6 shows the generated versus reconstructed simulation. The pions seem to have low acceptance at low momenta as expected. Nevertheless, this seems to be well modeled.

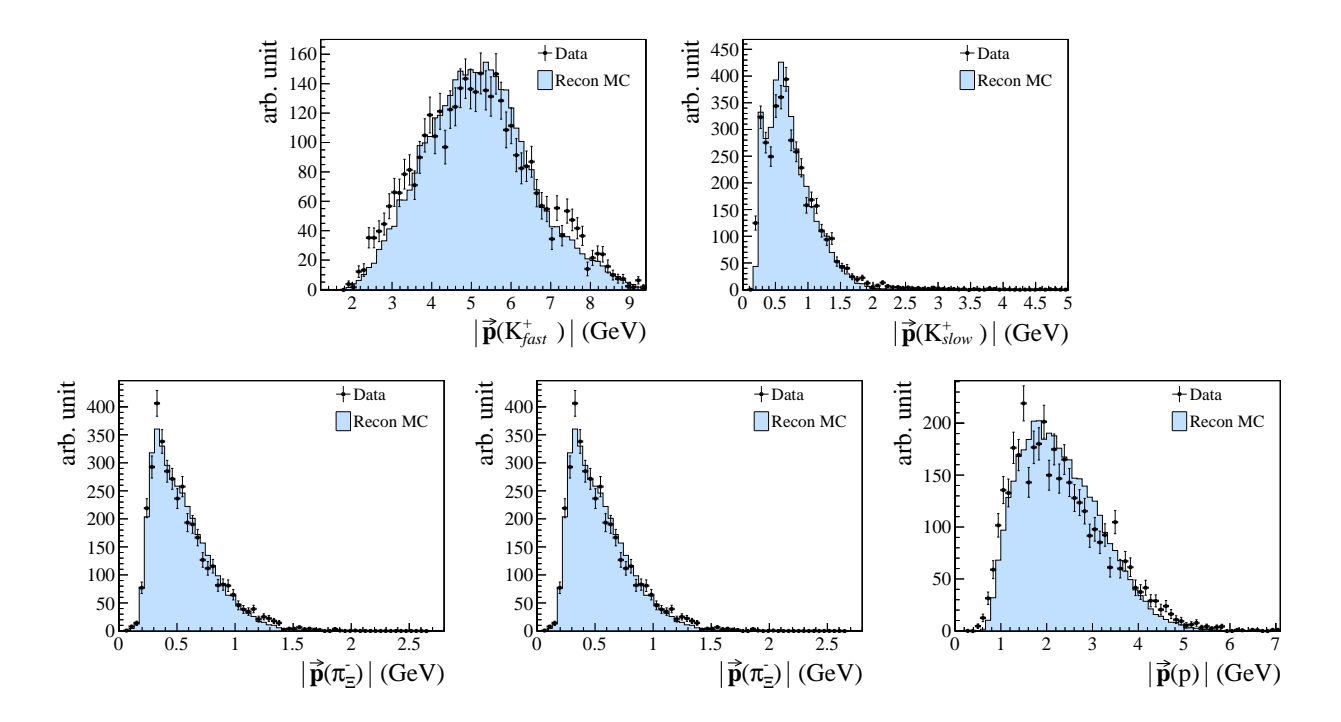


Figure 5.5: The momentum distribution for all final state particles for the Fall 2018 run period for data and reconstructed simulation.

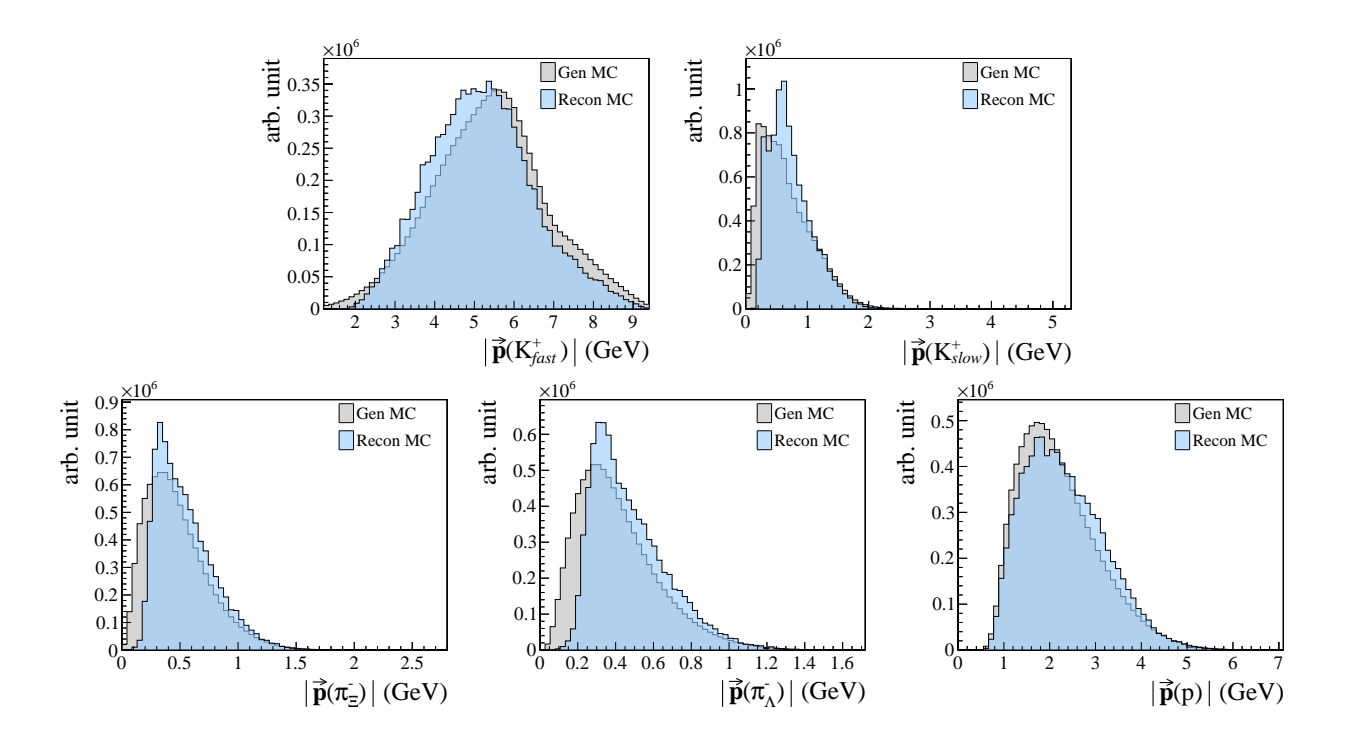


Figure 5.6: The momentum distribution for all final state particles for the Fall 2018 run period for reconstructed and generated simulation.

CHAPTER 6

EXPERIMENTAL METHODS AND RESULTS

For the proceeding extraction of the differential cross sections, all of the preceding work presented for the event selection and Monte Carlo simulation has been used to determine yields and generate the detector efficiencies.

6.1 Experimental Cross Section Methodology

The experimental differential cross section for the reaction of study, i.e., $\gamma p \to K^+ K^+ \Xi^-$, binned in incident photon energy, E_{γ} , and Mandelstam t (see Eq. (4.9)), is obtained through the following equation:

$$\frac{d\sigma(E_{\gamma},t)}{dt} = \frac{N_{\Xi}(E_{\gamma},t)}{\rho_t N_{\gamma}(E_{\gamma}) BR(\Lambda \to \pi^- p)\epsilon(E_{\gamma},t) \Delta t}.$$
 (6.1)

The components of Eq. (6.1) are:

 $N_{\Xi}(E_{\gamma},t)$: extracted Cascade yield per bin in E_{γ} and -t for data,

 $N_{\gamma}(E_{\gamma})$: photon flux or total number of photons on target per energy bin,

 $\epsilon((E_{\gamma},t))$: detector acceptance for all possible decay branches per bin,

 $BR(\Lambda \to p\pi^-)$: Branching fraction of the Λ decaying to proton and π^- .

 ρ_t : target area density for liquid hydrogen,

 Δt : bin width in -t.

The branching fraction for the $\Lambda \to \pi^- p$ decay quoted by the PDG is (0.641 ± 0.005) [30]. It is used in Eq. (6.1) since the simulation uses pure signal MC and ignores the $\Lambda \to \pi^0 n$ channel. The detector acceptance for a bin is given by the ratio of the generated and reconstructed MC yields:

$$\epsilon(E_{\gamma}, t) = \frac{N_R(E_{\gamma}, t)}{N_G(E_{\gamma}, t)},\tag{6.2}$$

where N_G , N_R are the generated and reconstructed MC yields, respectively. Furthermore, the target area density is defined as:

$$\rho_t = 2 \frac{\rho(H_2) N_A L}{MM(H_2)} = 1.22 \text{ b}^{-1} , \qquad (6.3)$$

where the components are the liquid hydrogen density $\rho(H_2)$, Avogadro's number N_A , the target length in centimeters L, and the molar mass of liquid hydrogen $MM(H_2)$. The target length is L=29 cm but because a production vertex cut is applied (see Section 4.2.8) the value used for the measurement reflects this L=28.7 cm.

The corresponding total cross section can be obtained in two ways, by either integrating the differential cross section over all possible values of -t (Eq. (6.4)) or by calculating the total cross section directly (Eq. (6.5)):

$$\sigma(E_{\gamma}) = \int_{t_{min}}^{t_{max}} \frac{\partial \sigma(E_{\gamma}, t)}{\partial t} dt, \tag{6.4}$$

$$\approx \frac{N_{\Xi}(E_{\gamma})}{\rho_t \ N_{\gamma}(E_{\gamma}) \ \epsilon(\Lambda \to XY)}.$$
 (6.5)

In practice, the method based on Eq. (6.4) is limited by the observable -t range because of experimental acceptance and the available statistics in each bin after the multidimensional binning. Therefore, the integrated total cross section is provided with the -t range used in the multidimensional analysis. This is the "correct" method to calculate the total cross section and therefore the method used in the calculation for this analysis.

The second method Eq. (6.5) lacks a proper multidimensional acceptance correction because -t is implicitly integrated without considering the correlation with the energy bins. Therefore, the second method is only approximate and may be used if there are insufficient statistics for a multidimensional analysis. This method is not used in this analysis and is only presented here for completeness.

6.1.1 Yield Extraction

Reconstructed Monte Carlo

The reconstructed Monte Carlo only contains signal events for the production of $\Xi(1320)^$ and therefore all the simulated events that are reconstructed are taken for the Monte Carlo yield. This means that no fit to the Monte Carlo data was used to get the yields. However, to determine the resolution shape of the detector, we fit the Monte Carlo with the signal function used to fit the data for each bin. The resolution shape is determined by the skewness and kurtosis parameters γ , δ in the Johnson function Eq. (4.18).

Real Data

For the extraction of the number of signal events, unbinned maximum likelihood fits were used, where the signal function is represented by a Johnson's S_U pdf (Eq. (4.18)), and the background function is represented by a Chebychev polynomial pdf of the first kind with two parameters. More specifically, the fitting is performed using the RooFIT package with a RooJohnson+RooChebychev model. To extract the yields for the differential cross section, eight energy bins are used and each energy bin is divided into seven -t-bins. Furthermore, for the stability and consistency of the fit in all the bins, the simulated data was fit using the Johnson's S_U pdf to extract ("resolution") parameters discussed previously. The procedure for fitting the data for each bin is described:

- 1. Fit MC with Johnson's S_U pdf to obtain the γ , δ parameters of the signal,
- 2. Fix the γ , δ parameters in the signal function for data that are obtained from the MC fit.
- 3. Fit the data with the signal and background function described above with the γ , δ parameters fixed.

This procedure is visualized in Fig. 6.1 where the left distribution shows the fit to MC for one of the bins and the right shows the fit to data with the set parameters from the MC.

Figure 6.2 shows the fits for the eight energy bins. In Fig. 6.3 the fit results to the data distributions are shown for all -t bins in one energy bin ($E_{\gamma} = (8.45, 8.68)$ GeV). Finally, the extracted yields from the performed fits for the differential cross section are shown in Fig. 6.4 for all three GlueX-I run periods.

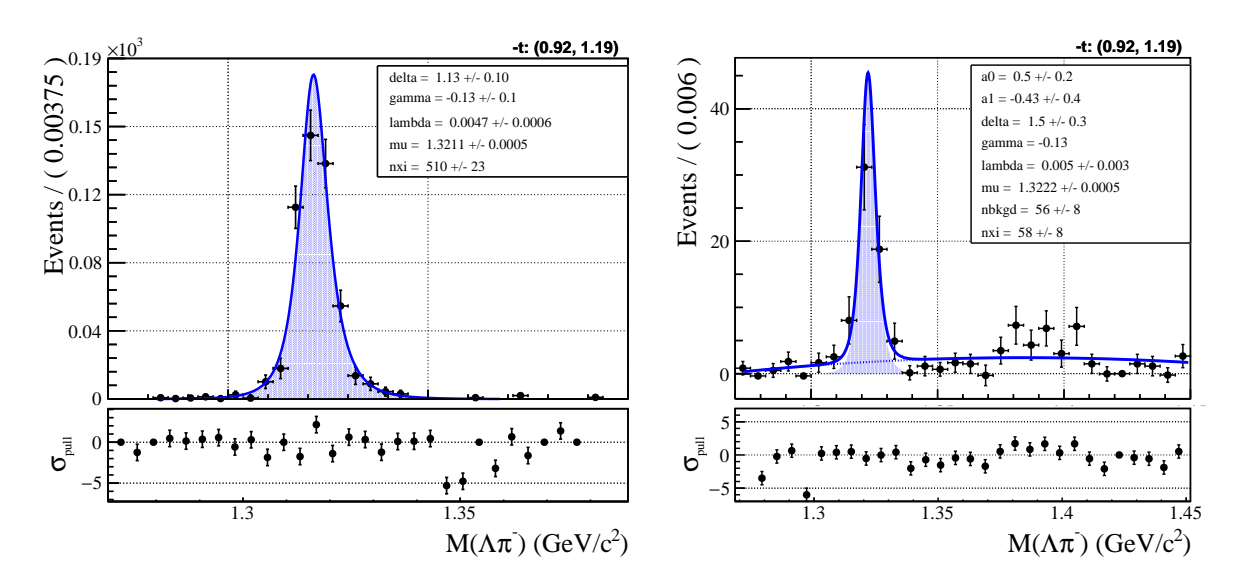


Figure 6.1: (Left) Shows the Johnson S_U fit to reconstructed MC used to obtain the resolution parameters. (Right) The fit to data using the γ , δ obtained from the MC fit on the left.

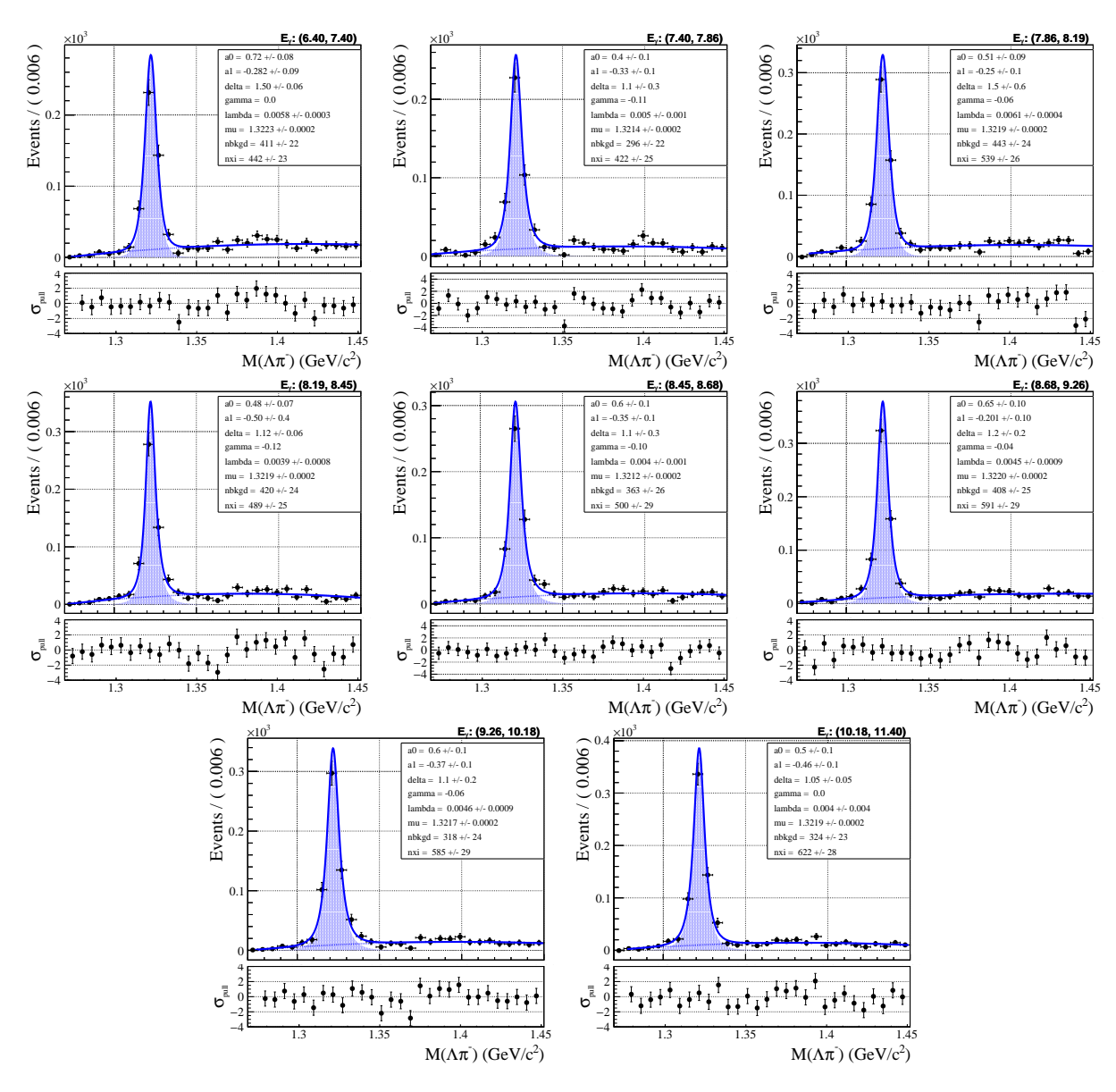


Figure 6.2: The fits to the $\Xi(1320)$ peak in the $\Lambda\pi^-$ invariant mass spectrum for all energy bins used in measuring the cross section for the GLUEX Fall 2018 run period. The fit used for the yield extraction uses a Johnson function for signal and a Chebychev polynomial for the background.

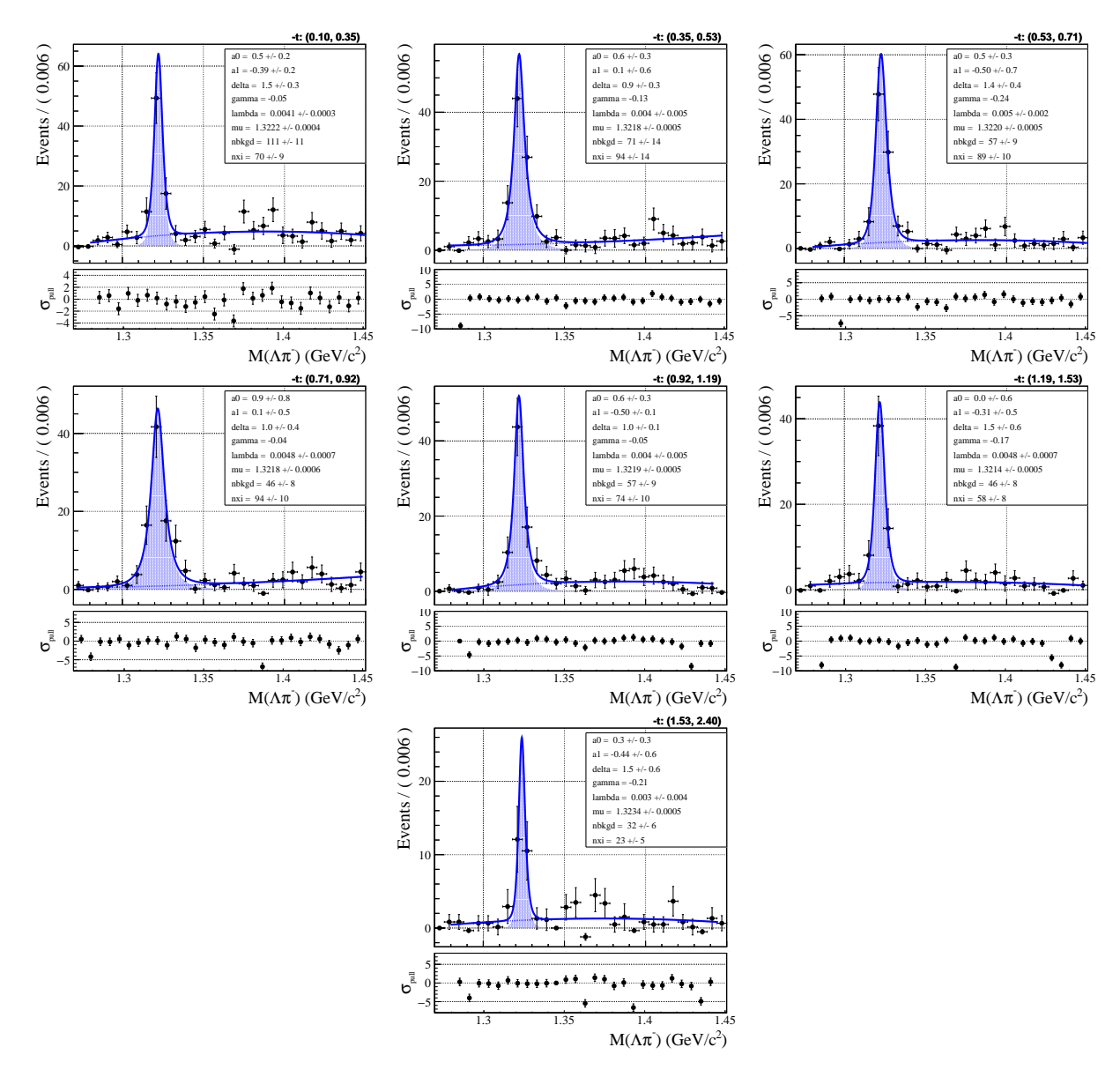


Figure 6.3: The unbinned maximum likelihood to the $\Xi(1320)$ peak in the $\Lambda\pi^-$ invariant mass spectrum for all -t-bins used in the energy bin $8.45 < E_{\gamma} < 8.68$ GeV for the GLUEX Fall 2018 run period. The fit used for the yield extraction uses a Johnson function for signal and a Chebychev polynomial for the background.

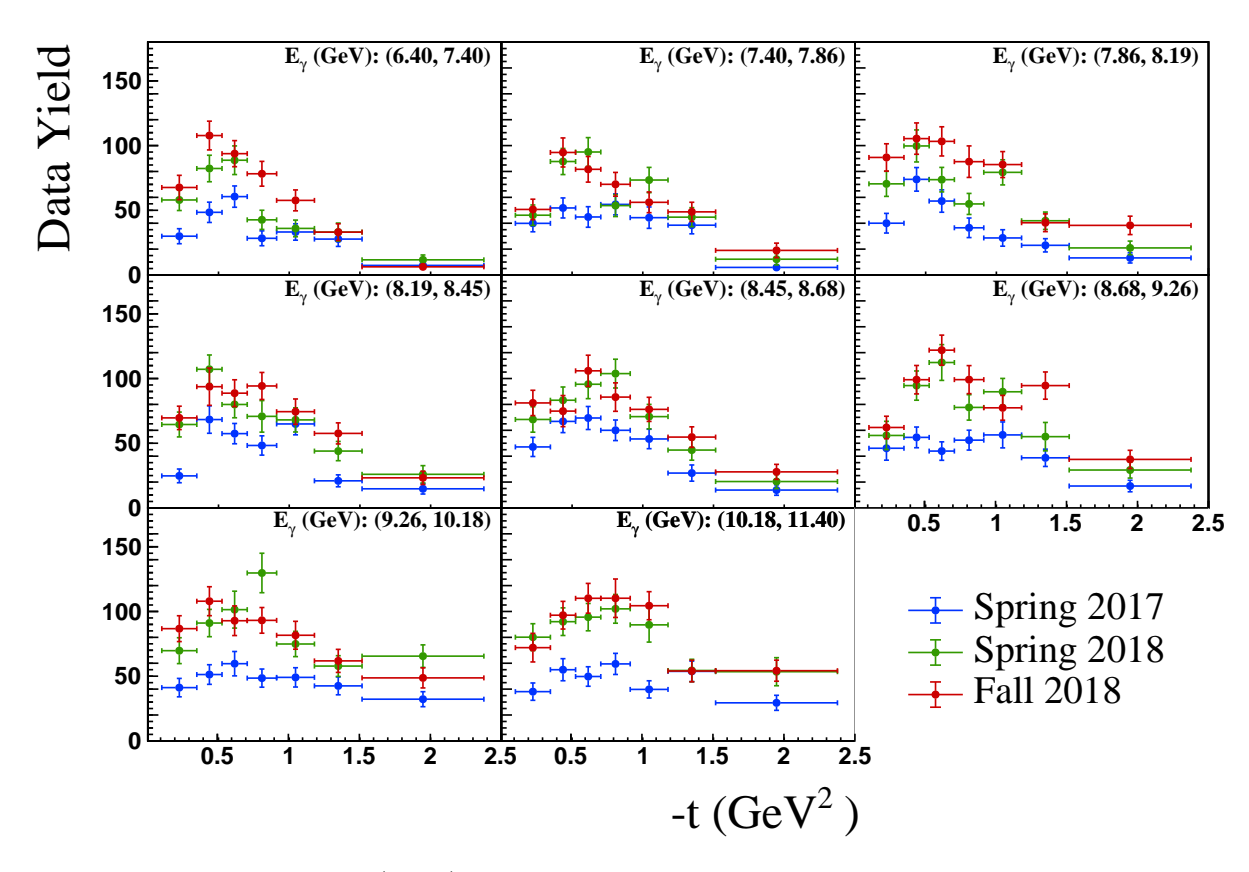


Figure 6.4: Number of $\Xi(1320)$ events found the $\Lambda\pi^-$ invariant mass spectrum extracted from data for all three GLUEX-I run periods.

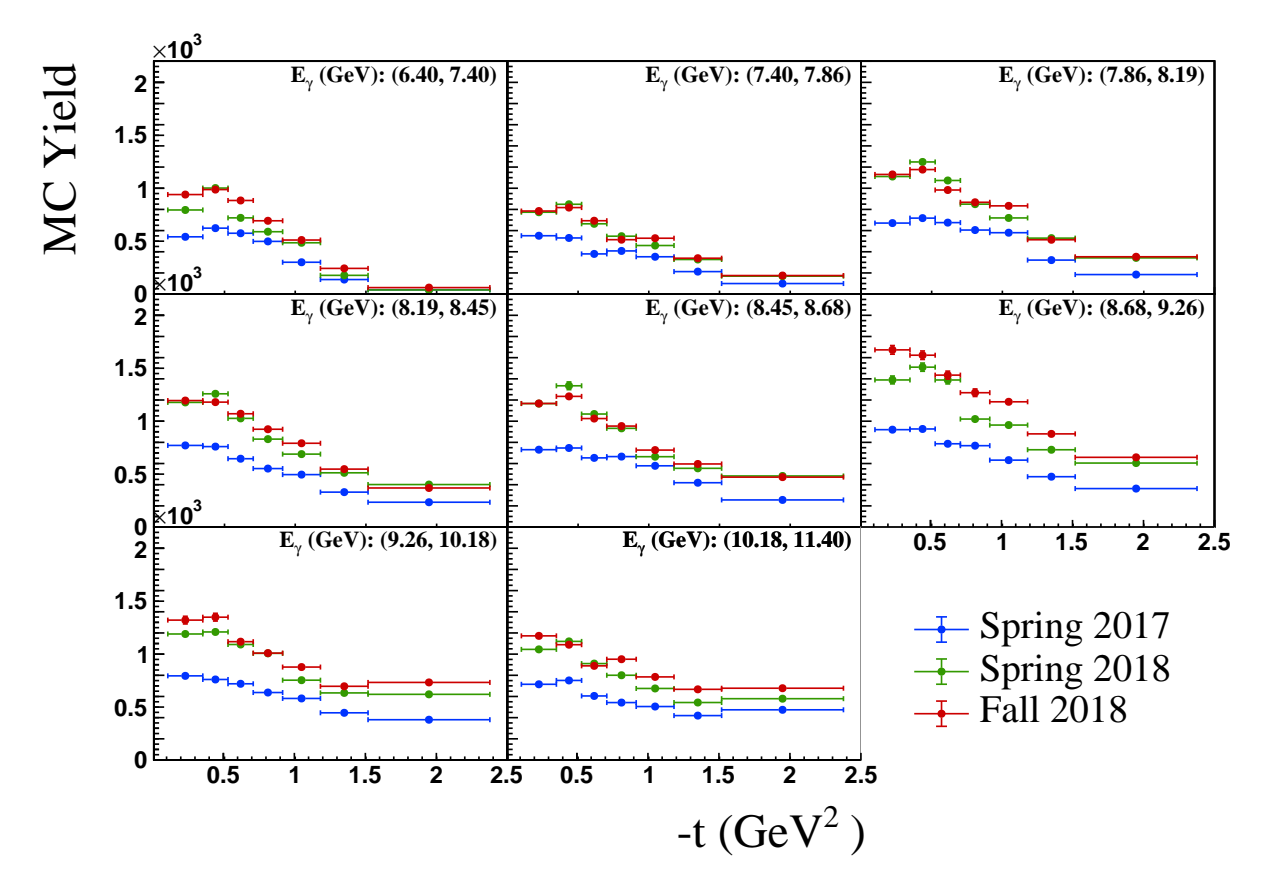


Figure 6.5: Number of $\Xi(1320)$ events found in the $\Lambda\pi^-$ invariant mass spectrum for reconstructed MC for all three GLUEX-I run periods.

Photon Flux. The photon flux is measured by the pair spectrometer at the GLUEX experiment as discussed in Section 3.1.2. The values are obtained from a database where the data is stored for every run and combines the output to a readable histogram.

Simulation Efficiency. The detector acceptance is retrieved for all bins in the measured cross section using the yields from the generated and reconstructed MC events as described in Section 6.1.1 using Eq. (6.2). Figure 6.5 shows the extracted yields from the simulated data distributions for every bin of the differential cross section by fitting these distributions with the same signal function used for data. Fig. 6.6 shows the number of generated events for the bins used for the differential cross section. Finally, Fig. 6.7 shows the detector efficiency for all bins used in the differential cross section by dividing the simulated yields by the thrown yields.

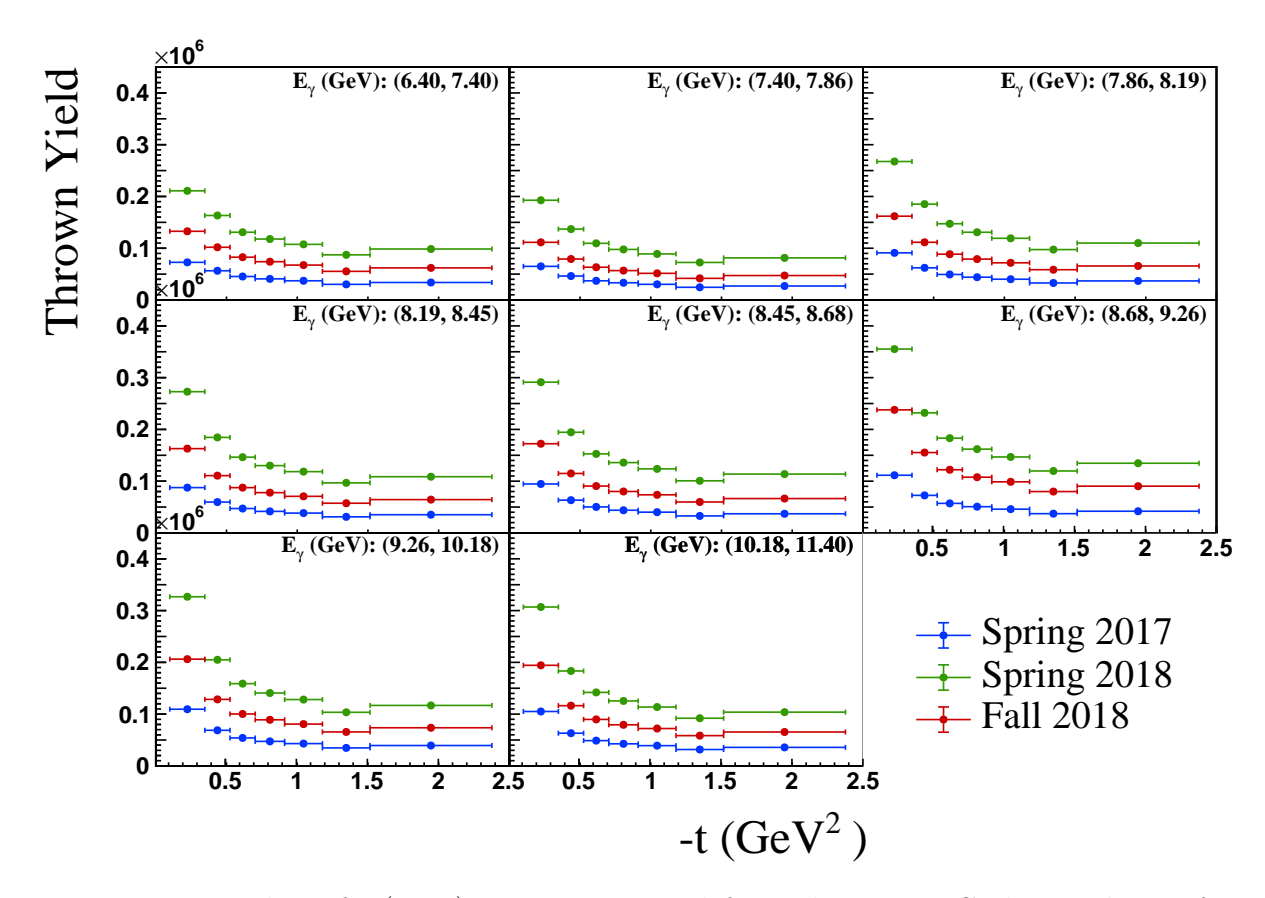


Figure 6.6: Number of $\Xi(1320)$ events generated from the Monte Carlo simulation for all three GlueX-I run periods.

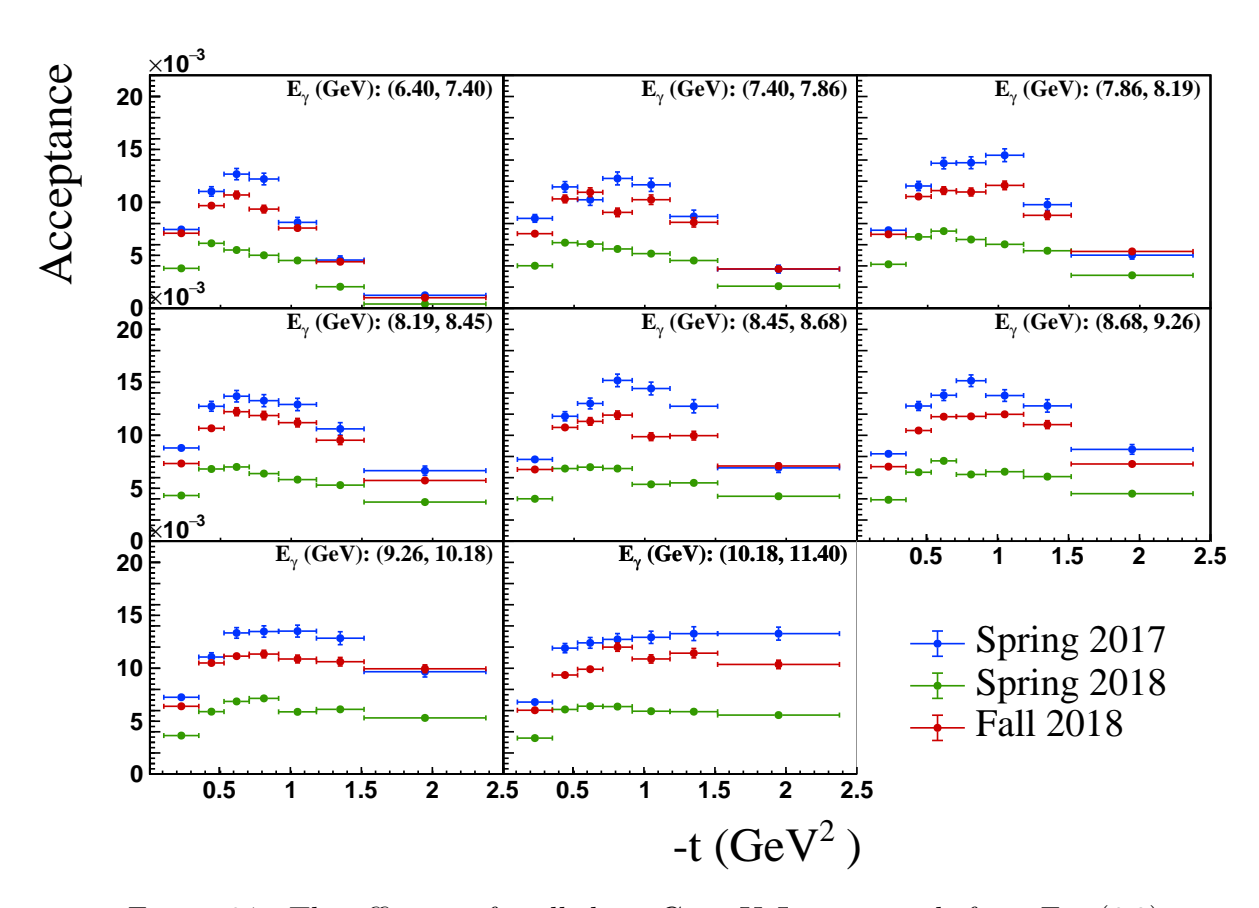


Figure 6.7: The efficiency for all three GLUEX-I run periods from Eq. (6.2).

6.2 Production Cross Section Results

6.2.1 Differential Cross Section

The differential cross section, $\frac{d\sigma}{dt}$, defined by Eq. (6.1) for the final state $\gamma p \to K^+ K^+ \pi^- \pi^- p'$, where a Ξ hyperon is reconstructed from $\Lambda \pi^-$, is shown in Fig. 6.8 for the three GLUEX-I run periods. Figure 6.9 shows the statistically weighted average differential cross section for all GLUEX-I run periods where the systematic uncertainties are also shown (blue shaded area). The weights are defined as

$$w_i = \frac{1}{\sigma_i^2},\tag{6.6}$$

where σ_i is the statistical uncertainty of the individual measurements. The individual run periods are weighted using the following formalism for a single point $X(E_{\gamma}, t) \equiv \frac{d\sigma(E_{\gamma}, t)}{dt}$:

$$X = \frac{\sum_{i} w_i x_i}{\sum_{i} w_i}, \qquad \delta X = \left(\sum_{i} w_i\right)^{-1/2}.$$
 (6.7)

The sum is over the three GLUEX-I run periods and the statistical uncertainties (δX) are also shown in Eqs. (6.6) and (6.7). Furthermore, a scalar factor will be added to any uncertainty in the weighted average through the procedure used by the Particle Data Group [86] of the form,

$$S = \left[\frac{\chi^2}{N-1}\right]^{1/2},\tag{6.8}$$

where $\chi^2 = \sum w_i(\bar{x} - x_i)^2$. For all points of the weighted differential cross section the scale factors are obtained and will be used to come up with a systematic uncertainty for the differences seen in the three GLUEX run periods and further discussed in Chapter 7.

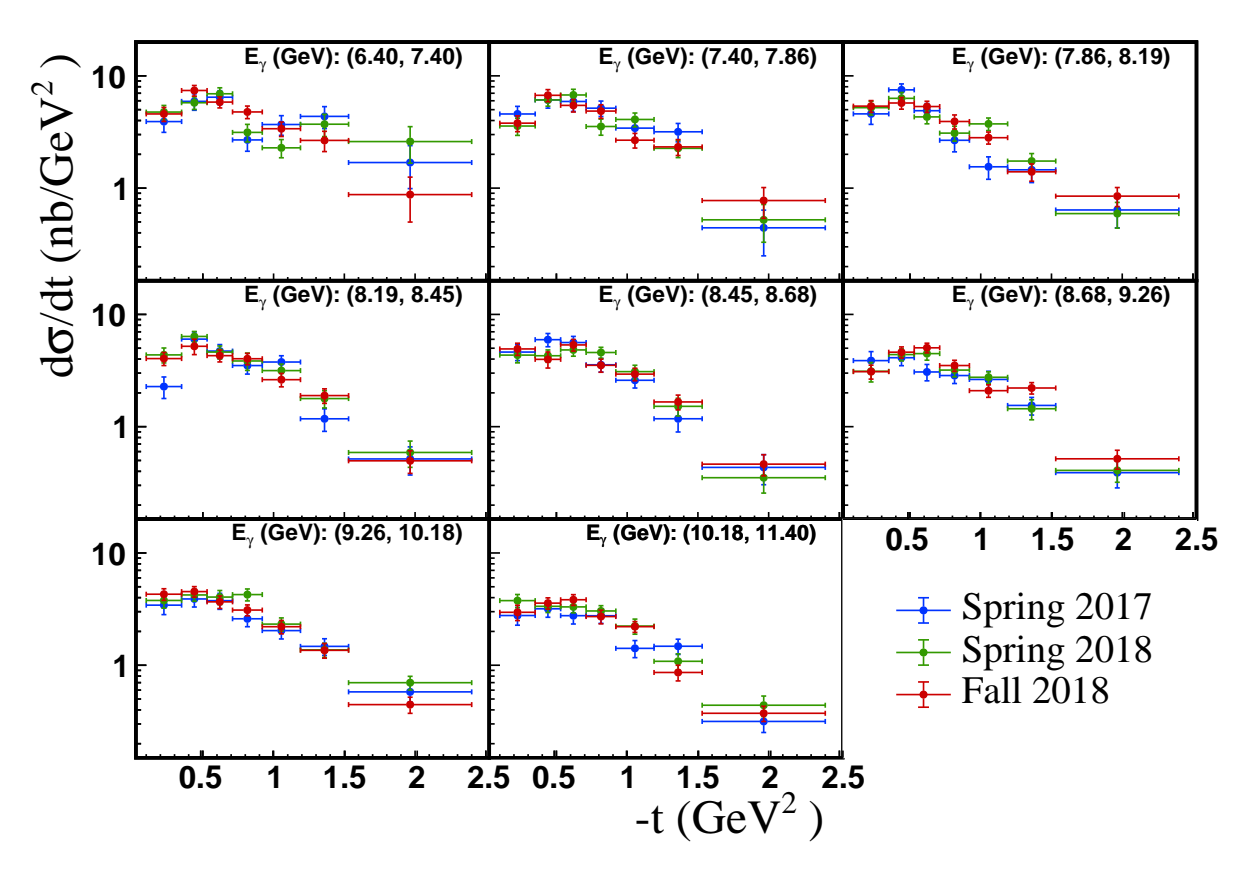


Figure 6.8: Differential cross section extracted for the eight E_{γ} bins and eight -t bins for all GLUEX-I run periods.

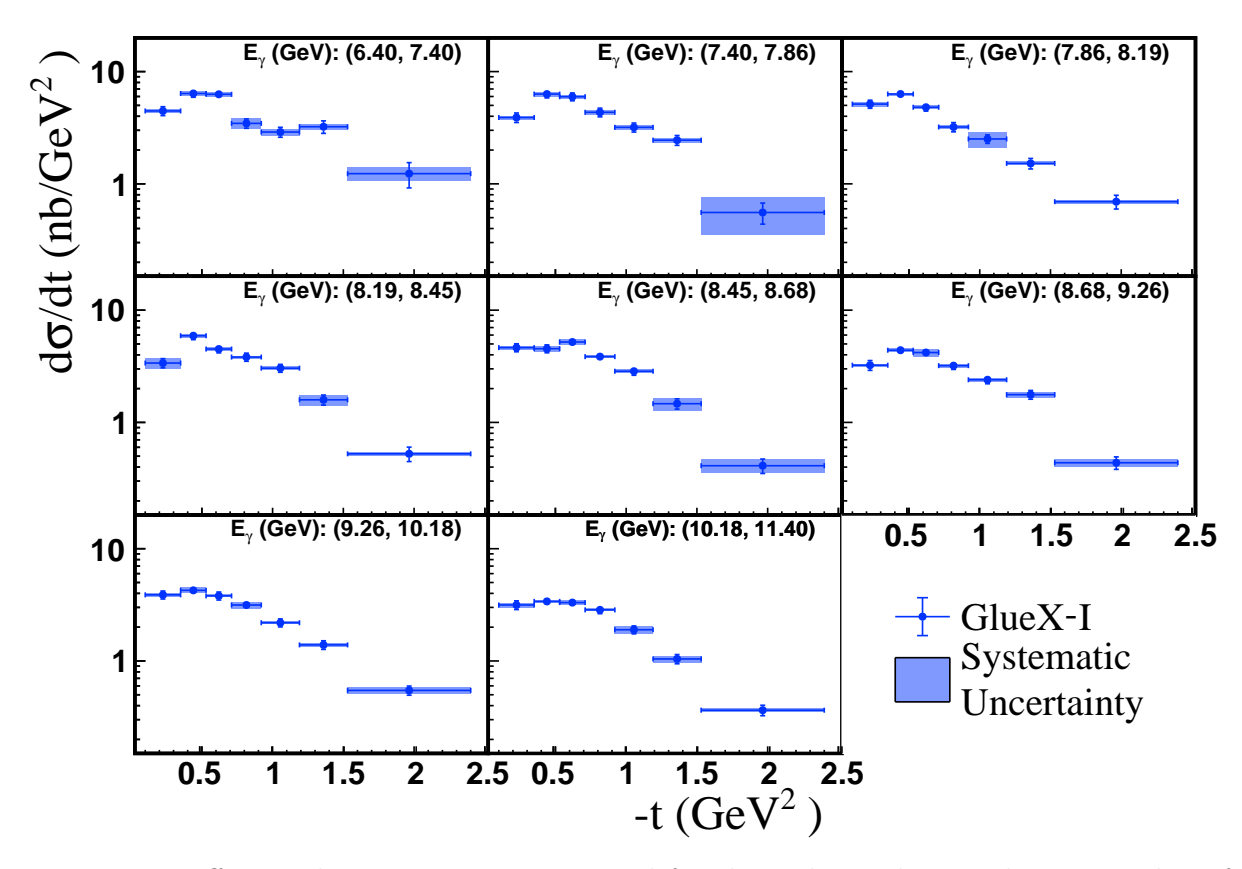


Figure 6.9: Differential cross sections extracted for the eight E_{γ} bins and seven -t bins for all GlueX-I run periods combined through a statistical weighting with systematic uncertainties (blue rectangles).

6.2.2 Integrated Total Cross Section

The total cross section with $t_{min} = 0.1 \text{ GeV}^2$ and $t_{max} = 2.4 \text{ GeV}^2$ defined by Eq. (6.4) is shown in Fig. 6.10 for the three GLUEX-I run periods (round points), their weighted average (gray band), and the measurements made by the g12 experiment by the CLAS collaboration (triangle points) at lower energies [73]. In the CLAS publication, they confirm that the results of the total cross section are obtained from integrating fits to the angular distributions of the differential cross sections. Therefore, the t range of the CLAS results are not known to us and Fig. 6.10 should only be seen as a visual comparison and no concrete conclusions to be drawn. In the figure, the dashed black line represents an exponential fit using the CLAS results and the results of the individual GLUEX-I run periods, where the weighted average is excluded; note that the exponential fit is a smooth continuous function and fits both sets of results well.

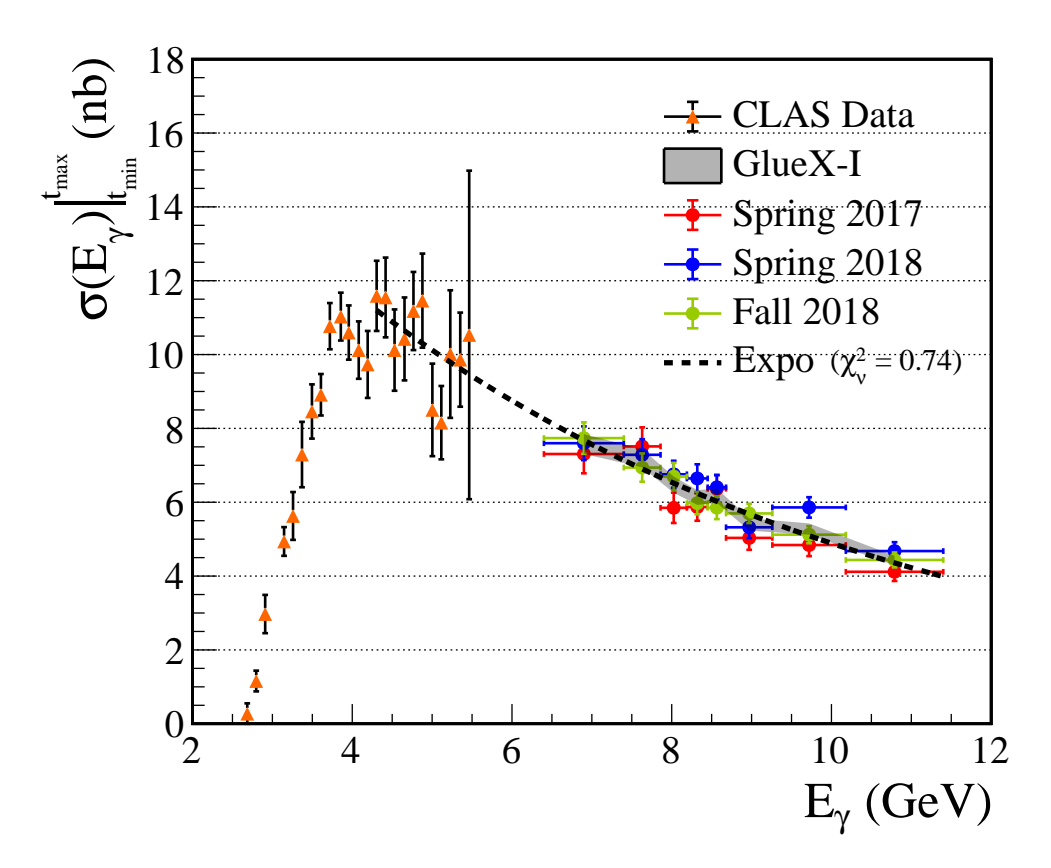


Figure 6.10: $\gamma p \to K^+ K^+ \Xi (1320)^-$ total cross section, for all three GLUEX-I run periods compared to the CLAS Collaboration cross section data at lower beam energies [73].

6.3 Cascade Properties

With the high-statistics data available from the GLUEX experiment and its detector capabilities, it is possible to measure many $\Xi(1320)$ properties. In this section, a spin measurement of the Ξ from the GLUEX-I data is discussed. A preliminary measurement of the Ξ mass has been discussed in Section 6.3.2.

6.3.1 Cascade Spin Measurement

Following the procedure in Refs. [87, 88] the angular intensity distribution of the π_{Ξ}^{-} in the rest frame of the Ξ^{-} in the data is given by

$$I \propto \sum_{\lambda_i, \lambda_f} \rho_{ii} \left| A_{\lambda_f}^J D_{\lambda_i \lambda_f}^{J*}(\phi, \theta_{\pi^-}, 0) \right|^2.$$
 (6.9)

$$I \propto \sum_{\lambda_i, \lambda_f} \rho_{ii} \left| A_{\lambda_f}^J D_{\lambda_i \lambda_f}^{J*}(\phi, \theta_{\pi^-}, 0) \right|^2, \tag{6.10}$$

where the sum is over the initial helicity projections (λ_i) of the Ξ^- and final helicity projections (λ_i) of the two-body system $\Lambda \pi^-$. The resulting π^- angular distribution in the Ξ^- rest frame integrated over ϕ is obtained for spin hypotheses $J_{\Xi(1320)} = 1/2$, 3/2, and 5/2, respectively, as follows:

$$dN/d\cos\theta_{\pi^{-}} \propto 1 + \beta\cos\theta_{\pi^{-}} \tag{6.11}$$

$$dN/d\cos\theta_{\pi^{-}} \propto 1 + 3\cos^{2}\theta_{\pi^{-}} + \beta\cos\theta_{\pi^{-}}(5 - 9\cos^{2}\theta_{\pi^{-}})$$
 (6.12)

$$dN/d\cos\theta_{\pi^-} \propto 1 - 2\cos^2\theta_{\pi^-} + 5\cos^4\theta_{\pi^-} +$$

$$\beta \cos \theta_{\pi^{-}} (5 - 26 \cos^{2} \theta_{\pi^{-}} + 25 \cos^{4} \theta_{\pi^{-}}).$$
 (6.13)

The coefficient of the asymmetric term, β , is a constant value that contains the density matrices (ρ_{ii}) and transition amplitudes $(A_{\lambda f}^{J})$ for all helicity projections of the quantization axis (along the Ξ^{-}). The density matrices and transition amplitudes are not accessible to the experiment yet and so β cannot be directly calculated. The β term is non-zero for the parity-violating weak decay of $\Xi(1320)^{-}$ to $\Lambda\pi^{-}$ where as, due to symmetry arguments, it is zero for parity-conserving decays (strong and electromagnetic). First, the data will be fit with β as a free parameter to extract its value under the assumption of different spin hypotheses.

Under each spin hypothesis, the extracted β value will be fixed and the angular intensity distribution will be fit again. The results to extract the β value for the $J = \{1/2, 3/2\}$ are shown in Table 6.1.

The procedure for boosting into the rest-frame of the Ξ baryon follows from Section 5.1.2 where we do one extra boost from the Y^* hyperon rest frame. The helicity axes are then also defined by Eq. (5.2) but now \hat{z} is along the direction of the Ξ^- baryon in the rest frame of the Y^* and \hat{y} is perpendicular to the reaction plane of the decay of the Ξ^- . The angular distribution of the decay pion is then constructed as

$$\cos \vartheta_{\mathcal{H}}^{\pi^-} = \frac{p_{z,\mathcal{H}}^{\pi^-}}{|\vec{p}_{\mathcal{H}}^{\pi^-}|}.$$
(6.14)

The data has been background-subtracted using the Q-Factor method discussed in Section 4.3. The background-free data sample is then efficiency-corrected using the ratio of the reconstructed and generated pi_{Ξ}^- angular intensity distributions. The result is the acceptance-corrected distribution described by Eq. (6.10). First, to extract the β value, we fit the data using Eq. (6.11) where, β is left as a free parameter; see Table 6.1 (Row 1) for the values for each GlueX-I run period. We also extract the β value under the assumption of J = 3/2 using Eq. (6.12); see Table 6.1 (Row 2) for the values for each GlueX-I run period. Next,

Run	Spring 2017	Spring 2018	Fall 2018	GLUEX-I
Fit $\beta_{J=1/2}$	0.070(5)	0.076(4)	0.083(4)	0.077(2)
Fit $\beta_{J=3/2}$	0	0	0	$5.55(2) \times 10^{-17}$

Table 6.1: The best fit β values extracted under the spin-1/2 hypothesis to the accepted-corrected angular distributions in data.

the extracted β values are used to fit the angular distributions to test the spin hypotheses. Figure 6.11 shows the acceptance-corrected helicity angular distribution for all three GLUEX-I runs (black points), spin-1/2 fit to data (blue), spin-3/2 fit to data (magenta) and the efficiency correction (red). The dotted lines plotted are Eqs. (6.11) and (6.12) under the assumption $\beta = 0$ (spin-3/2 beta value) and the χ^2_{ν} are plotted in the color associated with the fit used. The results indicate that the spin-1/2 fit is the best hypothesis with a $\chi^2_{\nu} \approx 1$ to the angular distributions, as expected for the ground state $\Xi(1320)^-$. The spin-3/2

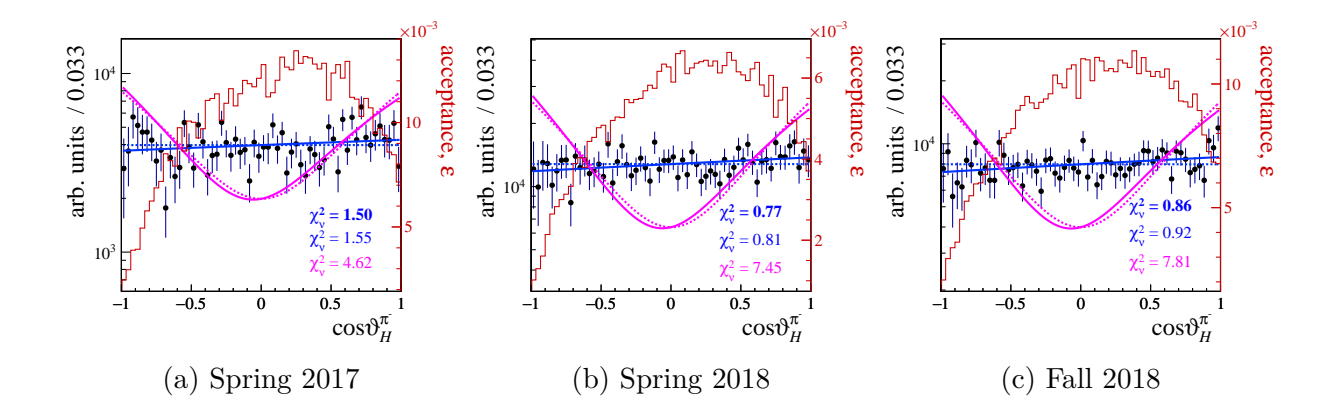


Figure 6.11: The acceptance-corrected helicity-angular distributions, indicating J=1/2 quantum number, for the three GlueX-I run periods, where the black points represent the data, the blue and magenta lines represent the fits and the detector efficiency is in red.

hypothesis has a visually worse fit and $\chi^2_{\nu} \gg 1$ shows that it is statistically not consistent with the data distribution. Finally, Fig. 6.12 shows the combined and reanalyzed GLUEX-I data that would be published.

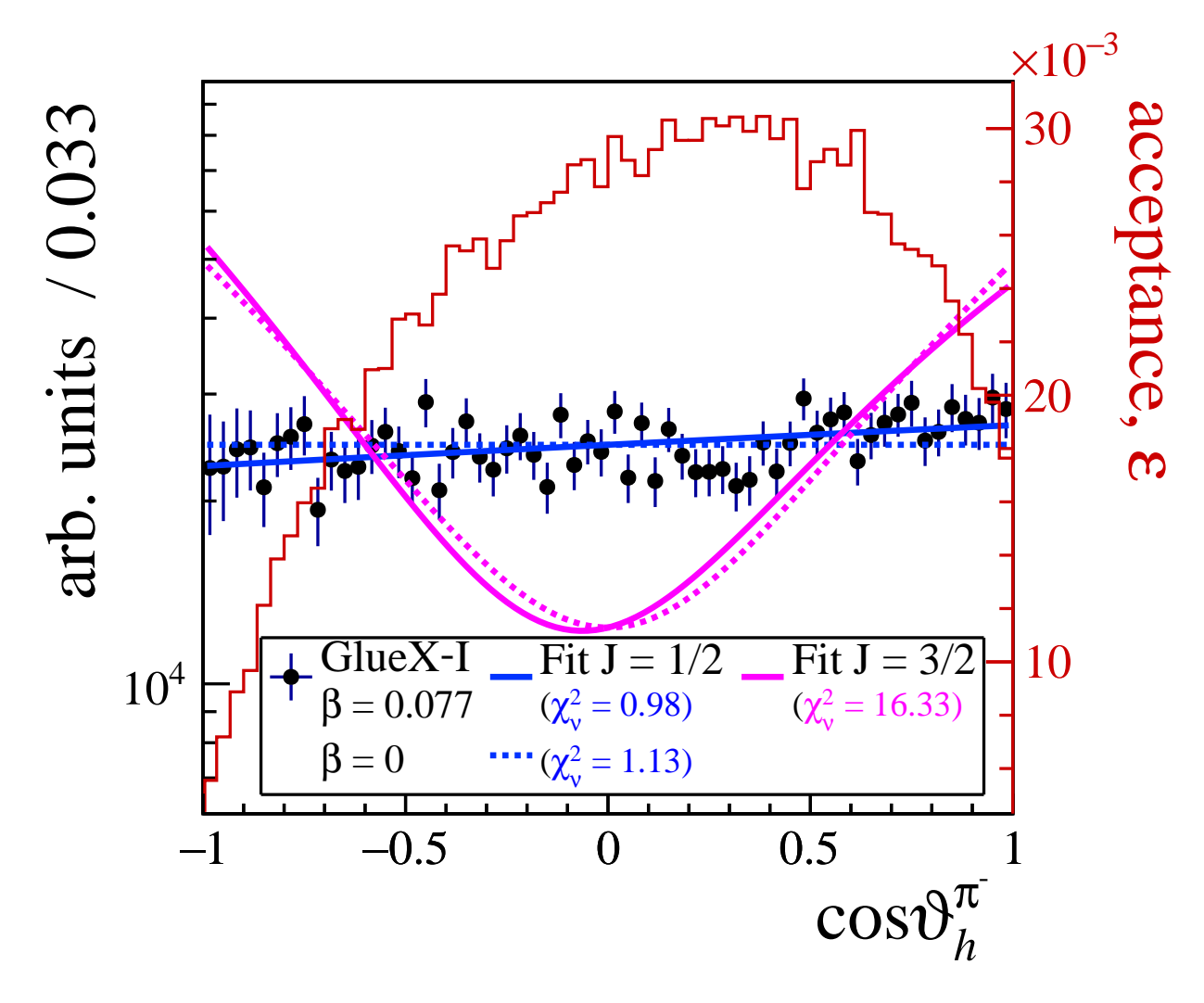


Figure 6.12: The acceptance-corrected helicity-angular distributions, indicating J=1/2 quantum number, for the three Gluex-I data, the black points represent the data, the blue line represents the fit with the fit results in the legend, and the detector efficiency in red.

Table 6.2: Table of extracted Ξ^- mass values for data and Monte Carlo simulation and the corrected mass.

Data Set	Spring 2017	Spring 2017	Fall 2018		
Data Mass MC Mass MC Correction	$ \begin{vmatrix} 1322.13(10) \\ 1322.52(18) \\ -0.81(19) \end{vmatrix} $	1322.40(9) 1322.54(14) -0.83(15)	$ \begin{vmatrix} 1322.04(8) \\ 1322.47(14) \\ -0.77(15) \end{vmatrix} $		
Corrected Mass 1321.32(26) 1321.57(21) 1321.27(21)					

6.3.2 Mass Measurement

The PDG has listed the mass of the ground-state Cascade at $\Xi(1320)^- = 1321.71 \pm 0.07$ MeV with only one experimental measurement used in the average [30]. The measurement by the DELPHI Collaboration using LEP data used about 2500 Ξ^- events [89]; a single GlueX-I data period is statistically competitive.

The mass of Ξ^- is extracted within the analysis framework that has been discussed in Section 4.2. The signal in the data is fitted with a Johnson S_u function (Eq. (4.18)) and the parameters from the fit are used in Eq. (4.20) to obtain the mass value. The mass value is then corrected using the generated and reconstructed MC. The correction term is obtained by also fitting the reconstructed MC with the same signal function as the data and comparing the extracted mean from the fit to the value used to generate the events, which is the PDG mass. The errors at each step are propagated appropriately. The error from the mass extraction must be carefully calculated because the mass is extracted from multiple fitted parameters with errors. This is done using this formalism for error propagation:

$$\sigma_x = \sum_i \sigma_{x_i} \left(\frac{\partial f(x_i)}{\partial x_i} \right) \tag{6.15}$$

on Eq. (4.20). The Table 6.2 shows the values extracted for the fits to data and reconstructed MC, the correction term and the final corrected Ξ^- mass value and their statistical uncertainties. Figure 6.13 shows the fits and extracted values to obtain the final mass measurements summarized in Table 6.2.

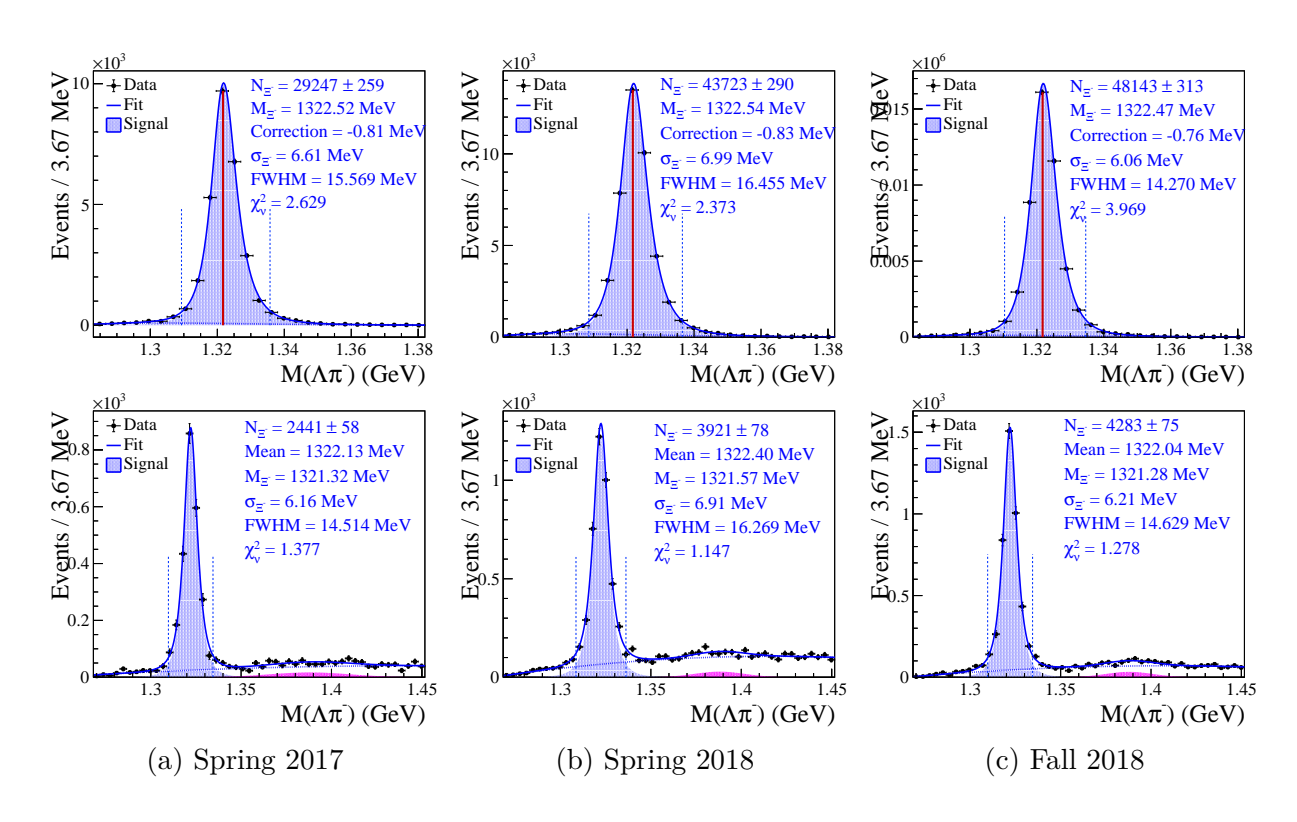


Figure 6.13: Fits done to the simulated data (Top) and data (Bottom) to extract the Ξ^- mass for the three GLUEX-I run periods.

6.4 Cascade Excitations

With the measured Ξ^* excitation spectrum from collider experiments discussed in Section 2.3, there has been a renewed interest in the structure of the $\Xi(1620)$, $\Xi(1690)$, and $\Xi(1820)$. Many quark model predictions put the first Ξ^* excitation at $\sim 1750 \text{ MeV}^2$. Like the $\Lambda(1405)$ these models tend to overestimate the first excitation making $\Xi(1620)$ or $\Xi(1690)$ good candidates. If they indeed have similar properties to the $\Lambda(1405)$ then they don't fit the conventional quark model assignments and theoretical groups are beginning to investigate these resonances as molecular states [90]. Moreover, if the mass difference relations are met then the $\Xi(1820)$ is a prime candidate for the first excitation and one of these states could be the first radial excitation. Again, theoretical interest in the pole structure of the $\Xi(1820)$ have also been recently investigated where it is proposed that this could also be a two-pole structure candidate [91]. With these theoretical interest it becomes more important for experiments to measure the properties of these states.

As alluded to in Section 1.5, the Ξ excitation spectrum in the ΛK^- decay channel (Eq. (1.14)) using GLUEX-I data will be explored. The excited Ξ^* resonances are studied in photoproduction through t-channel (meson exchange) in the decay of excited intermediate hyperons. Figure 6.14 shows the decay chain in a Feynman diagram representation where after the electromagnetic production $\gamma p \to K^+ Y^*$, the intermediate hyperon and Ξ resonance decay strongly $Y^* \to \Xi^* K^+ \to \Lambda K^-$ followed by the weak decay $\Lambda \to p \pi^-$. The topology of the final-state particles is very similar to the ground-state octet Ξ . This final state is also five charged tracks but with a K^- replacing the π^- and there is only one detached vertex. Therefore, studying this channel is less constrained by the kinematic fit and is more likely to have K/π misidentification for the higher momentum secondary kaons.

6.4.1 Event Selection

The standard GLUEX track reconstruction and preparation for event-level analysis discussed in Sections 4.1 and 4.2.1 remains the same. For the analysis launch reconstruction, we require five charged tracks with final-state particle track hypothesis $K^+K^+K^-\pi^-p$ and the kinematic fit constraints are momentum and energy of all track four-vectors, the mass

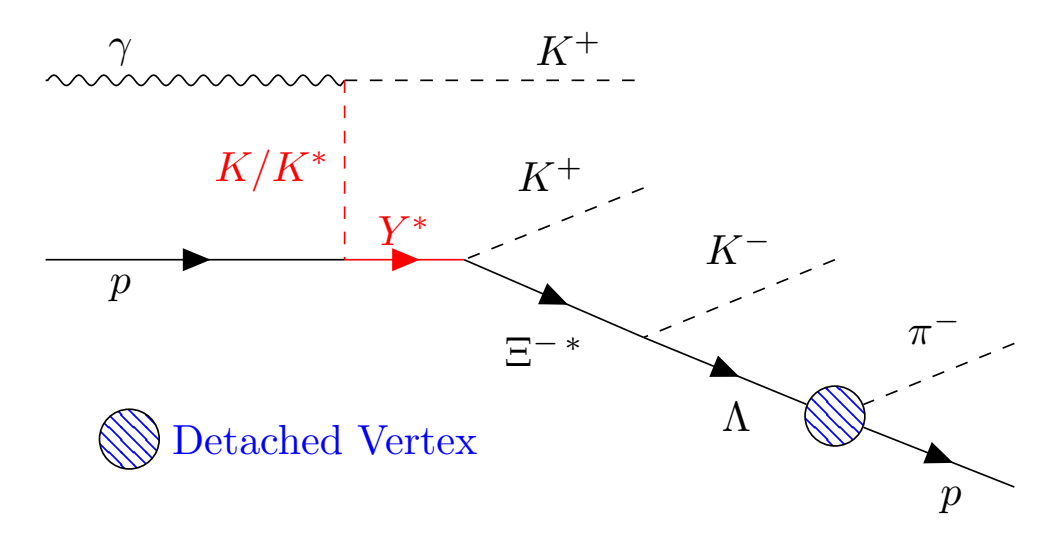


Figure 6.14: A depiction of the production and decay of excited Cascades in the decay $\Xi^{**} \to K^- \Lambda$ as assumed to be produced through t-channel meson exchange mediated through excited intermediate hyperons Y^* .

of the Λ is now kept unconstrained to resolve the Ξ^* resonances and two vertex constraints to the production vertex and the Λ detached vertex are used. The event-level analysis cuts are summarized in Table 6.3. For this preliminary work, the analysis cuts have been briefly investigated but are primarily motivated by the studies conducted on the ground-state octet in Section 4.2. Because this channel is less constrained and has a much larger combinatorial background the χ^2_{ν} cut is much tighter, the rapidity and Λ flight significance cuts are conservative, and the best- χ^2_{ν} method (Section 4.2.3) is used for simplicity. To investigate the cuts further a Monte Carlo simulation that matches the data needs to be used which has not been successful in past analysis. With the procedure developed in Chapter 5 the prospects for good Monte Carlo reconstruction of this data are very good. For now that is not important because we are only interested to see what kind of resonances can be resolved in the ΛK^+ invariant mass but will be very important to measure the line-shape of these resonances in detail.

6.4.2 Results

The result using all GLUEX-I data of the ΛK^+ invariant mass with the event-level analysis cuts applied are shown in Fig. 6.15. Although there is a large non-resonant background

Table 6.3: Table of tuned cuts on GlueX and simulated data in this analysis.

Event Selection	Selection Criteria	
Multiple Combos	Best χ^2_{ν} Combo	
$\chi^2_{ u}$	< 3	
$ \mathrm{MM}_X (\gamma p \to X K^+ K^+ \Xi^-)) ^2$	$< 20 \; ({\rm MeV}/c^2)^2$	
Kaon Selection	$ \overrightarrow{\boldsymbol{p}}(K_F^+) > \overrightarrow{\boldsymbol{p}}(K_S^+) $	
Rapidity, y	$y(K_{fast}^+) > 0$	
Target Region, Z_t	$50.4 < Z_t \text{ (cm)} < 79.1$	
Λ Flight Significance, $d_{\Lambda}^{\pm}/\sigma_{d_{\Lambda}}$	> 0	
$\frac{ \text{MM}_X (\gamma p \to X K^+ K^+ \Xi^-)) ^2}{\text{Kaon Selection}}$ Rapidity, y Target Region, Z_t	$ < 20 \text{ (MeV/}c^2)^2 $ $ \overrightarrow{\boldsymbol{p}}(K_F^+) > \overrightarrow{\boldsymbol{p}}(K_S^+) $ $ y(K_{fast}^+) > 0 $ $ 50.4 < Z_t \text{ (cm)} < 79. $	

the $\Xi(1690)$ and $\Xi(1820)$ are clearly present. Furthermore, the distribution is fit with a Breit-Wigner pdf for each of the Ξ^* resonances that are clearly visible and the background by a second-order Chebyshev Polynomial pdf in the range [1.61, 2.3] GeV². The dotted lines in the distribution are the PDG values of the $\Xi(1620)$, $\Xi(1950)$, and $\Xi(2030)$ from left to right. It is clear that their are no significant structures above the $\Xi(1820)$. With theoretical interest in these two excitations a line-shape measurement would be extremely valuable. Figure Fig. 6.16 shows the ΛK^+ invariant mass divided into three bins in the variable Mandalstam-t. From these results it is clear that the line shape of the resonance are dependent on the energy and unstable in the range -t = [0,2] GeV²². Further investigations are possible using the available GLUEX-II experiment and methods have been developed by collaborators in the extensive study of the line-shape and two-pole structure of the $\Lambda(1405)$ [92]. The prospects for studying the excitation spectrum with GLUEX-II will be discussed in Section 8.2.2.

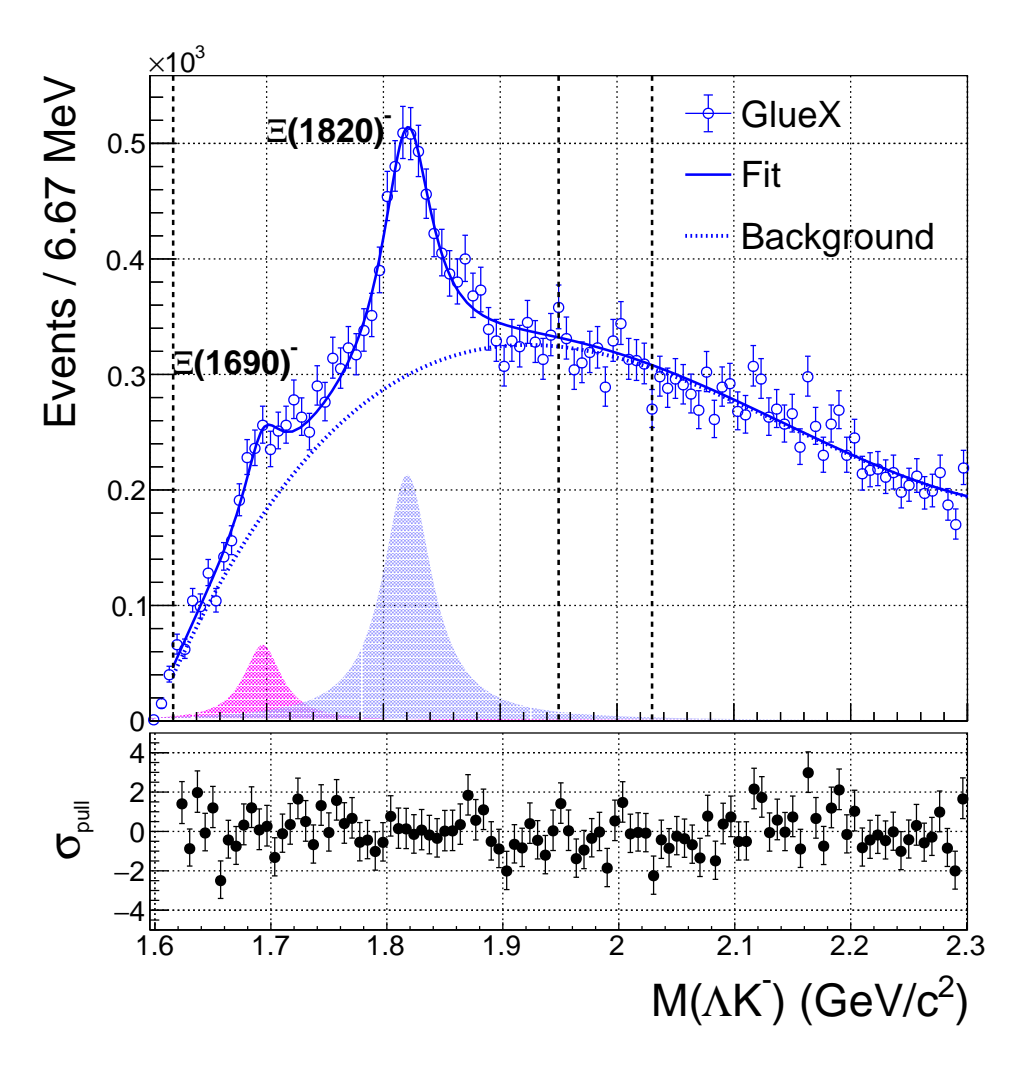


Figure 6.15: The invariant mass of the excited spectrum in the decay of $\Xi^{-*} \to \Lambda K^-$ from photoproduction of K^+Y^* fit with two Breit-Wigner line-shapes corresponding to the $\Xi(1690)^-$ and $\Xi(1820)^-$.

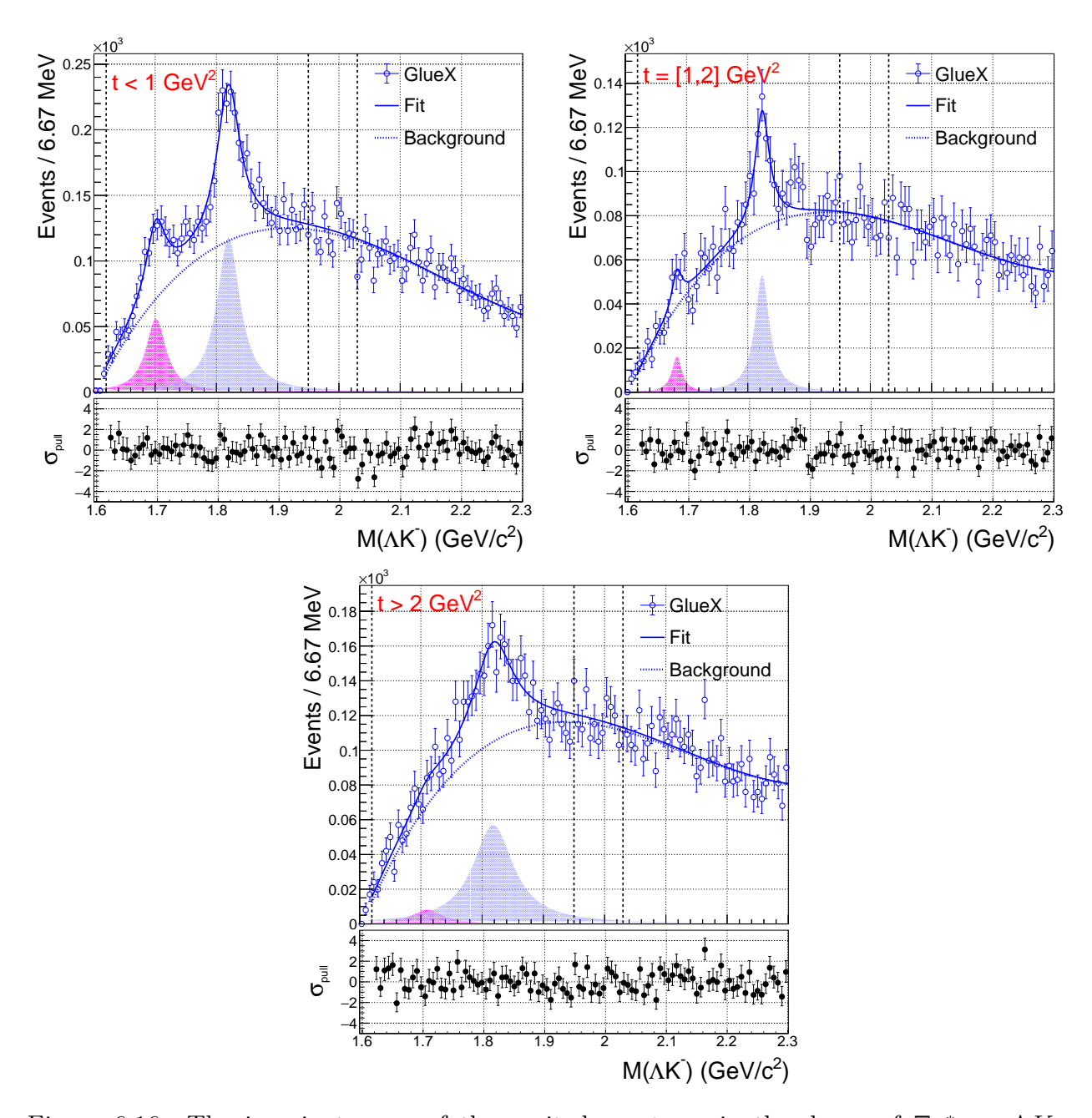


Figure 6.16: The invariant mass of the excited spectrum in the decay of $\Xi^{-*} \to \Lambda K^-$ from photoproduction of K^+Y^* fit with two Breit-Wigner line-shapes corresponding to the $\Xi(1690)^-$ and $\Xi(1820)^-$ for bins in Mandelstam t labeled in red at the top-left of each distribution.

CHAPTER 7

SYSTEMATIC UNCERTAINTIES

In this section the systematic uncertainties of the main measurement, $d\sigma/dt$ and the Xi(1320) spin, of this dissertation will be discussed along with the results. The other measurements such as the mass of the ground state Ξ have been conducted but no systematic studies completed and would be considered future work.

7.1 Barlow Test

Several sources of systematic uncertainties are discussed and combined into one final value. The methodology suggested by Barlow [93] is used to gauge the statistical significance of the systematic effects. Expressing the difference (ΔB) between the original and any new cross section value as a multiple of the standard deviation of this difference (σ_B) gives a measure of its significance. The significance σ_B is calculated as $\sqrt{|\sigma^2 - {\sigma'}^2|}$ for correlated results, where σ and σ' are the statistical uncertainties of the original and the new result, respectively. If $|\Delta B| < \sigma_B$, then a systematic effect is not significant. If the deviation is consistently larger than four times σ_B , it has to be treated as a systematic uncertainty.

All the event selection criteria are varied and shown in Table 7.1 where column 1 shows the nominal value, column 2 shows the variations, and column 3 shows the overall average Barlow result. The variations were chosen such that the number of Ξ^- events did not differ more than 10% from the nominal statistics.

The variations around the nominal cuts for the total and differential cross section are shown in the following sections with the Barlow test results as defined in Section 7.1.5 where, the light blue shaded region denotes $|\sigma_B| < 4$. It is shown in Figs. 7.1, 7.3, 7.5, 7.7 and 7.9 for the total cross section and all bins in the differential cross sections in Figs. 7.2, 7.4, 7.6, 7.8 and 7.10 consistency within the $4\sigma_B$ region with some random edge cases very close to $4\sigma_B$.

Table 7.1: All of the performed variations on the nominal cuts to calculate the Barlow test.

Selection	Variation	Barlow
	< 6	$< 4\sigma_B$
$\chi^2_{ u} < 8$	< 7	$< 4\sigma_B$
	< 9	$< 4\sigma_B$
	< 10	$< 4\sigma_B$
$ {\rm MM}_X ^2 < 20 \; ({\rm MeV})^2$	< 10	$< 4\sigma_B$
	< 15	$< 4\sigma_B$
	< 25	$< 4\sigma_B$
	< 30	$< 4\sigma_B$
	> 1.8	$< 4\sigma_B$
$y(K_{fast}) > 2$	> 2.1	$< 4\sigma_B$
		$< 4\sigma_B$
	> 1	$< 4\sigma_B$
	> 1.5	$< 4\sigma_B$
$\sigma_{flight}(\Xi^-) > 2$	> 2.5	$< 4\sigma_B$
	> 3.0	$< 4\sigma_B$
$\sigma_{flight}(\Lambda) > 0$	> 0.5	$< 4\sigma_B$
	> 1	$< 4\sigma_B$

7.1.1 χ^2_{ν} Variations

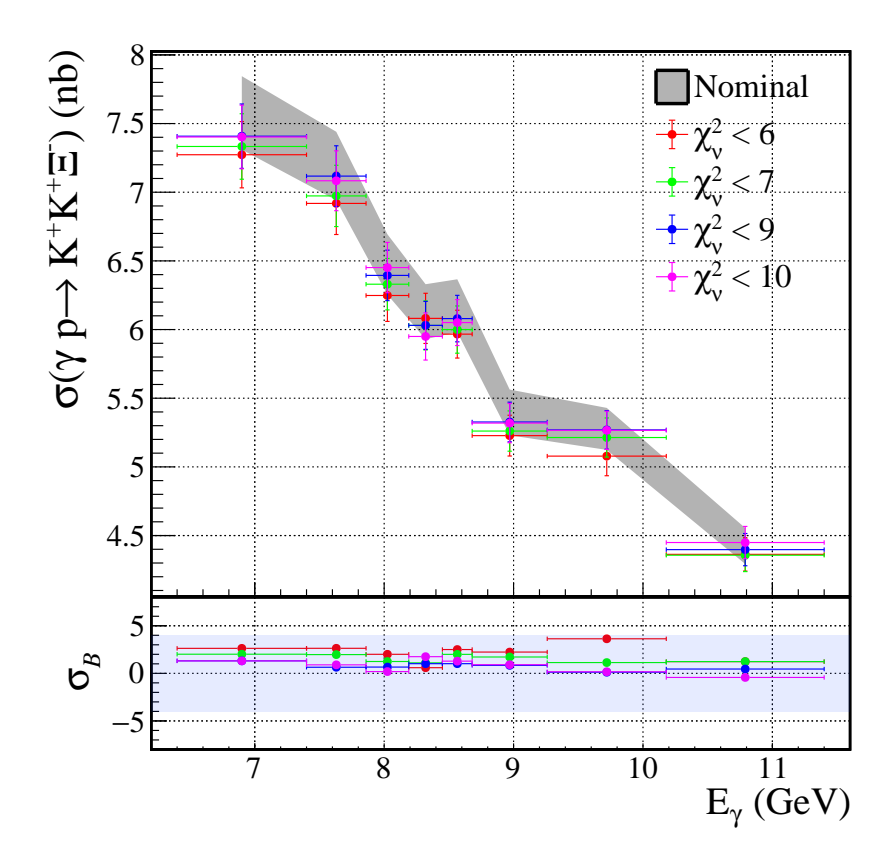


Figure 7.1: The total cross section and Barlow test significance for all χ^2_{ν} variations used in this study compared to the nominal data analysis.

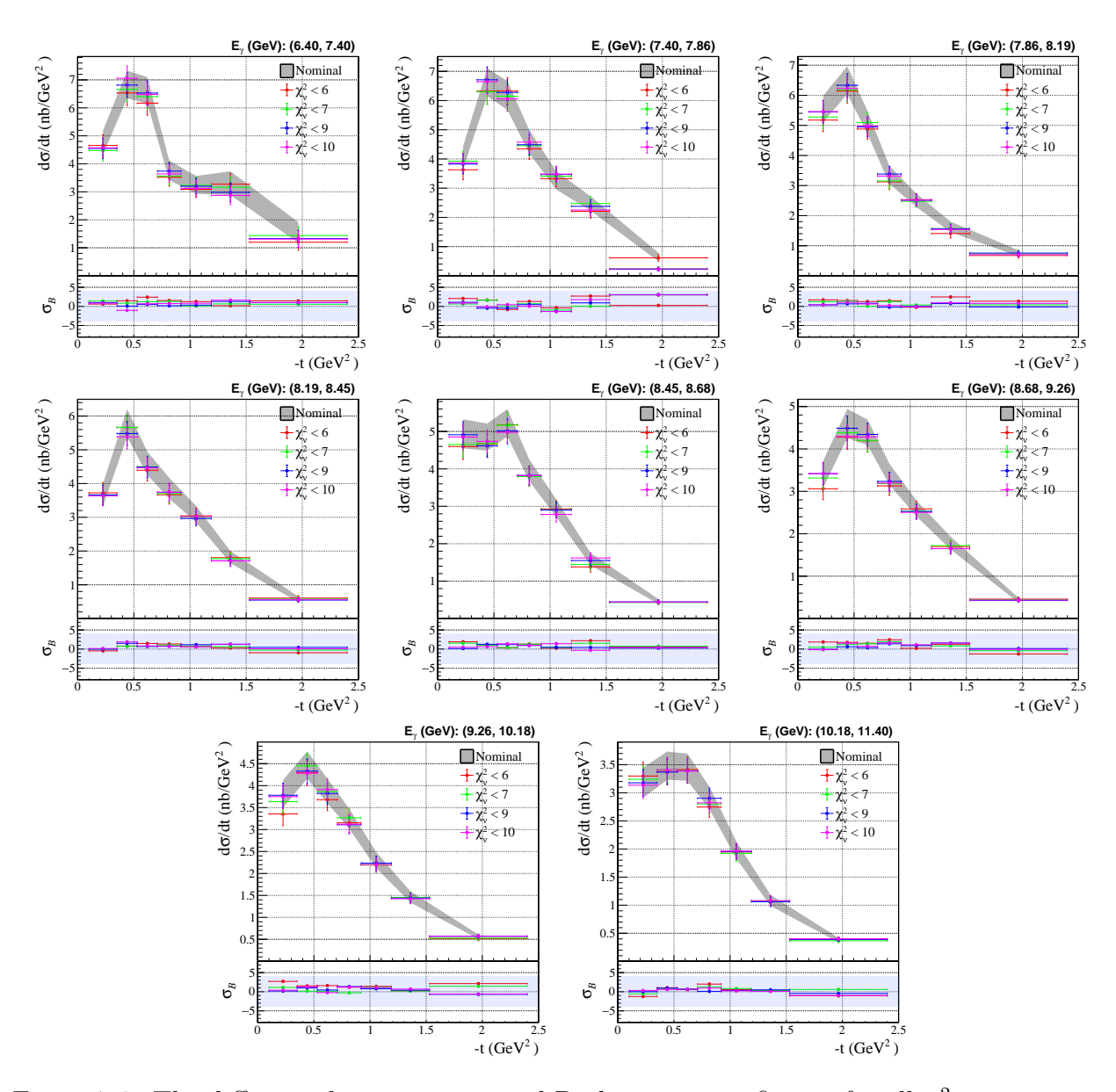


Figure 7.2: The differential cross section and Barlow test significance for all χ^2_{ν} variations in all energy bins used in this study compared to the nominal data analysis.

7.1.2 Missing Mass Variations

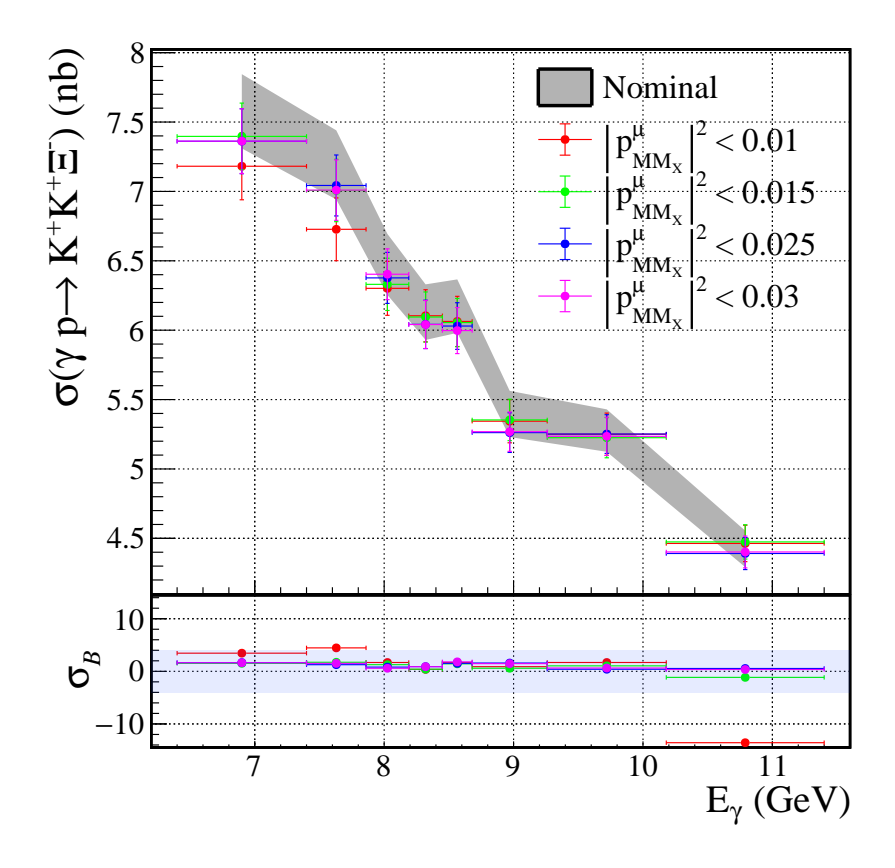


Figure 7.3: The total cross section and Barlow test significance for all missing-mass-squared variations used in this study compared to the nominal data analysis.

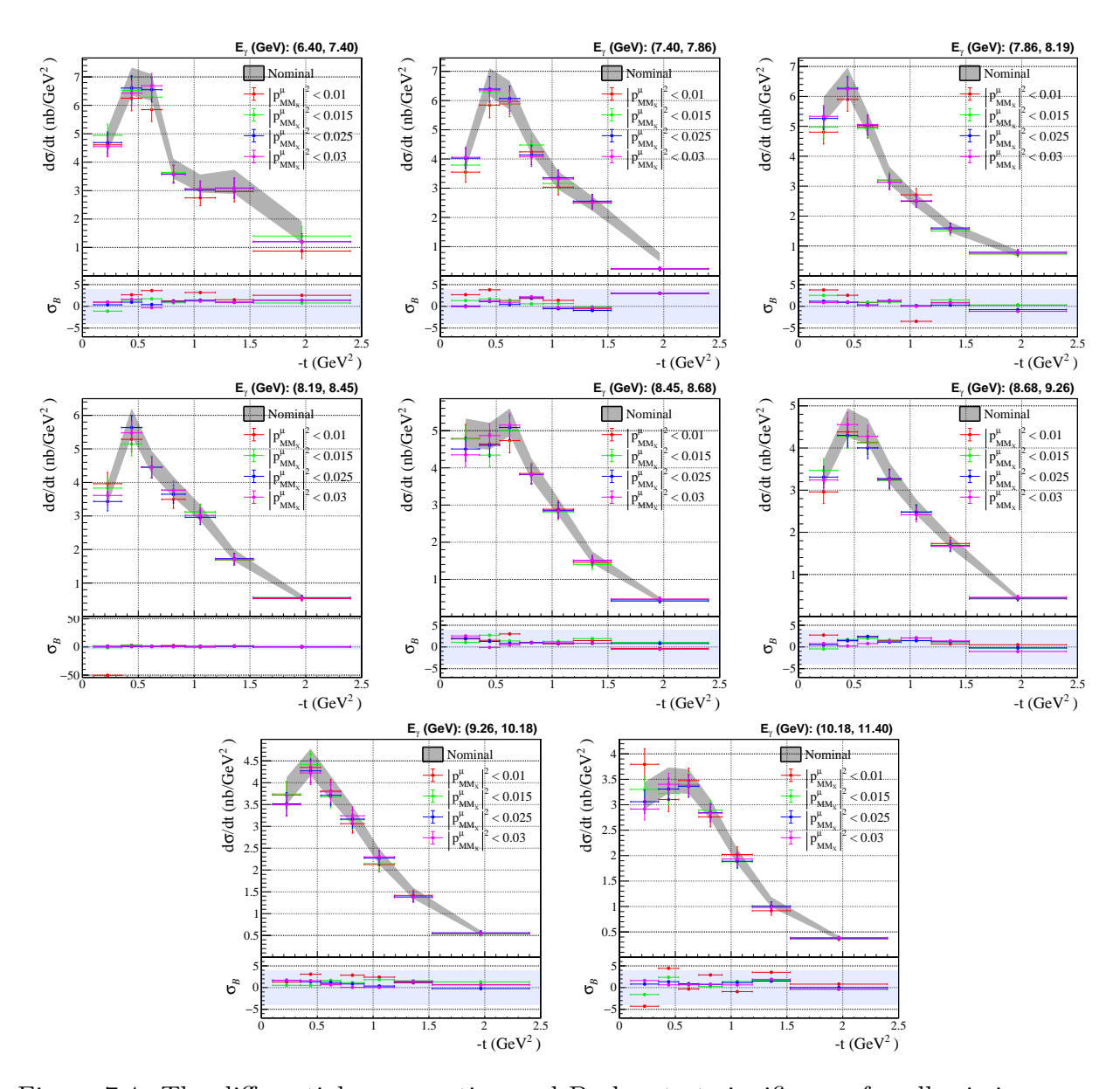


Figure 7.4: The differential cross section and Barlow test significance for all missing-mass-squared variations in all energy bins used in this study compared to the nominal data analysis.

7.1.3 K_{fast}^+ Rapidity Variations

In Section 4.2.7 and shown in Fig. 4.12 the specific nominal cut was chosen to preserve agreement with the simulated data. For this reason the specific variation of $y(K_F^+) > 1.6$ needs to be discussed. For this particular variation the fast kaon kinematics are deviating from the simulated data. For this reason there seems to be a larger deviation in the proceeding cross section and Barlow results for the specific cut deviation. And because it no longer describes the simulation well, the results with this specific variations are chosen to be ignored for any systematic effect.

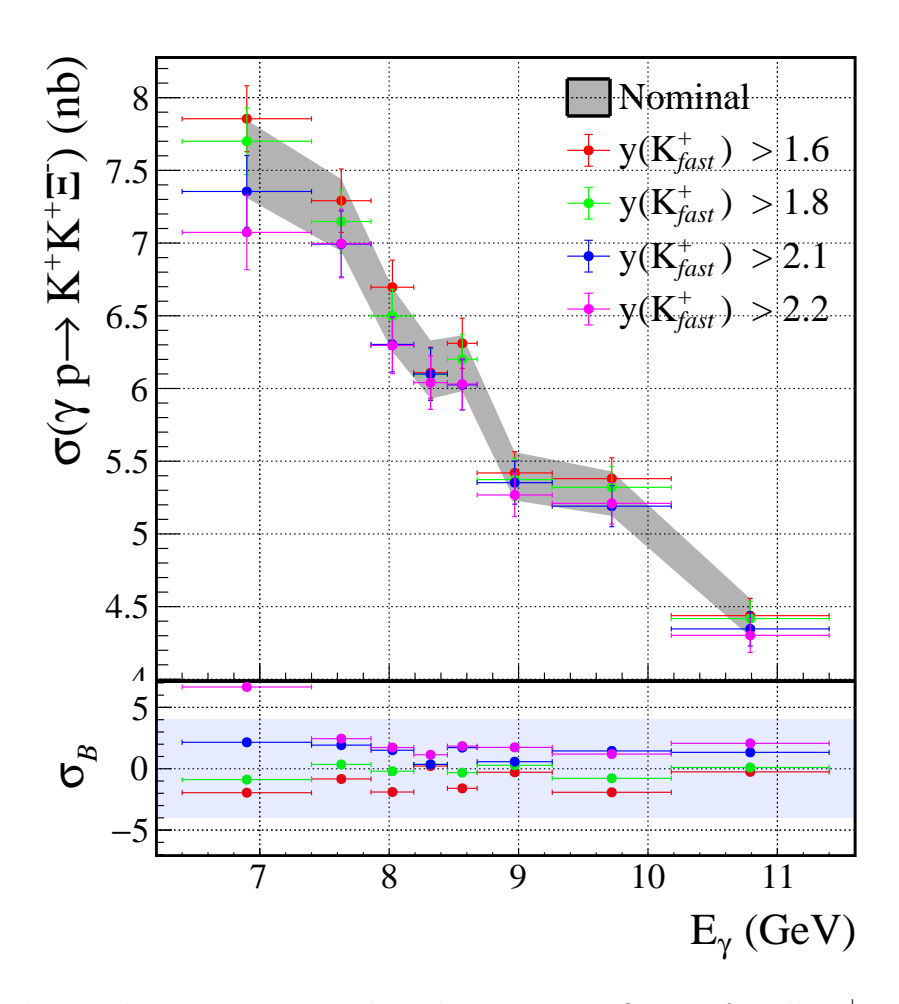


Figure 7.5: The total cross section and Barlow test significance for all K_F^+ pseudo-rapidity variations used in this study compared to the nominal data analysis.

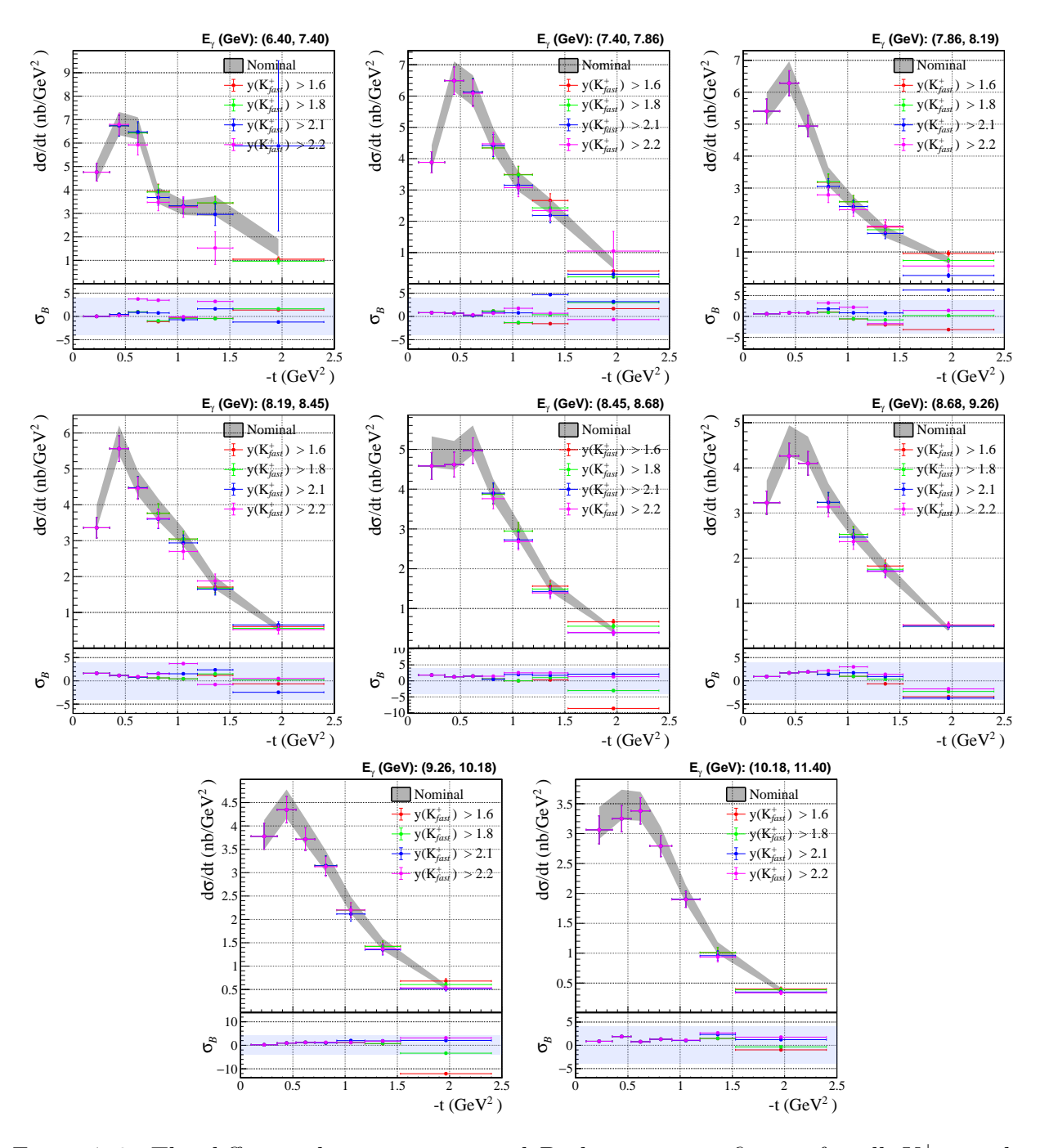


Figure 7.6: The differential cross section and Barlow test significance for all K_F^+ pseudorapidity variations in all energy bins used in this study compared to the nominal data analysis.

7.1.4 $\sigma_{flight}(\Xi^{-})$ Variations

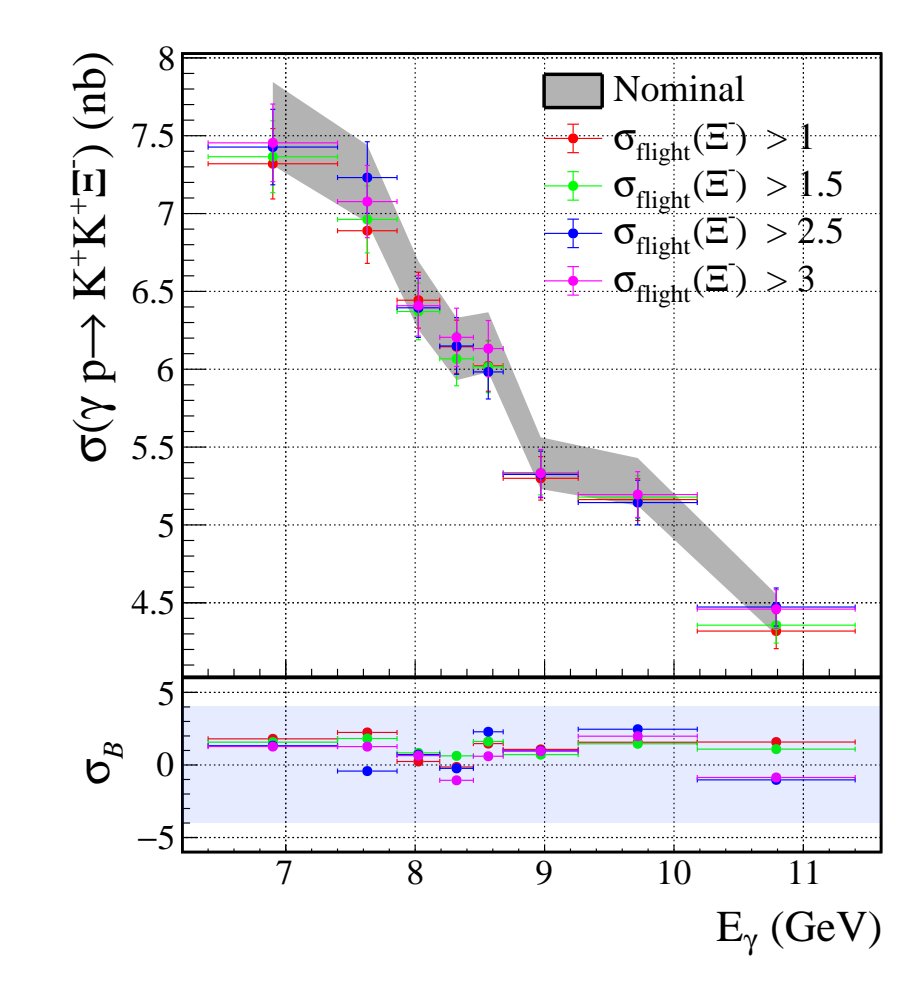


Figure 7.7: The total cross section and Barlow test significance for all Ξ flight significance variations used in this study compared to the nominal data analysis.

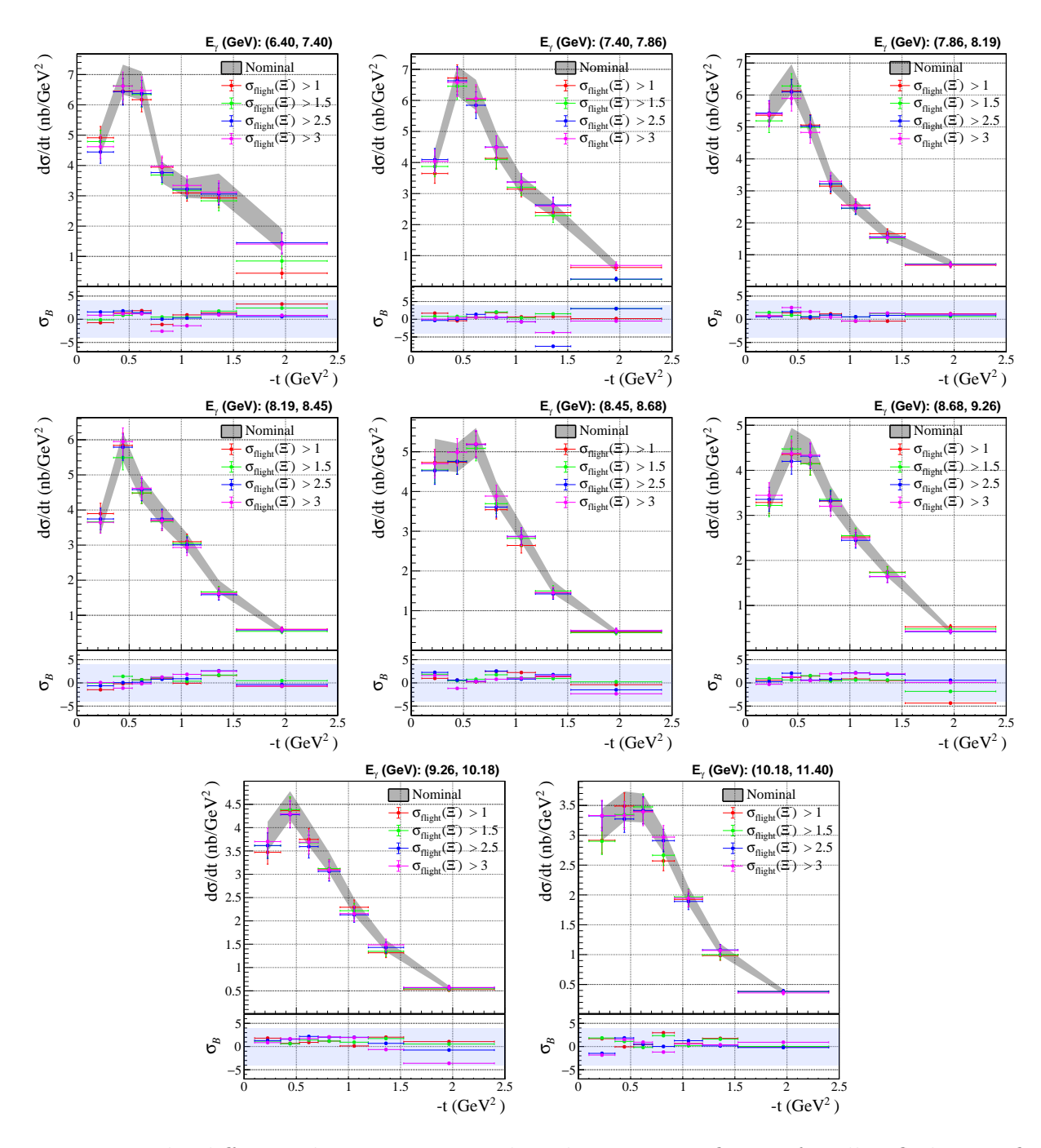


Figure 7.8: The differential cross section and Barlow test significance for all Ξ flight significance variations in all energy bins used in this study compared to the nominal data analysis.

7.1.5 $\sigma_{flight}(\Lambda)$ Variations

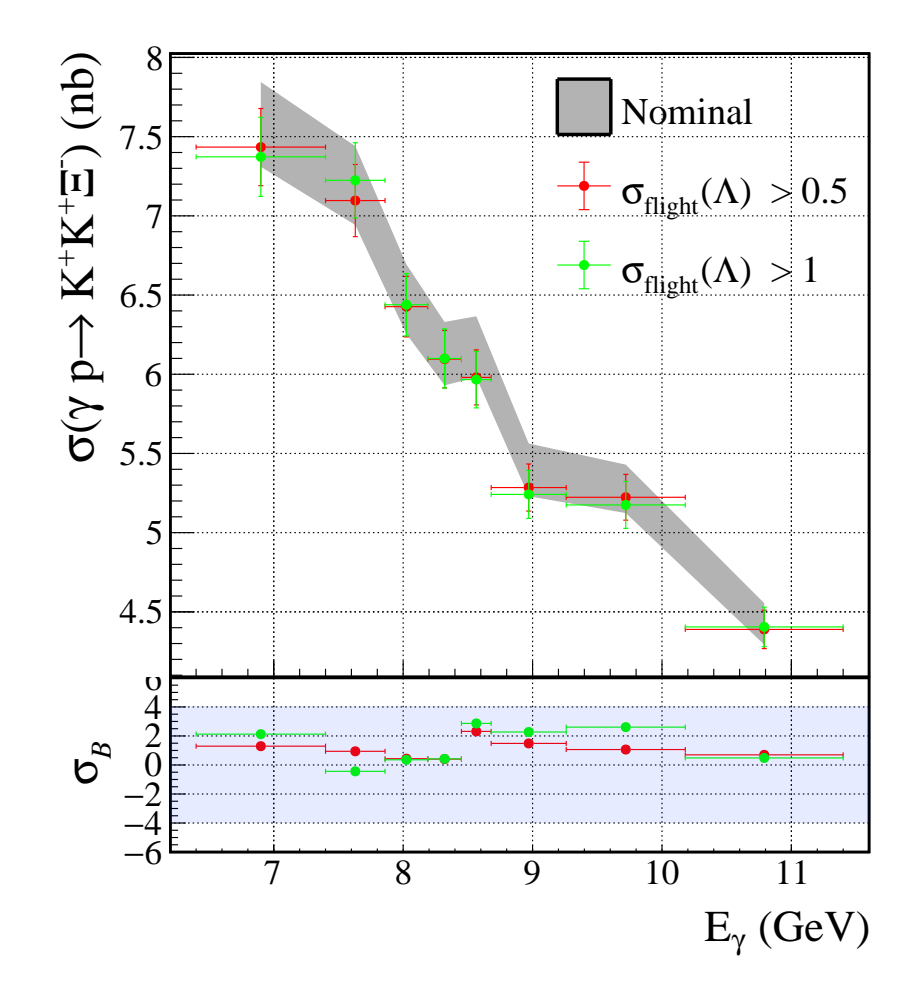


Figure 7.9: The total cross section and Barlow test significance for all Λ flight significance variations used in this study compared to the nominal data analysis.

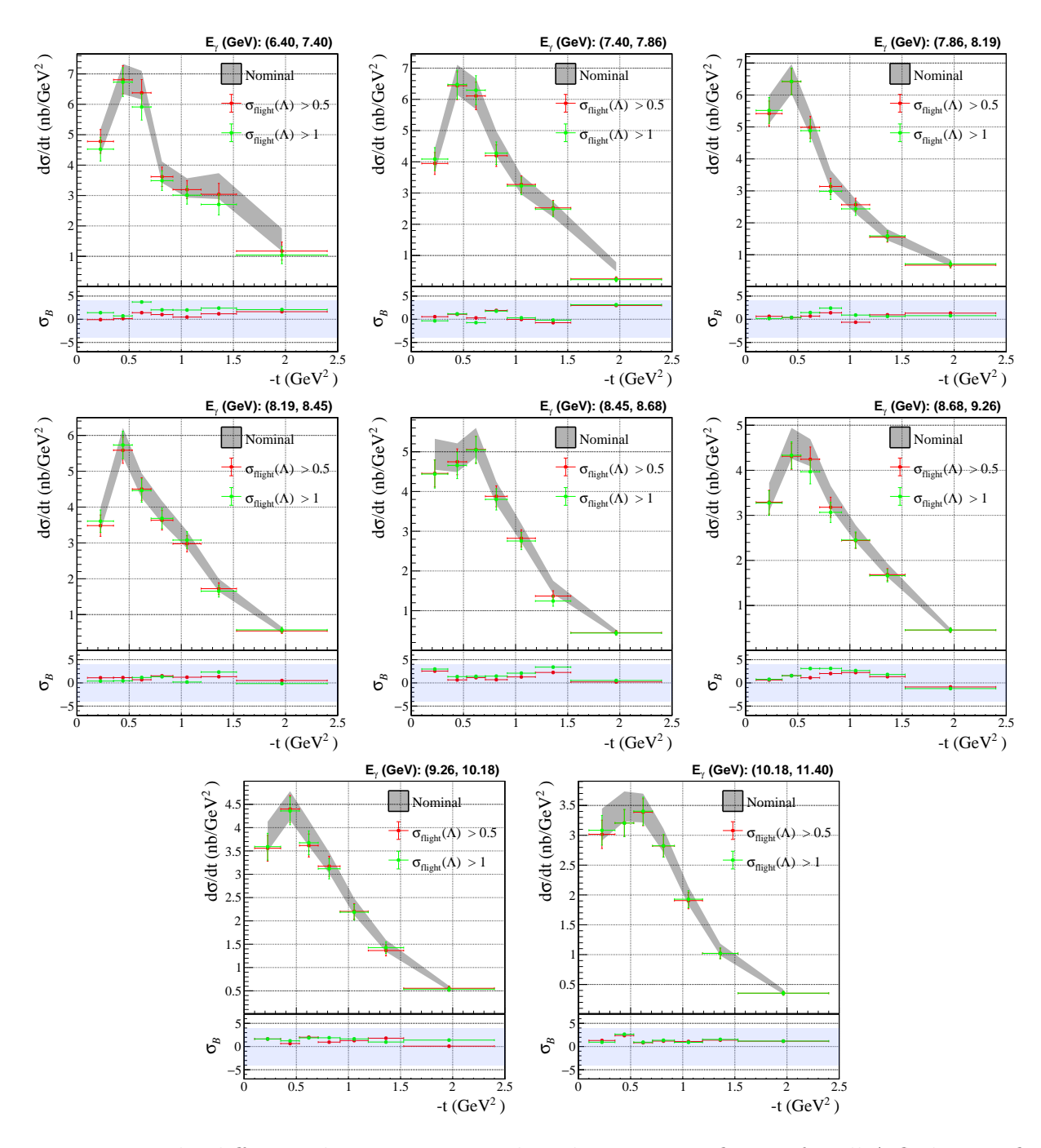


Figure 7.10: The differential cross section and Barlow test significance for all Λ flight significance variations in all energy bins used in this study compared to the nominal data analysis.

7.2 Internal Systematics

The internal systematic studies are primarily based on the event-based analysis and any uncertainties that arise from the analysis of the specific measurement.

7.2.1 Run Period Comparison

Figures 7.13-7.15 show the comparison between the three GLUEX-I run periods; the significance and ratio plots do not include error bars. The figures have three parts: the differential cross section energy bin for the two run periods that are being compared (top), and σ_{sig} described by Eq. (7.1) (middle), as well as the ratio between central values (bottom). The significance is constructed for uncorrelated sets of data using the formalism:

$$\sigma_{sigif} = \frac{\mathcal{O}_i - \mathcal{O}_j}{\sqrt{\delta_i^2 + \delta_j^2}} \,, \tag{7.1}$$

where \mathcal{O} is the observable, the differential cross section, and δ is the statistical uncertainty of the respective measurement. In this framework, anything with $\sigma_{sig} \lesssim 2$ is not statistically significant. The figures below show that most of the comparisons between run periods are in fact not statistically significant. On the other hand, for some bins, there seem to be percent differences of up to 20% and greater; although the majority of the bins differ by < 10% which is a great improvement from previous results.

It is not obvious that taking the standard deviation of the central values of the three run periods as the systematic uncertainty is correct because these fluctuations are statistical in nature and independent measurements. Furthermore, the significance over the pair-wise comparison is $\sigma_{sig} < 2$ which would indicate that these are statistically compatible measurements. We thought of two methods that may be used for the run period systematic.

Overall Systematic. We take all ratios from the pairwise comparison for the three data sets and measure its Gaussian deviation from unity and quote a percent systematic, then either take the average percent or add them in quadrature. The results of this procedure can be seen in Fig. 7.11 and the calculated overall systematic uncertainty shown in Table 7.2. The only issue with this method is that all points, even those is very good agreement, of the measurement will be receive this uncertainty.

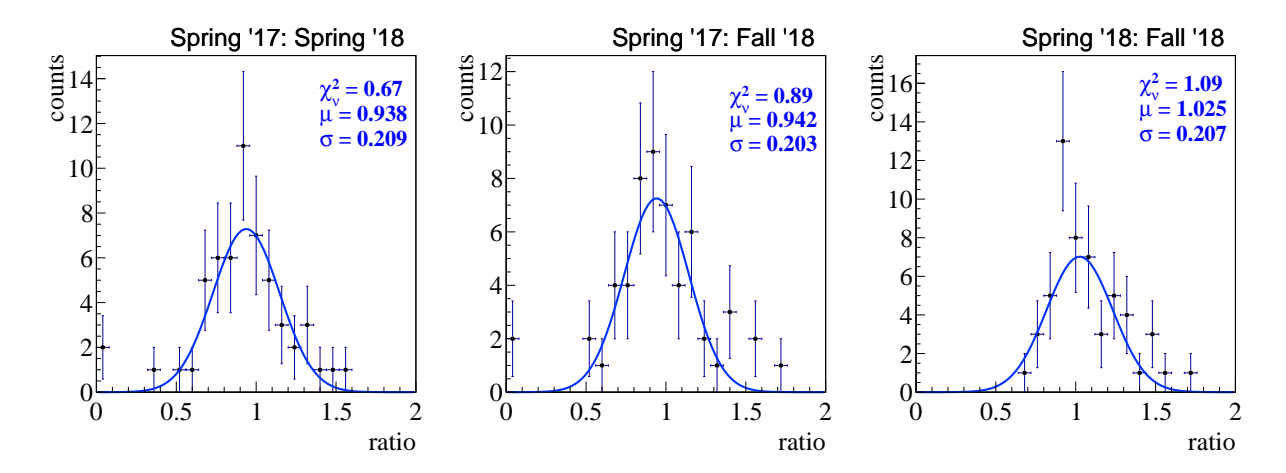


Figure 7.11: The ratio of the comparison of all three GLUEX-I run periods fit with a Gaussian function with χ^2_{ν} value shown in top right.

Table 7.2: Calculated systematic uncertainties for the Gluex-I run period comparison.

Run Comparison	Sp17:Sp18	Sp17:Fa18	S18:F18	Average	Quadrature
Uncertainty	6.2%	5.8%	2.5%	4.8%	8.9%

Figure 7.12 shows binned histograms filled with the significance values using Eq. (7.1) obtained from the comparison of all three GLUEX-I run periods. These histograms are then fit with a Gaussian function to show that the uncertainties of the comparisons are indeed not significant.

Point Systematic. We utilize the scale factors Eq. (6.8) discussed in Section 6.2 because these already tell us something about the statistical compatibility of all three run periods together and not as independent pairwise comparisons. The original purpose of the scale factor was to scale the combined uncertainty of the individual measurements to correct for any data points that have underestimated their uncertainty. The combined uncertainty would increase as $\delta \times S$ for the combined data sets. Because our combined data only contains statistical uncertainties, it wouldn't seem appropriate to scale this value because it is purely statistical. Instead, a systematic uncertainty could be constructed from the effect of the scale factor on the statistical uncertainty to make the three run periods statistically compatible for each point. Therefore, we construct a point systematic uncertainty for any measured differential cross section values that have S > 1 where the uncertainty is

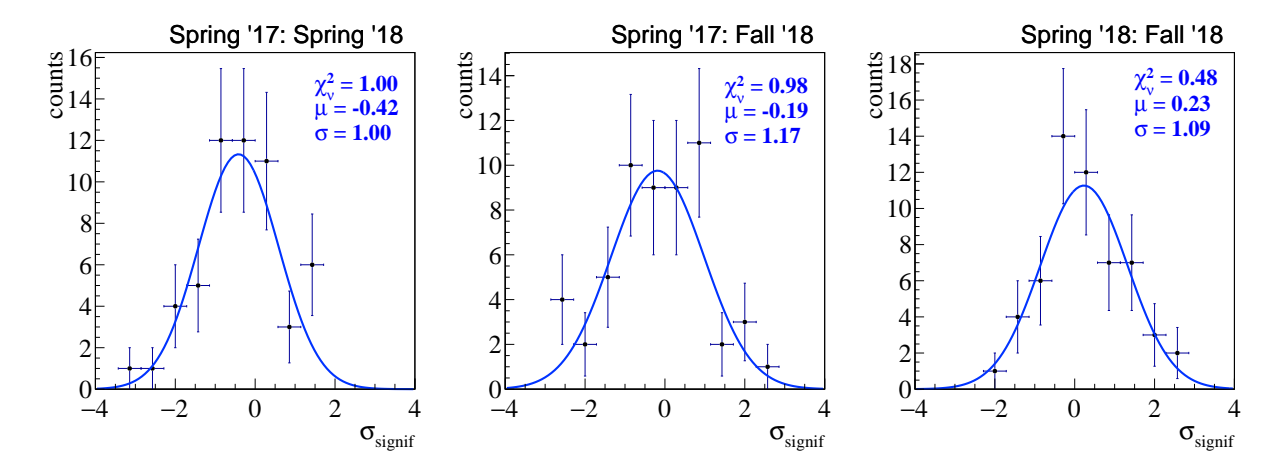


Figure 7.12: The significance (Eq. (7.1)) of the comparison of all three GLUEX-I run periods fit with a Gaussian function with χ^2_{ν} value shown in top right.

$$\delta_{syst} = \begin{cases} \delta_{stat}(S-1), & S > 1\\ 0, & S < 1 \end{cases}$$
 (7.2)

The result is outlined in Table 8.1. This gives the advantage that for measured points that are statistically compatible S < 1 does not receive an uncertainty an dilute the result.

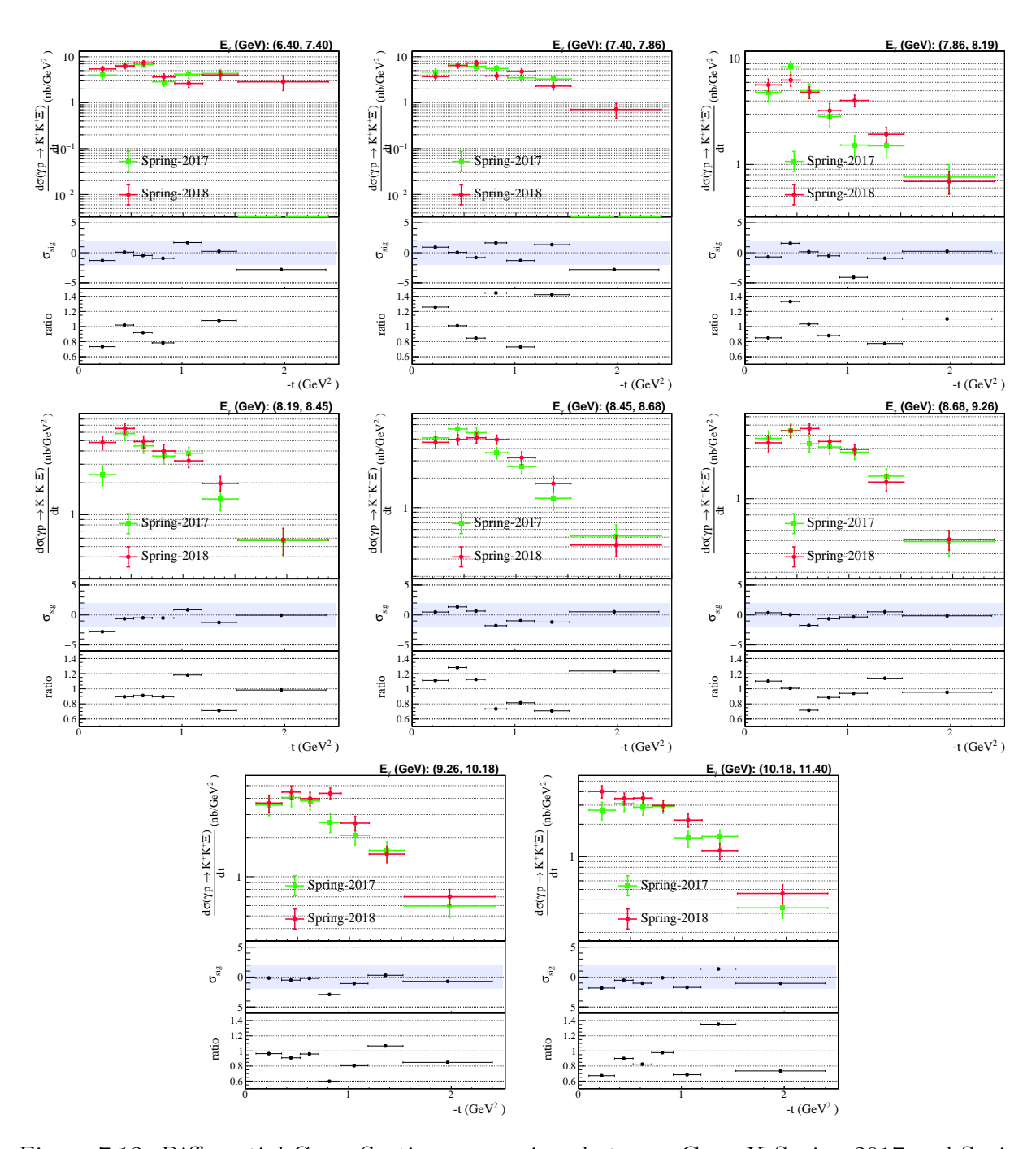


Figure 7.13: Differential Cross Section comparison between GLUEX Spring 2017 and Spring 2018 data sets.

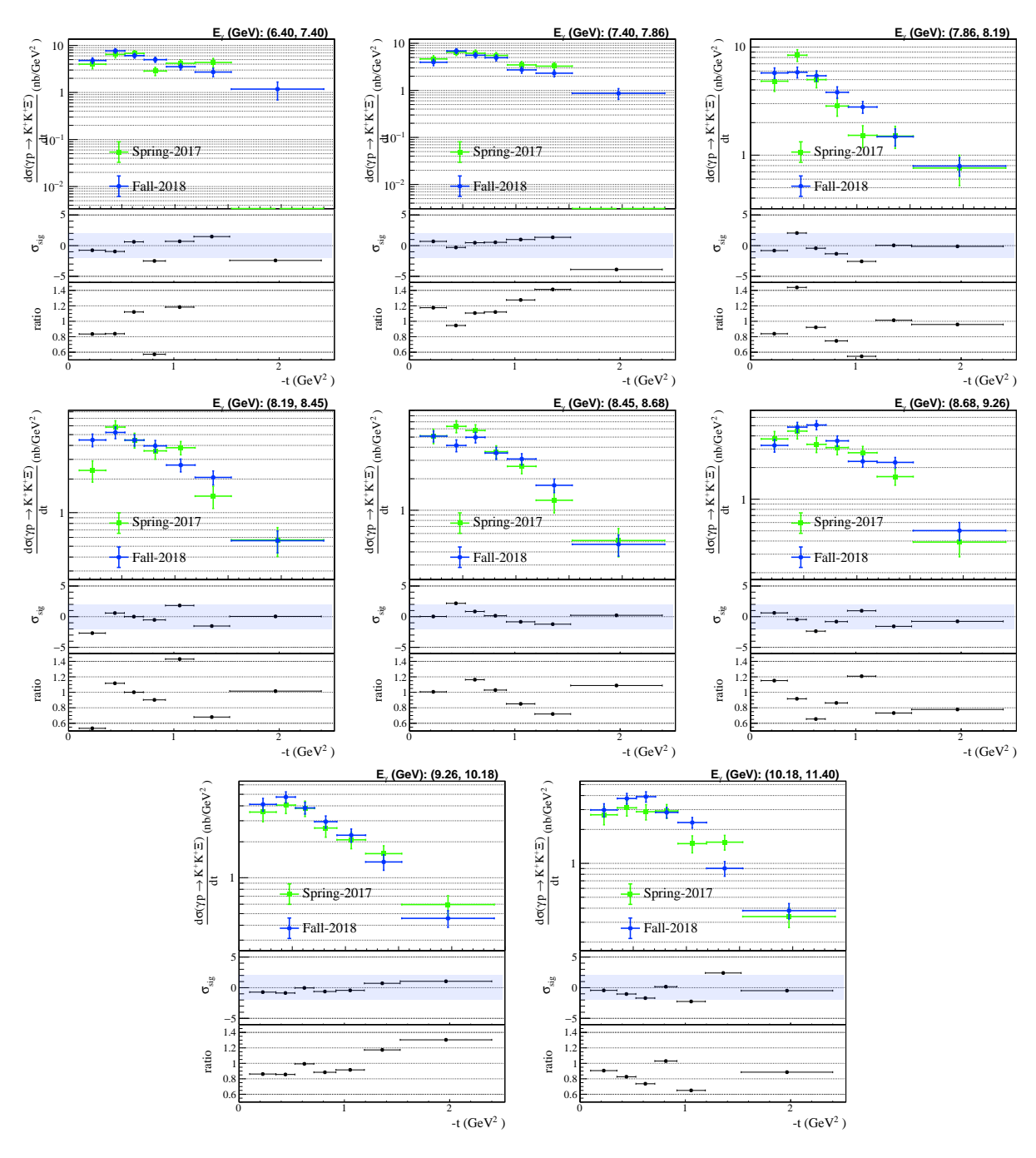


Figure 7.14: Differential Cross Section comparison between GLUEX Spring 2017 and Fall 2018 data sets.

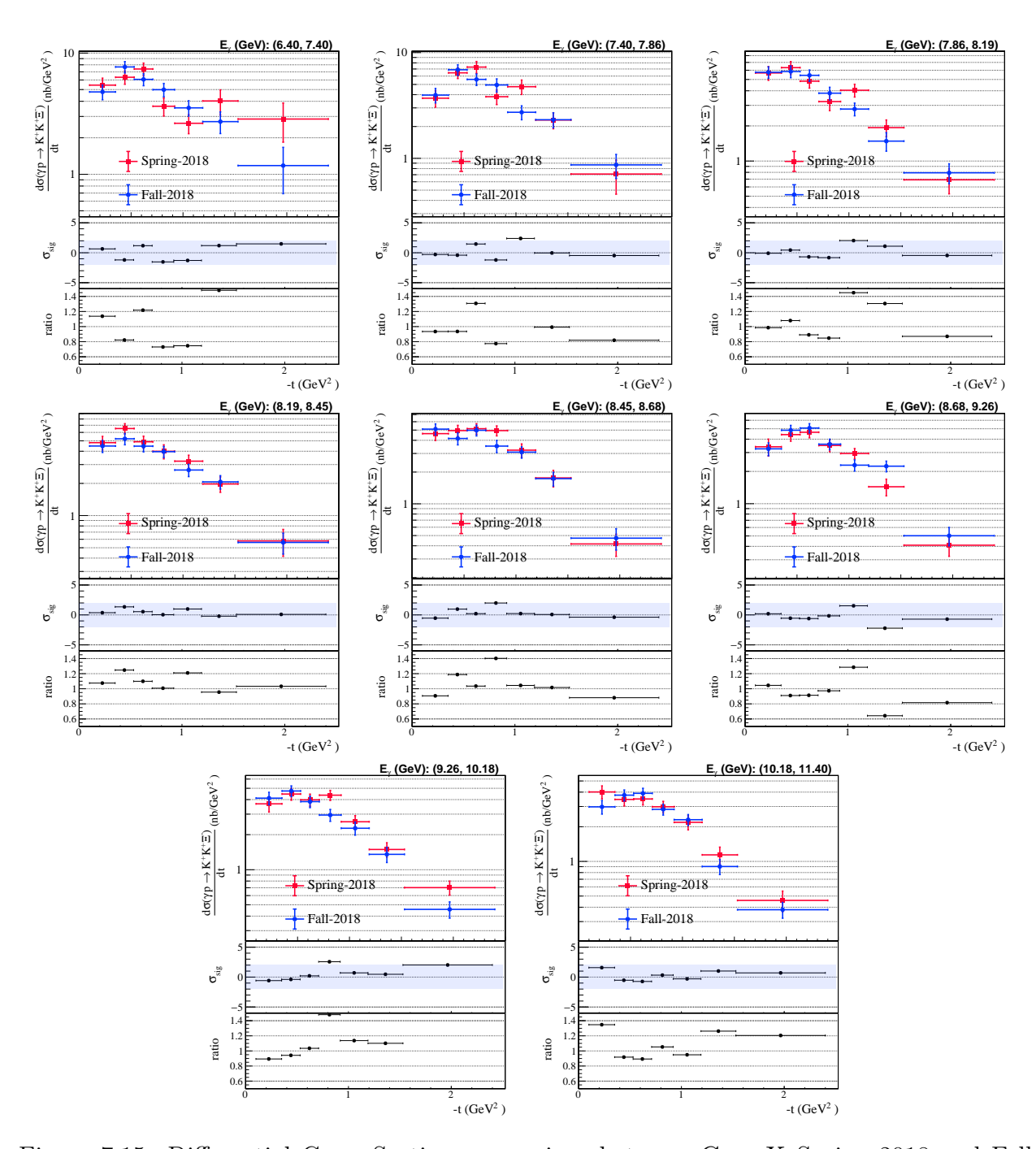


Figure 7.15: Differential Cross Section comparison between GLUEX Spring 2018 and Fall 2018 data sets.

7.2.2 Accidental Subtraction Method

In data analysis, the methods of subtracting accidental photons from the data are quite important. Figure 7.16 shows the differential cross section for the three methods described in Section 4.2.3 where the annotation for the average percent difference is compared to the RF subtraction method. From the figure it is seen that on average for different energy bins the hybrid χ^2_{ν} method agrees better compared to the best χ^2_{ν} method and the deviation of $\approx 5\%$ in most energy bins agrees with other collaboration findings. Lastly, the hybrid χ^2_{ν} method seems to show a small energy-dependent effect of $\simeq 1\%$ compared to the RF method.

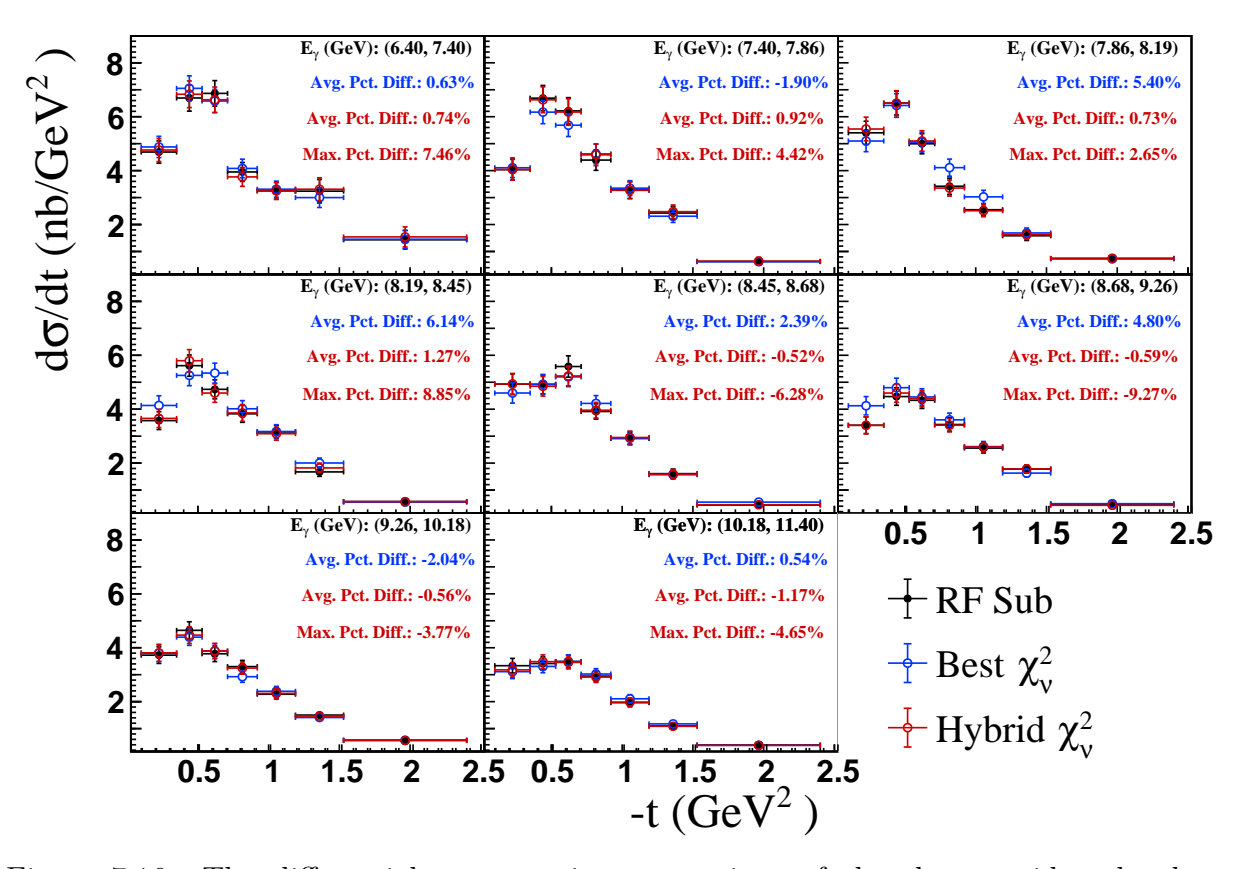


Figure 7.16: The differential cross section comparison of the three accidental subtraction methods for the RF method (black), the best χ^2_{ν} method (blue) and the hybrid χ^2_{ν} method (red).

To compute a systematic uncertainty on the accidental method used for the analysis the RF method and Hybrid method are compared directly and the standard deviation computed at each point. Figure 7.17 shows the calculated standard deviation (gray band) and Table 8.1 shows the point results that will be used for the systematic uncertainty on the accidental method. This may also be sufficient for the luminosity normalization uncertainty that the collaboration has placed a very conservative 5% normalization uncertainty.

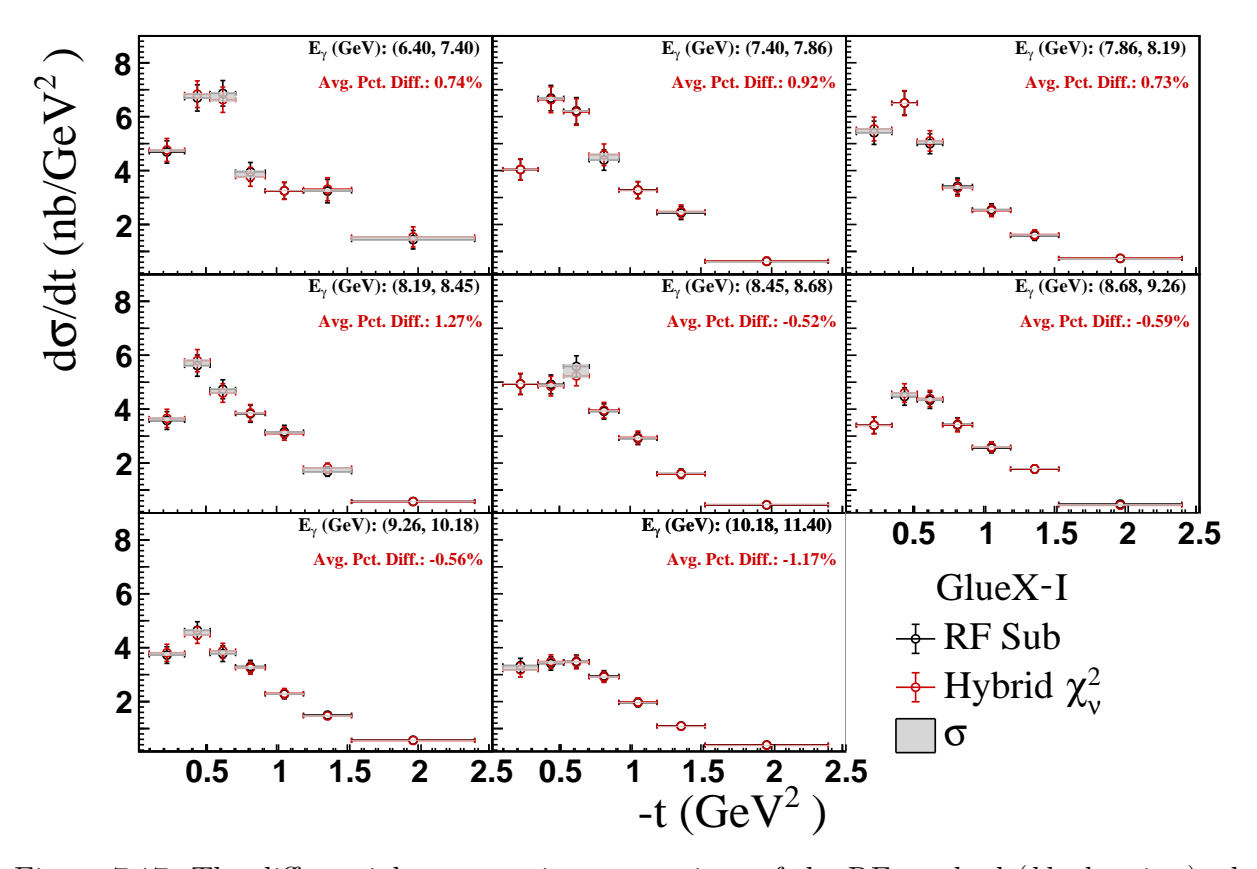


Figure 7.17: The differential cross section comparison of the RF method (black points), the hybrid χ^2_{ν} method (red), and the standard deviation of the methods (gray band).

7.2.3 Cascade Yield Extraction

In this section, the parameterization of the fit for the extraction of yield from our data is varied. For the signal the nominal data is fit with a Johnson pdf described in Section 6.1.1 and the variations used a Voigtian pdf (the convolution of a Breit Wigner and Gaussian) and a pdf constructed from the signal Monte Carlo mass shape (MC pdf). For the background, the nominal data was fit with a second-order Chebychev polynomial and for the variation a first-order Chebychev polynomial. An example of the fits for all the variations for one bin are shown in Fig. 7.18.

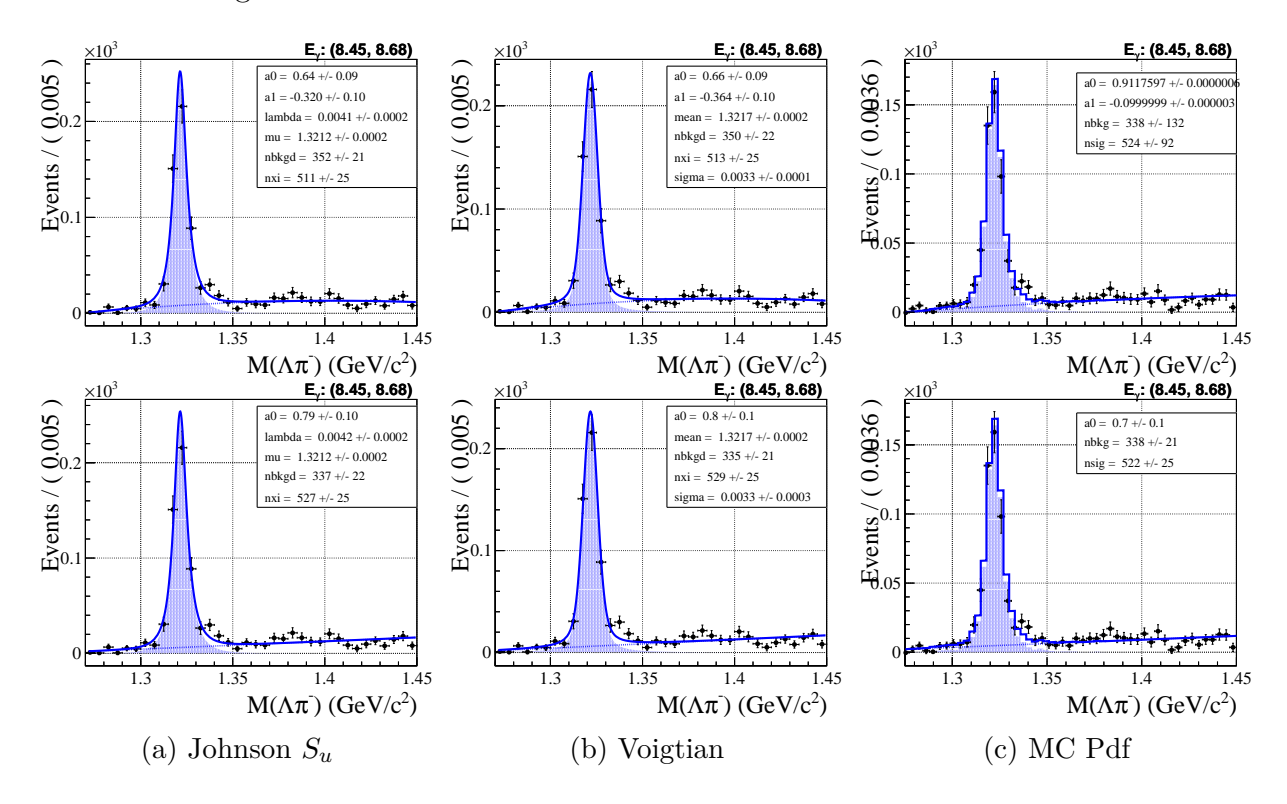


Figure 7.18: An example of the unbinned likelihood fits to data for one energy bin for all six parametrization where the signal function is the same and labeled for each column and the background function for the (top row) is a second-order Chebychev polynomial and for the (bottom row) is a first-order Chebychev polynomial.

The results of all combinations of the signal and background variations fit to data and used for the cross-section are shown in Fig. 7.19 where, the standard deviation of all variations is displayed with a gray band for all measured points. The values of the standard

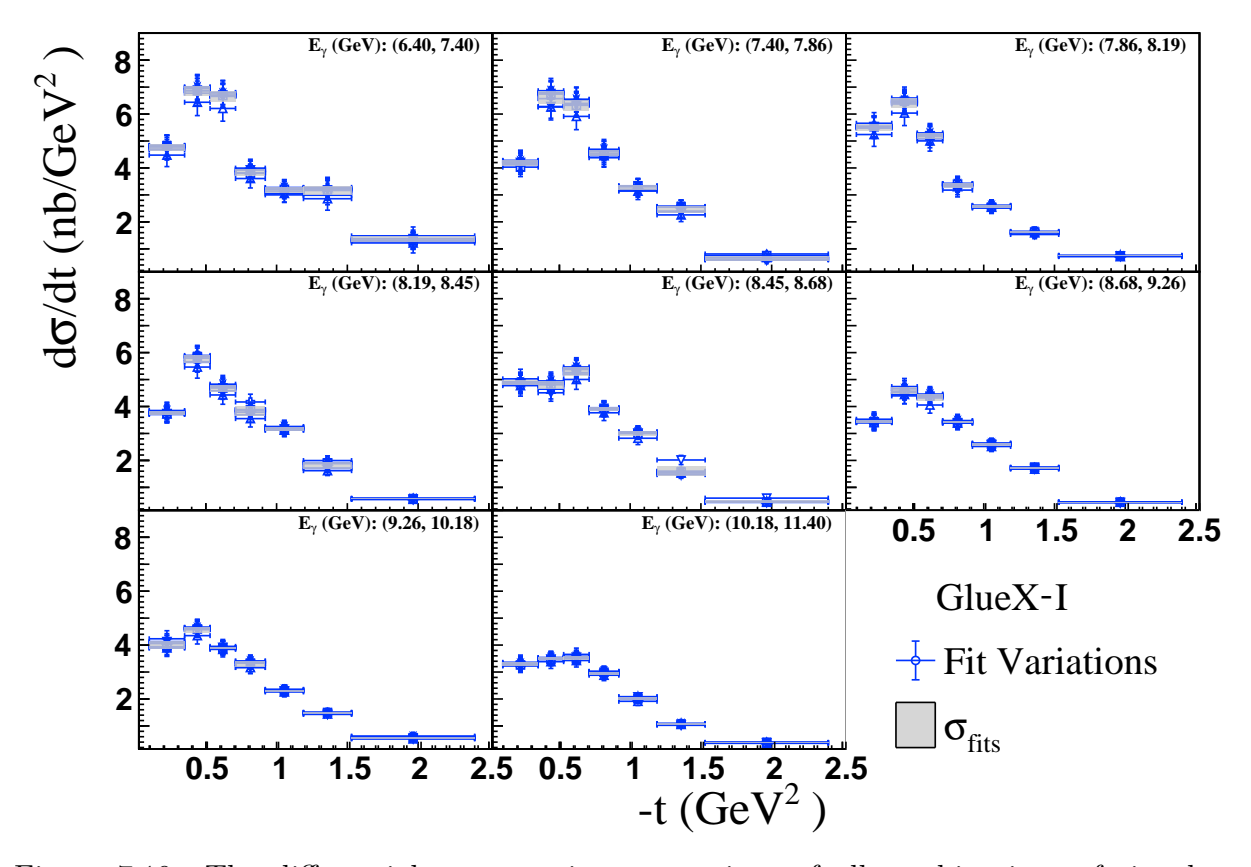


Figure 7.19: The differential cross section comparison of all combinations of signal and background fit variations to the data (*blue points*) and the standard deviation (*gray band*) to be used as a point-by-point systematic uncertainty.

deviation (point systematic uncertainty) of all the variations is shown in Table 8.1. Individual variations are also plotted in Figs. 7.20 to 7.22. From the distributions, the background variations for a given signal shape generally have a small uncertainty on the order of $\sim 1\%$. For the signal function, the Johnson and Voigtian line-shapes provide very similar deviations on the order of $\sim 1-3\%$ and the MC pdf gives the largest deviation on the order of $\sim 5\%$.

The Q-Factor method described in Section 4.3 was also used instead of the normal fitting procedure described in Section 6.1.1. To retrieve the differential cross-section using the Q-Factor yields the original cross section was scaled by the ratio of the yields of the two methods,

$$\left(\frac{d\sigma}{dt}\right)^Q = \frac{(N)^Q}{N} \frac{d\sigma}{dt}.\tag{7.3}$$

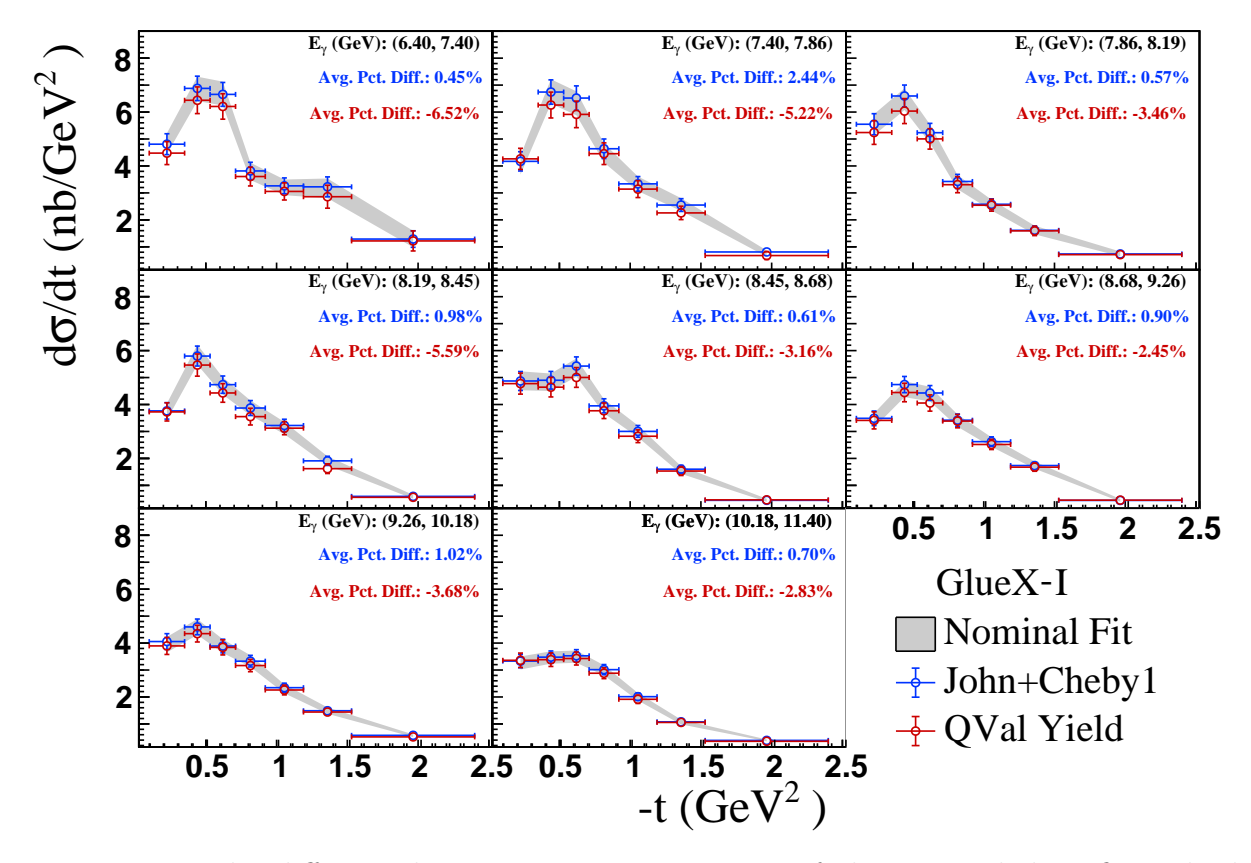


Figure 7.20: The differential cross section comparison of the nominal data fit with the signal being a Johnson pdf and second-order Chebychev pdf, Eq. (4.18)), (black points), the background variation being the first-order Chebychev (blue points) and using the extracted yields from the Q-Factor method (red points).

This is a valid method to extract the new cross-section because the only variable that is modified is the yield and all the other components of Eq. (6.1) remain the same. The result of the comparison is shown in Fig. 7.20 where the errors of the Q-Factor method are made to be the same as the original cross-section. Since the percent difference of the central points is the sought-after value extracted from this study and the method is not used in the final result, calculating the complex errors from the Q-Factor method is deemed unnecessary. It can be seen from Fig. 7.20 that there is an energy-dependent effect on the yield extraction method of $\simeq 3-6$ %.

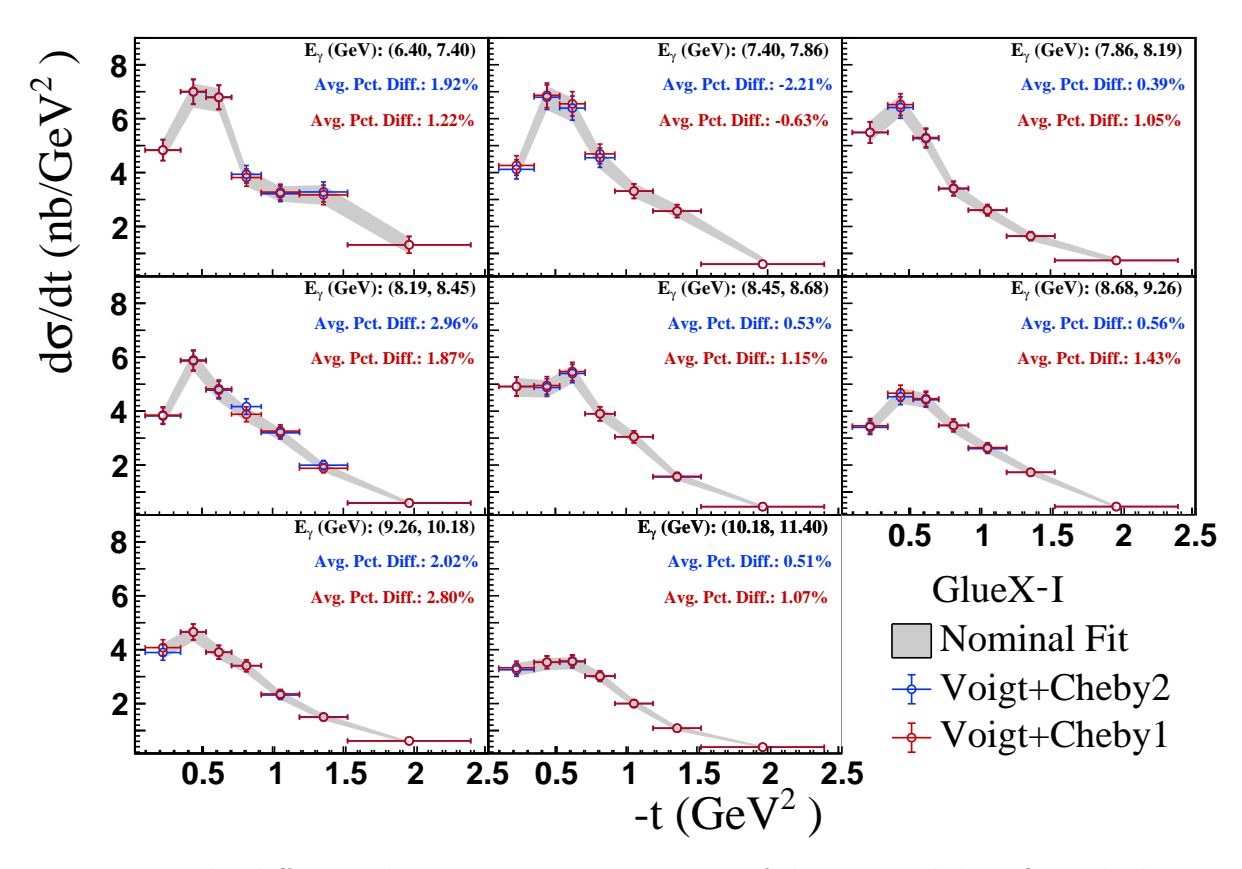


Figure 7.21: The differential cross section comparison of the nominal data fit with the signal being a Voigtian pdf (*black points*), and the background variations being the second-order Chenychev (*blue points*) and the first-order Chebychev (*red points*).

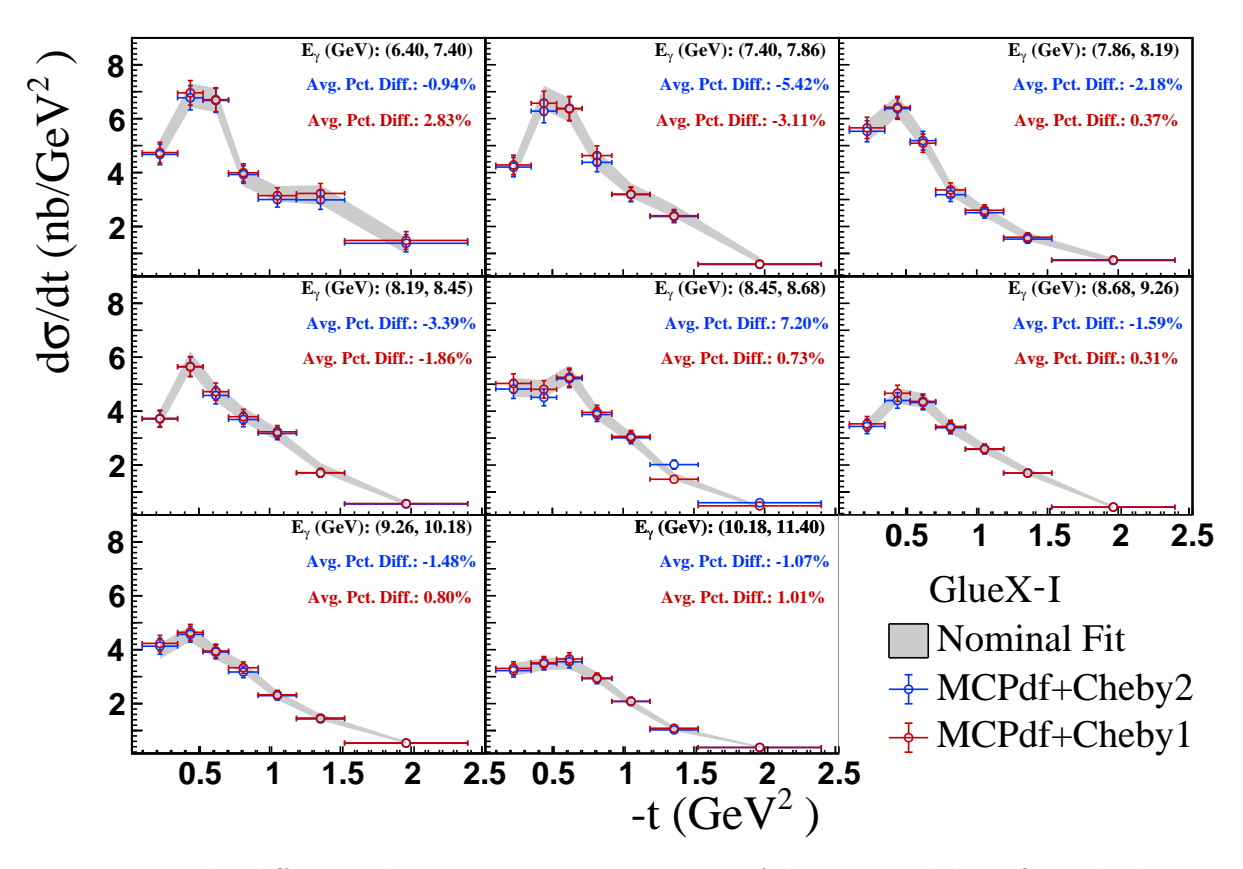


Figure 7.22: The differential cross section comparison of the nominal data fit with the signal being a Monte Carlo pdf (*black points*), and the background variations being the second-order Chenychev (*blue points*) and the first-order Chebychev (*red points*).

7.2.4 RF Beam Bunch Study

As discussed in Section 7.2.2 and seen in Fig. 4.4 the data launch used for the Spring 2017 data set contain two RF bunches (one per side) and both 2018 data sets contain eight RF bunches (four on each side). The first beam bunch is omitted if possible as shown for the Spring and Fall 2018 data sets in Fig. 4.4 because there could be some leakage from the in-time RF peaks. For this study the Spring and Fall 2018 GLUEX data sets are modified to match the RF bunch structure of the Fall 2017 data set also shown in Fig. 4.4 (one bunch per side). In principle, the choice of the number of out-of-time RF beam bunches should not affect the measurement. Figure 7.23 shows the weighted GLUEX-I nominal data compared to the weighted data when only one RF beam bunch is used for the 2018 data sets. It can be seen from Fig. 7.23 that their is an energy-dependent deviation on average on the differential cross section of $\simeq 2-10\%$.

Furthermore, to show where these deviations come from for the weighted GLUEX-I data, Figs. 7.24 and 7.25 are shown. These figures show the comparison of the nominal data for the Spring and Fall 2018 data sets with the modified RF beam bunches to match the Spring 2017 data. It is shown that the handling of the RF beam bunches does have some effect on the measurement of the differential cross section. The effect could be due to overlapping events not being handled properly by only using the first out-of-time RF beam bunch. A potential solution would be to provide an analysis launch of the Spring 2017 data set with eight beam bunches so we can handle all the data sets in a consistent way.

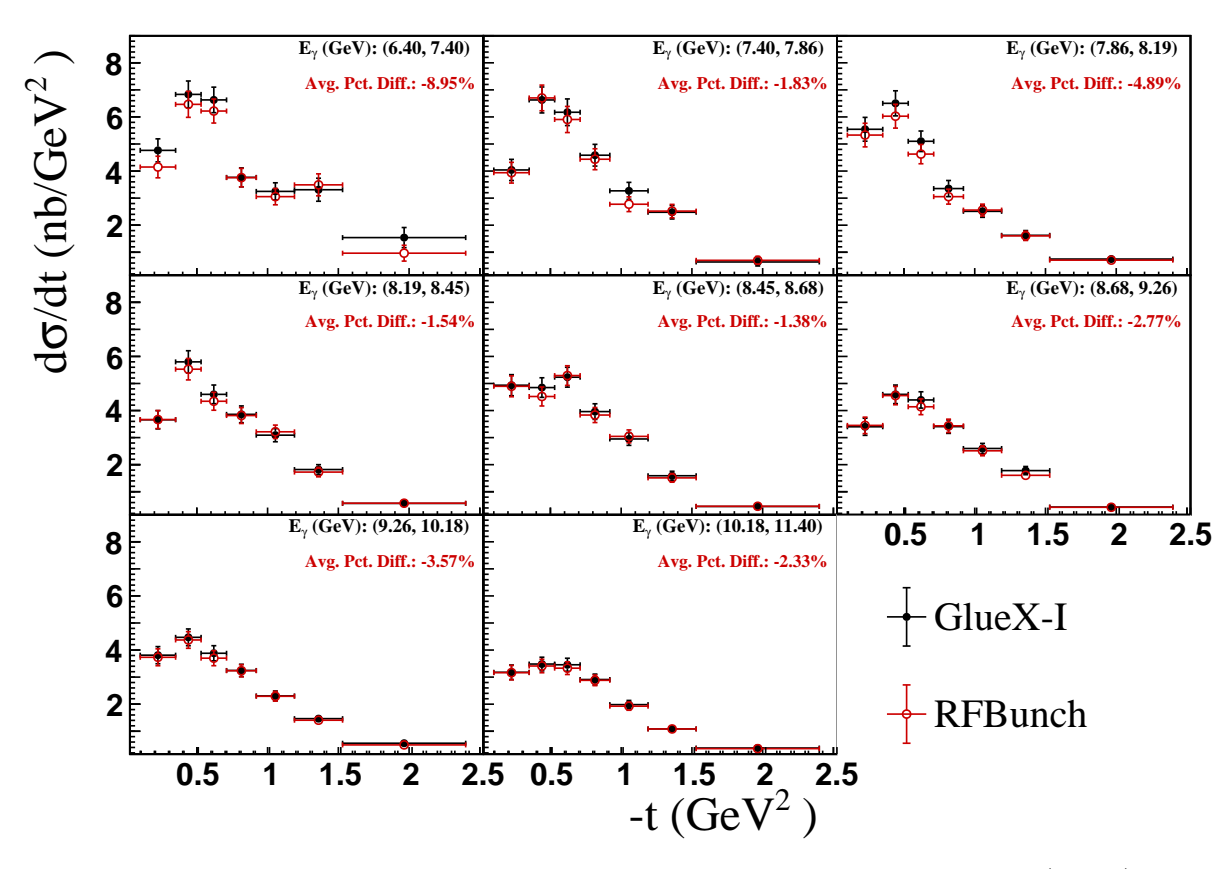


Figure 7.23: The differential cross section comparison of the nominal data (black) and the modified data (red) where, the RF-Bunch pattern of the 2018 data sets (8 bunches) were modified to match the 2017 data set (2 bunches).

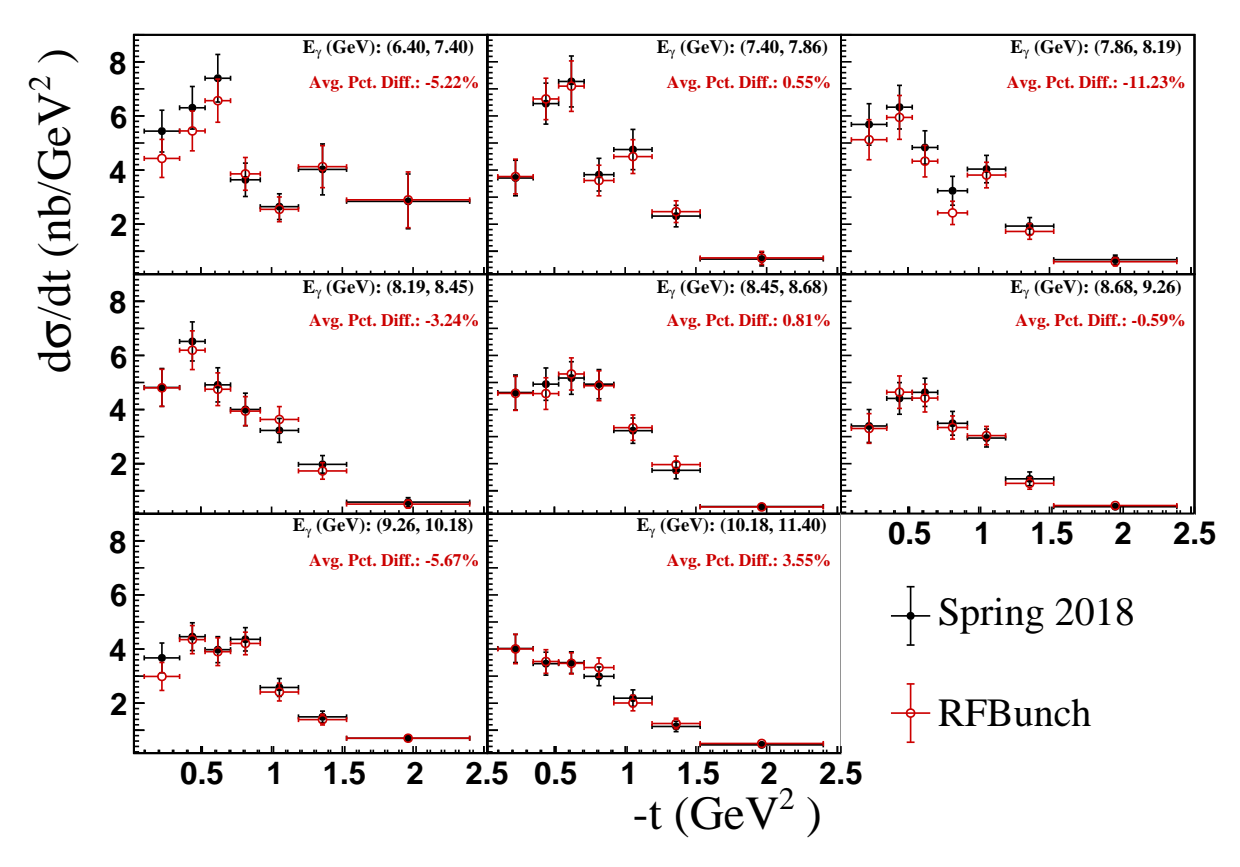


Figure 7.24: The differential cross section comparison of the Spring 2018 (red points) and nominal data (black points), where the RF-Bunch pattern of the 2018 data sets (8 bunches) was modified to match the 2017 data sets (2 bunches).

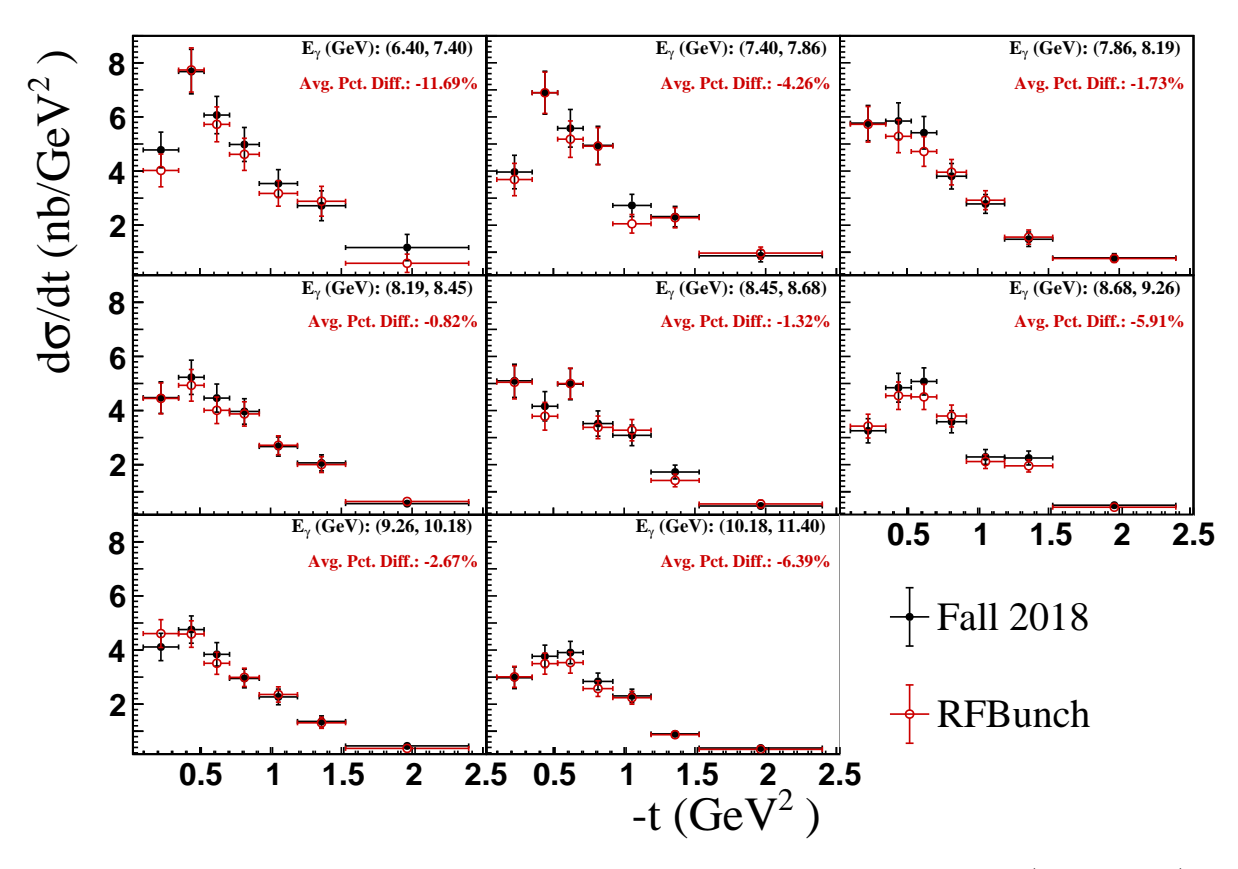


Figure 7.25: The differential cross section comparison of the Fall 2018 (red points) and nominal data (black points), where the RF-Bunch pattern of the 2018 data sets (8 bunches) was modified to match the 2017 data sets (2 bunches).

7.2.5 Spring 2017 Rest Version

For this analysis, the newest REST version 4 was used for the Spring 2017 data; the previous GLUEX publications use REST version 3 for the Spring 2017 data. For this reason, in this section the two REST analysis versions are compared to ensure that the results do not depend on the version set used. For the results, the Spring 2017 REST version 3 was replaced and the cross section extracted and used in the weighted averaging of the GLUEX-I runs and compared to version 4, shown in Fig. 7.26; their is no obvious difference over the entire energy range. The effect is also shown for the Spring 2017 data set individually in Fig. 7.27; this again shows very minimal effect over the entire energy range.

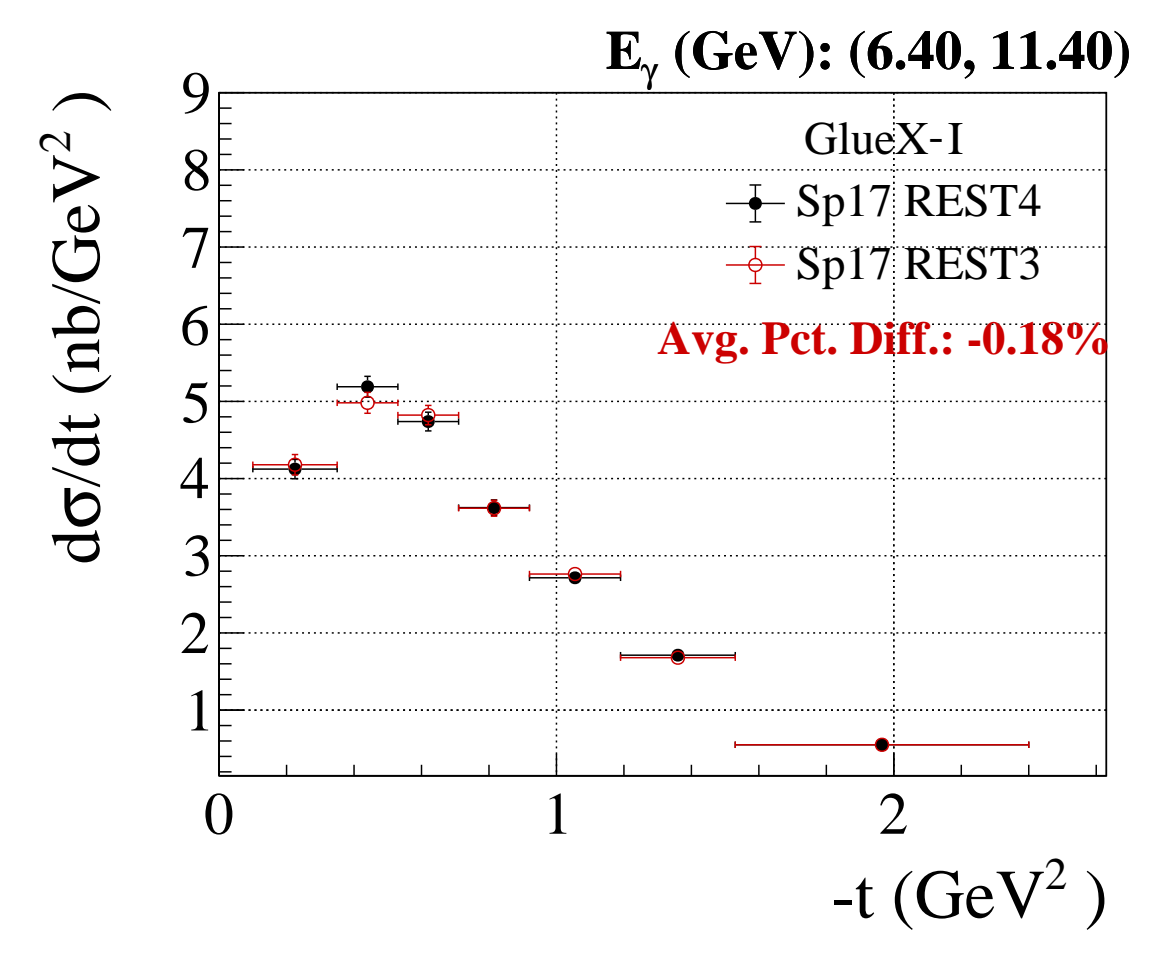


Figure 7.26: The differential cross section comparison of the nominal data (black) and the modified data (red) where, the REST version 3 was used for the Spring 2017 data set.

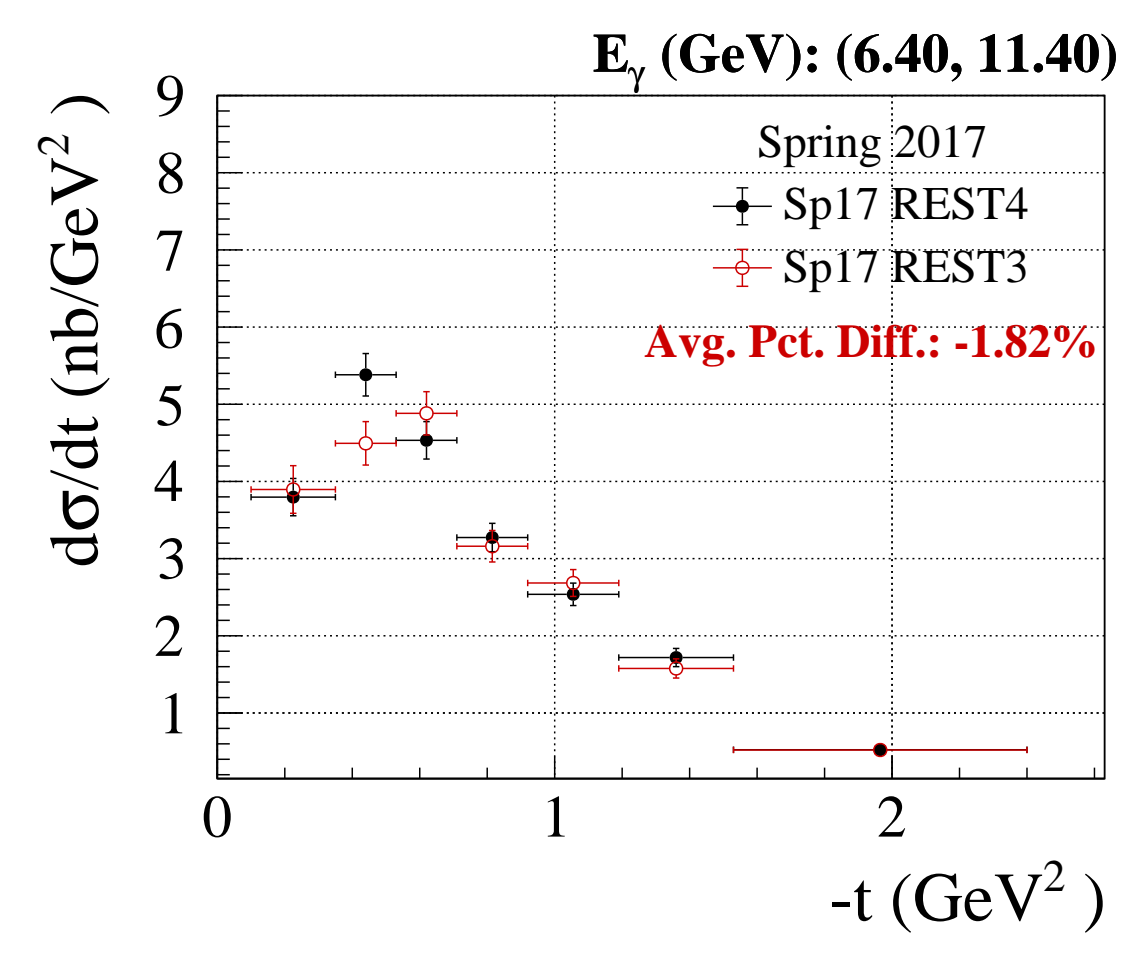


Figure 7.27: The differential cross section comparison of the Spring 2017 REST version 4 data (black) and the modified data (red) where, the REST version 3 was used for the Spring 2017 data set.

7.3 External Systematics

External systematics are defined by the experts of the experiments in the Gluex collaboration. These standards are based on the experimental hardware and procedures and affect the overall normalization any measurement with some reaction dependence.

7.3.1 Luminosity Normalization

This systematic study is determined by the beamline group. The uncertainty in the luminosity value is expected to be dominated by the understanding of the pair spectrometer. According to Richard Jones, a conservative value for the uncertainty is 5%. The final uncertainty is expected to be about half as large; for now, we use the conservative value of 5%.

In addition to the external systematic uncertainty, our own study of the different accidental photon methods are shown in Section 7.2.2. From this study, the 5% uncertainty using the best χ^2_{ν} method is verified. In this analysis, the hybrid χ^2_{ν} method is chosen and shows good agreement with the RF subtraction method, therefore, further systematic may not be warranted.

7.3.2 Track Efficiencies

We can obtain an initial estimate for the size of these systematic uncertainties by using the conservative values listed by the GLUEX collaboration. For our channel the charged tracks and proton guidance are all that are needed. The guidance says to assign systematic uncertainties of

- 5% for each proton
- 3% for each track with $\vartheta < 20^\circ$
- 5% for each track with $\vartheta > 20^{\circ}$

where, documented efficiency studies have been reviewed internally. Although, there have been some internal studies in other decay channels there needs to be much more rigorous studies conducted in this specific reaction. Therefore, it is emphasized that these track uncertainties are very conservative.

To determine these systematic uncertainties, we use our signal Monte Carlo since it is a high-statistic sample of the signal process; repeating the procedure on data gives very similar results. For each final state, we loop over all the final state particles and plot the reconstructed ϑ distribution for each track. The systematic uncertainty for a single track is determined by integrating the number of entries below 20° (N_{low}) and above 20° (N_{high}) and calculating the weighted average uncertainty from Monte Carlo

$$(3\% * N_{low} + 5\% * N_{high})/(N_{low} + N_{high}). \tag{7.4}$$

The efficiency is assumed to be the product of single particle efficiencies

$$\varepsilon = \prod_{i} \varepsilon_{tk,i} \tag{7.5}$$

where, all final systematic track uncertainties are summed for the final result. The single and total track efficiency systematic uncertainties obtained using this method are shown in Table 7.3 where taking the conservative value for the proton leads to a 20% uncertainty. It is noted that this is an extremely conservative uncertainty on the tracks and a full study would be needed on how these are correlated in this reaction. We conclude that for a measurement that is not a precision measurement this value can be quoted but will not be used for the uncertainties in the distributions. The plots showing the angular distribution

Table 7.3: Table showing the track efficiencies for the entire GlueX-I data.

Track	K_F^+	K_S^+	π_Ξ^-	π_{Λ}^-	p	Total
Uncertainty	3%	4.94%	3.83%	3.59%	5% (3.29%)	20.29% (18.58%)

and extracted uncertainty for all tracks are shown in Fig. 7.28. The proton distribution is also shown with the method listed above, although the conservative 5% uncertainty is used for the proton track.

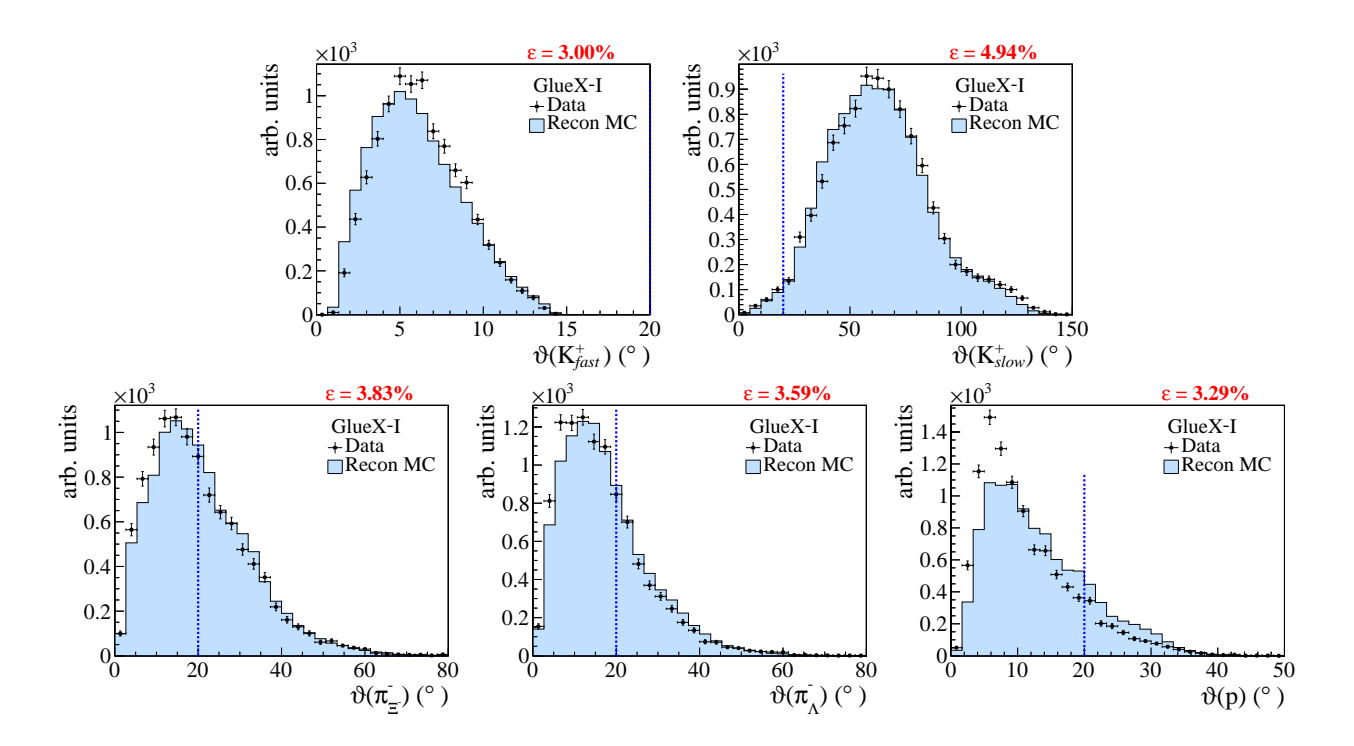


Figure 7.28: The angular distributions for all final state particles for the GLUEX-I data and reconstructed simulation. The dashed blue line indicated the cut off for measuring the track systematic uncertainties (shown in red).

CHAPTER 8

CONCLUSION

8.1 Summary

A general introduction to the topic of hadron physics, in particular doubly strange hyperon spectroscopy, motivations, and activities at GlueX has been discussed in Chapter 1. The previous experimental facilities and results of over 70 years of hyperon spectroscopy have also been discussed as related to this work in Chapter 2. A detailed overview of the experimental setup, sub-detector systems, and data acquisition protocol of the GLUEX experiment at Thomas Jefferson National Laboratory has been presented in Chapter 3. The experimental procedure for particle reconstruction at GLUEX, data preparation, and analysis of the cut criteria for event selection for this work have been presented in Chapter 4. The procedure for the generation of Monte Carlo samples using a novel data-driven approach to obtain good data-monte carlo agreement has been presented in Chapter 5. Based on the confidence of the previously discussed analysis, the procedures and results used for the measurement of the production cross section, the production properties of the ground state Ξ , and a brief discussion on the excitation spectrum in the ΛK channel are presented in Chapter 6. Finally, internal and external systematic studies for the production cross section measurement are presented in Chapter 7 to obtain the final cross section measurement to be published and peer reviewed.

The cross section measurement of the octet ground state Ξ hyperon marks a milestone in the capabilities and potential of the GLUEX experiment. To date, there have only been published measurements in much less complex decay channels of mesons and baryons at GLUEX. Furthermore, the novel methods to reconstruct the complex final state in Monte Carlo simulations was a monumental task and needed the development of new methods to achieve. The extraction of the production properties of the octet ground state Ξ , although preliminary and incomplete, give the first experimental spin measurement and will give ex-

perimental verification and checks to already established results with far greater statistical precision. Finally, the preliminary results with the GLUEX-I data of the spectrum of excited Ξ hyperons in the decay channel ΛK show great promise to study the controversial $\Xi(1690)$ and $\Xi(1820)$ with a line-shape measurement in the future as discussed in Section 6.4 with the accumulation of more statistics with the GLUEX-II experiment currently running (Section 8.2.2).

A brief discussion on the cross section results and systematic studies is also presented below. From the results of Section 7.1.5 where the Barlow test is applied to several variations to the event selection, we conclude that their are no extracted points that diverge from the $\sigma_B < 4$ standard to apply a systematic uncertainty. We see that the three GlueX-I run periods are statistically consistent for all points by summarizing the finding of $\sigma_{sig} < 2$ Eq. (7.1) and therefore avoid an overall run period systematic uncertainty. Instead, we choose to use the scaling factors obtained from the weighting procedure in Section 6.2 and assign a point systematic when S > 1 (Eq. (6.8)). The point-bt-pointsystematic uncertainties that we quote are from the run period comparison/combination, the accidental subtraction method and the yield extraction summarized in Table 8.1. The overall normalization uncertainties are based on collaboration standard systematics shown in Table 7.3. The track efficiencies are extremely conservative values for the uncertainties, in particular because our reaction has detached vertices and these tracks may not be highly correlated and justify combining the track uncertainties in an additive manner. Overall, because this is not a precision measurement the conservative track uncertainty will be quoted but not included in the resulting distributions. Table 8.1 below summarizes the systematic uncertainties calculated for each measured point of the differential cross section as described in Section 7.2. Table 8.2 summarizes all the differential cross section measured points with statistical and systematic uncertainties, where all systematic uncertainties from Table 8.1 are combined in quadrature. Furthermore, the statistical uncertainties dominate the cross section overall uncertainties and could also be improved with more data from the Gluex-II experiment.

Table 8.1: Table of the point-by-point systematics of the differential cross section for the ${\tt GLUEX-I}$ data.

	1	Systematic Source (nb/GeV ²)			
$E_{\gamma} \text{ (GeV)}$	$-t (GeV^2)$	Run Combination	Accidentals	Yield Extraction	
	(0.10, 0.35)	0.000	0.170	0.051	
	(0.35, 0.53)	0.061	0.280	0.095	
	(0.53, 0.71)	0.000	0.236	0.169	
(6.40, 7.40)	(0.71, 0.92)	0.281	0.208	0.130	
	(0.92, 1.19)	0.133	0.146	0.003	
	(1.19, 1.53)	0.074	0.173	0.050	
	(1.53, 2.40)	0.100	0.125	0.064	
	(0.10, 0.35)	0.000	0.143	0.001	
	(0.35, 0.53)	0.000	0.256	0.047	
	(0.53, 0.71)	0.000	0.219	0.032	
(7.40, 7.86)	(0.71, 0.92)	0.125	0.117	0.135	
	(0.92, 1.19)	0.133	0.046	0.011	
	(1.19, 1.53)	0.000	0.098	0.036	
	(1.53, 2.40)	0.000	0.177	0.103	
	(0.10, 0.35)	0.000	0.203	0.098	
	(0.35, 0.53)	0.027	0.169	0.004	
	(0.53, 0.71)	0.000	0.173	0.073	
(7.86, 8.19)	(0.71, 0.92)	0.042	0.087	0.049	
	(0.92, 1.19)	0.377	0.069	0.027	
	(1.19, 1.53)	0.000	0.045	0.029	
	(1.53, 2.40)	0.000	0.024	0.006	
	(0.10, 0.35)	0.345	0.134	0.058	
	(0.35, 0.53)	0.000	0.160	0.129	
	(0.53, 0.71)	0.000	0.126	0.100	
(8.19, 8.45)	(0.71, 0.92)	0.000	0.113	0.020	
	(0.92, 1.19)	0.075	0.074	0.047	
	(1.19, 1.53)	0.067	0.129	0.103	
	(1.53, 2.40)	0.000	0.020	0.006	

Continued on next page

Table 8.1: Continued

		Systematic Source (nb/GeV ²)			
E_{γ} (GeV)	$-t (\text{GeV}^2)$	Run Combination	Accidentals	Yield Extraction	
	(0.10, 0.35)	0.000	0.171	0.004	
	(0.35, 0.53)	0.158	0.180	0.051	
	(0.53, 0.71)	0.000	0.143	0.248	
(8.45, 8.68)	(0.71, 0.92)	0.055	0.063	0.032	
	(0.92, 1.19)	0.000	0.089	0.027	
	(1.19, 1.53)	0.000	0.181	0.013	
	(1.53, 2.40)	0.000	0.057	0.008	
	(0.10, 0.35)	0.000	0.084	0.003	
	(0.35, 0.53)	0.000	0.117	0.093	
	(0.53, 0.71)	0.300	0.136	0.043	
(8.68, 9.26)	(0.71, 0.92)	0.000	0.098	0.019	
	(0.92, 1.19)	0.032	0.087	0.029	
	(1.19, 1.53)	0.087	0.038	0.000	
	(1.53, 2.40)	0.000	0.013	0.032	
	(0.10, 0.35)	0.000	0.144	0.060	
	(0.35, 0.53)	0.000	0.183	0.125	
	(0.53, 0.71)	0.000	0.046	0.074	
(9.26, 10.18)	(0.71, 0.92)	0.190	0.104	0.039	
	(0.92, 1.19)	0.000	0.050	0.020	
	(1.19, 1.53)	0.000	0.042	0.027	
	(1.53, 2.40)	0.025	0.028	0.010	
	(0.10, 0.35)	0.015	0.076	0.110	
(10.18, 11.40)	(0.35, 0.53)	0.000	0.067	0.048	
	(0.53, 0.71)	0.059	0.122	0.024	
	(0.71, 0.92)	0.000	0.063	0.026	
	(0.92, 1.19)	0.123	0.070	0.014	
	(1.19, 1.53)	0.063	0.028	0.009	
	(1.53, 2.40)	0.000	0.009	0.009	

Table 8.2: Table of the differential cross section for the GlueX-I data.

$E_{\gamma} \text{ (GeV)}$	$-t \text{ (GeV}^2)$	$d\sigma/dt \text{ (nb/GeV}^2$	$\delta y \ (stat)$	$\delta y \ (syst)$
	(0.10, 0.35)	4.460	0.405	0.177
	(0.35, 0.53)	6.382	0.477	0.302
	(0.53, 0.71)	6.276	0.461	0.290
(6.40, 7.40)	(0.71, 0.92)	3.457	0.332	0.374
	(0.92, 1.19)	2.894	0.295	0.198
	(1.19, 1.53)	3.228	0.412	0.194
	(1.53, 2.40)	1.233	0.313	0.172
	(0.10, 0.35)	3.899	0.380	0.143
	(0.35, 0.53)	6.304	0.477	0.260
	(0.53, 0.71)	5.974	0.480	0.221
(7.40, 7.86)	(0.71, 0.92)	4.339	0.386	0.218
	(0.92, 1.19)	3.187	0.294	0.141
	(1.19, 1.53)	2.450	0.247	0.104
	(1.53, 2.40)	0.556	0.118	0.205
	(0.10, 0.35)	5.136	0.426	0.226
	(0.35, 0.53)	6.314	0.458	0.171
	(0.53, 0.71)	4.811	0.365	0.188
(7.86, 8.19)	(0.71, 0.92)	3.210	0.304	0.109
	(0.92, 1.19)	2.511	0.219	0.384
	(1.19, 1.53)	1.521	0.163	0.053
	(1.53, 2.40)	0.694	0.097	0.025
(8.19, 8.45)	(0.10, 0.35)	3.380	0.319	0.375
	(0.35, 0.53)	5.917	0.460	0.206
	(0.53, 0.71)	4.502	0.341	0.161
	(0.71, 0.92)	3.822	0.317	0.115
	(0.92, 1.19)	3.043	0.247	0.115
	(1.19, 1.53)	1.590	0.164	0.178
	(1.53, 2.40)	0.525	0.077	0.020

Continued on next page

Table 8.2: Continued

E_{γ} (GeV)	$-t (\text{GeV}^2)$	$d\sigma/dt \text{ (nb/GeV}^2)$	$\delta y \ (stat)$	$\delta y \ (syst)$
	(0.10, 0.35)	4.638	0.380	0.171
	(0.35, 0.53)	4.538	0.369	0.245
	(0.53, 0.71)	5.200	0.373	0.287
(8.45, 8.68)	(0.71, 0.92)	3.854	0.283	0.090
	(0.92, 1.19)	2.857	0.228	0.093
	(1.19, 1.53)	1.468	0.154	0.182
	(1.53, 2.40)	0.411	0.061	0.058
	(0.10, 0.35)	3.232	0.325	0.084
	(0.35, 0.53)	4.397	0.321	0.149
	(0.53, 0.71)	4.192	0.302	0.332
(8.68, 9.26)	(0.71, 0.92)	3.202	0.239	0.100
	(0.92, 1.19)	2.399	0.190	0.097
	(1.19, 1.53)	1.768	0.159	0.095
	(1.53, 2.40)	0.437	0.056	0.034
	(0.10, 0.35)	3.882	0.319	0.156
	(0.35, 0.53)	4.257	0.302	0.221
	(0.53, 0.71)	3.801	0.313	0.087
(9.26, 10.18)	(0.71, 0.92)	3.151	0.231	0.220
	(0.92, 1.19)	2.190	0.180	0.054
	(1.19, 1.53)	1.391	0.123	0.049
	(1.53, 2.40)	0.547	0.051	0.039
	(0.10, 0.35)	3.152	0.281	0.135
(10.18, 11.40)	(0.35, 0.53)	3.392	0.250	0.082
	(0.53, 0.71)	3.311	0.237	0.137
	(0.71, 0.92)	2.852	0.215	0.068
	(0.92, 1.19)	1.898	0.154	0.142
	(1.19, 1.53)	1.042	0.098	0.069
	(1.53, 2.40)	0.364	0.039	0.013

8.2 Outlook

In this section, the future studies and experimental prospects for doubly strange hyperon spectroscopy at GlueX are briefly investigated.

8.2.1 Ξ Polarization Observables

As discussed in Section 2.4 the extraction of polarization observables is a powerful tool to elucidate the production mechanism of the Ξ hyperons. With current and future statistics for the $\Lambda \pi$ channel of the Ξ decay, extracting these will be possible at GLUEX energies for the first time. In this section, I will discuss the procedure for extracting the induced polarization for the ground state octet Ξ inspired by the previous CLAS work.

For single-(pseudoscalar) meson production the polarization observables can be written in a general way

$$\frac{\mathrm{d}\,\sigma}{\mathrm{d}\,\Omega} = \sigma_{\mathbf{0}} \left\{ 1 - \delta_{l}\,\mathbf{\Sigma}\cos 2\phi + \Lambda_{x} \left(-\delta_{l}\,\mathbf{H}\sin 2\phi + \delta_{\odot}\,\mathbf{F} \right) - \Lambda_{y} \left(-\mathbf{T} + \delta_{l}\,\mathbf{P}\cos 2\phi \right) - \Lambda_{z} \left(-\delta_{l}\,\mathbf{G}\sin 2\phi + \delta_{\odot}\,\mathbf{E} \right) \right\}, \tag{8.1}$$

where σ_0 is the unpolarized cross section, the bold symbols are the polarization observables, the δ_l , δ_{\odot} are the linear and circular degrees of photon polarization, respectively, the Λ_i are target polarization vectors, and ϕ is the angle from the photon polarization vector and the production plane [94]. For the GLUEX experiment, $\mathbf{T} = 0$ because the target is not polarized and $\mathbf{F} = \mathbf{E} = 0$ because the photon is not circularly polarized. The Σ is the beam asymmetry, and \mathbf{P} is the baryon recoil polarization and restricted to the y-axis due to parity conservation in the strong decay of the intermediate hyperon [95].

The photon beam asymmetry is related to the parallel and perpendicular component of the differential cross section,

$$\Sigma = \left[\frac{d\sigma_{\perp}}{dt} - \frac{d\sigma_{\parallel}}{dt} \right] / \left[\frac{d\sigma_{\perp}}{dt} + \frac{d\sigma_{\parallel}}{dt} \right], \tag{8.2}$$

where, the symbols \perp , \parallel stand for perpendicular and parallel to the floor with respect to the beam and t is defined by Eq. 5.1 [96]. We can also extract the recoil baryon polarization observable by taking advantage of the parity violating weak decay of the Ξ .

The recoil polarization of the Ξ is related to the forward-backward asymmetry of the decay pion in the rest frame of the Ξ [74],

$$A_y = \frac{N_y^+ - N_y^-}{N_y^+ + N_y^-} \tag{8.3}$$

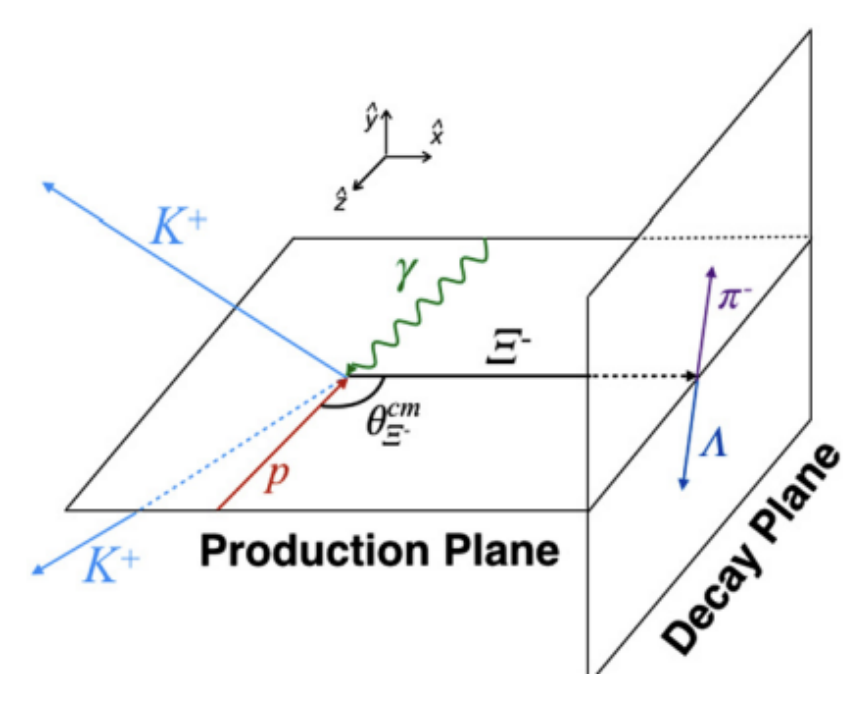


Figure 8.1: This figure is showing the axis orientation needed in order to calculate the polarization observables, where we are in the center of mass of the beam and target forming the production plane [74]

where N_y^{\pm} refers to the number of pions above or below the production plane, shown in Fig. 8.1. The relation for the recoil polarization is then written as,

$$\mathbf{P} = -\frac{2A_y}{\alpha} \tag{8.4}$$

where α is the Ξ^- weak-decay asymmetry or analyzing power with $\alpha = -0.458 \pm 0.012$ [97].

8.2.2 Excitation Spectrum with GlueX-II

The commissioning of the GLUEX-II experiment is an important step in the mission of studying hyperons. At the time of writing, the collection of GLUEX-II data is ongoing and more than half of the PAC days have been completed. The GLUEX-II experiment is now running at higher beam intensities, which will result in a quadrupling of the current data statistics. There is also improved particle identification, specifically of pions and kaons, with the addition of the DIRC (Detection of Internally Reflected Cherenkov light) detector. As discussed in Fig. 4.1, π/K separation is good up to 2 GeV with the timing information from the TOF for GLUEX-I. With the DIRC installed, the separation capabilities between the

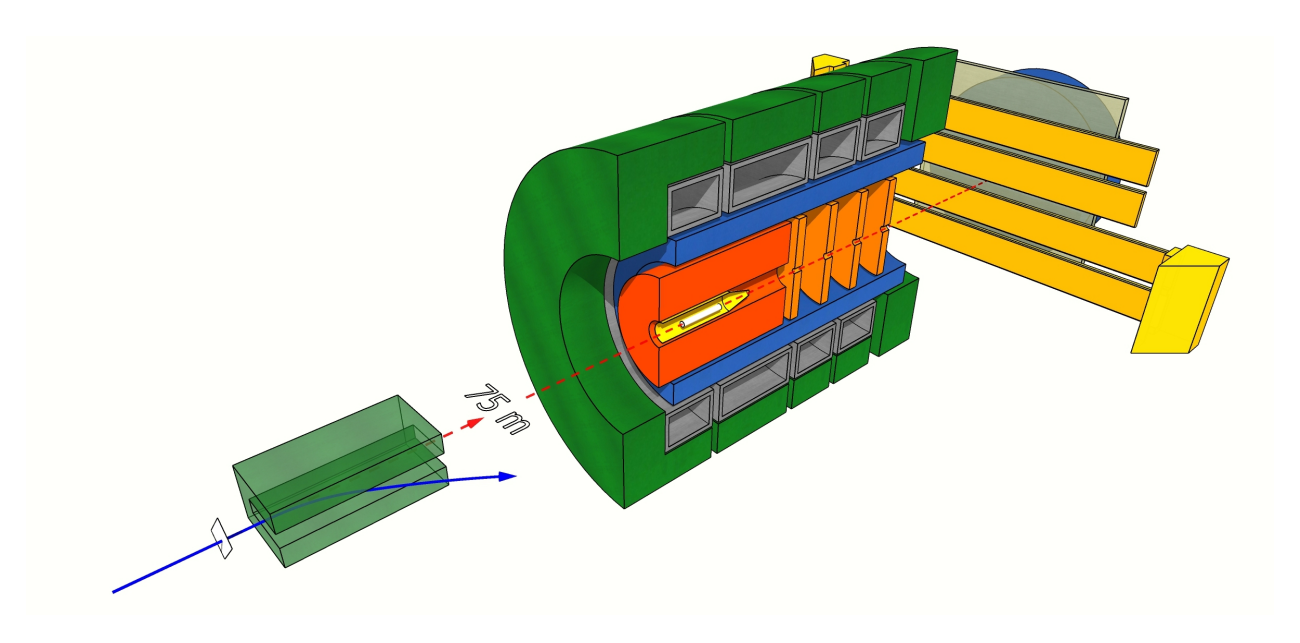


Figure 8.2: GlueX-II spectrometer with added DIRC detector showcasing four long horizontal bar boxes (cherekov radiators) and two photon cameras.

pions and kaons are increased up to 4 GeV. This is particularly important in search for higher mass Ξ excitations because the secondary decays of kaons that are essential to reconstruct begin to carry a greater proportion of momentum > 2 GeV, where they are more likely to lead to misidentification. This could be why there is a large combinatorial background in the spectrum of ΛK associated with these high-momentum secondary kaons, Section 6.4. Therefore, it becomes pivotal for the search of higher mass Ξ resonances to be able to discriminate between kaons and pions in this critical region between 2 and 4 GeV. Similarly, with the improved particle identification and much higher statistics, there is a much greater chance to observe the higher excitations in the spectrum.

DIRC Detector. The GLUEX PID upgrade is based on the DIRC principle first presented for the identification of charged particles at e^+e^- B factories [98]. Charged particles emit Cherenkov light in a cone around the trajectory of the particle when traveling in the radiator, e.g., quartz or fused silica bar box. The Cherenkov light trapped inside the radiator undergoes internal reflection traveling down the bar box and recorded by a photon camera, where it is imaged on a pixilated photodetection plane. The angular properties of the internal reflection inside the bar box are preserved and related to the velocity of the

charged particle. This information is extracted from the hit pattern of the imaging in the photon camera of the Cherenkov light with the given momentum vector information that is reconstructed using the drift chambers. The DIRC detector at GLUEX-II is placed downstream of the TOF detector, 4 meters from the target center, and covers the forward region with polar angle coverage from 2° to 11°. It uses four BaBar DIRC bar boxes (unmodified); each pair of boxes is attached to a newly designed photon camera inspired by the SuperB FDIRC prototype [99]. Figure 8.2 shows the schematic view of the GLUEX-II spectrometer with the added DIRC detector in the forward direction showing the long rectangular bar boxes attached to the photon camera on either side.

8.2.3 K_L Facility at GlueX

The K_L Facility (KLF) PAC48 proposal was accepted for 100 days of running in 2020. Since then, the construction of the sub-detector systems, software development for event reconstruction and Monte Carlo studies have been conducted and are ongoing. The KLF will use the CEBAF 12 GeV electron beam to produce a high-intensity photon beam and convert it to a kaon beam in the process $\gamma p \to p\phi$. The high-intensity photon beam will produce a kaon flux on the order of $\sim 1 \times 10^4 K_L/s$ which far exceeds any previous kaon experiments discussed in Section 2.1 by three times. The resulting beam will be incident on a cryogenic liguid hydrogen/deuterium target to study two body and quasi-two body reactions in $K_L N$ decays to nucleons and hyprons with strangeness -1 and strangeness -2. The beamline schematic of the experiment is shown in Fig. 8.3.

For a sufficient kaon flux, the photon beam for KLF has to be produced at much higher beam intensities that is currently used at GLUEX ($\sim 5 \times 10^7 \, \gamma/s$). For this, the Compact Photon Source (CPS) was developed to produce photon beam intensities of $4.7 \times 10^{12} \, \gamma/s$. The CPS in the schematic of the beamline is upstream of the spectrometer and functions as an independent fully shielded photon production source. The photon beam is produced when the electron beam is incident on a copper absorber and the remaining electrons are curved to an electron dump by a dipole magnet shown in Fig. 8.4 (left). The Kaon Production Target (KPT) Fig. 8.4 (right) has also been developed to produce the high-intensity kaon beams by having the photon beam incident on a beryllium target which is also shielded to reduce

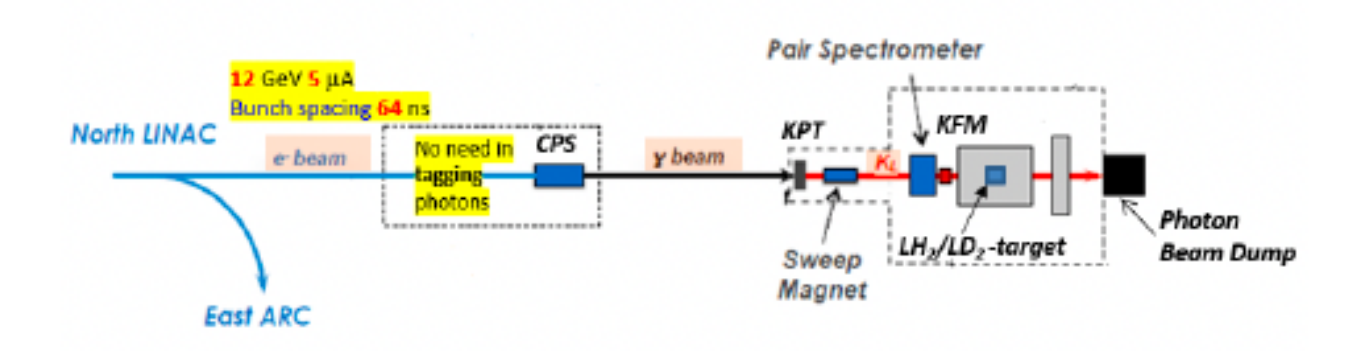


Figure 8.3: The annotated proposed beamline for the K_L facility of the GLUEX experiment.

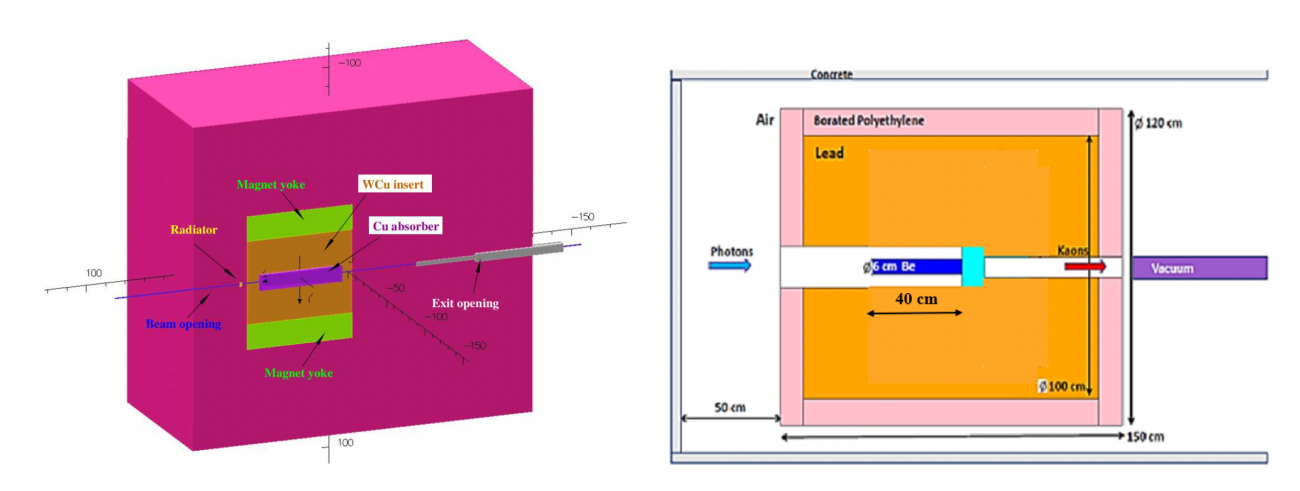


Figure 8.4: (Left) The schematic of the CPS detector and (Right) the schematic of the KPT used in the production of the photon and secondary kaon beam for the K_L experiment.

gamma and neutron radiation rates at production. With the commissioning and running of the KLF at Jefferson Lab the prospects for studying hyperons with strangeness -1 and strangeness -2 are extremely promising.

REFERENCES

- [1] James Clerk Maxwell. "VIII. A dynamical theory of the electromagnetic field". In: *Phil. Trans. R. Soc.* 155 (Jan. 1865), pp. 459–512. DOI: 10.1098/rstl.1865.0008. URL: https://royalsocietypublishing.org/doi/10.1098/rstl.1865.0008.
- [2] Albert Einstein. "On the Electrodynamics of Moving Bodies". In: Ann. Phys. 17 (Jan. 1905), pp. 891–921. DOI: 10.1002/andp.19053221004. URL: https://doi.org/10.1002/andp.19053221004.
- [3] Max Planck. "On the Law of the Energy Distribution in the Normal Spectrum". In: Ann. Phys. 4 (Jan. 1901), pp. 553-562. DOI: 10.1002/andp.19013090310. URL: https://doi.org/10.1002/andp.19013090310.
- [4] Steven Weinberg. "The Search for Unity: Notes for a History of Quantum Field Theory". In: Daedalus 106.4 (1977), pp. 17–35. ISSN: 00115266. URL: http://www.jstor.org/stable/20024506 (visited on 06/10/2025).
- [5] Paul Adrien Maurice Dirac. "The quantum theory of the emission and absorption of radiation". In: *Proc. R. Soc. Lond. A* 114 (Mar. 1927), pp. 243–265. DOI: 10.1098/rspa.1927.0039. URL: https://royalsocietypublishing.org/doi/10.1098/rspa.1927.0039.
- [6] J. R. Oppenheimer. "Note on the Theory of the Interaction of Field and Matter". In: *Phys. Rev.* 35 (5 Mar. 1930), pp. 461-477. DOI: 10.1103/PhysRev.35.461. URL: https://link.aps.org/doi/10.1103/PhysRev.35.461.
- [7] H. A. Bethe. "The Electromagnetic Shift of Energy Levels". In: Phys. Rev. 72 (4 July 1947), pp. 339–341. DOI: 10.1103/PhysRev.72.339. URL: https://link.aps.org/doi/10.1103/PhysRev.72.339.
- [8] C. N. Yang and R. L. Mills. "Conservation of Isotopic Spin and Isotopic Gauge Invariance". In: *Phys. Rev.* 96 (1 Oct. 1954), pp. 191–195. DOI: 10.1103/PhysRev.96.191. URL: https://link.aps.org/doi/10.1103/PhysRev.96.191.
- [9] Peter W. Higgs. "Broken Symmetries and the Masses of Gauge Bosons". In: *Phys. Rev. Lett.* 13 (16 Oct. 1964), pp. 508-509. DOI: 10.1103/PhysRevLett.13.508. URL: https://link.aps.org/doi/10.1103/PhysRevLett.13.508.

- [10] G. 't Hooft and M. Veltman. "Regularization and renormalization of gauge fields". In: Nuclear Physics B 44.1 (1972), pp. 189-213. ISSN: 0550-3213. DOI: https://doi.org/10.1016/0550-3213(72)90279-9. URL: https://www.sciencedirect.com/science/article/pii/0550321372902799.
- [11] Gerard't Hooft. "The Evolution of Quantum Field Theory: From <italic>QED</italic> to Grand Unification". In: *The Standard Theory of Particle Physics*. Chap. Chapter 1, pp. 1–27. DOI: 10.1142/9789814733519_0001. URL: https://www.worldscientific.com/doi/abs/10.1142/9789814733519_0001.
- [12] C. S. Wu et al. "Experimental Test of Parity Conservation in Beta Decay". In: *Phys. Rev.* 105 (4 Feb. 1957), pp. 1413–1415. DOI: 10.1103/PhysRev.105.1413. URL: https://link.aps.org/doi/10.1103/PhysRev.105.1413.
- [13] T. D. Lee and C. N. Yang. "Question of Parity Conservation in Weak Interactions". In: *Phys. Rev.* 104 (1 Oct. 1956), pp. 254–258. DOI: 10.1103/PhysRev.104.254. URL: https://link.aps.org/doi/10.1103/PhysRev.104.254.
- [14] A. Salam and J.C. Ward. "Electromagnetic and weak interactions". In: *Physics Letters* 13.2 (1964), pp. 168-171. ISSN: 0031-9163. DOI: https://doi.org/10.1016/0031-9163(64)90711-5. URL: https://www.sciencedirect.com/science/article/pii/0031916364907115.
- [15] Steven Weinberg. "A Model of Leptons". In: Phys. Rev. Lett. 19 (21 Nov. 1967), pp. 1264-1266. DOI: 10.1103/PhysRevLett.19.1264. URL: https://link.aps. org/doi/10.1103/PhysRevLett.19.1264.
- [16] M. Gell-Mann. "Isotopic Spin and New Unstable Particles". In: Phys. Rev. 92 (3 Nov. 1953), pp. 833–834. DOI: 10.1103/PhysRev.92.833. URL: https://link.aps.org/doi/10.1103/PhysRev.92.833.
- [17] Murray Gell-Mann. The Eightfold Way: A Theory Of Strong Interacting Symmetry. Tech. rep. California Institute of Technology, 1961. URL: https://www.osti.gov/servlets/purl/4008239/.
- [18] M. Gell-Mann. "A schematic model of baryons and mesons". In: *Physics Letters* 8.3 (1964), pp. 214–215. ISSN: 0031-9163. DOI: https://doi.org/10.1016/S0031-9163(64)92001-3. URL: https://www.sciencedirect.com/science/article/pii/S0031916364920013.
- [19] M. Y. Han and Y. Nambu. "Three-Triplet Model with Double SU(3) Symmetry". In: Phys. Rev. 139 (4B July 1965), B1006-B1010. DOI: 10.1103/PhysRev.139.B1006. URL: https://link.aps.org/doi/10.1103/PhysRev.139.B1006.

- [20] H. Fritzsch, M. Gell-Mann, and H. Leutwyler. "Advantages of the color octet gluon picture". In: *Physics Letters B* 47.4 (1973), pp. 365–368. ISSN: 0370-2693. DOI: https://doi.org/10.1016/0370-2693(73)90625-4. URL: https://www.sciencedirect.com/science/article/pii/0370269373906254.
- [21] David J. Gross and Frank Wilczek. "Ultraviolet Behavior of Non-Abelian Gauge Theories". In: *Phys. Rev. Lett.* 30 (26 June 1973), pp. 1343–1346. DOI: 10.1103/PhysRevLett. 30.1343. URL: https://link.aps.org/doi/10.1103/PhysRevLett.30.1343.
- [22] H. David Politzer. "Reliable Perturbative Results for Strong Interactions?" In: *Phys. Rev. Lett.* 30 (26 June 1973), pp. 1346–1349. DOI: 10.1103/PhysRevLett.30.1346. URL: https://link.aps.org/doi/10.1103/PhysRevLett.30.1346.
- [23] Richard P. Feynman. "Very High-Energy Collisions of Hadrons". In: *Phys. Rev. Lett.* 23 (24 Dec. 1969), pp. 1415–1417. DOI: 10.1103/PhysRevLett.23.1415. URL: https://link.aps.org/doi/10.1103/PhysRevLett.23.1415.
- [24] Particle Data Group et al. "Review of Particle Physics". In: Progress of Theoretical and Experimental Physics 2020.8 (Aug. 2020), p. 083C01. ISSN: 2050-3911. DOI: 10. 1093/ptep/ptaa104. eprint: https://academic.oup.com/ptep/article-pdf/2020/8/083C01/34673725/rpp2020-vol1-29-134_3.pdf. URL: https://doi.org/10.1093/ptep/ptaa104.
- [25] Y. Nambu and G. Jona-Lasinio. "Dynamical Model of Elementary Particles Based on an Analogy with Superconductivity. II". In: *Phys. Rev.* 124 (1 Oct. 1961), pp. 246—254. DOI: 10.1103/PhysRev.124.246. URL: https://link.aps.org/doi/10.1103/PhysRev.124.246.
- [26] S. Capstick and W. Roberts. "Quark models of baryon masses and decays". In: *Progress in Particle and Nuclear Physics* 45 (2000), S241–S331. ISSN: 0146-6410. DOI: https://doi.org/10.1016/S0146-6410(00)00109-5. URL: https://www.sciencedirect.com/science/article/pii/S0146641000001095.
- [27] Kenneth G. Wilson. "Confinement of quarks". In: Phys. Rev. D 10 (8 Oct. 1974), pp. 2445-2459. DOI: 10.1103/PhysRevD.10.2445. URL: https://link.aps.org/doi/10.1103/PhysRevD.10.2445.
- [28] Franz Gross et al. "50 Years of quantum chromodynamics". In: *The European Physical Journal C* 83.12 (2023), p. 1125. DOI: 10.1140/epjc/s10052-023-11949-2. URL: https://doi.org/10.1140/epjc/s10052-023-11949-2.
- [29] Robert G. Edwards et al. "Flavor structure of the excited baryon spectra from lattice QCD". In: *Phys. Rev. D* 87 (5 Mar. 2013), p. 054506. DOI: 10.1103/PhysRevD.87.054506. URL: https://link.aps.org/doi/10.1103/PhysRevD.87.054506.

- [30] S. Navas et al. "Review of Particle Physics". In: Phys. Rev. D 110 (3 Aug. 2024), p. 030001. DOI: 10.1103/PhysRevD.110.030001. URL: https://link.aps.org/doi/ 10.1103/PhysRevD.110.030001.
- [31] Bernard Aubert et al. "Measurement of the Spin of the Xi(1530) Resonance". In: *Phys. Rev. D* 78 (2008), p. 034008. DOI: 10.1103/PhysRevD.78.034008. arXiv: 0803.1863 [hep-ex].
- [32] S. F. Biagi et al. "Xi* Resonances in Xi- Be Interactions. 2. Properties of Xi (1820) and Xi (1960) in the Lambda anti-K0 and Sigma-0 anti-K0 Channels". In: *Z. Phys. C* 34 (1987), p. 175. DOI: 10.1007/BF01566758.
- [33] Volker Crede and John Yelton. "70 years of hyperon spectroscopy: a review of strange Ξ, Ω baryons, and the spectrum of charmed and bottom baryons". In: *Reports on Progress in Physics* 87.10 (Sept. 2024), p. 106301. DOI: 10.1088/1361-6633/ad7610. URL: https://dx.doi.org/10.1088/1361-6633/ad7610.
- [34] K. Nakayama, Yongseok Oh, and H. Haberzettl. "Photoproduction of Ξ off nucleons". In: *Phys. Rev. C* 74 (3 Sept. 2006), p. 035205. DOI: 10.1103/PhysRevC.74.035205. URL: https://link.aps.org/doi/10.1103/PhysRevC.74.035205.
- [35] J. Ka Shing Man, Yongseok Oh, and K. Nakayama. "Role of high-spin hyperon resonances in the reaction of $\gamma p \to K^+K^+\Xi^-$ ". In: *Phys. Rev. C* 83 (5 May 2011), p. 055201. DOI: 10.1103/PhysRevC.83.055201. URL: https://link.aps.org/doi/10.1103/PhysRevC.83.055201.
- [36] S. L. Glashow, J. Iliopoulos, and L. Maiani. "Weak Interactions with Lepton-Hadron Symmetry". In: *Phys. Rev. D* 2 (7 Oct. 1970), pp. 1285–1292. DOI: 10.1103/PhysRevD. 2.1285. URL: https://link.aps.org/doi/10.1103/PhysRevD.2.1285.
- [37] Donald A. Glaser. "Some Effects of Ionizing Radiation on the Formation of Bubbles in Liquids". In: *Phys. Rev.* 87 (4 Aug. 1952), pp. 665–665. DOI: 10.1103/PhysRev.87.665. URL: https://link.aps.org/doi/10.1103/PhysRev.87.665.
- [38] J. Peter Berge et al. "Some Properties of Ξ^- and Ξ^0 Hyperons Produced in K^-p Interactions between 1.05 and 1.7 BeV/c". In: *Phys. Rev.* 147 (4 July 1966), pp. 945–961. DOI: 10.1103/PhysRev.147.945. URL: https://link.aps.org/doi/10.1103/PhysRev.147.945.
- [39] Gerald A. Smith et al. "Study of S=-2 Baryon Systems up to 2 BeV". In: *Phys. Rev. Lett.* 13 (2 July 1964), pp. 61-66. DOI: 10.1103/PhysRevLett.13.61. URL: https://link.aps.org/doi/10.1103/PhysRevLett.13.61.

- [40] Gerald A. Smith et al. "Production and Decay of \(\pi^*(1820)\)". In: *Phys. Rev. Lett.* 14 (1 Jan. 1965), pp. 25–28. DOI: 10.1103/PhysRevLett.14.25. URL: https://link.aps.org/doi/10.1103/PhysRevLett.14.25.
- [41] J. Badier et al. "Baryonic states of strangeness -2 produced in K-p interactions at 3.0 GeV/c". In: *Physics Letters* 16.2 (1965), pp. 171-174. ISSN: 0031-9163. DOI: https://doi.org/10.1016/0031-9163(65)90173-3. URL: https://www.sciencedirect.com/science/article/pii/0031916365901733.
- [42] J. Alitti et al. "Evidence for Ξ^* Resonance with Mass 1930 MeV". In: *Phys. Rev. Lett.* 21 (15 Oct. 1968), pp. 1119–1123. DOI: 10.1103/PhysRevLett.21.1119. URL: https://link.aps.org/doi/10.1103/PhysRevLett.21.1119.
- [43] J. Alitti et al. "Strangeness S=-2 Baryon Resonance". In: *Phys. Rev. Lett.* 22 (2 Jan. 1969), pp. 79–82. DOI: 10.1103/PhysRevLett.22.79. URL: https://link.aps.org/doi/10.1103/PhysRevLett.22.79.
- [44] S. Apsell et al. " Ξ Resonances in $K^-p \to \Xi \pi K$ AT 2.87 GeV/c". In: *Phys. Rev. Lett.* 23 (15 Oct. 1969), pp. 884-886. DOI: 10.1103/PhysRevLett.23.884. URL: https://link.aps.org/doi/10.1103/PhysRevLett.23.884.
- [45] E. Briefel et al. "Search for Ξ^* production in K^-p interactions at 2.87 GeV/c". In: *Phys. Rev. D* 16 (9 Nov. 1977), pp. 2706–2726. DOI: 10.1103/PhysRevD.16.2706. URL: https://link.aps.org/doi/10.1103/PhysRevD.16.2706.
- [46] C. M. Jenkins et al. "Existence of Ξ Resonances above 2 GeV". In: *Phys. Rev. Lett.* 51 (11 Sept. 1983), pp. 951–954. DOI: 10.1103/PhysRevLett.51.951. URL: https://link.aps.org/doi/10.1103/PhysRevLett.51.951.
- [47] E. L. Goldwasser and P. F. Schultz. "Ξ- Production in 5.5-GeV/c K-p Interactions". In: *Phys. Rev. D* 1 (7 Apr. 1970), pp. 1960–1966. DOI: 10.1103/PhysRevD.1.1960. URL: https://link.aps.org/doi/10.1103/PhysRevD.1.1960.
- [48] J. Bartsch et al. "Evidence for a new Ξ resonance at 2500 MeV in 10 GeV/c K-p interactions". In: *Physics Letters B* 28.6 (1969), pp. 439–442. ISSN: 0370-2693. DOI: https://doi.org/10.1016/0370-2693(69)90346-3. URL: https://www.sciencedirect.com/science/article/pii/0370269369903463.
- [49] R.T. Ross et al. " $\Xi\pi$ Resonance with mass 1606 MeV/c2". In: *Physics Letters B* 38.3 (1972), pp. 177–180. ISSN: 0370-2693. DOI: https://doi.org/10.1016/0370-2693(72)90043-3. URL: https://www.sciencedirect.com/science/article/pii/0370269372900433.

- [50] C. Dionisi et al. "An enhancement at the ΣK threshold (1680) MeV observed in K^-p reactions at 4.2 GeV/c". In: *Physics Letters B* 80.1 (1978), pp. 145–149. ISSN: 0370–2693. DOI: https://doi.org/10.1016/0370-2693(78)90329-5. URL: https://www.sciencedirect.com/science/article/pii/0370269378903295.
- [51] D Aston et al. The LASS (Larger Aperture Superconducting Solenoid) spectrometer. Tech. rep. SLAC National Accelerator Lab., Menlo Park, CA (United States), Apr. 1986. DOI: 10.2172/6160488. URL: https://www.osti.gov/biblio/6160488.
- [52] D. Aston et al. "Inclusive production of multistrange hyperons from 11-GeV/c K^- p interactions". In: *Phys. Rev. D* 32 (9 Nov. 1985), pp. 2270–2287. DOI: 10.1103/PhysRevD.32.2270. URL: https://link.aps.org/doi/10.1103/PhysRevD.32.2270.
- [53] S. F. Biagi et al. " Ξ * resonances in Ξ -be interactions". In: Zeitschrift für Physik C Particles and Fields 34.1 (1987), pp. 15–22. DOI: 10.1007/BF01561109. URL: https://doi.org/10.1007/BF01561109.
- [54] M. Bourquin and J.-P. Repellin. "Experiments with the CERN SPS hyperon beam". In: *Physics Reports* 114.2 (1984), pp. 99–180. ISSN: 0370-1573. DOI: https://doi.org/10.1016/0370-1573(84)90041-3. URL: https://www.sciencedirect.com/science/article/pii/0370157384900413.
- [55] Yu.A Alexandrov et al. "The high-intensity hyperon beam at CERN". In: Nuclear Instruments and Methods in Physics Research Section A: Accelerators, Spectrometers, Detectors and Associated Equipment 408.2 (1998), pp. 359-372. ISSN: 0168-9002. DOI: https://doi.org/10.1016/S0168-9002(98)00228-9. URL: https://www.sciencedirect.com/science/article/pii/S0168900298002289.
- [56] S. F. Biagi et al. "Production of hyperons and hyperon resonances in Ξ⁻N interactions at 102 and 135 GeV/c*". In: Zeitschrift für Physik C Particles and Fields 9.4 (1981), pp. 305–314. DOI: 10.1007/BF01548765. URL: https://doi.org/10.1007/BF01548765.
- [57] S. F. Biagi et al. " Ξ^* Resonances in Ξ^- Be interactions II. Properties of $\Xi(1820)$ and $\Xi(1960)$ in the $\Lambda \overline{K}^0$ and $\Sigma^0 \overline{K}^0$ channels". In: Zeitschrift für Physik C Particles and Fields 34.2 (1987), pp. 175–185. DOI: 10.1007/BF01566758. URL: https://doi.org/10.1007/BF01566758.
- [58] M. I. Adamovich et al. and WA89 Collaboration. "First observation of the $\Xi^-\pi^+$ decay mode of the $\Xi^0(1690)$ hyperon". In: The European Physical Journal C Particles and Fields 5.4 (1998), pp. 621–624. DOI: 10.1007/s100529800902. URL: https://doi.org/10.1007/s100529800902.

- [59] J Lach L Stutte. "A Proposal To Construct-SELEX-Segmented Large-x Baryon Spectrometer". In: (1987).
- [60] S. Kurokawa and E. Kikutani. "Overview of the KEKB accelerators". In: Nuclear Instruments and Methods in Physics Research Section A: Accelerators, Spectrometers, Detectors and Associated Equipment 499.1 (2003). KEK-B: The KEK B-factory, pp. 1-7. ISSN: 0168-9002. DOI: https://doi.org/10.1016/S0168-9002(02)01771-0. URL: https://www.sciencedirect.com/science/article/pii/S0168900202017710.
- [61] A. Abashian et al. "The Belle detector". In: Nuclear Instruments and Methods in Physics Research Section A: Accelerators, Spectrometers, Detectors and Associated Equipment 479.1 (2002). Detectors for Asymmetric B-factories, pp. 117-232. ISSN: 0168-9002. DOI: https://doi.org/10.1016/S0168-9002(01)02013-7. URL: https://www.sciencedirect.com/science/article/pii/S0168900201020137.
- [62] K. Abe et al. "Observation of Cabibbo-suppressed and W-exchange Λ_c^+ baryon decays". In: *Physics Letters B* 524.1 (2002), pp. 33-43. ISSN: 0370-2693. DOI: https://doi.org/10.1016/S0370-2693(01)01373-9. URL: https://www.sciencedirect.com/science/article/pii/S0370269301013739.
- [63] M. Sumihama et al. "Observation of $\Xi(1620)^0$ and Evidence for $\Xi(1690)^0$ in $\Xi_c^+ \to \Xi^-\pi^+\pi^+$ Decays". In: *Phys. Rev. Lett.* 122 (7 Feb. 2019), p. 072501. DOI: 10.1103/PhysRevLett.122.072501. URL: https://link.aps.org/doi/10.1103/PhysRevLett.122.072501.
- [64] The BABAR Collaboration and B. Aubert. Measurement of the Mass and Width and Study of the Spin of the $\Xi(1690)^0$ Resonance from $\Lambda_c^+ \to \Lambda \overline{K}^0 K^+$ Decay at Babar. 2006. arXiv: hep-ex/0607043 [hep-ex]. URL: https://arxiv.org/abs/hep-ex/0607043.
- [65] B. Aubert et al. "Measurement of the spin of the Ξ(1530) resonance". In: *Phys. Rev.* D 78 (3 Aug. 2008), p. 034008. DOI: 10.1103/PhysRevD.78.034008. URL: https://link.aps.org/doi/10.1103/PhysRevD.78.034008.
- [66] M. Ablikim et al. "Design and construction of the BESIII detector". In: Nuclear Instruments and Methods in Physics Research Section A: Accelerators, Spectrometers, Detectors and Associated Equipment 614.3 (2010), pp. 345-399. ISSN: 0168-9002. DOI: https://doi.org/10.1016/j.nima.2009.12.050. URL: https://www.sciencedirect.com/science/article/pii/S0168900209023870.
- [67] M. Ablikim et al. "Measurement of the Cross Section for $e^+e^- \to \Xi^-\overline{\Xi}^+$ and Observation of an Excited Ξ Baryon". In: *Phys. Rev. Lett.* 124 (3 Jan. 2020), p. 032002. DOI: 10.1103/PhysRevLett.124.032002. URL: https://link.aps.org/doi/10.1103/PhysRevLett.124.032002.

- [68] M. Ablikim et al. "Study of excited Ξ states in $\psi(3686) \to K^-\Lambda \overline{\Xi}^+ + \text{c.c.}$ ". In: *Phys. Rev. D* 109 (7 Apr. 2024), p. 072008. DOI: 10.1103/PhysRevD.109.072008. URL: https://link.aps.org/doi/10.1103/PhysRevD.109.072008.
- [69] "Evidence of a $J/\psi\Lambda$ structure and observation of excited Ξ^- states in the $\Xi_b^+ \to J/\psi\Lambda K^-$ decay". In: Science Bulletin 66.13 (2021), pp. 1278–1287. ISSN: 2095-9273. DOI: https://doi.org/10.1016/j.scib.2021.02.030. URL: https://www.sciencedirect.com/science/article/pii/S2095927321001717.
- [70] B.A. Mecking et al. "The CEBAF large acceptance spectrometer". In: Nuclear Instruments and Methods in Physics Research Section A 503.3 (2003), pp. 513-553. ISSN: 0168-9002. DOI: https://doi.org/10.1016/S0168-9002(03)01001-5. URL: https://www.sciencedirect.com/science/article/pii/S0168900203010015.
- [71] J. W. Price et al. "Exclusive photoproduction of the cascade (Ξ) hyperons". In: *Phys. Rev. C* 71 (5 May 2005), p. 058201. DOI: 10.1103/PhysRevC.71.058201. URL: https://link.aps.org/doi/10.1103/PhysRevC.71.058201.
- [72] L. Guo et al. "Cascade production in the reactions $\gamma p \to K^+K^+(X)$ and $\gamma p \to K^+K^+\pi^-(X)$ ". In: *Phys. Rev. C* 76 (2 July 2007), p. 025208. DOI: 10.1103/PhysRevC. 76.025208. URL: https://link.aps.org/doi/10.1103/PhysRevC.76.025208.
- [73] " Ξ^* photoproduction from threshold to $W=3.3~{\rm GeV}$ ". In: *Phys. Rev. C* 98 (6 Dec. 2018), p. 062201. DOI: 10.1103/PhysRevC.98.062201. URL: https://link.aps.org/doi/10.1103/PhysRevC.98.062201.
- [74] J. Bono et al. "First measurement of Ξ⁻ polarization in photoproduction". In: Physics Letters B 783 (2018), pp. 280-286. ISSN: 0370-2693. DOI: https://doi.org/10. 1016/j.physletb.2018.07.004. URL: https://www.sciencedirect.com/science/article/pii/S0370269318305392.
- [75] S. Adhikari et al. "The GlueX beamline and detector". In: Nuclear Instruments and Methods in Physics Research Section A: Accelerators, Spectrometers, Detectors and Associated Equipment 987 (2021), p. 164807. ISSN: 0168-9002. DOI: https://doi.org/10.1016/j.nima.2020.164807. URL: https://www.sciencedirect.com/science/article/pii/S0168900220312043.
- [76] Paul Mattione. Least Squares Kinematic Fitting of Physics Reactions. 2016. URL: https://halldweb.jlab.org/DocDB/0021/002112/005/KinematicFitting.pdf (visited on 06/2025).
- [77] Jefferson Lab. JANA. 2024. URL: https://github.com/JeffersonLab/JANA.

- [78] M Williams, M Bellis, and C A Meyer. "Multivariate side-band subtraction using probabilistic event weights". In: Journal of Instrumentation 4.10 (Oct. 2009), P10003. DOI: 10.1088/1748-0221/4/10/P10003. URL: https://dx.doi.org/10.1088/1748-0221/4/10/P10003.
- [79] D. Kirkby W. Verkerke. RooFit Users Manual v2.91. Version 2.91-33. 2008.
- [80] N. L. Johnson. "Systems of Frequency Curves Generated by Methods of Translation". In: *Biometrika* 36.1/2 (1949), pp. 149–176. ISSN: 00063444, 14643510. URL: http://www.jstor.org/stable/2332539 (visited on 07/06/2025).
- [81] J. Allison et al. "Recent developments in Geant4". In: Nuclear Instruments and Methods in Physics Research Section A: Accelerators, Spectrometers, Detectors and Associated Equipment 835 (2016), pp. 186–225. ISSN: 0168-9002. DOI: https://doi.org/10.1016/j.nima.2016.06.125. URL: https://www.sciencedirect.com/science/article/pii/S0168900216306957.
- [82] GlueX Collaboration. Gen Amp V2. 2024. URL: https://github.com/JeffersonLab/halld_sim/tree/master/src/programs/Simulation/gen_amp_V2.
- [83] GlueX Collaboration. Genr8. 2010. URL: https://github.com/JeffersonLab/halld_sim/tree/master/src/programs/Simulation/genr8.
- [84] GlueX Collaboration. Amp Tools. 2023. URL: https://github.com/mashephe/AmpTools.
- [85] Curtis A. Meyer. *Coordinate Systems in GlueX*. 2021. URL: https://halldweb.jlab.org/DocDB/0048/004829/005/coordinates.pdf.
- [86] M. Tanabashi et al. "Review of Particle Physics". In: Phys. Rev. D 98 (3 July 2018), p. 030001. DOI: 10.1103/PhysRevD.98.030001. URL: https://link.aps.org/doi/ 10.1103/PhysRevD.98.030001.
- [87] B. Aubert et al. "Measurement of the Spin of the Ω⁻ Hyperon". In: *Phys. Rev. Lett.* 97 (11 Sept. 2006), p. 112001. DOI: 10.1103/PhysRevLett.97.112001. URL: https://link.aps.org/doi/10.1103/PhysRevLett.97.112001.
- [88] B. Aubert et al. "Measurement of the spin of the \(\pi(1530)\) resonance". In: Phys. Rev. D 78 (3 July 2008), p. 034008. DOI: 10.1103/PhysRevD.78.034008. URL: https://link.aps.org/doi/10.1103/PhysRevD.78.034008.
- [89] J. Abdallah et al. "Masses, lifetimes and production rates of Ξ⁻ and Ξ̄ at LEP 1". In: Physics Letters B 639.3 (2006), pp. 179-191. ISSN: 0370-2693. DOI: https://doi.org/10.1016/j.physletb.2006.06.029. URL: https://www.sciencedirect.com/science/article/pii/S0370269306007659.

- [90] Hai-Peng Li et al. "Theoretical interpretation of the \$\$\Xi (1620)\$\$ and \$\$\Xi (1690)\$\$ resonances seen in \$\$\Xi _c^+ \rightarrow \Xi ^- \pi ^+ \pi ^+\$\$ decay". In: The European Physical Journal C 83.10 (2023), p. 954. DOI: 10.1140/epjc/s10052-023-12131-4. URL: https://doi.org/10.1140/epjc/s10052-023-12131-4.
- [91] Man-Yu Duan et al. "On the search for the two poles of the \$\Xi (1820)\\$in the \$\psi (3686) \rightarrow \bar{\Xi}^+ \bar{K}^0 \Sigma ^{*-}(\pi ^- \Lambda)\\$decay". In: The European Physical Journal C 84.9 (Sept. 2024), p. 947. DOI: 10. 1140/epjc/s10052-024-13293-5. URL: https://doi.org/10.1140/epjc/s10052-024-13293-5.
- [92] Nilanga Wickramaarachchi, Reinhard A. Schumacher, and Grzegorz Kalicy. "Decay of the Λ(1405) hyperon to Σ⁰π⁰ measured at GlueX". In: vol. 271. Thomas Jefferson National Accelerator Facility (TJNAF), Newport News, VA (United States). EDP Sciences, Nov. 2022. DOI: 10.1051/epjconf/202227107005. URL: https://www.osti.gov/biblio/1972817.
- [93] Roger Barlow. Systematic Errors: facts and fictions. 2002. arXiv: hep-ex/0207026 [hep-ex]. URL: https://arxiv.org/abs/hep-ex/0207026.
- [94] V. Crede and W. Roberts. "Progress towards understanding baryon resonances". In: Rept. Prog. Phys. 76 (2013), p. 076301. DOI: 10.1088/0034-4885/76/7/076301. arXiv: 1302.7299 [nucl-ex].
- [95] A M Sandorfi et al. "Determining pseudoscalar meson photoproduction amplitudes from complete experiments". In: Journal of Physics G: Nuclear and Particle Physics 38.5 (Apr. 2011), p. 053001. DOI: 10.1088/0954-3899/38/5/053001. URL: https://doi.org/10.1088/0954-3899/38/5/053001.
- [96] S. Adhikari et al. "Measurement of the photon beam asymmetry in $\gamma p \to K^+ \Sigma^0$ at $E_{\gamma}=8.5$ GeV". In: *Phys. Rev. C* 101 (6 June 2020), p. 065206. DOI: 10.1103/PhysRevC.101.065206. URL: https://link.aps.org/doi/10.1103/PhysRevC.101.065206.
- [97] M. Huang et al. "New Measurement of $\Xi^- \to \Lambda \pi^-$ Decay Parameters". In: *Phys. Rev. Lett.* 93 (1 June 2004), p. 011802. DOI: 10.1103/PhysRevLett.93.011802. URL: https://link.aps.org/doi/10.1103/PhysRevLett.93.011802.
- [98] P. Coyle et al. "The DIRC counter: a new type of particle identification device for B factories". In: Nuclear Instruments and Methods in Physics Research Section A: Accelerators, Spectrometers, Detectors and Associated Equipment 343.1 (1994), pp. 292—299. ISSN: 0168-9002. DOI: https://doi.org/10.1016/0168-9002(94)90568-1. URL: https://www.sciencedirect.com/science/article/pii/0168900294905681.

[99] F. Barbosa et al. "The GlueX DIRC detector". In: Nuclear Instruments and Methods in Physics Research Section A: Accelerators, Spectrometers, Detectors and Associated Equipment 876 (2017). The 9th international workshop on Ring Imaging Cherenkov Detectors (RICH2016), pp. 69-71. ISSN: 0168-9002. DOI: https://doi.org/10.1016/j.nima.2017.01.054. URL: https://www.sciencedirect.com/science/article/pii/S0168900217301122.

BIOGRAPHICAL SKETCH

Jesse António Hernández was born on June 10, 1994 on Long Island, New York to Ana Maria De Jesus and Joseph Ydani Hernández. He attended Valley Stream South High School for early education, where he graduated with honors in 2012. Following graduation, he was admitted and attended the State University of New York (SUNY) at Buffalo as a Bachelors of Science (B.Sc.) in physics. In 2016, he graduated from SUNY Buffalo with his B.Sc. in physics and a minor in mathematics. Following graduation from SUNY Buffalo, in the summer of 2017, he was accepted as a graduate student at Florida State University (FSU) as a bridge student. At FSU he researched theoretical nuclear physics culminating in a successful Masters Thesis and awarded his Masters of Science (M.Sc.) degree from FSU. He continued in physics by pursuing his Doctor of Philosophy (Ph.D.) degree at FSU researching experimental hadron physics.

Jesse A. Hernández, MSc

Curriculum Vitae

Education

Spring 2020 – **Doctor of Philosophy in Physics**, Florida State University, College of ongoing Arts and Sciences

• Doctoral Thesis: "Doubly-Strange Baryon Spectroscopy with GlueX Experiment:

Ground State Cascade Production Cross Section and Properties," under supervision of **Prof. Volker Credé**

Fall 2017 – Master of Science in Physics, Florida State University, College of Arts Fall 2019 – and Sciences

o Master's Thesis: "The Weak Form Factor: Nuclear Structure & Coherent Elastic Neutrino-Nucleus Scattering" under supervision of Prof. Jorge Piekarewicz

Fall 2012— **Bachelor of Science in Physics**, *University at Buffalo (SUNY)*, College Fall 2016 of Arts and Sciences

O Minor: Mathematics

Experience

Fall 2020— **Graduate Research Assistant**, Florida State University, Hadron Physics ongoing Group, under supervision of **Prof. Volker Crede**

 \circ Working to provide data analysis of the ground state and excited state Ξ baryon resonance states and extract relevant experimental measurements.

Spring 2017– Graduate Supervised Research, Florida State University, Nuclear The-Fall 2019 ory Group, under supervision of Prof. Jorge Piekarewicz

 Worked with density functional theory to understand electroweak probes for nuclear structure of various nuclei of interest as well as producing predictions for relevant observables such as cross section calculations from first principles and extracting model dependent parameters.

Fall 2018– **Graduate Assistant in Teaching**, Various Introductory Courses, Florida Spring 2019 State University

o Interacted with undergraduate students to facilitate learning in studio classes, held office hours on a weekly basis, and responsible for grading quizzes, midterms, and papers.

Jan 2018– **Private Physics and Math Tutor**, Varsity Tutors Platform, New York July 2018

 Provided high quality physics and math tutoring to college students in introductory courses.
 174 Undergraduate Supervised Research, SUNY Buffalo, High Energy Theory Particle Group, under supervision of **Prof. Cirian Williams**

- Worked on generating and developing monte carlo for femptobarn processes and simulating data such as invariant masses and cross section measurements for these processes.
- Spring 2016 **Undergraduate Supervised Research**, SUNY Buffalo, High Energy Fall 2016 Theory Particle Group, under supervision of **Prof. Cirian Williams**
 - Worked on generating and developing monte carlo for femptobarn processes and simulating data such as invariant masses and cross section measurements for these processes.

Public Presentations

- April 4, 2024 Invited Talk, Overview of Hyperon Physics in Photoproduction at GlueX, Hadron Spectroscopy with Strangeness, University at Glasgow
 - March 31, **Seminar Talk**, Photoproduction of Ground State Cascade at GlueX: 2023 Road to Cascade Production Cross Section, Nuclear Seminar, Florida State University
- November 9, **Conference Talk**, Measuring the Photoproduction Cross Section of the 2022 Ground State Cascade Baryon, Baryons 2022 International Conference on the Structure of Baryons, Universidad Pablo de Olavide de Sevilla
- November 19, Conference Talk, $\Xi(1320)^-$ Differential Cross Section in Photoproduc-2021 tion, 88th Annual Meeting of the APS Southeastern Section, Florida State University
 - September Seminar Talk, Nuclear Weak Form Factor: Nuclear Structure and CEνNS, 17, 2019 Nuclear Seminar, Florida State University

Publications

November **Editor's Suggestion**, Junjie Yang, Jesse A. Hernández, and J. 2019 Piekarewicz, "*Electroweak probes of ground state densities*" in *Phys. Rev. C*, vol. 100, iss.5

Honors & Awards

- o Department Award
- Invited Speaker
- o Recognition of External Fellowships and Awards, FSU Graduate School
- o JSA/Jlab Graduate Fellowship
- APS Bridge Program Fellow

Independent/Group Projects

Special Topics in Hadron Physics, Missing Cascade Baryons: 'Missing Resonance Problem'

 Objective was to relate what we learned in class to a project of interest, write up a proposal demonstrating the problem and methods to solve it and present our findings.

Scattering Theory Course at University of Indiana, Dalitz-plot decomposition for $Y(1^-) \to J/\psi(1^-)\pi^+\pi^-$

 Responsible for constructing the dalitz-plot function including particles with arbitrary spin and analyzing its properties to verify the methodology for this approach and present the results.

Activities

Member of GlueX Collaboration

Spring 2017– Board Member of Physics Graduate Student Association, First Fall 2019 Year Representative and Treasurer

- As the first year representative I was responsible for making sure that the new student's voices were heard and needs provided for.
- As the treasurer I was responsible for budgeting and applying for funding through the university, provided any funding for events hosted by the PGSA, and coordinated all sales and funding for the bi-annual Circus of Physics, a large departmental event to provide scientific outreach to the community, at FSU.

Skills

Programing Languages
 Python, C/C++, ROOT, Julia, Mathematica, Latex